Macromolecular Symposia
www.ms-journal.de

Thermal Insulation Capacity of a 3D Printed Material

Andrei Mihalache, Adelina Hriţuc, Marius Boca, Bogdan Oroian, Ionuţ Condrea, Carmen Botezatu, and Laurenţiu Slătineanu*

The 3D printing process allows obtaining parts with different interior structures and made of different materials. Such parts can be used to avoid overheating of various objects under the action of thermal radiation. The existence of different internal structures of the parts, as well as the 3D printing conditions and the distinct physical properties of the materials used, determine a different behavior of the parts in terms of their thermal insulation capacity. To obtain an image of the thermal conductivity of thin parallelepiped-shaped parts achieved by 3D printing, experimental research is conceived and materialized. The experiments involve the use of an infrared heat source, respectively, measurement of temperature on the surface opposite to that exposed to thermal radiation. The obtained results are mathematically processed to obtain empirical mathematical models that would highlight 3D printed parts' ability to be used as thermal insulating materials.

1. Introduction

The 3D printing process can be used to manufacture parts with different internal structures and made of different materials. Sometimes, such parts are the components of the walls used to avoid overheating various objects under thermal radiation. The 3D printing conditions, the distinct physical properties of the materials, and the heating conditions determine the parts' different behavior in terms of their thermal insulation capacity.

The industrial practice has highlighted situations when plates made of different materials are used to avoid or reduce parts' heating under the action of thermal radiation emitted by a heat source. Such plates can be obtained by different processes, one of which is 3D printing. On the other hand, there are situations in which the heat transfer must be done with a certain intensity in certain parts. The main feature pursued in such situations is the thermal insulation capacity of the plate material. From a thermal point of view, the investigation focuses on thermal conductivity. This property is defined as a physical size that characterizes a material's ability to transmit heat by thermal conduction when there is a temperature difference between the part's surfaces made of the investigated material.

A. Mihalache, A. Hriţuc, M. Boca, B. Oroian, I. Condrea, C. Botezatu, L. Slătineanu
"Gheorghe Asachi" Technical University of Iaşi
D. Mangeron Blvd 39A
Iaşi 700050, Romania
E-mail: hrituc.adelina3295@yahoo.com

DOI: 10.1002/masy.202000286

The thermal conductivity of materials incorporated in 3D printed parts was investigated using different methods and means. Thus, Flaata et al. have designed and materialized a device capable of testing composite materials' thermal conductivity included in parts obtained by 3D printing.[1] Elkholy and Kempers studied the influence of factors that characterize the fused deposition modeling process on the thermal properties of 3D printed materials.[2] The anisotropy of some composite materials' thermal conductivity from the parts of the space-based cube satellites was investigated by Shemelya et al.[3]

The research presented in this paper aimed to highlight the influence exerted by some factors on the thermal insulation capacity of small plates made of a polymeric material by 3D printing.

2. Theoretical Premises

For the study of the thermal insulation capacity of 3D printed materials, the case of a small panel (of a plate) was taken into account, subjected to the heating action under the action of an infrared lamp. We will accept that due to the positioning of the infrared radiation lamp, along with the smallest distance between the lamp and the panel, the radiation will propagate perpendicular to the panel (**Figure 1**). It is expected the radiation will lose its intensity with the increase of the radius of a spherical sector with the center in the infrared lamp.

When contacting the test sample surface, the heat flux will increase in temperature primarily in the surface layer (**Figure 2**a). Next, the heat will propagate through the panel, causing the temperature to rise and the surface opposite to the lamp-oriented one. By measuring the increase in temperature of the material heated by infrared radiation over the minimum distance between the lamp and the panel, we obtain an image of the surface's heating speed facing the lamp. If the temperature on the panel's opposite surface is measured over time, additional information will be obtained regarding the heat transfer through the panel material. For a certain power of the heating source (of the lamp with infrared radiation), for a certain distance between the lamp and the panel, and a certain structure of the panel material, a stationary temperature will be reached at some points on the two opposite sides of the panel. This situation corresponds to a thermal balance when the entire amount of heat received from the lamp dissipates in the plate and the environment.

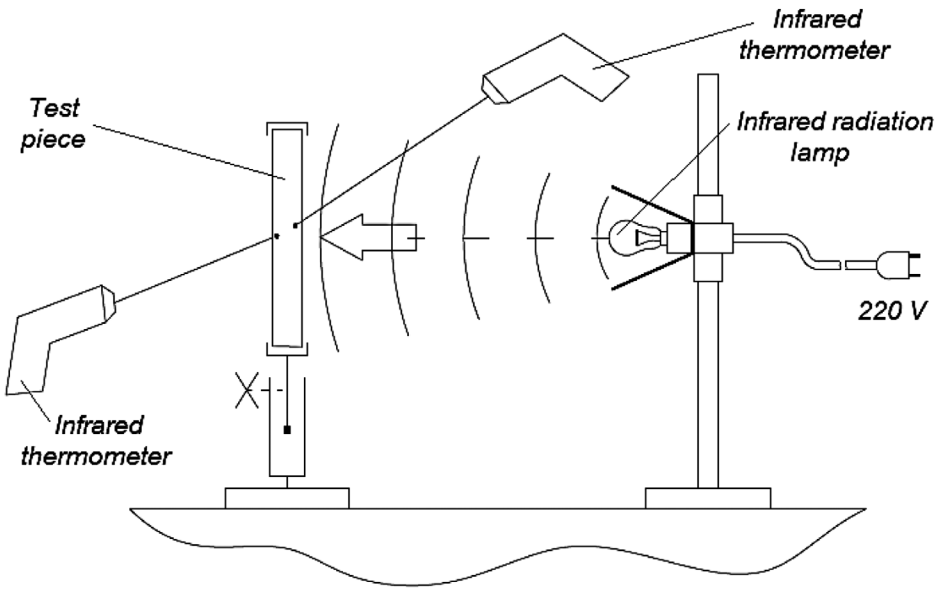

Figure 1. The testing scheme used.

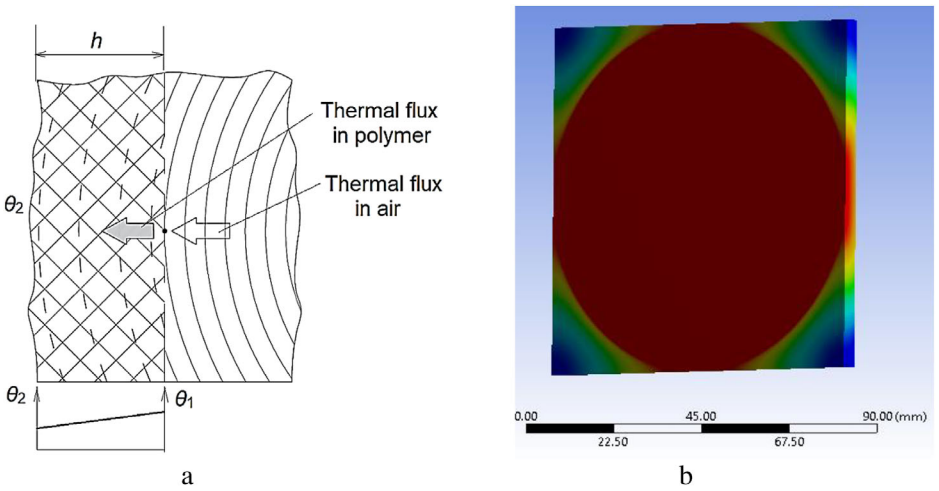

Figure 2. Temperature variation between the plate-type test sample walls (a) and FEM model of the heat propagation in the plate-type test sample (software: ANSYS R19.2) (b).

It is accepted that the temperature reached behind the plate and the speed of heat transmission through the plate are dependent on the power of the infrared radiation source, the distance between the source and the panel, the characteristics of the panel material, and its internal structure.

3. FEM Model

Modeling using the finite elements method (FEM) of the hypothetical situation presented above could lead to a better evaluation and understanding of the behavior of 3D printed materials subjected to the effects of a heat source. Due to the smaller distance between the infrared radiation source and the test sample, the test sample has a central area with a higher temperature due to the propagation of infrared radiation. Simultaneously, the corners remain colder due to the shape of heat waves (Figure 2b). Examining from the side of the graphical representation obtained by FEM simulation, it is possible to observe the tendency of temperature decrease along with the test sample's thickness. This fact is due to the low thermal conductivity of the test sample obtained by 3D printing.

4. Experimental Conditions and Results

The experimental research aimed to determine the extent to which the panel material's thermal insulation capacity is influenced in principle by the thickness of the test sample obtained the 3D printing process used in the manufacture of the panel. The elements taken into account are those existing in the sketch in Figure 1. Infrared radiation lamps with nominal powers of

Table 1. Experimental conditions and results.

Exp.No.	Input factors (coded value/real value)				Output parameters	
	Nominal power, N_s, [W]	Distance d, [mm]	Panel thic-kness, h, [mm]	Time t, [min]	Tempe-rature, θ_1, [°C]	Tempe-rature, θ_2, [°C]
1	1/100	1/200	1/2	1/2	39	38
2	1/100	1/200	1/2	2/12	49	48
3	1/100	2/250	2/4	1/2	36	32
4	1/100	2/250	2/4	2/12	45	41
5	2/250	1/200	2/4	1/2	38	36
6	2/250	1/200	2/4	2/12	55	50
7	2/250	2/250	1/2	1/2	39	38
8	2/250	2/250	1/2	2/12	47	46

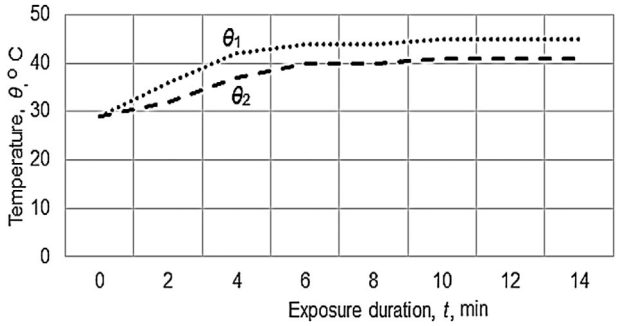

Figure 3. The effect of exposure time t on the temperatures θ_1 on the face directly exposed to the action of infrared radiation and on θ_2 on the back of the panel, respectively (N_s = 100 W, d = 250 mm, h = 4 mm).

100 and 250 W were used. The polymeric material panels were square, with dimensions of 100 × 100 mm^2 and two different thicknesses (2 and 4 mm). The test sample material was polylactic acid provided by Ultimaker.[4] The temperature measurement was performed using an industrial digital thermometer. It was preferred to perform experimental tests according to a factorial experiment's requirements with four input factors at two levels.[5] A fraction of a factorial experiment of the Taguchi L9 type was used. The four input factors were the power of the heating source N_s, the distance d between the lamp and test sample, the thickness h of the test sample, the duration t of exposure of the test sample to the action of infrared radiation. The values of the mentioned above process input factors were shown in the columns nos. 2–5 in **Table 1**. The temperatures measured in the center of the test sample surface and on the opposite side of the test sample were shown in the last two columns in Table 1. **Figure 3** shows the increase in temperature over time on the two surfaces of the test sample.

The mathematical processing of the experimental results when using a computer program based on the use of the least squares method [6] led to the following mathematical model for the temperatures θ_1 (measured along the axis corresponding to the smallest distance between the infrared lamp and the test sample, on the surface facing the lamp) and θ_2 (measured along the same axis, but at the back of the test sample):

$$\vartheta_1 = 156 N_s^{0.0581} d^{-0.332} h^{-1.225} t^{0.140} \quad (1)$$

$$\vartheta_2 = 220.3 N_s^{0.0746} d^{-0.402} h^{-0.108} t^{0.139} \quad (2)$$

where N_s is the nominal source power (W), d – the distance between the infrared lamp and the test sample (mm), h – the test sample thickness (mm), and t – the duration of the exposure to

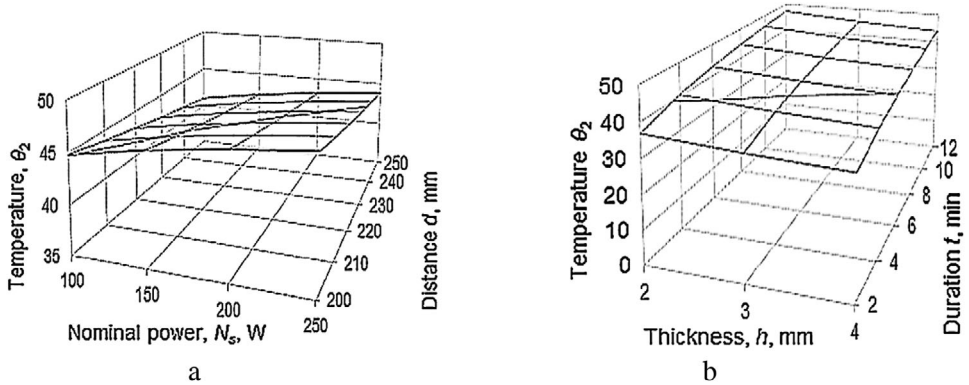

Figure 4. Effect of nominal power N_s and distance d on the temperatures θ_2 on the back of the test sample (h = 4 mm, t = 12 min) (a), and effect of the test sample thickness h and the exposure duration on the temperature θ_2 (N_s = 250 W, d = 250 mm) (b).

the action of the infrared radiation (min). In the empirical models, some exponents' values are quite close. This fact means similar aspects in the evolution of the temperature on the test sample's two surfaces.

As expected, there is an increase in temperatures as the infrared lamp nominal power and the duration of exposure increase and, at the same time, a decrease in temperatures as the distance between the lamp and the test sample and the sample's thickness increase. The empirical mathematical model corresponding to the Equation (2) was used to elaborate the graphical representations in **Figures** 3 and **4**.

5. Conclusions

There are situations when the 3D printed parts could be used to generate an obstacle to the thermal effects. Experimental research was designed and performed to highlight the intensity of the influence exerted by several input factors in the process of exposure to infrared radiation on the temperature on two opposite surfaces of the test sample. The mathematical processing of the experimental results showed that a stronger influence was exerted by the distance between the infrared radiation lamp and the test sample, the thickness of the 3D printed test sample, and the duration of the exposure on the action of the heat source.

Conflict of Interest

The authors declare no conflict of interest.

Keywords

3D printing, empirical mathematical model, experimental research, temperature measurement, thermal conductivity

[1] T. Flaata, G. J. Michna, T. Letcher, presented at ASME 2017 Summer Heat Transfer Conference, HT2017, Bellevue, Washington, USA, July, **2017**.
[2] A. Elkholy, R. Kempers, *Proceedings of the CSME International Congress*, **2018**.
[3] C. Shemelya, A. De La Rosa, A. R. Torrado, K. Yu, J. Domanowski, P. J. Bonacuse, R. E. Martin, M. Juhasz, F. Hurwitz, R. B. Wicker, B. Conner, E. MacDonald, D. A. Roberson, *Addit. Manuf.* **2017**, *16*, 186.
[4] https://ultimaker.com/materials/pla, accessed 20.09.2020.
[5] L. Slătineanu, *Fundamentals of Scientific Research (in Romanian)*, PIM, Iaşi, Romania, **2019**.
[6] G. Creţu, *Fundamentals of experimental research. Laboratory handbook (in Romanian)*, "Gheorghe Asachi" Technical University of Iaşi, Romania, **1992**.

machines

MDPI

Article

Evaluation of the Ability to Accurately Produce Angular Details by 3D Printing of Plastic Parts

Andrei Marius Mihalache [1], Gheorghe Nagîț [1], Laurențiu Slătineanu [1], Adelina Hrițuc [1], Angelos Markopoulos [2] and Oana Dodun [1,*]

[1] Department of Machine Manufacturing Technology, Gheorghe Asachi Technical University of Iasi, 700050 Iaşi, Romania; andrei.mihalache@tuiasi.ro (A.M.M.); nagit@tcm.tuiasi.ro (G.N.); slati@tcm.tuiasi.ro (L.S.); adelina.hrituc@student.tuiasi.ro (A.H.)

[2] Department of Mechanical Engineering, National Technical University of Athens, 15780 Athens, Greece; amark@mail.ntua.gr

* Correspondence: oanad@tcm.tuiasi.ro; Tel.: +40-747144604

Abstract: 3D printing is a process that has become widely used in recent years, allowing the production of parts with relatively complicated shapes from metallic and non-metallic materials. In some cases, it is challenging to evaluate the ability of 3D printers to make fine details of parts. For such an assessment, the printing of samples showing intersections of surfaces with low angle values was considered. An experimental plan was designed and materialized to highlight the influence of different factors, such as the thickness of the deposited material layer, the printing speed, the cooling and filling conditions of the 3D-printed part, and the thickness of the sample. Samples using areas in the form of isosceles triangles with constant height or bases with the same length, respectively, were used. The mathematical processing of the experimental results allowed the determination of empirical mathematical models of the power-function type. It allowed the detection of both the direction of actions and the intensity of the influence exerted by the input factors. It is concluded that the strongest influence on the printer's ability to produce fine detail, from the point of view addressed in the paper, is exerted by the vertex angle, whose reduction leads to a decrease in printing accuracy.

Keywords: 3D printing; printing accuracy; isosceles triangular samples; influence factors; empirical mathematical models

Citation: Mihalache, A.M.; Nagîț, G.; Slătineanu, L.; Hrițuc, A.; Markopoulos, A.; Dodun, O. Evaluation of the Ability to Accurately Produce Angular Details by 3D Printing of Plastic Parts. *Machines* **2021**, *9*, 150. https://doi.org/10.3390/machines9080150

Academic Editor: César M. A. Vasques

Received: 30 June 2021
Accepted: 27 July 2021
Published: 29 July 2021

1. Introduction

A remarkable expansion, both in manufacturing and in research in different fields, can be seen at present in additive manufacturing.

The manufacturing technologies included in additive manufacturing are based on the gradual generation of a part due to the successive deposition of the material layers through different processes until producing the complete part. In some cases, post-additive-manufacturing operations may be required to fit the part within the prescribed quality parameters. The successive deposition of the layers of material can occur through processes such as fused-deposition modeling, plastic jet printing, selective laser melting, selective laser sintering, digital light processing, laminated object manufacturing, and stereolithography [1–4].

The main advantage of additive manufacturing is versatility, as it is possible to produce parts with very different shapes and sizes in a wide range of materials, including both plastics and metals. A disadvantage of additive manufacturing is its relatively low productivity in the case of series or mass production. The problem has been solved, for the time being, by increasing the quantity of equipment involved in the additive manufacturing of the desired product. This has been facilitated in the last decade by a significant reduction in the prices of certain categories of equipment used for 3D printing.

When selecting one of the additive manufacturing processes, it is necessary to take into account different criteria, such as the functional role of the future part [5–11], the nature of the material from which the part will be made, the physical and mechanical properties of the part material [12–19], the performance of the 3D-printing process [11,20], the accuracy and roughness of the surfaces obtained, and last but not least, the cost of manufacturing the part [7,21].

Concerning manufacturing accuracy, there are some differences of opinion between applicants as to how it should be assessed.

Thus, many researchers have followed the extent to which it is possible to make parts usable for medical purposes by 3D printing. Msallem et al. investigated the achievable accuracy using five additive manufacturing technologies to produce anatomical mandibular models [22]. They found that the highest accuracy corresponds to fused-filament fabrication technology. According to one of their conclusions, when selecting the additive manufacturing technology, the available materials, the destination, and the final product cost must still be considered.

Three 3D-printing procedures were analyzed by Yoo et al. to evaluate the dimensional accuracy that can be obtained in the case of dental models for three-unit prostheses [23]. The most accurate models were produced using the multi-jet printing process, but these models had disadvantages in buccolingual contraction and surface roughness. Taking into account such aspects, in the end, a procedure using a stereolithography apparatus was preferred.

Dorweiller et al. aimed to evaluate the accuracy of vascular anatomy models manufactured by two 3D-printing technologies, namely fused-deposition modeling and PolyJet [24]. The comparison of the processes was performed considering the deviations of the wall thickness from the dimensions entered in the original STL file. The results were assessed as acceptable for the two procedures under analysis.

A 3D-printing process based on fused-filament fabrication was used by Lee et al. to generate 3D-printed models to delineate congenital heart disease [25]. The verification of the manufacturing accuracy of these models was performed by comparison with computed tomography images and standard tessellation language (STL) and by using specific comparison indicators. They considered the necessary accuracy requirements to be met.

A comparison of dental stone models with some 3D-printed acrylic replicas was made by Czajkowska et al. [26]. Precision and mechanical properties were used as comparison criteria. The results proved the superiority of 3D-printed models in terms of the comparison criteria used compared to dental stone models.

A comprehensive control system designed to meet the requirements of Industry 4.0 was proposed by Budzik et al. for the evaluation of products made of polymeric materials [27]. They appreciated that the manufacture of thermoplastic ABS by the MEM (melted and extruded modeling) method could ensure the highest accuracy. However, in evaluating manufactured products, economic aspects must be taken into account.

Another group of researchers aimed to identify different shapes of parts that could be used to test the ability of additive manufacturing processes to produce certain details of the part [28,29] accurately.

To investigate the accuracy of 3D printing of patient aortic anatomies, Kaschwich et al. [30] studied the differences between some computed tomography data from people and the deviation of the 3D vascular models. The relative deviations of the measured values showed no significant differences, proving that 3D printing can create vascular models with reliable accuracy.

Additionally, in the medical field, some researchers compared a dental implant made by FDM 3D printing with a light-cured template [31]. The conclusion was that the printed implant replacement was as accurate as the light-cured template and more efficient.

Interest in the uses of 3D printing is high in the medical field, so a comparison can also be found between milling and 3D-printing processes in the case of try-in dentures.

The results highlighted the overall performance of 3D printing, with an excellent accuracy placing it in the clinically acceptable range for try-in prostheses [32].

Like any process based on temperatures corresponding to the melting of material, residual stresses are expected to occur. Appropriate solutions were analyzed and proposed to reduce the influence of residual stresses on the manufacturing accuracy of parts, including by considering the correlations between strength and ductility of the material [33].

2. Hypotheses

Traditionally, manufacturing processes address all actions and procedures needed to transform raw materials and blanks into finite products. Its main stages include: producing the blanks, manufacturing, technical checkups, assembly, dyeing, packaging, and shipment. One of the most significant parameters that influences the ability of equipment to produce fine details is processing accuracy. It can be defined by considering the consistency degree between dimensions, surface quality, geometrical shape, and relative position accuracy. In machining, it often takes into account dimensional and shape accuracy and the reciprocal position of surfaces.

In the case of 3D printing, most of the ways mentioned above of assessing the ability of equipment to produce high-precision parts could be supplemented by taking into account other aspects. Given the specific conditions for generating surfaces, a 3D printer may lead to better results than its equivalent alternatives, but these results may be affected by certain limitations.

This paper investigates the possibilities of 3D printing of parts with areas characterized by the intersection of surfaces at small angles. It has been assumed that the smaller the value of the angle, the lower the accuracy of some dimensions. First, it was decided to print samples that included triangles of the same height but with smaller and smaller angle values. Subsequently, attention was paid to the 3D printing of samples that included isosceles triangles characterized by the identical lengths of their bases.

The hypothesis that the accuracy of making areas with intersections in the form of sharp vertices could be improved if the thickness of the sample were large was still considered. Previously obtained results in the case of profiles generated on a plate had confirmed that areas characterized by intersection angles with sizes below a certain limit would no longer be able to be materialized by 3D printing, which will affect some dimensions of the produced parts [28]. Such a result could be even more obvious if the areas with sharp angles were not supported by a plate to which they were attached (Figure 1a).

As mentioned, in the case proposed for investigation, the samples were first considered small prisms, with a cross-section in the form of isosceles triangles with decreasing angles, but with the same height of all triangles (Figure 1a).

Based on the above, the question arose as to what would result from producing prisms with cross-sections in the form of isosceles triangles with bases of the same length b and heights h depending on the sizes of the angles of the vertices of the isosceles triangle (Figure 1a). In such a triangle, we can write a theoretical relation that shows the dependence of the height h of the isosceles triangle on the length b of the base of the isosceles triangle and the dependence of both, respectively, on the size of the vertex angle α:

$$h = f(b, \alpha) \tag{1}$$

Based on geometric considerations, it can be written as follows:

$$h = \frac{b}{2tan\frac{\alpha}{2}} \tag{2}$$

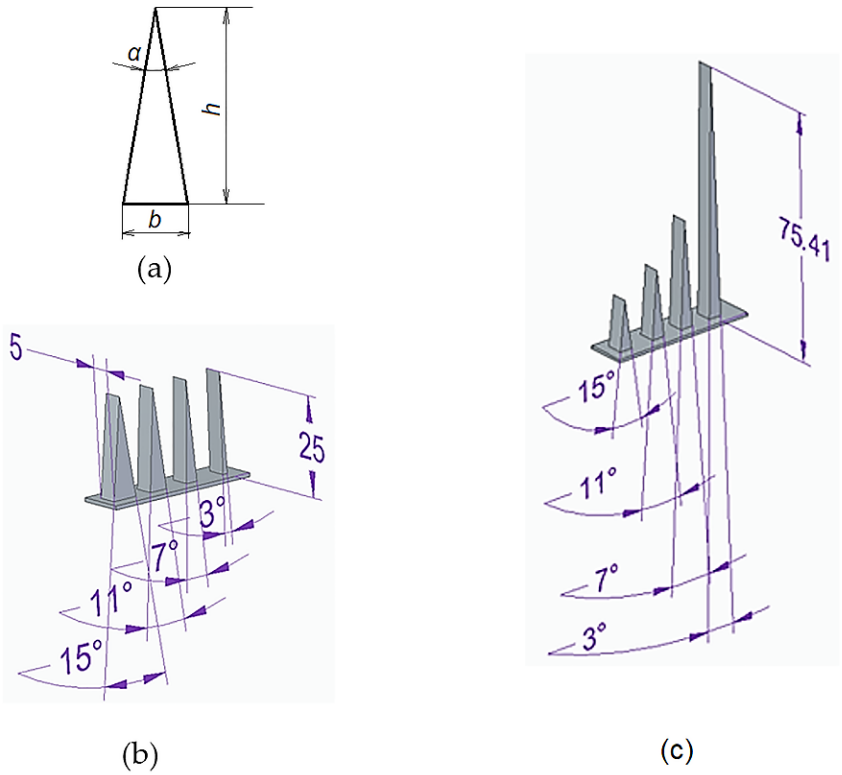

Figure 1. Considered dimensions of the triangle (**a**) and a sample consisting of triangles: (**b**) that have the same height h; (**c**) that have the same length l of the base.

Therefore, the form $h = f(\alpha, b)$ function will be valid in this case. The values of the angle α and the common value b of the size of the base of the triangle are known. Thus, it will be possible to determine the theoretical heights of the triangles. However, because it is expected (as in the previous case) that the areas characterized by low values of angles α cannot be produced by 3D printing, there will also be a dimensional deviation of the heights of the real samples from the theoretical variation assumed by Equation (1).

Not only the values of the angles corresponding to the vertices of the isosceles triangles in the previous case will influence the accuracy of achieving the height h of the triangles when making samples by 3D printing. The research carried out so far highlights groups of factors with possible influence on the ability of equipment to make fine details by 3D printing. Some such groups of factors are the following:

- The values of certain dimensions that characterize the shape of the sample surfaces to be produced (the presence of some intersections made by small values of the intersection angles or the connection radii, the thickness of the sample, the coefficient of the slenderness of some areas of the sample, etc.);
- Characteristics of the wire/filament generated by the printer nozzle (diameter of the deposition filament, corresponding to the diameter of the nozzle hole) and of the filament material (melting temperature, viscosity, specific heat and thermal conductivity, thermal shrinkage, the adhesion capacity between the deposited layers, etc.);
- Elements of thermal conditions of operation of some components/subassemblies of the printer (heating temperature of the nozzle, temperature of the plate on which the deposition takes place, ventilation cooling, etc.);
- Parameters that characterize the deposition conditions (travel speed between nozzle and printer table, the thickness of the deposited layer, etc.);
- The degree of filling of the spaces between the walls of the sample, etc.

Experiments carried out by printer manufacturers have led to the formulation of recommendations by printer manufacturers for the values of some of the working parameters that their users could take into account.

The values of the input factors used in the 3D printing of samples consisting of triangles designed to have the same height h were included in Table 1.

Table 1. Experimental conditions and results in 3D printing of samples consisting of triangles designed to have the same height h.

Exp. No.	Values of the Input Factors					Achievable Height h of the Triangle, mm, by Considering G Code/Real Height of the Triangle, mm, for Vertex Angle α, °, of:				Deviation, Δ, mm
	Deposited Layer Thickness t_l, mm	Printing Speed v, mm/s	Cooling c, %	Infill i, %	Sample Thickness t_s, mm	15	11	7	3	
1	0.06	50	0	22	5	23.9343/23.8	23.2522/23.4	21.9121/22.2	17.3723/17.8	0.7568
2	0.06	55	50	20	7.5	23.8254/24	23.1613/23.5	22.0139/22.1	17.5799/17.8	0.5568
3	0.06	60	100	18	10	23.815/23.9	23.4581/23.4	22.1120/22.2	18.4442/17.8	0.6568
4	0.1	50	50	18	5	23.8652/24	23.2738/23.4	22.5883/22.2	17.9017/17.7	0.5568
5	0.1	55	100	22	7.5	23.8883/24	23.4691/23.4	22.0833/22.2	17.6337/17.7	0.5568
6	0.1	60	0	20	10	23.8816/23.9	23.4008/23.4	21.9920/22.2	17.6675/17.7	0.6568
7	0.15	50	100	20	5	23.8882/24	23.3956/23.4	21.9474/22.3	17.4919/17.7	0.5568
8	0.15	55	0	18	7.5	23.8784/23.9	23.1641/23.4	22.2486/22.2	17.5280/17.7	0.6568
9	0.15	60	50	22	10	23.8670/23.9	23.4079/23.4	22.1936/22.1	17.7187/17.8	0.6568

3. Materials and Methods

A test sample with the shape and dimensions shown in Figure 1b was first designed to verify experimentally some of the theoretical considerations mentioned above.

The actual samples were made of polylactic acid (PLA), one of the most attractive materials for the planned experiment due to its high versatility. From the multitude of factors capable of influencing the height of isosceles triangles, in experimental research, the thickness t_l of the deposited layer, printing speed v, cooling c, infill I, and the size of the isosceles vertex angle α were taken into account.

The samples were produced on an Ultimaker 2+ type of equipment (made by Ultimaker—Netherlands) with its own designated software Ultimaker Cura.

To reduce the number of experimental tests and, at the same time, to arrive at a sufficiently precise image of the influence exerted by the variation of the input factors in the printing process on the values of the output parameters, a planned factorial experiment using the Taguchi L9 method was used, with five independent variables (layer thickness, printing speed, cooling, infill, and sample thickness) at three experimental levels. An L9 orthogonal array allows the use of a minimum number of experimental trials to study the effect of 5 independent factors, each with three levels of evaluation. Such an experiment can be used when accepting the hypothesis that there is no interaction between any two factors [34].

There are many input factors of the 3D-printing process that could be considered as independent variables. From this multitude of factors, those factors were taken into account that could be assumed to have a significant influence on the values of the output parameters. Attention was also paid to the possibilities of using different values for input factors on the available 3D-printing equipment.

When establishing the initial values of the independent variables (of the input factors in the 3D-printing process), the printer manufacturer's recommendations were taken into account first. Thus, three distinct thicknesses t_l of the deposited layers were used (0.06 mm, 0.1 mm, and 0.15 mm), as well as three printing speeds v (50 mm/s, 55 mm/s, and 60 mm/s, three characterized cooling regimes c (0%, 50%, and 100%), three levels of filling (infill) i of the inner space of the sample (18%, 20%, and 22%), and three thicknesses t_s of the samples (5 mm, 7.5 mm, 10 mm).

Intending to arrive at some empirical mathematical models that highlight the influence of other input factors in the 3D-printing process, apart from those initially considered by using the planned Taguchi L9 factorial experiment, blocks of 4 adjacent isosceles triangles were printed, as can be seen in Figures 2 and 3 and Table 1, with vertex angles of 15°, 11°, 7°, and 3°.

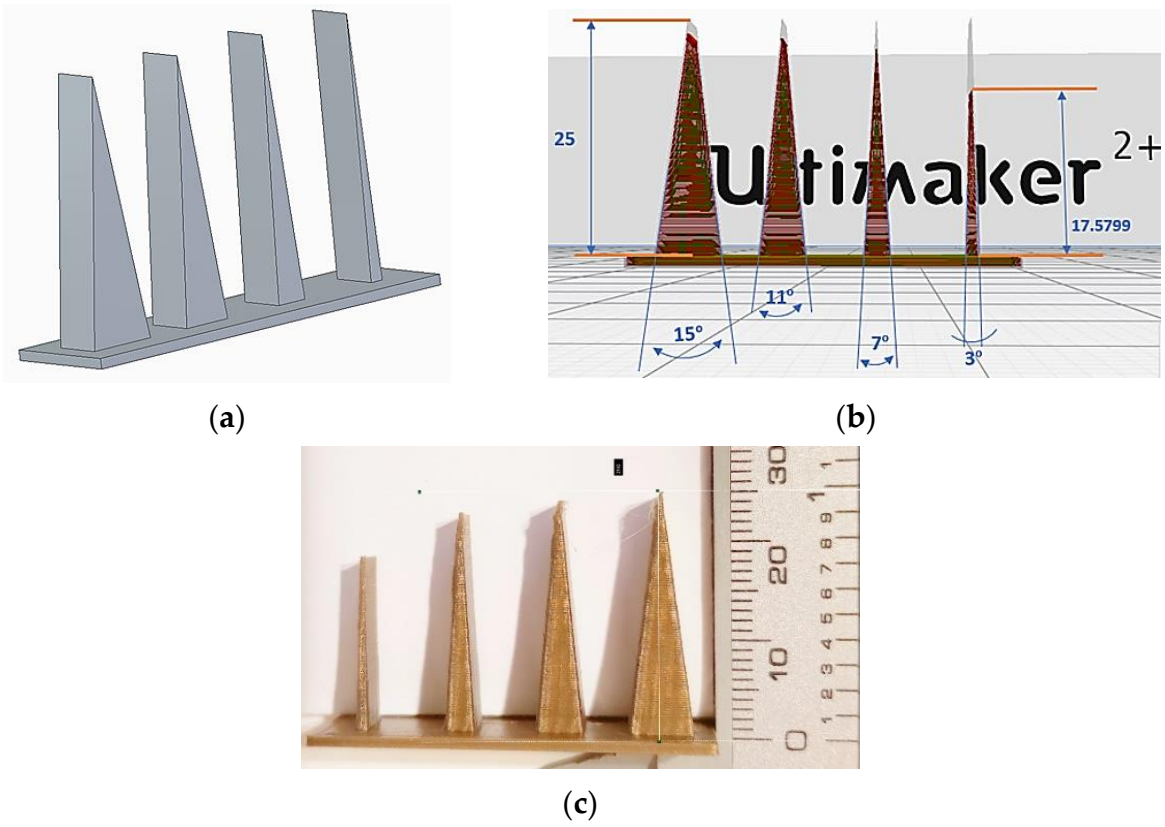

Figure 2. Images of the designed sample (**a**), the sample produced using reverse engineering and G code (**b**), and the real sample (**c**) (work conditions: t_l = 0.06 mm, v = 60 mm/s, *cool* = 100%, I = 18%, t_s = 10 mm), in case of the need to obtain triangles of the same height h, but with different values of the vertex angle α.

Preliminary tests showed, however, that it is not possible to produce acceptable samples with a thickness below 5 mm in the same setup as the authors used. In the latter case, due to a less acceptable combination of the values of the printing parameters (values established based on the printer manufacturer's recommendations), thin samples were found that do not interrupt when switching from one isosceles triangle to another.

The values of the input factors in the process of 3D printing the samples aimed at obtaining triangles with the same height are included in Table 1.

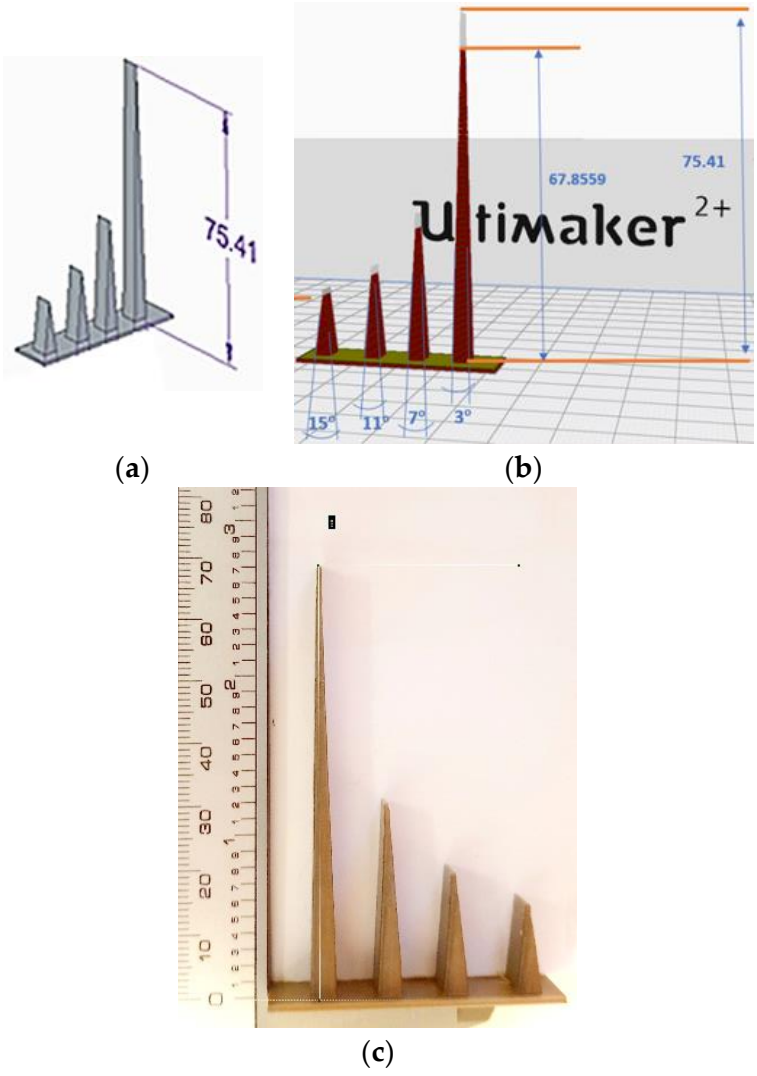

Figure 3. Images of the designed sample (**a**), of the sample, produced using the inverse engineering and G code (**b**), and of the real sample (**c**) (work conditions: t_l = 0.06 mm, v = 60 mm/s, c = 100%, I = 18%, t_s = 10 mm), in case of the need to obtain triangles with the same length b of the base for different values of the vertex angle α.

4. Results

According to the hypotheses initially adopted, the tests showed different heights of the four isosceles triangles with visibly different values of the vertex angles α, in the case of tests that were to lead to the same height h for all four isosceles triangles. In this way, additional information was obtained on the ability of the printing equipment to achieve precise details of the printed parts.

It was also expected that, from a practical point of view, differences in the heights of the triangles would occur when the execution of isosceles triangles with the same size of the base length was considered.

The actual heights h of the triangles were determined by measurement using a LeeXo 50-1600X digital optical microscope (China). The values of the heights of the triangles are also included in Table 1.

Examination of the facilities offered by the software used to program the printing process showed that an image of the heights of isosceles triangles achievable by 3D printing could be obtained using a reverse-engineering process applied to the G codes developed by the software for each situation. Thus, we designed the 3D prisms in a CAD environment,

namely SolidEdge. We saved our samples in .stl format and imported them into the Ultimaker Cure software, where we used specific settings for each sample. After all the printing parameters were established, we sliced each sample and saved the document in a .gcode file format. These files were fed to the 3D printer, and each sample was produced. We reverse-engineered the .gcode files by importing each of them into the Voxelizer software where, specifying exactly the same layer height as the one used for each sample, we converted them to the .stl format. Each new .stl format document was imported into Ansys SpaceClaim, where we measured the height h of each sample accurately.

Thus, it was possible to highlight some aspects of the printer's capability before the actual printing process. For a sample thickness t_s = 10 mm, and for certain values of the parameters of the printing conditions, in Figure 2, the solid model of the sample, the model obtained by reverse engineering, and the real image of the printed sample can be observed. Images similar to those in Figure 2, but valid for the situation when it was proposed to obtain isosceles triangles that have the same length b of the base of the triangle and heights h determined by the value of the vertex angle α, can be seen in Figure 3.

5. Discussion

The experimental results included in Tables 1 and 2 were mathematically processed using specialized software [35]. Thus, empirical mathematical models of the power-function type were determined. It was preferred to identify some mathematical functions such as power-type functions, considering that due to the intervals of variation of the input factor values, monotone variations of the values of the heights of the isosceles triangles will be produced from the 3D-printing process. Such mathematical models of the power-function type are also frequently used in various situations in machine manufacturing. The mathematical processing of the experimental results included in Tables 1 and 2 with the help of specialized software was based on the least-squares method.

Table 2. Experimental conditions and results in 3D printing of samples consisting of isosceles triangles designed to have the same length b of the base.

Exp. No.	Values of the Input Factors					Intended Height of the Triangle, mm, by Considering the G Code/Real Height of the Triangle, mm, for Vertex Angle α, °, of:				Deviation Δ, mm
	Deposited Layer Thickness t_l, mm	Printing Speed v, mm/s	Cooling c, %	Infill i, %	Sample Thickness, t_s, mm	15	11	7	3	
1	0.06	50	0	22	5	13.9293/13.8	18.7728/18.8	29.1808/29.5	67.8049/71	0.9416
2	0.06	55	50	20	7.5	13.8192/13.9	19.2261/19	29.2671/29.6	67.8508/68.5	0.8416
3	0.06	60	100	18	10	13.9112/13.9	18.9852/19.1	29.4398/29.5	67.8559/68.4	0.8416
4	0.10	50	50	18	5	13.8178/14	19.7232/19	29.9709/29.6	68.1037/68.8	0.7416
5	0.10	55	100	22	7.5	13.8361/14	18.7852/18.9	29.4599/29.5	68.246/68.5	0.7416
6	0.10	60	0	20	10	13.8679/14	19.125/18.8	30.0142/29.6	68.0931/68.5	0.7416
7	0.15	50	100	20	5	13.9187/14	20.1006/19	29.5744/29.5	67.8714/68.5	0.7416
8	0.15	55	0	18	7.5	13.919/14	19.161/19	29.6599/29.5	68.0868/69.4	0.7416
9	0.15	60	50	22	10	14.3825/14	19.4766/19	30.1188/29.5	68.0014/68.8	0.7416
Theoretical height h of the isosceles triangle, mm, taking into account a base length b = 3.95 mm and distinct values of the vertex angle α						14.7416	20.3209	32.1701	75.3704	

In the case of samples including triangles with desired constant height h, the following empirical mathematical models were obtained:

- For the height determined by using G code:

$$h = 5.162 t_l^{-0.00121} v^{0.324} c^{0.000330} i^{-0.0343} t_s^{-0.0781} \alpha^{0.190} \quad (3)$$

- By using the experimental results:

$$h = 19.929 t_l^{-0.000713} v^{-0.0860} c^{0.000078} i^{-0.00131} t_s^{0.0215} \alpha^{0.190} \quad (4)$$

Regarding the samples containing isosceles triangles with bases of the same length b, the following mathematical models were determined:

- For the theoretical variation of the height h of the triangles, Equation (2) remains valid;
1. For the variation of the height h of the triangles determined by taking into account the G code:

$$h = 43.405 t_l^{0.0228} v^{0.441} c^{0.000645} i^{0.0165} t_s^{-0.123} \alpha^{-0.975} \quad (5)$$

- By taking into account the experimental results:

$$h = 320.696 t_l^{0.00120} v^{-0.122} c^{-0.0000890} i^{-0.00440} t_s^{0.0290} \alpha^{-0.992} \quad (6)$$

Using the empirical mathematical models corresponding to Equations (3)–(6), the graphical representations in Figures 4 and 5 were elaborated. Analysis of these graphical representations and of the empirical mathematical models constituted by Equations (3)–(6) allowed the following comments to be made.

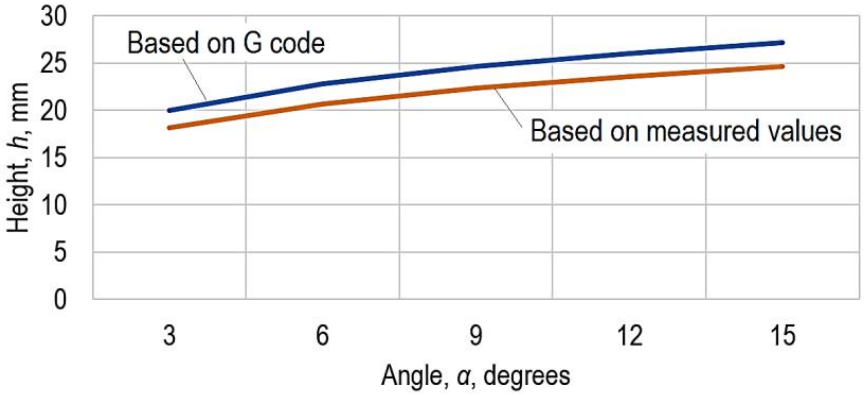

Figure 4. The influence exerted by the size of the angle α on the height h of the isosceles triangle, when the intent was to obtain triangles with the same height h (t_l = 0.1 mm, v = 55 mm/s, c = 55%, I = 20, t_s = 7.5 mm; the blue line corresponds to the mathematical model established by using G code; the red line corresponds to the mathematical model determined by taking into account the measured values).

The absolute values of the exponents attached to each of the input factors used in the 3D-printing process can be examined to reveal the intensity of the influence exerted by the factors taken into account. It is thus found that when triangles of the same height h must be obtained, the strongest influence is exerted by the size of the α angle at the vertices of the isosceles triangle, since the values of the exponents attached to the α size are much higher compared to the values of the exponents attached to the other process input factors. It can still be seen that as the size of the α angle increases, there is an increase in the height h, since the value of the exponent is positive. The other input factors taken into account exert a minimal and negligible influence on the considered output parameter.

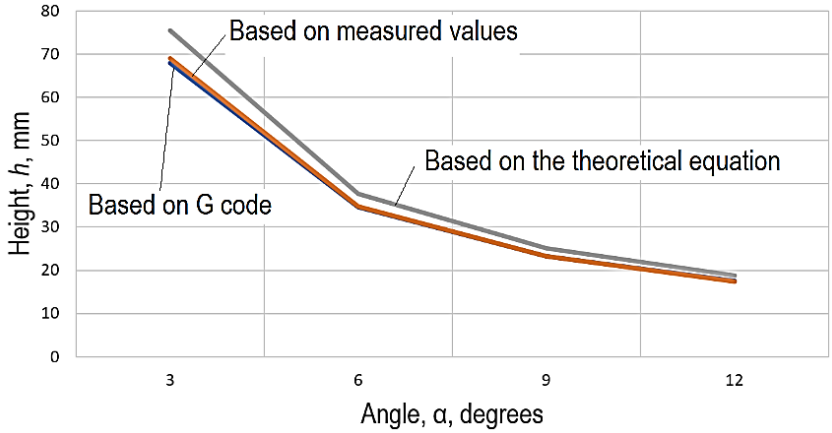

Figure 5. The influence exerted by the size of the angle α on the height h of the isosceles triangle, when the intent was to obtain triangles with the same length b of the base (t_l = 0.1 mm, v = 55 mm/s, c = 50%, I = 20%, t_s = 7.5 mm; the blue line corresponds to the mathematical model established by using G code; the red line corresponds to the mathematical model determined by taking into account the measured values; the grey line corresponds to the theoretical model constituted by the Equation (1)).

The diagram in Figure 4 shows that the values obtained using G code are higher than those determined experimentally.

In the case of isosceles triangles that were to have the same length b of the base, increasing the value of the α angle leads to a decrease in the height h of the isosceles triangles, as shown in Equations (5) and (6). As in the previous case and as expected, the strongest influence is exerted by the size of the α angle, at the increase of which there is a decrease in the height h of the isosceles triangles. It should be noted that both mathematical models lead to identical values of the exponent attached to the size of the α angle (-0.975).

In this case, the values based on the G code are lower compared to the measured values and those corresponding to the theoretical model constituted by Equation (2). It can be seen that the values obtained using the empirical mathematical model are close enough to those determined by using the theoretical mathematical model that in the graphical representation in Figure 5, the two curves almost coincide. An explanation could consider the thermal phenomena that develop during the printing process and the material's behavior when brought into the plastic state by melting during the 3D-printing process.

An assessment of the situation in which it is possible to obtain the lowest value Δ for the difference between the values obtained by experimental tests and the values corresponding to the theoretical model of Equation (2) can be made by following the values included in the last columns of Tables 1 and 2. Thus, it can be found that there are several combinations of the values of the input factors in the 3D-printing process that led to the reduction of the deviation Δ from the desired values of the heights h. In the case of triangles that should have the same height h (Table 1), it is found that the combinations of values of the input factors corresponding to the experiments with numbers 4–9 ensure minimum deviation values Δ. For triangles that had to have the same length b of the base (Table 2), the input factors corresponding to the experimental tests with numbers 4–9 lead to minimal deviations.

6. Conclusions

The problem of producing fine detail by 3D-printing processes continues to be a concern for researchers involved in the investigation and use of such processes. Complete factorial experiments were designed and materialized based on the initial use of Taguchi L9 factorial experiments, with five independent variables at three experimental levels. Additionally, four values of the intersection angles of the flat surfaces corresponding to prismatic surfaces with cross-sections in the form of isosceles triangles were taken into

account. In this way, the input factors considered were the thickness of the deposited layer, the printing speed, the degree of cooling, the infill level, the thickness of the sample, and the size of the intersection angle of the flat surfaces, respectively.

The experimental tests first aimed at obtaining isosceles triangles with the same height but with different values of the vertex angle. Subsequently, other triangles characterized by the same value of the base length and by distinct values of the vertex angle were considered. The mathematical processing using specialized software led to obtaining some empirical mathematical models of the power-function type.

The analysis of these mathematical models showed that the factors with the strongest influence on the deviations from the theoretically designed heights of the triangles were the value of the vertex angle of the isosceles triangle and the printing speed, respectively. The analysis of the differences between the theoretical values of the heights of isosceles triangles and the values of these heights determined experimentally highlighted the existence of some combinations of the values of the input factors for which the deviations are minimal. In the future, the intent is to continue experimental research by considering the influence of other input factors in the 3D-printing process, one of these factors being the nature of the material used for deposition.

Author Contributions: Conceptualization, L.S.; Data curation, A.M.M. and G.N.; Formal analysis, A.M.M. and A.H.; Investigation, A.M.M.; Methodology, A.H. and O.D.; Project administration, L.S.; Resources, G.N.; Validation, A.M.; Visualization, O.D.; Writing—original draft, L.S.; Writing—review & editing, A.M.M. and A.H. All authors have read and agreed to the published version of the manuscript.

Funding: This research received no external funding.

Institutional Review Board Statement: Not applicable.

Informed Consent Statement: Not applicable.

Conflicts of Interest: The authors declare no conflict of interest.

References

1. Brischetto, S.; Maggiore, P.; Ferro, C.G. (Eds.) *Additive Manufacturing Technologies and Applications*; MDPI: Basel, Switzerland, 2017; pp. 1–180. [CrossRef]
2. Ponis, S.; Aretoulaki, E.; Maroutas, T.N.; Plakas, G.; Dimogiorgi, K. A systematic literature review on additive manufacturing in the context of circular economy. *Sustainability* **2021**, *13*, 6007. [CrossRef]
3. Mehrpouya, M.; Dehghanghadikolaei, A.; Fotovvati, B.; Vosooghnia, A.; Emamian, S.S.; Gisario, A. The potential of additive manufacturing in the smart factory industrial 4.0: A review. *Appl. Sci.* **2019**, *9*, 3865. [CrossRef]
4. Asnaf, N. Metal Additive Manufacturing—State of the Art 2020. *Metals* **2021**, *11*, 867. [CrossRef]
5. Arefin, A.M.E.; Khatri, N.R.; Kulkarni, N.; Egan, P.F. Polymer 3D Printing Review: Materials, Process, and Design Strategies for Medical Applications. *Polymers* **2021**, *13*, 1499. [CrossRef]
6. Azad, M.A.; Olawuni, D.; Kimbell, G.; Badruddoza, A.Z.M.; Hossain, M.S.; Sultana, T. Polymers for extrusion-based 3D printing of pharmaceuticals: A holistic materials–process perspective. *Pharmaceutics* **2020**, *12*, 124. [CrossRef]
7. Bagalkot, A.; Pons, D.; Symons, D.; Clucas, D. Analysis of raised feature failures on 3D printed injection moulds. *Polymers* **2021**, *13*, 1541. [CrossRef] [PubMed]
8. Gwamuri, J.; Franco, D.; Khan, K.Y.; Gauchia, L.; Pearce, J.M. High-efficiency solar-powered 3-D printers for sustainable development. *Machines* **2016**, *4*, 3. [CrossRef]
9. Mantelli, A.; Romani, A.; Suriano, R.; Diani, M.; Colledani, M.; Sarlin, E.; Turri, S.; Levi, M. UV-Assisted 3D printing of polymer composites from thermally and mechanically recycled carbon fibers. *Polymers* **2021**, *13*, 726. [CrossRef] [PubMed]
10. Nath, S.D.; Nilufar, S. An Overview of Additive Manufacturing of Polymers and Associated Composites. *Polymers* **2020**, *12*, 2719. [CrossRef] [PubMed]
11. Ziółkowski, M.; Dyl, T. Possible Applications of Additive Manufacturing Technologies in Shipbuilding: A Review. *Machines* **2020**, *8*, 84. [CrossRef]
12. Amza, C.G.; Zapciu, A.; Constantin, G.; Baciu, F.; Vasile, M.I. Enhancing mechanical properties of polymer 3D printed parts. *Polymers* **2021**, *13*, 562. [CrossRef] [PubMed]
13. Avdeev, A.; Shvets, A.; Gushchin, I.; Torubarov, I.; Drobotov, A.; Makarov, A.; Plotnikov, A.; Serdobintsev, Y. Strength increasing additive manufacturing fused filament fabrication technology, based on spiral toolpath material deposition. *Machines* **2019**, *7*, 57. [CrossRef]

14. Calignano, F.; Lorusso, M.; Roppolo, I.; Minetola, P. Investigation of the Mechanical Properties of a Carbon Fibre-Reinforced Nylon Filament for 3D Printing. *Machines* **2020**, *8*, 52. [CrossRef]
15. Ferrari, F.; Corcione, C.E.; Montagna, F.; Maffezzoli, A. 3D printing of polymerwaste for improving people's awareness about marine litter. *Polymers* **2020**, *12*, 1738. [CrossRef]
16. Mazzanti, V.; Malagutti, L.; Mollica, F. FDM 3D printing of polymers containing natural fillers: A review of their mechanical properties. *Polymers* **2019**, *11*, 1094. [CrossRef]
17. Pezzana, L.; Riccucci, G.; Spriano, S.; Battegazzore, D.; Sangermano, M.; Chiappone, A. 3D printing of PDMS-like polymer nanocomposites with enhanced thermal conductivity: Boron nitride based photocuring system. *Nanomaterials* **2021**, *11*, 373. [CrossRef]
18. Ritzen, L.; Montano, V.; Garcia, S.J. 3D printing of a self-healing thermoplastic polyurethane through fdm: From polymer slab to mechanical assessment. *Polymers* **2021**, *13*, 305. [CrossRef]
19. Wickramasinghe, S.; Do, T.; Tran, P. FDM-based 3D printing of polymer and associated composite: A review on mechanical properties, defects and treatments. *Polymers* **2020**, *12*, 1529. [CrossRef] [PubMed]
20. Jones, A.; Straub, J. Concepts for 3D printing-based self-replicating robot command and coordination techniques. *Machines* **2017**, *5*, 12. [CrossRef]
21. Straub, J. Initial Work on the Characterization of Additive Manufacturing (3D Printing) Using Software Image Analysis. *Machines* **2015**, *3*, 55–71. [CrossRef]
22. Msallem, B.; Sharma, N.; Cao, S.; Halbeisen, F.S.; Zeilhofer, H.F.; Thieringer, F.M. Evaluation of the dimensional accuracy of 3d-printed anatomical mandibular models using FFF, SLA, SLS, MJ, and BJ printing technology. *J. Clin. Med.* **2020**, *9*, 817. [CrossRef]
23. Yoo, S.-Y.; Kim, S.-K.; Heo, S.-J.; Koak, J.-Y.; Kim, J.-G. Dimensional accuracy of dental models for three-unit prostheses fabricated by various 3d printing technologies. *Materials* **2021**, *14*, 1550. [CrossRef]
24. Dorweiler, B.; Baqué, P.E.; Chaban, R.; Ghazy, A.; Salem, O. Quality control in 3D printing: Accuracy analysis of 3D-printed models of patient-specific anatomy. *Materials* **2021**, *14*, 1021. [CrossRef]
25. Lee, S.; Squelch, A.; Sunm, Z. Quantitative assessment of 3D printed model accuracy in delineating congenital heart disease. *Biomolecules* **2021**, *11*, 270. [CrossRef]
26. Czajkowska, M.; Walejewska, E.; Zadrozny, Ł.; Wieczorek, M.; Swieszkowski, W.; Wagner, L.; Mijiritsky, E.; Markowski, J. Comparison of dental stone models and their 3D printed acrylic replicas for the accuracy and mechanical properties. *Materials* **2020**, *13*, 4066. [CrossRef] [PubMed]
27. Budzik, G.; Wozniak, J.; Paszkiewicz, A.; Przeszłowski, Ł.; Dziubek, T.; Debski, M. Methodology for the quality control process of additive manufacturing products made of polymer materials. *Materials* **2021**, *14*, 2202. [CrossRef]
28. Slătineanu, L.; Dodun, O.; Nagit, G.; Coteață, M.; Bosoancă, G.; Beșliu, I. Fine details obtained by 3D printing and using polymers. *Mater. Plast.* **2018**, *55*, 474–477. [CrossRef]
29. Boca, M.-A.; Sover, A.; Slătineanu, L. The dimensional accuracy of the test parts made of various plastic materials by the fused filament fabrication process. *IOP Conf. Ser. Mater. Sci. Eng.* **2020**, *997*, 012021. [CrossRef]
30. Kaschwich, M.; Horn, M.; Matthiensen, S.; Stahlberg, E.; Behrendt, C.A.; Matysiak, F.; Bouchagiar, J.; Dell, A.; Ellebrecht, D.; Bayer, A.; et al. Accuracy evaluation of patient-specific 3D-printed aortic anatomy. *Ann. Anat.* **2021**, *234*. [CrossRef]
31. Sun, Y.; Ding, Q.; Tang, L.; Zhang, L.; Sun, Y.; Xie, Q. Accuracy of a chairside fused deposition modeling 3D-printed single-tooth surgical template for implant placement: An in vitro comparison with a light cured template. *J. Cranio Maxillofac. Surg.* **2019**, *47*, 1216–1221. [CrossRef]
32. Herpel, C.; Tasaka, A.; Higuchi, S.; Finke, D.; Kühle, R.; Odaka, K.; Rues, S.; Lux, C.-J.; Yamashita, S.; Rammelsberg, P.; et al. Accuracy of 3D printing compared with milling—A multi-center analysis of try-in dentures. *J. Dent.* **2021**, *110*, 103681. [CrossRef] [PubMed]
33. Wu, H.; Fan, G. An overview of tailoring strain delocalization for strength-ductility synergy. *Prog. Mater. Sci.* **2020**, *113*, 100675. [CrossRef]
34. Chapter 2 Introduction to Taguchi Method. University of Massachusetts Amherst. Available online: http://www.ecs.umass.edu/mie/labs/mda/fea/sankar/chap2.html (accessed on 16 July 2021).
35. Crețu, G. *Fundamentals of Experimental Research*; "Gheorghe Asachi" Technical University of Iasi: Iasi, Romania, 1992. (In Romanian)

polymers

MDPI

Article

Theoretical, Numerical and Experimental Assessment of Temperature Response in Polylactic Acid and Acrylonitrile Butadiene Styrene Used in Additive Manufacturing

Camen Ema Panaite [1], Andrei-Marius Mihalache [2], Oana Dodun [2], Laurențiu Slătineanu [2], Aristotel Popescu [1], Adelina Hrițuc [2,*] and Gheorghe Nagîț [1]

[1] Department of Mechanical Engineering and Road Automotive Engineering, "Gheorghe Asachi" Technical University of Iași, Blvd. D. Mangeron, 43, 700050 Iași, Romania; carmen-ema.panaite@academic.tuiasi.ro (C.E.P.); aristotel.popescu@academic.tuiasi.ro (A.P.); nagit@tcm.tuiasi.ro (G.N.)

[2] Department of Machine Manufacturing Technology, "Gheorghe Asachi" Technical University of Iaşi, Blvd. D. Mangeron, 59A, 700050 Iasi, Romania; andrei.mihalache@tuiasi.ro (A.-M.M.); oanadodun@tcm.tuiasi.ro (O.D.); slati@tcm.tuiasi.ro (L.S.)

* Correspondence: adelina.hrituc@student.tuiasi.ro; Tel.: +40-751640117

Abstract: A better understanding of heat transfer through materials used for 3D-printed parts could lead to an extension and an optimization of their use. A topic of interest could be analyzing temperature variation in these materials during cooling processes. Experimental research and equipment were designed to obtain additional information on the surface temperature decrease when the opposite wall surface is exposed to a freezing temperature. Experimental tests were performed on samples made of polylactic acid (PLA) and acrylonitrile butadiene styrene (ABS). An experimental Taguchi L8 program was used, with seven independent variables at two levels of variation. The experimental data analysis with specialized software based on the least-squares method identified a mathematical model of first-degree polynomial type. The coefficients for each input factor involved provide information on the magnitude and trend of the considered output parameter when the input factors' values change. It was found that the thickness of the 3D printing layer, the thickness of the test sample, and the 3D printing speed are the main factors that affect the temperature decrease rate.

Keywords: heat transfer; polymer materials; 3D printing; influencing factors; empirical mathematical model; experimental Taguchi L8 program

Citation: Panaite, C.E.; Mihalache, A.-M.; Dodun, O.; Slătineanu, L.; Popescu, A.; Hrițuc, A.; Nagîț, G. Theoretical, Numerical and Experimental Assessment of Temperature Response in Polylactic Acid and Acrylonitrile Butadiene Styrene Used in Additive Manufacturing. *Polymers* **2022**, *14*, 1714. https://doi.org/10.3390/polym14091714

Academic Editor: Luigi Sorrentino

Received: 29 March 2022
Accepted: 20 April 2022
Published: 22 April 2022

1. Introduction

Thermal conductivity is a physical property that evaluates the ability of a material to conduct heat. Its importance becomes significant when choosing proper materials for different applications. For cooling or heating purposes, materials with higher thermal conductivity are chosen, while lower thermal conductivity materials are recommended for insulation applications.

Various methods are employed to determine the thermal conductivity of materials, mainly based on measuring temperatures on opposite walls of a test sample of known material and dimensions under a specified heat flux. Methods used to evaluate the thermal conductivity of materials include the guarded hot plate method, axial flow method, cylinder method, flash method, hot wire method, needle probe method, and transient plane method [1–8].

Metallic materials are good heat conductors, as temperature variation on one surface causes a relatively rapid temperature variation on its other surfaces. On the contrary, materials that are poor heat conductors are considered thermally insulating. This category includes polymeric materials, usually with low thermal conductivity values.

The last decades have highlighted an expansion of polymeric material usage in many areas (automotive or other means of transportation [9–11], household items [10,12–14], industrial equipment [15,16], medicine [17–19], etc.). Moreover, there is a clear trend toward expanding the fabrication of polymer parts through 3D printing processes. As 3Dprinting equipment patents expired more than two decades ago, many companies got involved in the industrial manufacturing of 3D printers.

3D printing is part of the broader category of additive manufacturing processes, i.e., parts are obtained gradually by successive addition of new layers of a material. 3D printing processes developed further when software advancements made part dimensional characterization possible with adequate accuracy, which is crucial for successive layer deposition.

One of the 3D printing processes is based on melting a polymer wire and gradual molten material deposition, with the part being generated from successive layers. The shape of each layer is generated by complex relative movement between the nozzle with the molten material and the printer base plate. This is called the fused filament fabrication method.

The analysis of some practical aspects of this manufacturing method revealed several input factors that influence the material properties of the final product. Therefore, researchers performed more in-depth investigations on fused filament additive manufacturing processes regarding input factors that influence different physical and mechanical properties of the 3D-printed part, such as thermal conductivity.

There is a special interest in using polymeric materials for thermal insulation of residential, commercial, or industrial buildings to reduce the effects of excessive cold or heat. Such materials' low heat transfer conductive capacity may represent a significant argument for using polymers as thermal insulating materials [8,9,15,16,20–26]. However, the material properties of a part manufactured by 3D printing can be influenced by thermal interactions during the 3D printing process between the process components (filaments, printing support, environment) [20].

Elkholy and Kempers evaluated the thermal properties of polymers test samples manufactured by 3D printing [27]. The test sample is placed between two blocks, one for cooling and one for heating, and the blocks' temperatures are determined. Elkholy et al. developed research that aimed to highlight the anisotropic behavior of some samples made by fused filament fabrication [28].

In a review paper on expanded polystyrene in building construction, Ramli Sulong et al. also highlighted this material's good thermal insulation capacity [21].

Extensive research completed by a doctoral thesis that addresses issues related to the thermal insulation capacity of 3D-printed materials was conducted by M. Harris [22]. Experimental research was performed on samples of polylactic acid and blends of high-density polyethylene and polypropylene with different thermoplastics (acrylonitrile butadiene styrene and polylactic acid).

Doğan and Tan [23] theoretically investigated (using a model based on finite elements and ANSYS software) and performed experimental research on the thermal behavior of some expanded polystyrene blocks.

An evaluation of the thermal insulation capability of some polystyrene foam structures containing rice hulls was made by Flores [29]. The author estimated that the density of a material could significantly influence the thermal insulation value. Polystyrene is currently used as a thermally insulating material where appropriate conditions are available and there are no health risks.

Eom et al. conducted experimental research to highlight the behavior of the thermal insulation capacity of structures made of 3D-printed thermoplastic polyurethane [24]. They found that increasing the air gap is more effective than increasing the pore size.

Grabowska and Kasperski addressed the issue of structure optimization for 3D-printed polypropylene multilayer films, with closures of different shapes and sizes [25]. The authors found that the best thermal insulation corresponds to single-layer quadrangle and

hexagonal closures, with a structural density of 180 kg/m^3. The thermal conductivity was 0.0591 W/(m·K).

T. de Rubeis addressed the issue of manufacturing 3D-printed blocks used as thermal insulation materials for buildings [26]. The author used a specially designed hot box to assess the thermal insulation capability to ensure known, repeatable, and steady thermal experimental conditions. The infrared thermography technique and heat flow meter method were also used to characterize the thermal insulation of the 3D-printed blocks.

Other published research assessed the ability of polymeric materials as a heat transfer medium or issues involving the thermal conductivity of polymers [30,31].

Given the fairly widespread use of polystyrene as thermal insulation for buildings, researchers have been concerned with better characterizing the behavior of this material from the point of view of thermal conductivity [21,29,32–35].

The research presented in this paper aimed to highlight the influence of some factors regarding test sample thickness or the influence of manufacturing conditions on a temperature decrease for test samples of polylactic acid (PLA) and acrylonitrile butadiene styrene (ABS), respectively. It also identified empirical mathematical models that would provide information on the temperature decrease rate for changing values of several factors defining test sample thickness and the conditions of the 3D printing process.

2. Materials and Methods

Assumptions Regarding Heat Transfer in Plastic Parts Made by Additive Manufacturing

The quality of thermally insulating materials of 3D-printed parts can effectively refer to the decrease in heat transfer rate for different materials.

The test arrangement shown in Figure 1 was considered. A flexible-wall package containing a low-temperature liquid solution (gel coolant) was used. The package flexibility enables contact over a large area between the coolant and the test sample surface of the 3D-printed material.

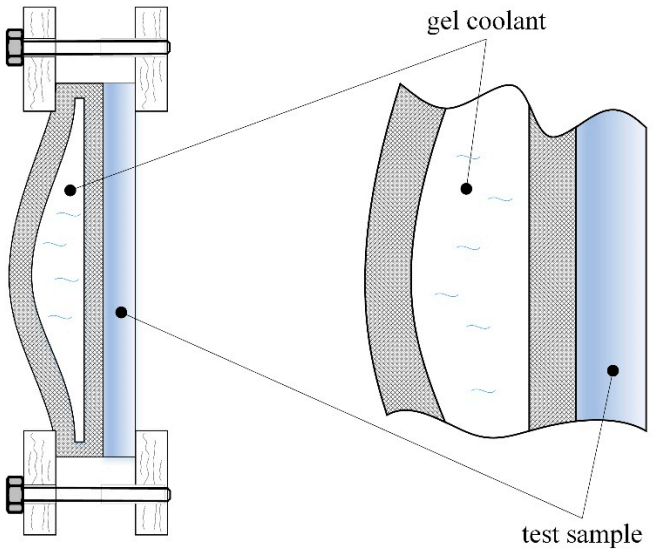

Figure 1. Clamping of the flexible-wall package with gel coolant on the test sample side.

This research aimed to develop diagrams of temperature variation on the free surface of the 3D-printed test samples manufactured with different adjustments to the printer's working parameters. Measurements were performed on the test sample's free flat surface opposite the cooled surface. The flexible-wall package ensured that the gel coolant was initially at −15 °C. It is expected that the temperature of the free flat surface will gradually decrease due to heat transfer through the test sample material. The rate of this process depends on the material thermal properties, especially its thermal conductivity.

There are heat gains towards the gel-coolant package during measurements from the test sample and from the environment. All components shown in Figure 1 were enclosed in a wooden box (low thermal conductivity) and insulated with polystyrene foam to minimize the latter ones. To ease the process of changing the test samples and cooling packages, the box was provided with two doors with holes in the central areas; these doors were also used to perform periodic temperature measurements using IR thermometers (Figure 2).

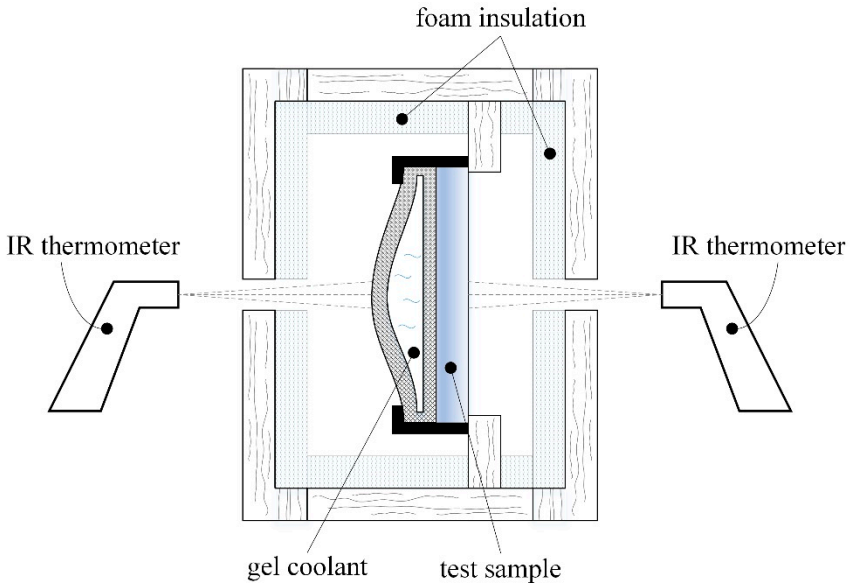

Figure 2. Schematic representation of the experimental arrangement.

The test materials were PLA and ABS. They are two polymeric materials frequently used in 3D printing processes.

The PLA filament used in this experimental research was brown and was delivered by Fillamentum Manufacturing Czech s.r.o. (Hulín, Czech Republic). The filament of the second material (white ABS) was produced by the manufacturer of the 3D printing equipment (Ultimaker, Utrecht, Netherlands). The use of ABS filament made by the manufacturer of the 3D printing equipment was preferred, considering that this is a safer solution and verified by the manufacturer. It was estimated that more rigorous requirements would accomplish ABS test sample manufacturing by printing.

Observation. The glass transition temperature is when the material changes from a brittle, hard state to a soft rubbery state. The Differential Scanning Calorimetry (DSC) evaluates the heat flow and compares the amount of heat supplied to the test sample with a similarly heated "reference" to establish the transition points. The Dynamic Mechanical Analysis (DMA) evaluates a material's response to an applied oscillating stress and the influence of temperature and frequency on that response [36].

ABS white is a mixture of acrylonitrile-co-butadiene-co-styrene, polyethylene terephthalate, and polycarbonate. The manufacturers indicated the characteristics of the two materials. Thus, PLA is an industrial composter containing more than 98% polylactide resin. Similar information and compositions on the two filament materials (ABS and PLA) are also provided by other manufacturers of materials used in 3D printing. Some physical properties of the two materials analyzed in this research are presented in Table 1.

Table 1. Some physical properties of the materials of test samples made by 3D printing [37,38].

Physical Property	Material	
	PLA	**ABS**
Thermal conductivity [W/(m·K)]	0.13	0.173
Density [kg/m^3]	1240	1040
Glass transition [°C]	57 by DSC 63 by DMA	105 by DSC 108 by DMA
Heat deflection temperature [°C]	49	96
Coefficient of thermal expansion [m/m·K]	41×10^{-6}	72×10^{-6}
Heat capacity [J/kg·K]	1800	1670

Theoretically, a model of heat transfer following the first law of thermodynamics [39] yields the equation:

$$\frac{dE_\Omega}{dt} = P_{str} + Q_{exch}, \quad (1)$$

A mathematical model such as Equation (1) can be used to detect possible thermal degradation of polymeric material when chemical changes occur due to exposure to higher temperatures in the absence of oxygen, where E_Ω is the internal energy, t is the time, P_{str} is the stress power, and Q_{exch} is the exchanged heat rate. This theoretical relationship considers the stress power factor when the power is converted into heat by dissipation [39].

3. Results

3.1. Finite Element Modeling of Thermal Conductivity Variation

The finite element analysis models the temperature variation within the test sample for a certain time after the flexible-wall package with gel coolant was placed on the sample side surface. Using the ANSYS R19.2 software, the graphical representation in Figure 3 provides an image of temperature distribution in a PLA test sample.

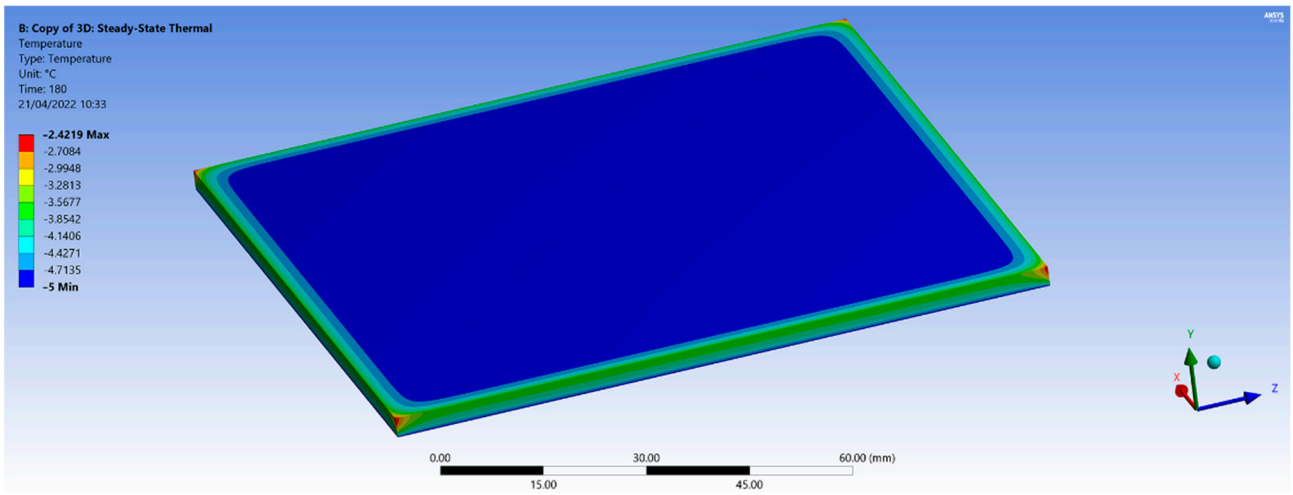

Figure 3. Result of finite element modeling of the temperature variation in the sample test plate (modeling using ANSYS, PLA specimen thickness: 3 mm).

Test samples of various thicknesses were subjected to a gel coolant at a temperature of about −15 °C on one of the large side flat surfaces. The experimental research intended to analyze the temperature variation in time during the cooling process, especially in the

center of the surface opposite the one being cooled. Numerical modeling used the finite element method with the working conditions mentioned in Table 2. Thermal conductivities values of 0.13 W/(m·K) for PLA and 0.173 W/(m·K) for ABS were considered.

Figure 3 shows the temperature distribution of the investigated area after 180 s from the start of the cooling process. The test sample temperature reaches −5 °C in the center and has higher values towards the edges of the test sample. The smaller values of temperature decrease at the edges and corners of the test sample may be explained by the larger influence of the clamping subsystem and the heat gain effect from the outside.

Eventually, the corners will reach the same temperature as the center area, provided the test sample's cooling process is long enough. In the case of the ABS material, with a thickness of 3 mm, the temperature difference between the corners and the center area of the test sample is about 1.5 °C. In contrast, for the case of PLA material, the difference is 2.5 °C. The numerical model developed using the finite element method shows that the ABS polymeric material cools faster and is more uniform than the PLA material.

Similar behavior is observed for thinner samples of 1 mm, but the samples cooled faster than the 3 mm thick ones.

Graphical representations obtained using the finite element method agree with the results obtained from thermal imaging infrared camera (Figure 4). The temperature distribution images from the IR camera provided visual information on temperature variation during the cooling process. The ST 660 Series infrared thermometer performed more accurate temperature measurements at a particular location on the sample surface. Knowing the temperature distribution within the part used for the FEM analysis is important when the parts are subjected to mechanical stress in an environment with large temperature variations.

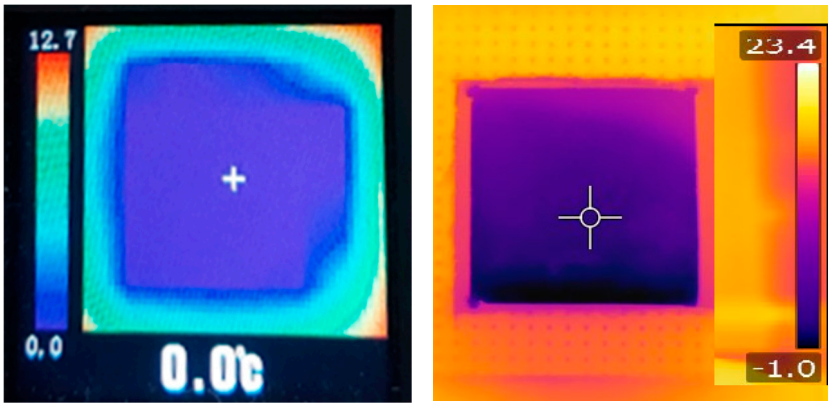

(**a**) (**b**)

Figure 4. Images of the free surface of the test sample obtained using thermal imaging cameras: (**a**) image obtained using the thermal imaging camera AMG8833, after 180 s from the start of the cooling process for the test sample no. 3; (**b**) image obtained using the infrared camera FLIR T630 SC after 120 s from the start of the cooling process for the test sample no. 8.

Table 2. Experimental conditions and results for a factorial experimental plan L_8 (2^{7-4} = 8 experimental tests).

Experiment No.	Input Factors (Coded Value/Real Value)							Output Parameter		
	1 Test Sample Material, *m*(PLA/ABS)	**2 Test Sample Thickness, *h*, mm**	**3 Printing Speed, *s*, mm/s**	**4 Cooling, *c*, %**	**5 Infill, *i*, %**	**6 Deposited Layer Thickness, *l*, mm**	**7 Time, *t*, min**	**Real Value, $\Delta\theta$, after 120 s**	**According to the Polynomial of First-Order Empirical Model**	**According to the Power Type Empirical Model**
Column No. 1	**2**	**3**	**4**	**5**	**6**	**7**	**8**	**9**	**10**	**11**
1	1/PLA	1/1	1/45	1/0	1/22	1/0.06	1/0	36	35.98	38.5
2	1/PLA	1/1	1/45	2/100	2/18	2/0.15	2/120	31	30.97	31.3
3	1/PLA	2/3	2/55	1/0	1/22	2/0.15	2/120	22	21.97	22.5
4	1/PLA	2/3	2/55	2/100	2/18	1/0.06	1/0	25	24.99	24.4
5	2/ABS	1/1	2/55	1/0	2/18	1/0.06	2/120	38	37.97	38.8
6	2/ABS	1/1	2/55	2/100	1/22	2/0.15	1/0	25	24.98	24.3
7	2/ABS	2/3	1/45	1/0	2/18	2/0.15	1/0	11	10.99	10.8
8	2/ABS	2/3	1/45	2/100	1/22	1/0.06	2/120	24	23.97	24.2

3.2. Experimental Conditions

The main objective of the experimental research was to study the behavior of some 3D-printed test samples of two different polymers subjected to a temperature decrease. Another objective was to model the influence exerted by some factors that characterize the 3D printing process on the temperature decrease rate when one of the test sample surfaces was subjected to a forced decrease in temperature.

An Ultimaker 2 printer was used as 3D printing equipment to manufacture the eight test samples (Figure 5).

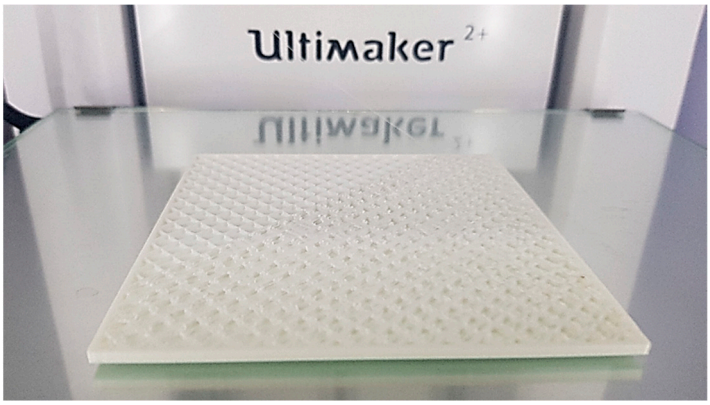

Figure 5. Image while printing a test sample (experiment no. 8).

The possibility of using an experimental test program was considered [40,41]. A Taguchi L8 program with seven independent variables at two levels of experimentation was preferred, which accepts a monotonous variation of the values of the output parameters of the investigated process, i.e., without the presence of minimums or maximums. The statement may be valid for not-too-large intervals of the input factor values in the investigated process. However, processing the results of the experimental tests by the least-squares method may also lead to the identification of mathematical models for the variation of an output parameter, which is more complex than the mathematical model corresponding to a polynomial of first-degree.

Two levels of variation were adopted for each of the variables considered. In columns 2–8 of Table 2, the coded values of the input factor values were taken into account as independent variables (at the fraction numerator), and the actual values of those factors (at the fraction denominator) were entered as fractions.

The seven independent variables were as follows:

1. The nature of the test sample material. Test samples of polylactic acid (PLA) and acrylonitrile butyl styrene (ABS) with dimensions of 100 mm × 100 mm × (1 or 3) mm were printed, respectively. In Table 2, the values defining the experimental conditions and the values of an output parameter were entered. The PLA material and the ABS material were assigned symbols 1 and symbol 2, respectively. The symbol *m* was used for the material identified as an independent variable;
2. The test sample thickness *h*. The two levels of this factor correspond to a thickness of 1 mm and 3 mm, respectively;
3. Printing speed *s*. The values of this input factor were 45 mm/s and 55 mm/s, respectively. It was considered that the printing speed could affect the arrangement of the molten polymer when the layers of the future test sample were generated, and thus, the thermal conductivity of the deposited material could be affected;
4. The cooling conditions provided by the 3D printer, symbolized by the letter *c* and expressed as a percentage, using the symbol 1 for lack of cooling and 2 for the maximum use of the cooling subsystem of the 3D printer;
5. Level *i* of the infill, for which the values used were 22% (level 1) and 18% (level 2), respectively;

6. The thickness l of the layer deposited during 3D printing is 0.06 mm and 0.15 mm, respectively. The values of the input factors that define the working conditions used for the 3D printing process were established by taking into account the recommendations for such a manufacturing process;
7. The size t of the time interval at which the temperature measurement was performed.

In Figure 6, the eight test samples (four of PLA and four of ABS) used in the experiment can be observed, with the corresponding data listed in Table 2. After a flexible-wall package containing the gel coolant was placed in contact with one test sample surface, the temperature was measured on the opposite surface at 60 s intervals using an ST 660 Series infrared thermometer.

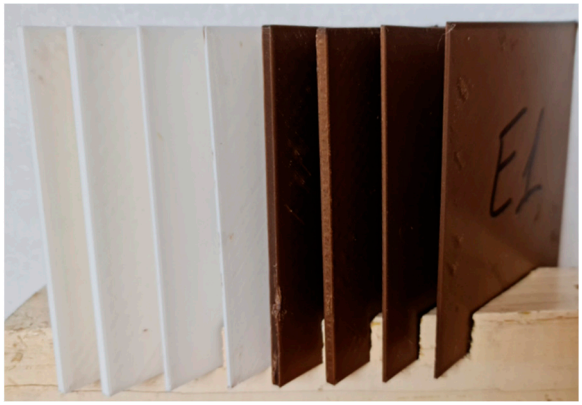

Figure 6. Test samples obtained by 3D printing of ABS (white) and PLA (brown) used to evaluate the temperature decrease in a certain time interval.

The IR thermometer can measure temperatures between −50 °C and 999 °C. According to the manufacturer's specifications, the thermometer has a repeatability of ±1 °C and a resolution of 1 °C.

To verify the accuracy of the IR thermometer, test measurements were performed to determine the temperature at the bottom of an aluminum container with a 30 mm thick layer of boiling distilled water. The temperature indicated by the infrared thermometer from a distance of 250 mm was 99 °C. The experimental results were consistent with the device characteristics provided by the manufacturer, even if possible influences of the presence of water, the variation of the water layer thickness due to the boiling, and the thermal behavior of the aluminum container's bottom wall are taken into account.

First measurements of temperature variation were taken (as shown in the schematic representations in Figures 1 and 2) to establish the magnitude of the time interval required to determine the empirical mathematical model. As the parameter of interest was the ability of the test sample material to sense the temperature decrease, measurements were performed until, after the initial decrease, the temperature remained somewhat constant for a short time and then began to rise. The results of the measurements are listed in Table 3.

A graphical representation of the temperature decrease measured on the free surface of the test sample can be seen in Figure 7. The analysis of the data in Table 3 and Figure 7 defined the initial 120 s as the optimum time interval that could provide useful information on the thermal conductivity of the test sample material by a certain temperature decrease $\Delta\theta$.

The graph in Figure 7 shows that for the time interval between 0 and 120 s, the temperature of the test sample free surface decreased continuously, even reaching the approximately constant temperature period before starting to grow again. For each test sample made of the two materials (PLA and ABS) and each experiment, the values $\Delta\theta$ of the temperature decrease were entered for 0–120 s in column 9 of Table 2.

Table 3. The time variation of the free surface temperature after bringing the opposite test sample surface in contact with the gel coolant package.

Exp. No.	Time, *t*, s											
	0	**60**	**120**	**180**	**240**	**300**	**360**	**420**	**480**	**540**	**600**	**660**
1	23	−8	−13	−15	−16	−17	−15	−13				
2	23	−5	−8	−12	−12	−9	−5	−5				
3	23	4	1	0	−3	−3	−8	−7	−6	−5		
4	23	5	−2	−5	−6	−7	−8	−9	−9	−8	−8	−8
5	23	−15	−15	−14	−11	−11	−11	−11				
6	23	5	−2	−4	−5	−5	−5	−3	−2			
7	23	17	12	8	5	3	2	0	−1	0	1	
8	23	3	−1	−6	−8	−6	−5	−8				

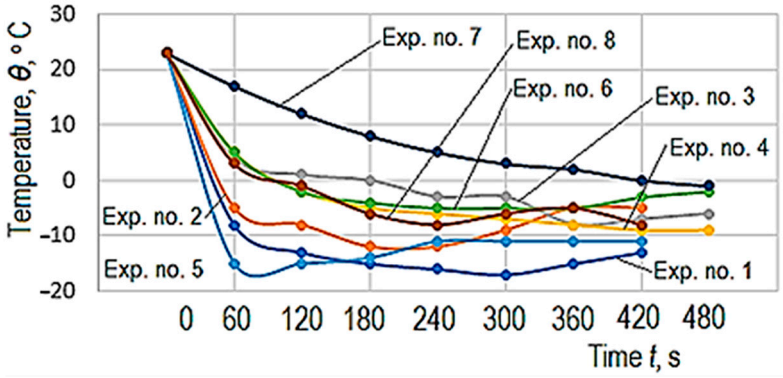

Figure 7. Graphical representation of the temperature decrease on the surface of the test sample opposite to that affected by a cooling process, for all 8 experimental tests, according to the values entered in Table 3.

4. Discussion

The values of the input factors taken into account and the values $\Delta\theta$ of the temperature decrease were introduced in a specialized software designed to identify an empirical mathematical model according to the results of the experimental tests [42]. This program is based on the least-squares method. It allows the selection of the most appropriate empirical mathematical model from five such possible models (first-degree polynomial, second-degree polynomial, power type function, logarithmic function, and hyperbolic function). The selection of the most appropriate program is based on the value of the so-called Gauss criterion.

The value of the Gauss criterion is calculated as a sum of the squares of the ordinate differences corresponding to the experimental results and those determined using the empirical mathematical model considered for the same values of the input factors. The lower the value of Gauss's criterion, the better the empirical mathematical model considered agrees with the experimental results.

It was found that, among the five versions of empirical mathematical models, the most appropriate concerning the experimental results is the first-degree polynomial type, which has the form:

$$\Delta\theta = 39.916 - 3.999m - 5.999h + 0.200s - 0.00499c + 0.124i - 94.444l + 0.0374t, \quad (2)$$

where the value of Gauss's criterion is $S_G = 2.379693 \times 10^{-9}$.

Note that this first-degree polynomial provides direct information about the magnitude and direction of the variation of the output parameter ($\Delta\theta$) to the variation of each input factor value by analyzing the values of the coefficients attached to each of the input factors considered. A similar property is presented by the mathematical model of the

power-type function. Power-type empirical mathematical models have often been preferred (for example, to highlight the influence of cutting conditions on tool life, surface roughness, cutting force component sizes, etc.). For this reason, it was considered useful to take into account, for the analyzed situation, an empirical mathematical model of the power function type, which has the form:

$$\Delta\theta = 0.214 m^{-0.336} h^{-0.457} s^{0.691} c^{0.00415} i^{0.512} l^{-0.411} t^{0.016}, \quad (3)$$

where the value of the Gauss's criterion is $S_G = 2.430406 \cdot \times 10^{-7}$, a value higher than that when using the mathematical model of the first-degree polynomial type, identified by the software used as the most suitable for the experimental results.

The last two columns (10 and 11) in Table 2 list the values calculated for those two empirical mathematical models. Thus, the extent to which the values determined by using the two types of empirical mathematical models (first-degree polynomial and power-type function) approach the values determined by experimental research may be observed.

Analysis of the differences between the real values of the temperature decrease $\Delta\theta$ and the values determined using the first-degree polynomial empirical mathematical model shows that these errors are between the limits of 0.19 °C (for experiment no. 7) and 2.53 °C (for experiment no. 1). One may observe the relatively low differences between the values obtained experimentally and those determined using the proposed empirical mathematical models, highlighting the empirical models' adequacy to the experimental results.

Using the mathematical model based on Equation (2), the graphical representations from Figures 8–10 were elaborated.

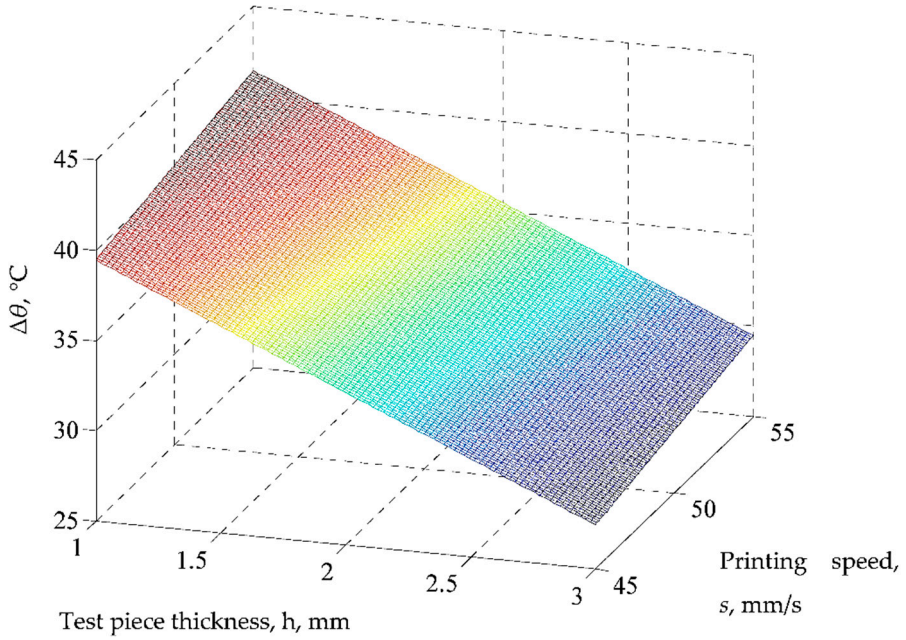

Figure 8. Influence of test sample thickness h and printing speed s on the temperature decrease $\Delta\theta$ (m = 1 (PLA), c = 100%, i = 18%, l = 0.06 mm, t = 120 s; the differences between the real values and those implied by the proposed empirical mathematical model are between the limits of 0.19 °C (for experiment no. 7) and 2.53 °C (for experiment no. 1)).

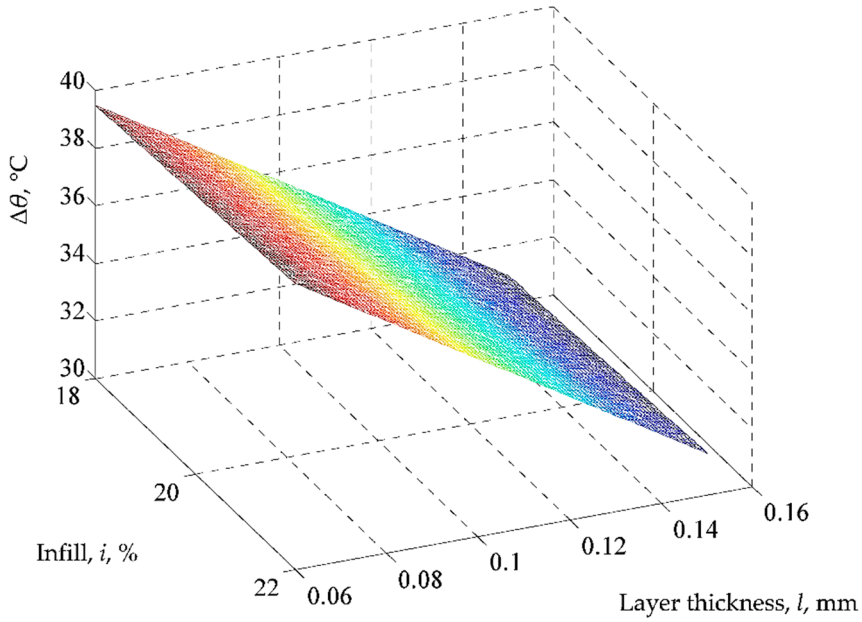

Figure 9. Influence of infill i and layer thickness l on temperature decrease $\Delta\theta$ (m = 1 (PLA), h = 1 mm, s = 45 mm/s, c = 100%, t = 120 s; the differences between the real values and those implied by the proposed empirical mathematical model are between the limits of 0.19 °C (for experiment no. 7) and 2.53 °C (for experiment no. 1)).

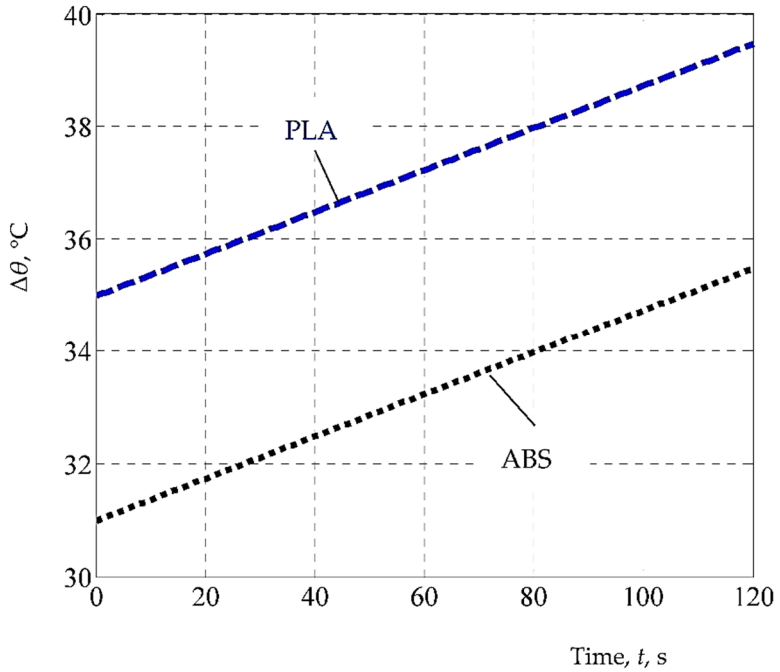

Figure 10. The influence exerted by time t on the temperature decrease $\Delta\theta$ for the two mate-rials considered (h = 1 mm, s = 45 mm/s, c = 100%, i = 18%, l = 0.06 mm; the differences between the real values and those implied by the proposed empirical mathematical model are between the limits of 0.19 °C (for experiment no. 7) and 2.53 °C (for experiment no. 1)).

Thus, an increase in the values of printing speed s, infill i, deposited layer thickness l, and time t increases the temperature $\Delta\theta$ because the values of coefficients attached to the respective input factors in the first-degree polynomials are positive. At the same time, an increase in the test sample thickness h and the characteristic related to cooling conditions c lead to a reduction in the temperature decrease $\Delta\theta$, which is highlighted by the negative

values of the coefficients associated with the factors concerned in Equation (2). One cannot obtain qualitative information based on the value of factor m, as this factor is used only to differentiate the results obtained for the two test samples materials (PLA and ABS).

Among all six factors considered and whose values can be modified, the strongest influence is exerted by the deposited layer thickness l and by the test sample thickness h, which corresponds, in this order, to the highest absolute values of the coefficients attached in the first-degree polynomial empirical mathematical model (2). It was also expected that an increase in the test sample thickness h would reduce the temperature decrease $\Delta\theta$ for the same time interval due to the larger distance traveled by the heat flow. A minimal influence is exerted by the factor c, which considers the cooling conditions. This is emphasized by the low value of the coefficient attached to this factor in Equation (2) and thus has virtually no influence on the output parameter taken into account.

The diagram in Figure 10 depicts the evolution of the temperature decrease $\Delta\theta$ as a function of time t for the two materials, according to the empirical mathematical model constituted by Equation (2). As expected, the increase in time t results in an increase in temperature decrease $\Delta\theta$, but values recorded for the ABS material are lower than those in the case of the PLA material, which shows a lower thermal conductivity of the latter material.

5. Conclusions

The thermal conductivity of materials for parts made by 3D printing is important when used for the thermal insulation of some spaces affected by temperature variations. The research highlighted the transmission of temperature through various 3D-printed plates of polylactic acid (PLA) and acrylonitrile butadiene styrene (ABS), respectively. On one surface of the test sample, a flexible-wall package with a gel coolant at -15 °C was placed. The influence of the thickness of the test samples and the values of some input factors in the 3D printing process on the decrease of the temperature on the opposite surface were taken into account. Equipment to ensure conditions for fixing the test sample inside a box of insulating material, placing a flexible-wall package, and temperature measuring possibilities was designed and fabricated. Following the recommendations for a Taguchi type L8 factorial experiment, experimental tests were performed with $2^{7-4} = 8$ experimental tests. The experiments involved using seven input factors at two levels of variation. By mathematical processing of the experimental results, using specialized software based on the least-squares method, an empirical mathematical model of the first-degree polynomial type was identified. The values of the coefficients attached to each of the input factors in this first-degree polynomial provide information on the variation direction, and the magnitude of the temperature decrease when the values of the input factors change within certain limits. The analysis of the empirical mathematical model and graphic representations highlighted that the ABS material ensures better thermal insulation conditions than the PLA material. Among the input factors in the 3D printing process, the strongest influence is exerted by the deposited layer thickness, test sample thickness, and printing speed. The cooling conditions during the 3D printing process have a lesser influence on the decrease in temperature over time.

In the future, it is intended to expand the theoretical and experimental research on thermal conductivity and other materials used in parts manufacturing by 3D printing.

Author Contributions: Conceptualization, C.E.P. and L.S.; methodology, O.D. and A.P.; software, A.-M.M.; validation, A.H. and L.S.; formal analysis, G.N.; investigation, A.P.; resources, O.D.; writing—original draft preparation, L.S.; writing—review and editing, C.E.P., A.P. and O.D.; visualization, G.N.; supervision, C.E.P. All authors have read and agreed to the published version of the manuscript.

Funding: This research received no external funding.

Institutional Review Board Statement: Not applicable.

Informed Consent Statement: Not applicable.

Data Availability Statement: Not applicable.

Conflicts of Interest: The authors declare no conflict of interest.

References

1. Llavona, M.A.; Zapico, R.; Blanco, F.; Verdeja, L.F.; Sancho, J.P. Methods for Measuring Thermal Conductivity. *Rev. Minas* **1991**, *6*, 89–98.
2. Dai, H.; Wang, R. Methods for Measuring Thermal Conductivity of Two-Dimensional Materials: A Review. *Nanomaterials* **2022**, *12*, 589. [CrossRef] [PubMed]
3. Themax Ingénierie. Measuring Thermal Conductivity. Available online: https://themacs-engineering.com/wp-content/uploads/2020/05/Thermal-conductivity.pdf (accessed on 10 January 2022).
4. Dziob, D.; Čepič, M. Simple method for measuring thermal conductivity. *Phys. Educ.* **2020**, *55*, 045004. [CrossRef]
5. Chen, L.; Shi, X.; Yu, N.; Zhang, X.; Du, X.; Lin, J. Measurement and analysis of thermal conductivity of Ti3C2Tx MXene films. *Materials* **2018**, *11*, 1701. [CrossRef]
6. Prado, J.I.; Calviño, U.; Lugo, L. Experimental Methodology to Determine Thermal Conductivity of Nanofluids by Using a Commercial Transient Hot-Wire Device. *Appl. Sci.* **2021**, *12*, 329. [CrossRef]
7. Sekhu, K.S.; Singh, P. Various Methods for Measuring Thermal Conductivity—A Review. *IJRDO J. Mech. Civ. Eng.* **2015**, *1*, 17.
8. Palacios, A.; Cong, L.; Navarro, M.; Ding, Y.; Barreneche, C. Thermal conductivity measurement techniques for characterizing thermal energy storage materials—A review. *Renew. Sustain. Energy Rev.* **2019**, *108*, 32–52. [CrossRef]
9. Srivastava, V.; Srivastava, R. Advances in Automotive Polymer Applications and Recycling. *Int. J. Innov. Res. Sci. Technol.* **2013**, *2*, 744–746.
10. Wickramasinghe, S.; Do, T.; Tran, P. FDM-Based 3D Printing of Polymer and Associated Composite: A Review on Mechanical Properties, Defects and Treatments. *Polymers* **2020**, *12*, 1529. [CrossRef]
11. Xu, W.; Jambhulkar, S.; Zhu, Y.; Ravichandran, D.; Kakarla, M.; Vernon, B.; Lott, D.G.; Cornella, J.L.; Shefi, O.; Miquelard-Garnier, G.; et al. 3D printing for polymer/particle-based processing: A review. *Compos. Part B Eng.* **2021**, *223*, 109102. [CrossRef]
12. Kovalcik, A. Recent Advances in 3D Printing of Polyhydroxyalkanoates: A Review. *EuroBiotech J.* **2021**, *5*, 48–55. [CrossRef]
13. Cruz Sanchez, F.A.; Boudaoud, H.; Hoppe, S.; Camargo, M. Polymer recycling in an open-source additive manufacturing context: Mechanical issues. *Addit. Manuf.* **2017**, *17*, 87–105. [CrossRef]
14. Little, H.A.; Tanikella, N.G.; Reich, M.J.; Fiedler, M.J.; Snabes, S.L.; Pearce, J.M. Towards Distributed Recycling with Additive Manufacturing of PET Flake Feedstocks. *Materials* **2020**, *13*, 4273. [CrossRef] [PubMed]
15. Schuldt, S.J.; Jagoda, J.A.; Hoisington, A.J.; Delorit, J.D. A systematic review and analysis of the viability of 3D-printed construction in remote environments. *Autom. Constr.* **2021**, *125*, 103642. [CrossRef]
16. Budzik, G.; Tomaszewski, K.; Soboń, A. Opportunities for the Application of 3D Printing in the Critical Infrastructure System. *Energies* **2022**, *15*, 1656. [CrossRef]
17. Azad, M.A.; Olawuni, D.; Kimbell, G.; Badruddoza, A.Z.M.; Hossain, S.; Sultana, T. Polymers for Extrusion-Based 3D Printing of Pharmaceuticals: A Holistic Materials–Process Perspective. *Pharmaceutics* **2020**, *12*, 124. [CrossRef]
18. Chen, Q.; Maalihan, R.D.; Ren, J.; da Silva, Í.G.M.; Dugos, N.P.; Caldona, E.B.; Rigoberto, C.A. 3D printing of biomedically relevant polymer materials and biocompatibility. *MRS Commun.* **2021**, *11*, 197–212. [CrossRef]
19. Nejad, Z.M.; Zamanian, A.; Saeidifar, M.; Vanaei, H.R.; Amoli, M.S. 3D Bioprinting of Polycaprolactone-Based Scaffolds for Pulp-Dentin Regeneration: Investigation of Physicochemical and Biological Behavior. *Polymers* **2021**, *13*, 4442. [CrossRef]
20. Vanaei, H.; Khelladi, S.; Deligant, M.; Shirinbayan, M.; Tcharkhtchi, A. Numerical Prediction for Temperature Profile of Parts Manufactured using Fused Filament Fabrication. *J. Manuf. Process.* **2022**, *76*, 548–558. [CrossRef]
21. Sulong, N.H.R.; Mustapa, S.A.S.; Rashid, M.K.A. Application of expanded polystyrene (EPS) in buildings and constructions: A review. *J. Appl. Polym. Sci.* **2019**, *136*, 47529. [CrossRef]
22. Harris, M. 3D Printing Materials for Large-Scale Insulation and Support Matrices. Ph.D. Thesis, Massey University, Albany, New Zealand, 2019. Available online: http://hdl.handle.net/10179/15784 (accessed on 17 August 2021).
23. Doğan, B.; Tan, H. The Numerical and Experimental Investigation of the Change of the Thermal Conductivity of Expanded Polystyrene at Different Temperatures and Densities. *Int. J. Polym. Sci.* **2019**, *2019*, 6350326. [CrossRef]
24. Eom, R.-I.; Lee, E.; Lee, H.; Lee, Y. Evaluation of Thermal Properties of 3D Spacer Technical Materials in Cold Environments using 3D Printing Technology. *Polymers* **2019**, *11*, 1438. [CrossRef] [PubMed]
25. Grabowska, B.; Kasperski, J. The Thermal Conductivity of 3D Printed Plastic Insulation Materials—The Effect of Optimizing the Regular Structure of Closures. *Materials* **2020**, *13*, 4400. [CrossRef] [PubMed]
26. De Rubeis, T. 3D-Printed Blocks: Thermal Performance Analysis and Opportunities for Insulating Materials. *Sustainability* **2022**, *14*, 1077. [CrossRef]
27. Elkholy, A.; Kempers, R. Investigation into the Influence of Fused Deposition Modeling (FDM) Process Parameters on the Thermal Properties of 3D-Printed Parts. In Proceedings of the 2018 Canadian Society for Mechanical Engineering (CSME) International Congress, Toronto, ON, Canada, 27–30 May 2018. [CrossRef]
28. Elkholy, A.; Rouby, M.; Kempers, R. Characterization of the anisotropic thermal conductivity of additively manufactured components by fused filament fabrication. *Prog. Addit. Manuf.* **2019**, *4*, 497–515. [CrossRef]

29. Flores, F.C. Thermal Insulation of Rice Hull and Waste Polystyrene Foam as a Composite Material. Available online: https://www.researchgate.net/publication/343501446_Thermal_Insulation_of_Rice_Hull_and_Waste_Polystyrene_Foam_as_a_Composite_Material (accessed on 23 January 2022).
30. Mihalache, A.; Hriţuc, A.; Boca, M.; Oroian, B.; Condrea, I.; Botezatu, C.; Slătineanu, L. Thermal Insulation Capacity of a 3D Printed Material. *Macromol. Symp.* **2021**, *396*, 2000286. [CrossRef]
31. Panaite, C.E.; Mihalache, A.M.; Slătineanu, L.; Popescu, A.; Nagîț, G.; Hrițuc, A.; Dodun, O. Numerical and experimental investigations of thermal conductivity of 3D printed polystyrene. *Macromol. Symp.* **2022**, accepted.
32. Trhlíková, L.; Zmeskal, O.; Psencik, P.; Florian, P. Study of the thermal properties of filaments for 3D printing. In Proceedings of the AIP Conference Proceedings, Terchova, Slovakia, 12–14 October 2016; Volume 1752, p. 040027. [CrossRef]
33. Weiss, K.-P.; Bagrets, N.; Lange, C.; Goldacker, W.; Wohlgemuth, J. Thermal and mechanical properties of selected 3D printed thermoplastics in the cryogenic temperature regime. *IOP Conf. Ser. Mater. Sci. Eng.* **2015**, *102*, 012022. [CrossRef]
34. Flaata, T.; Michna, G.J.; Letcher, T. Thermal conductivity testing apparatus for 3d printed materials. In Proceedings of the ASME 2017 Summer Heat Transfer Conference HT2017 Bellevue, Washington, DC, USA, 9–14 July 2017. [CrossRef]
35. Codorníu, D.M.; Moyano, J.; Belmonte, M.; Osendi, M.; Miranzo, P. Thermal conduction in three-dimensional printed porous samples by high resolution infrared thermography. *Open Ceram.* **2020**, *4*, 100028. [CrossRef]
36. SD3D. ABS Technical Data Sheet. Available online: https://www.sd3d.com/wp-content/uploads/2015/10/MaterialTDS-ABS-Web.pdf (accessed on 10 January 2022).
37. Comsol. The Heat Balance Equation. Available online: https://doc.comsol.com/5.5/doc/com.comsol.help.heat/heat_ug_theory.07.05.html#586456 (accessed on 12 January 2022).
38. SD3D. PLA Technical Data Sheet. Available online: https://www.sd3d.com/wp-content/uploads/2017/06/MaterialTDS-PLA_01.pdf (accessed on 10 January 2022).
39. Sime, G.A. Closer Look: Techniques for Obtaining Glass Transition Temperature of Polymeric Materials. 2013. Available online: https://www.intertek.com/blog/2013-04-15-glass-transition-temperature/ (accessed on 4 March 2022).
40. Pillet, M. *Introduction aux Plans d'Expériences par la Méthode Taguchi*; Les Éditions d'Organisation: Paris, France, 1992.
41. Slătineanu, L. *Fundamentals of Scientific Research*; PIM Publishing House: Iași, Romania, 2019. (In Romanian)
42. Crețu, G. Fundamentals of Experimental Research. In *Laboratory Handbook*; "Gheorghe Asachi" Technical University of Iași: Iași, Romania, 1992. (In Romanian)

polymers

MDPI

Article

Thermal Expansion of Plastics Used for 3D Printing

Bruno Rădulescu [1], Andrei Marius Mihalache [2], Adelina Hrițuc [2,*], Mara Rădulescu [1], Laurențiu Slătineanu [2], Adriana Munteanu [1], Oana Dodun [2] and Gheorghe Nagîț [2]

[1] Department of Digital Production Systems, "Gheorghe Asachi" Technical University of Iași, 700050 Iaşi, Romania; bruno.radulescu@academic.tuiasi.ro (B.R.); mara.radulescu@academic.tuiasi.ro (M.R.); adriana.munteanu@academic.tuiasi.ro (A.M.)

[2] Department of Machine Manufacturing Technology, "Gheorghe Asachi" Technical University of Iași, 700050 Iaşi, Romania; andrei.mihalache@tuiasi.ro (A.M.M.); slati@tcm.tuiasi.ro (L.S.); oanad@tcm.tuiasi.ro (O.D.); nagit@tcm.tuiasi.ro (G.N.)

* Correspondence: adelina.hrituc@student.tuiasi.ro; Tel.: +40-751640117

Abstract: The thermal properties of parts obtained by 3D printing from polymeric materials may be interesting in certain practical situations. One of these thermal properties is the ability of a material to expand as the temperature rises or shrink when the temperature drops. A test experiment device was designed based on the thermal expansion or negative thermal expansion of spiral test samples, made by 3D printing of polymeric materials to investigate the behavior of some polymeric materials in terms of thermal expansion or contraction. A spiral test sample was placed on an aluminum alloy plate in a spiral groove. A finite element modeling highlighted the possibility that areas of the plate and the spiral test sample have different temperatures, which means thermal expansions or contractions have different values in the spiral areas. A global experimental evaluation of four spiral test samples was made by 3D printing four distinct polymeric materials: styrene-butadiene acrylonitrile, polyethylene terephthalate, thermoplastic polyurethane, and polylactic acid, has been proposed. The mathematical processing of the experimental results using specialized software led to establishing empirical mathematical models valid for heating the test samples from −9 °C to 13 °C and cooling the test samples in temperature ranges between 70 °C and 30 °C, respectively. It was found that the negative thermal expansion has the highest values in the case of polyethylene terephthalate and the lowest in the case of thermoplastic polyurethane.

Keywords: thermal expansion; experimental device; acrylonitrile butadiene styrene; polyethylene terephthalate; thermoplastic polyurethane; polylactic acid; experimental measurements; empirical mathematical models

Citation: Rădulescu, B.; Mihalache, A.M.; Hrițuc, A.; Rădulescu, M.; Slătineanu, L.; Munteanu, A.; Dodun, O.; Nagîț, G. Thermal Expansion of Plastics Used for 3D Printing. *Polymers* **2022**, *14*, 3061. https://doi.org/10.3390/polym14153061

Academic Editor: Diego Antonioli

Received: 7 June 2022
Accepted: 25 July 2022
Published: 28 July 2022

1. Introduction

Thermal expansion of solid materials is a property that considers the increase in size that characterizes the solid body as its temperature rises. The inverse property of thermal expansion is thermal contraction or negative thermal expansion.

Thermal expansion of a part is important in situations where this expansion could affect the integrity or behavior of the assembly of which the part is a component. Because the forces that occur during thermal expansion can be relatively large, they can cause deformation or even breakage of other parts or even the part affected by the expansion.

Thermal expansion is evaluated by considering the ratio between the increase in size under the action of increasing the temperature and the initial value of the dimension affected by heating. This ratio is the coefficient of thermal expansion and is usually used in the case of linear dimensions or volumes of parts affected by thermal expansion.

Significant differences exist between the expansion of metallic materials, plastics, or ceramics. It is appreciated that, in general, the thermal expansion of ceramic materials is less than the thermal expansion of metallic materials, as polymeric plastics have an expansion

of about 10 times greater than those of metallic materials. Devices called dilatometers are used to evaluate linear thermal expansion.

With the increasing use of parts made of polymers by 3D printing, it has become important to know the thermal properties of polymers. These properties include thermal expansion.

Seven additive manufacturing technologies are currently considered: vat photopolymerization, material extrusion, material jetting, binder jetting, powder bed fusion, direct energy deposition, and sheet lamination [1]. The process used in this paper was material extrusion. This process involves a wire advanced and extruded through a heated nozzle and deposited in successive layers as a result of precisely controlled movements between the nozzle and the table of the 3D printer until the final part is obtained. Many input factors influence how successive layering occurs in the 3D printing process. These factors include the nozzle hole diameter, the relative movement speed between the nozzle and the printer table, the proposed level for the density of the workpiece material, the nozzle and printer table temperatures, and the cooling level during the 3D printing process, etc.). Due to the values of the input factors, the material of the part manufactured by 3D printing may have different degrees of densification and filling of the space inside the part, which will affect some thermal properties of the part material. Among these properties, there is thermal capacity expansion.

The need to consider thermal expansion as a property of the materials from which 3D printing processes made parts was highlighted by researchers [2–5]. Effective experimental attempts to study thermal expansion specific to polymeric materials used in manufacturing parts by 3D printing were performed by Wang [3] and Miller [6]. The importance of thermal expansion in the use of thermoactivated morphing materials has been highlighted by Nam [7]. The analysis of some thermal properties of the filaments used for 3D printing of parts of polymeric materials was developed by Trhlikova et al. [8] and Savu [9]. Zhang referred to the thermal expansion of power electronic components when he studied applications of additive manufacturing in this field [10].

The generation of 3D printed parts' deviations due to thermal and negative thermal expansion was analyzed by researchers interested in a better knowledge of additive manufacturing processes, namely those of 3D printing [3,5,8,9].

Wang et al. [11] studied some characteristics of isotactic polypropylene. They found that the high crystallization rate of isotactic polypropylene can cause significant difficulties in the case of additive manufacturing processes. When studying the behavior of a composite material based on isotactic polypropylene, it was observed that the value of the coefficient of thermal expansion of isotactic polypropylene is about 10% higher than that of a composite material containing spray-dried cellulose nanofibrils.

Blanco considered thermal expansion when reviewing the applications of thermal analysis methods that can be used to manufacture parts by 3D printing processes [12]. He highlighted the availability of thermogravimetric analysis, differential scanning calorimetry, and dynamic mechanical analysis to assess the thermal expansion capacity of materials used to manufacture filaments when applying 3D printing processes.

In an overview of the additive manufacturing of polymer and polymer composite parts, Nat and Nilufar appreciated that the negative thermal expansion of parts after applying an additive manufacturing process induces residual stresses that can affect the behavior of parts during mechanical stresses [13]. They found a library created by Huang et al. [14] in connection with the possibilities of designing the parts so that the dimensions of the 3D printed part are affected as little as possible after the thermal shrinkage.

Zohdi et al. investigated the anisotropy of some thermal properties, as it is, among others, thermal expansion [15].

Hwang et al. have shown that a reduction in the value of the coefficient of thermal expansion is possible when copper particles are introduced into the ABS specimens [16]. For example, for a content of 50 wt.% of copper, the coefficient of thermal expansion decreases by about 29.5% compared to the value of the same coefficient valid for pure ABS, which means a decrease in the coefficient of thermal expansion from 108.2 ppm/°C to

76.2 ppm/°C. This way, the test samples' significant deformation during thermal shrinkage is avoided.

The anisotropic character of the thermal expansion was highlighted by Baker et al. [17]. They compared the values of the coefficient of thermal expansion for test pieces printed along with longitudinal and transverse directions.

A relatively simple device has been proposed to allow direct observation of the spiral polymeric test samples during thermal or negative thermal expansion. This paper presents the research results to highlight the thermal expansion of spiral test parts made by the 3D printing of four different polymeric materials (styrene-butadiene acrylonitrile, polyethylene terephthalate, thermoplastic polyurethane, and polylactic acid). The experimental results were mathematically processed, and empirical mathematical models corresponding to the thermal contraction of the test samples were determined.

2. Materials and Methods

2.1. Initial Considerations

In principle, it is considered that thermal expansion can be explained by the asymmetry of the potential energy, which determines an increase in the mean distance between atoms when the atoms vibrate along the line of interaction between them. However, non-vibrational contributions to the development of the thermal expansion process have also been highlighted [18].

When increasing the body temperature from a value θ_1 to a value θ_2, the magnitude ΔL of the thermal expansion of the body of length L_0 is determined by using the relation:

$$\Delta L = \alpha L_0(\theta_1 - \theta_2), \tag{1}$$

or:

$$\Delta L = \alpha L_0 \Delta\theta, \tag{2}$$

where α is the coefficient of linear thermal expansion, and $\Delta\theta$ is the temperature variation.

Consistent with the above equation, the values of the coefficient of linear thermal expansion α correspond to the following relation:

$$\alpha = \frac{\Delta L}{L_0 \Delta\theta}. \tag{3}$$

It is still possible to investigate the thermal expansion of the volume of a body. In this case, the volume thermal expansion coefficient β is valid:

$$\beta = \frac{\Delta V}{V_0 \Delta\theta}. \tag{4}$$

where V_0 is the initial volume of the body, and ΔV—the increase in body volume.

In most cases, the value of the linear expansion coefficient is important.

Devices called dilatometers, or dilatation analyzers, are used to determine the thermal expansion coefficients' values experimentally. Pushrod dilatometers using optical interferometry or X-ray diffraction, optical dilatometers, capacitance dilatometers, etc., are known. A mention shall be made about horizontal and vertical dilatometers, respectively, concerning the position of a rod made of a material whose coefficient of thermal expansion is determined. In principle, when the temperature of a rod in the investigated material increases, the displacement of the edge of one end of the rod is determined using suitable optical means.

The expansion of the use of polymeric materials has led to the need to know some characteristics of the behavior of parts made of such materials to temperature variation. Manufacturers of polymeric materials generally provide brief information on the expansion properties of these materials. In industrial practice, there is sometimes the problem of

more detailed knowledge of the thermal expansion of a body of polymeric materials at different temperatures.

On the other hand, the last decades have highlighted the possibilities of obtaining polymer parts of various shapes and sizes.

Under the conditions mentioned above and to design and materialize an easily accessible dilatometer, the idea of increasing the length of the bar in the material whose thermal expansion is of interest was formulated using a polymer test sample in the shape of an Archimedean spiral. It was accepted that, among the different categories of spirals, the Archimedean spiral ensures a maximum length of the test sample within a flat surface of predetermined dimensions.

Using a spiral-shaped test sample located in a spiral-shaped groove and allowing the spiral to elongate only in the direction of the outer end of the spiral test sample, the length of the test sample whose thermal expansion is to be measured could be increased (Figure 1). In this way, it would be possible to increase the accuracy of assessing the value of the linear thermal expansion coefficient due to considering the longer length of the test sample.

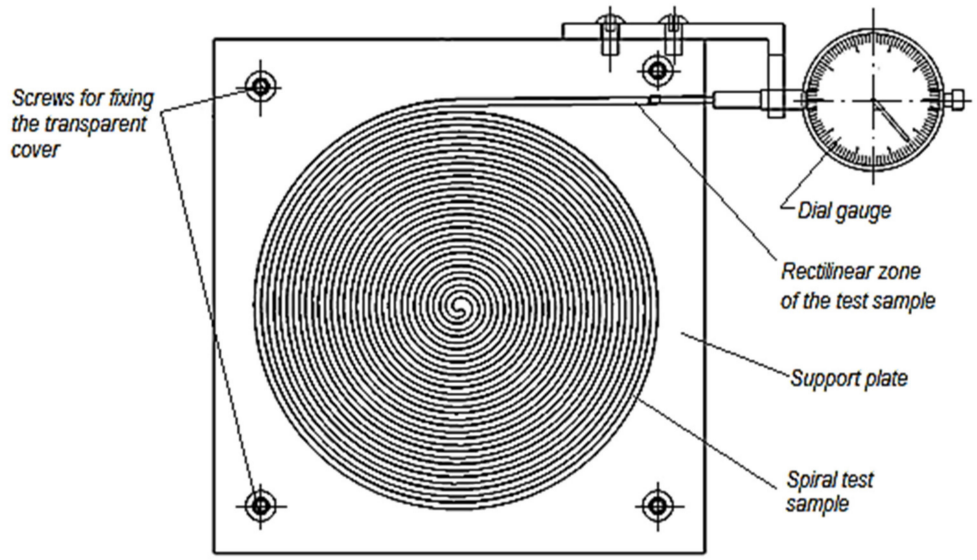

Figure 1. Schematic representation of the device for measuring the thermal expansion of a polymer spiral test sample in the variant involving a dial gauge.

2.2. Experimental Conditions

Under the theoretical conditions mentioned above, a device has been designed to measure the thermal expansion of a spiral-shaped polymer test sample (Figure 1).

A groove in the shape of an Archimedean spiral was machined by milling on a numerically controlled machine tool [19]. An essential part of the device was an aluminum alloy plate. The outer end of the spiral groove is provided with a rectilinear segment. Inside the groove with a cross-section of 1.8×2.3 mm^2, a polymeric test sample can be placed, having a shape corresponding to that of the groove in the aluminum alloy plate, providing a lateral gap of about 0.03 mm. A transparent material cover can be placed over the aluminum alloy plate and fixed to the plate with screws to avoid the external deformation of the test sample during thermal expansion.

The aluminum alloy from which the plate was made was of the EN-AW-2017 type AlCu4MgSi(A) alloy and contained 0.2–0.8% Si, 0.70% Fe, 3.5–4.5% Cu, 0.4–1.0% Mn, 0.4–1.0% Mg, 0.10% Cr, 0.25% Zn, 0.25% Ti, 0.05% other chemical elements and the rest—aluminum. As values of the main thermal properties of the aluminum alloy, it can mention solidification temperature 510 °C, melting temperature 645 °C, heat transfer capacity 873 J·kg^{-1}·K^{-1}, thermal expansion coefficient 22.9 μm·m^{-1}·K^{-1}, thermal conductivity 134 W·m^{-1}·K^{-1}.

The free end movement from outside the spiral test sample in the rectilinear segment could be highlighted using a dial gauge (Figure 1). However, it was appreciated that a higher accuracy would be obtained using an optical microscope. The microscope objective was fixed near the outer end of the linear segment of the test sample (Figure 2).

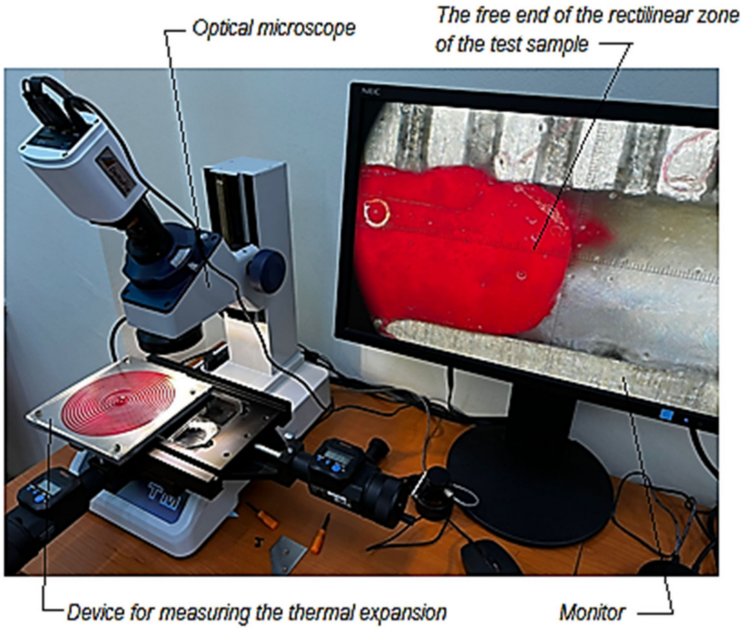

Figure 2. Image of the device for measuring the thermal or negative thermal expansion of the spiral test sample made of polymeric material Flexifill 98A, in the variant involving an optical microscope.

Regarding the proper way of measuring the variation of the length of the test sample, the cooling of the test sample in a freezer was first considered. The aluminum alloy plate, together with the test sample, could be removed from the freezer and placed in the working area of the optical microscope so that minute-by-minute measurements of the thermal expansion of the test sample could be performed. Therefore, the temperature of the aluminum alloy plate and the polymeric test sample could be measured using a gun-type infrared thermometer, which measures the infrared radiation emitted by a given surface. A non-contact infrared thermometer (manufactured by HOPPLINE—Hungary) was used for this purpose, with a measuring range between −50 °C and +400 °C (measuring distance of 5–15 cm, measuring accuracy of ±1.5 °C).

The approximate distance from which the temperature was measured using the infrared thermometer was about 15 cm. Since the process of heat exchange between the aluminum alloy plate together with the spiral test piece and the external environment does not develop with the same intensity in all directions, the aluminum alloy plate temperature has different values at different points of the aluminum plate and, therefore, the average values of three measurements were considered.

The temperature evaluation of the aluminum plate was performed at 1-min intervals, determined by using a digital clock with a stopwatch (approximate time measurement accuracy of ±5 s). In the calculations, the average values of the measured temperatures were taken into account. As observed by using the finite element method and by measuring the temperature in different areas of the aluminum alloy plate, there are temperature differences, even when heated on the table of the 3D printer.

The following materials were considered as materials for the spiral test samples:

(1) Black ABS (styrene-butadiene acrylonitrile). This material is used, for example, for the manufacture of general-purpose goods, such as toys, carcass parts, furniture, refrigerator interiors, helmets, etc.;

(2) Red PET G (polyethylene terephthalate type G). Such material is used mainly in the textile industry, but also as a bottling or packaging material due to the lack of reaction with water or food;
(3) Red color thermoplastic polyurethane (trade name: Flexfill 98A). This material has a hardness equal to that of rubber (98A). It is used especially in the manufacture of solid wheels for scooters and skateboards or in the manufacture of protective cases of smartphones;
(4) Polylactic acid (type T PLA) silver color. This material is well adapted to the requirements of 3D printing processes. Its use in 3D printing does not require a heated substrate or a high melting temperature and increases the printing speed. It also ensures low manufacturing costs. A disadvantage is the increased sensitivity to the action of ultraviolet radiation. Parts with fine details can be easily made from polylactic acid. This material can be used to manufacture toys, jewelry, statues, etc.

The coefficient values of thermal expansion of these materials indicated in some specialized works can be observed in the second column of Table 1.

Table 1. Values of thermal expansion coefficients for materials used in experimental research.

Polymeric Material	Values of the Coefficient of Thermal Expansion Indicated in Specialized Documents, in m/(m·K) [20,21]
ABS (black)	$72 \cdot 10^{-6}$
PET G (violet)	$7 \cdot 10^{-5}$
Flexfill 98A (red)	$145 \cdot 10^{-6}$ (approximate value, determined by comparison with those of similar materials)
PLA (silver)	$41 \cdot 10^{-6}$

The thermal expansion of the polymer test sample from a temperature of about −9 °C (when it was removed from the freezer) to a temperature close to that of the environment in the laboratory, 13 °C) was thus measured using an optical microscope TM-1005B (manufactured by the Japanese company Mitutoyo.

2.3. Evaluation of the Length of an Archimedean Spiral Test Sample

There are different ways to determine the length of an Archimedes spiral segment [22]. The length of the test sample in the form of an Archimedean spiral was calculated using the "Measure" function in the SolidWorks software. The lengths of the two side surfaces of the profile (with a rectangular cross-section, measuring 1.8 × 2.3 mm^2) were measured. The arithmetic mean of the lengths of the two side surfaces was calculated, resulting in an average fiber length of 3337.63 mm.

A problem with the device is that during the thermal expansion or contraction of the polymer spiral test sample, not only the spiral test sample expands or contracts but also the aluminum alloy plate in which the spiral groove the test sample is placed.

It is generally considered that the value of the coefficient of thermal expansion in the case of a metallic material is about ten times lower than that of a polymeric material. Specifically, in the case of aluminum alloy, the value indicated of the coefficient of thermal expansion is α_{Al} = 22.9 m/(m·K), while, for example, in the case of the PLA polymer is indicated $\alpha_{\mathrm{PLA}} = 41 \cdot 10^{-6}$ m/m·K, and in the case of the ABS polymer, $\alpha_{\mathrm{ABS}} = 72 \cdot 10^{-6}$ m/(m·K).

Suppose it takes into account that the size of the side of the square-shaped area of the aluminum alloy plate in which the spiral groove is located is about 128 mm, and assuming a temperature difference of 40 °C, this means a linear variation of the size of the aluminum alloy plate side:

$$\Delta L_{Al} = \alpha_{Al} L_{0\ Al} \Delta\theta = 22.9 \cdot 128 \cdot 40 = 117.2\ \mu\mathrm{m}. \quad (5)$$

Taking into account a length L ≈ 3337.63 mm of the spiral test sample in PLA and, respectively, in ABS and considering the values indicated for the coefficients of thermal expansion [20,21], it would be possible to increase the length of the spiral test sample

ΔL_{PLA} = 5.47 mm and ΔL_{ABS} = 9.61 mm. It is found that the share w of the influence of the linear expansion of the aluminum alloy plate on the thermal expansion of the spiral test sample is very low ($w = 0.1172 \cdot 100/5.47 = 2.14\%$ in the case of the spiral test sample made of PLA and $w = 0.1172 \cdot 100/9.61 = 1.21\%$ in the case of the ABS spiral test sample, respectively. This situation allows us to neglect the influence exerted by the linear thermal expansion of the aluminum alloy plate on the thermal expansion of the spiral test sample of polymeric material.

2.4. Simulation by the Finite Element Method of the Thermal Expansion of the Test Piece

The investigated process was modeled using the finite element method (FEM) and the ANSYS 3D software to evaluate the thermal expansion capacity of the spiral test samples of polymeric materials used in manufacturing parts by 3D printing. For the purpose mentioned above, the situation of a spiral test sample located in the spiral-shaped groove in the aluminum alloy plate was considered.

One of the results of finite element modeling is shown in Figure 3. The experimental tests will manage an uneven cooling or heating of the aluminum alloy plate. Due to heating or cooling at uneven speeds of different areas of the aluminum alloy plate where the polymer spiral test sample is located, there will be a distributed variation in temperature along with the spiral test sample. The value of the thermal expansion coefficient is variable with the temperature of the polymer spiral test sample. This means that the results will lead to an overall value of the evolution of the magnitude of the thermal expansion coefficient or negative thermal expansion coefficient.

It was developed a steady-state thermal FEM analysis considering the convection phenomena. Approximate convection coefficient values for aluminum alloys were confronted with those presented by Geng et al. [23]. It has conducted the analyses on ABS simulating the heat transfer for the cool environment, which starts from around −10 ° C and records about 13 °C on the top side of the cover plate (Table 2). The results are consistent with those measured by experimental means (Figure 3a). The FEM.-based purpose was to analyze further heat transfer on the spiral test sample by transferring steady-state thermal results into the static structural analysis. Results were plotted in the form of thermal strain, equivalent stress von Mises, equivalent elastic strain, and directional deformation in the direction of the heat flow. Thus, it may further visually assess the influence of heat transfer on various polymers. For example, it was clear that uneven cooling leads to a random distribution in the case of equivalent elastic strain (Figure 3b). The spiral undergoes multiple stages of deformation before it shrinks or expands in the designated groove. Static structural results highlight changes that occur to the original body. Directional deformation on the Y-axis gives approximate values to those obtained by experimental means.

Table 2. Experimental results regarding the thermal expansion of some polymeric materials.

Time, min	ABS Black		PET G Violet		FLEXIFILL 98A Red		PLA Silver	
	Temperature, °C	Thermal Expansion, mm	Temperature, °C	Thermal Expansion, mm	Temperature, °C	Thermal Expansion, mm	Temperature, °C	Thermal Expansion, mm
0	−8.8	0	−11.5	0	−8.3	0	−9.2	0
1	−2.6	−0.009	−2.5	−0.015	−5.7	−0.008	−6.3	−0.006235
2	−2.3	−0.015	−2.3	−0.022	−3.9	−0.01	−3.7	−0.009896
3	−0.6	−0.022	−1.3	−0.027	−3.4	−0.015	−2.5	−0.012831
4	−0.6	−0.029	−0.5	−0.03	−1.2	−0.019	−1.1	−0.0147
5	1.3	−0.036	0	−0.035	−0	−0.021	−0.1	−0.017148
6	2.2	−0.044	1.7	−0.041	−0.1	−0.026	−0.9	−0.021195
7	2.4	−0.048	2.7	−0.051	1.8	−0.028	1.7	−0.027816
8	4	−0.055	3.4	−0.066	3	−0.031	3.2	−0.037932
9	5	−0.061	4.7	−0.071	3.9	−0.034	4.3	−0.042731

Table 2. *Cont.*

Time, min	ABS Black		PET G Violet		FLEXIFILL 98A Red		PLA Silver	
	Temperature, °C	Thermal Expansion, mm	Temperature, °C	Thermal Expansion, mm	Temperature, °C	Thermal Expansion, mm	Temperature, °C	Thermal Expansion, mm
10	6	−0.062	5.2	−0.079	4.1	−0.037	4.8	−0.046699
11	6.5	−0.065	5.5	−0.085	4.6	−0.04	5.5	−0.053651
12	6.8	−0.066	6.5	−0.09	5.7	−0.043	6.3	−0.056203
13	7.4	−0.067	7.2	−0.094	6.5	−0.048	7.4	−0.060043
14	8.2	−0.067	7.5	−0.098	6.8	−0.051	7.9	−0.06196
15	8.3	−0.068	7.9	−0.103	7.2	−0.053	8.2	−0.067081
16	9.1	−0.069	8.3	−0.106	7.9	−0.056	8.7	−0.069362
17	9.3	−0.071	8.8	−0.111	8.5	−0.058	9.2	−0.073242
18	9.8	−0.073	9.5	−0.114	9.2	−0.059	9.7	−0.075759
19	10.1	−0.076	10	−0.117	9.9	−0.061	10.2	−0.078333
20	10.6	−0.077	10.2	−0.119	10.4	−0.063	10.6	−0.079781
21	10.9	−0.078	10.5	−0.121	10.8	−0.066	10.9	−0.08126
22	11	−0.079	10.8	−0.124	11.1	−0.068	11.2	−0.085492
23	11.5	−0.081	11	−0.126	11.4	−0.071	11.5	−0.086936
24	11.9	−0.083	11.3	−0.13	11.6	−0.073	11.8	−0.090123
25	12	−0.085	11.9	−0.131	12.1	−0.075	12.1	−0.090997
26	12.1	−0.086	12	−0.132	12.3	−0.076	12.3	−0.091983
27	12.3	−0.088	12.2	−0.133	12.5	−0.077	12.4	−0.093028
28	12.4	−0.089	12.4	−0.135	12.6	−0.078	12.6	−0.094724
29	12.5	−0.091	12.5	−0.137	12.7	−0.08	12.7	−0.096244
30	12.7	−0.091	12.6	−0.138	12.9	−0.081	12.9	−0.094936
31	12.8	−0.092	12.9	−0.141	13.1	−0.081	13.2	−0.09782
32	12.9	−0.092	13.1	−0.143	13.2	−0.081	13.3	−0.09745
33	13.1	−0.092	13.2	−0.143	13.2	−0.081	13.4	−0.098847

The initial conditions for steady-state thermal analysis include an initial ambient temperature of 22 °C and a temperature of −13.1 °C applied in increments on the lower surface of the plate, respectively. A process of free air convection of up to 2.5 W/mm^2 °C applied to the upper surface of the plate was considered. The boundary conditions took into account both the contacts and the joints. The contacts are of three types, two of which include the frictionless thermal expansion of the 3D printed spiral and one that takes into account the friction between the spiral test sample and the groove walls. The joints refer to the spiral's contact with the groove's flat surface. Such conditions make it easier for the software to consider the material must flow only along the spiral groove.

The thermal imaging camera HT-18 (produced by Hti Instrument) was used to check the uneven heating of the aluminum plate on the table of the 3D printer. As it can be seen from Figure 3c, the image obtained by using the thermal imaging camera shows a real unevenness in the heating of the aluminum plate under the action of the table of the 3D printer. This uneven heating of the aluminum plate results in an uneven distribution of the spiral test sample temperature.

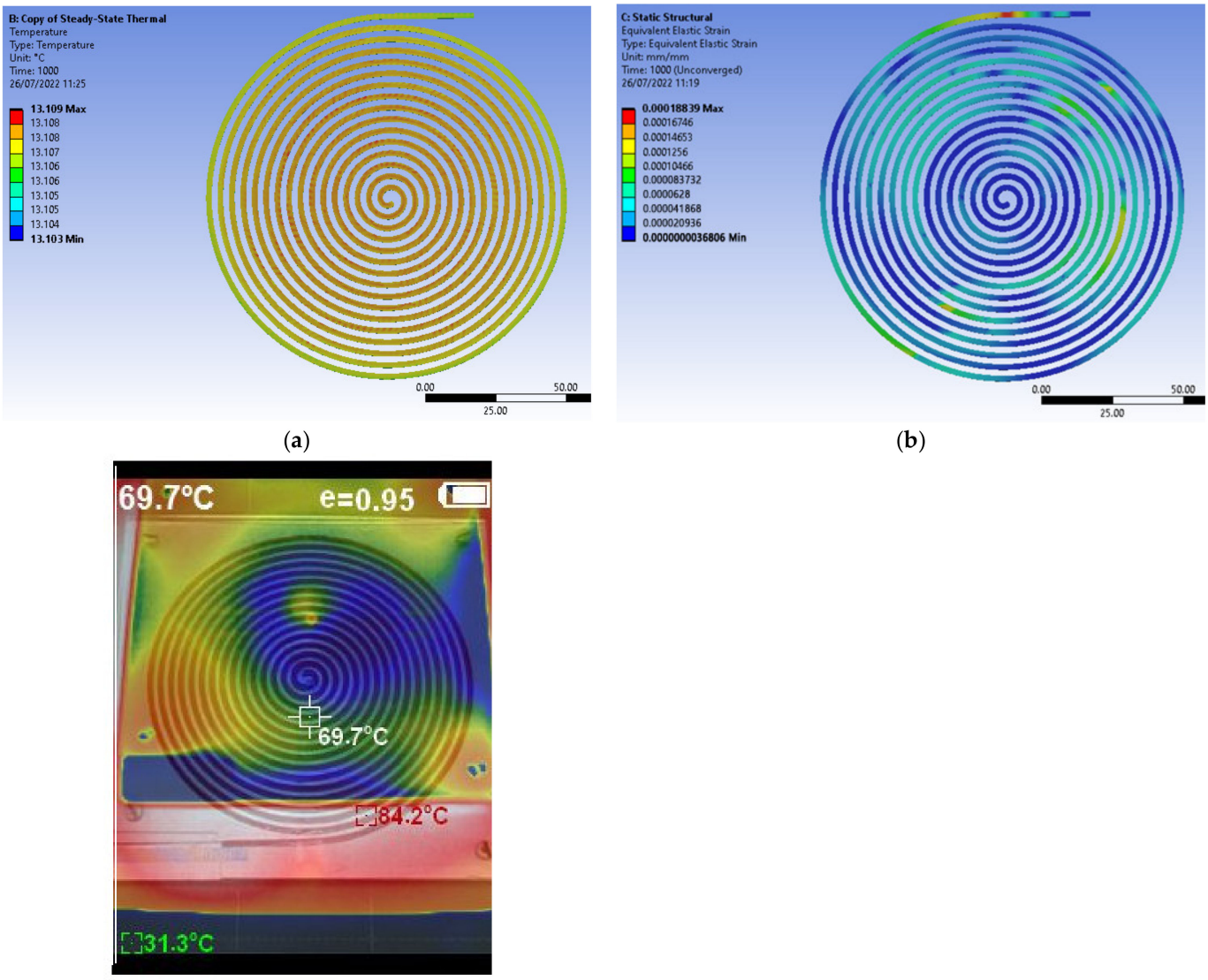

Figure 3. Uneven cooling/heating of the spiral test sample due to different heat transfer rates in distinct areas of the aluminum alloy plate: (**a**) temperature distribution in the steady-state thermal scenario; (**b**) equivalent elastic strain distribution in the static-structural scenario; (**c**) image obtained using the thermal imaging camera.

3. Results

The results obtained in the experimental tests regarding the thermal expansion of the test samples made of the four materials are presented in Table 2. A graphical representation of the ΔL increase in the lengths of the test samples made of polymeric materials when the temperature increases from approximately −9 °C to +13 °C and corresponding to the experimental results in Table 2 can be observed in Figure 4.

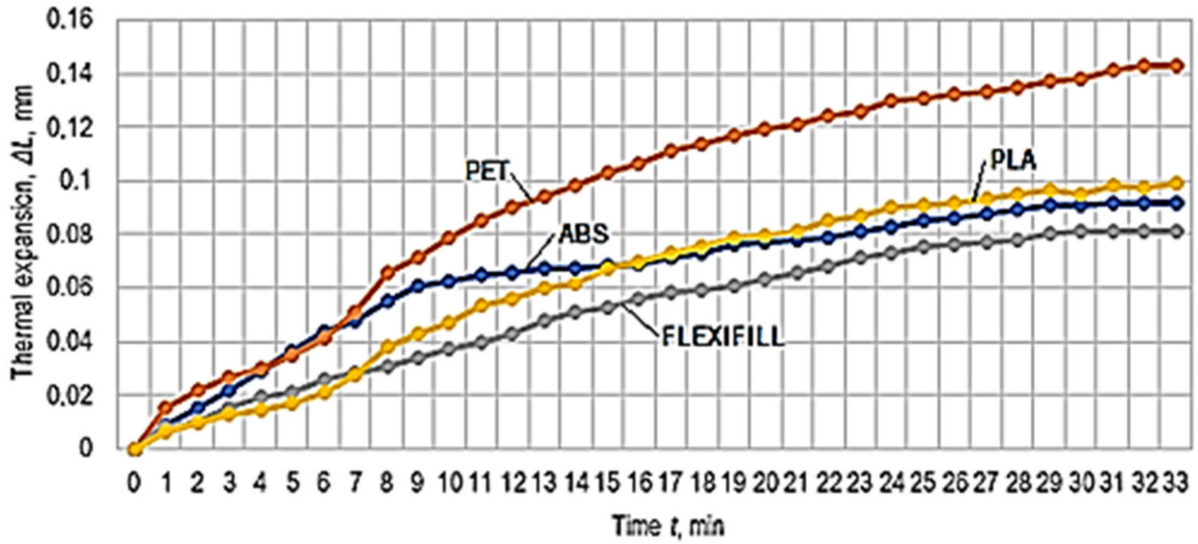

Figure 4. The evolution of thermal expansion over time, with small differences between the initial temperatures.

Later, the idea of measuring the linear negative thermal expansion of the test samples appeared. The heating of the aluminum alloy plate on the table of a 3D printer was considered (Figure 5). In such a case, the temperature of the upper area of the table can be programmed, this being an input factor in the 3D printing process. Thus, measurements of the negative thermal expansion were performed when the test sample cooled, from a temperature of 70 °C to the ambient temperature in the laboratory (30 °C), during the measurements. The measurement results of the test samples shrinkage are included in Table 3. By considering the results in Table 3, a graphical representation of the evolution of negative thermal expansion over time was made (Figure 6).

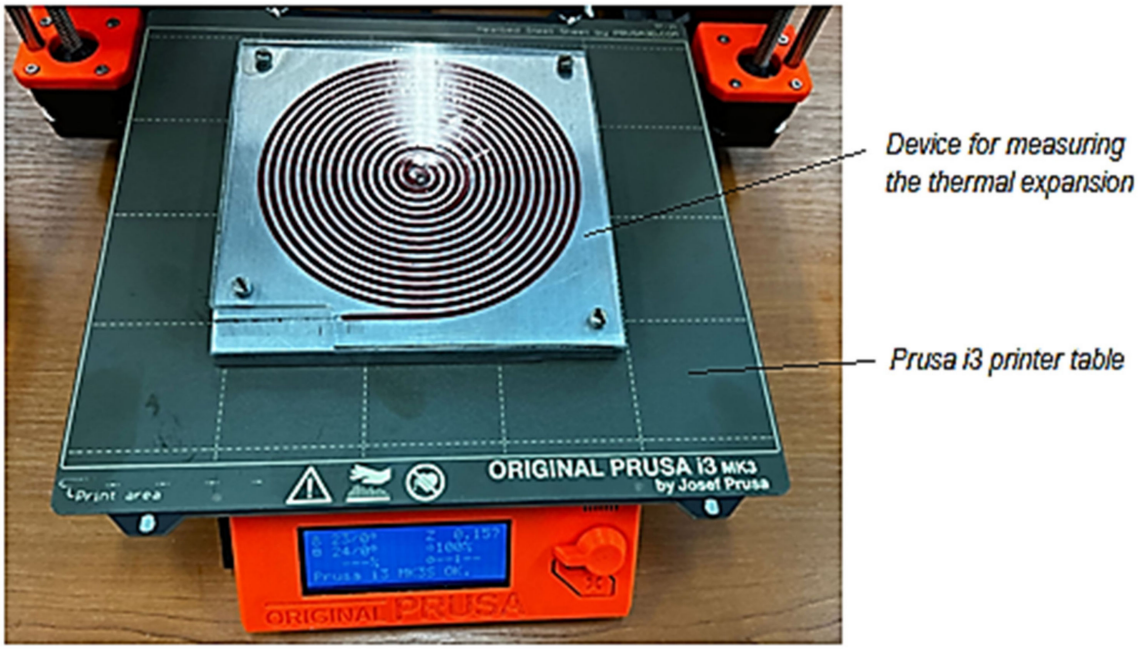

Figure 5. Image of a device for measuring the expansion or thermal shrinkage of a polymer spiral test sample together with the aluminum alloy plate placed on the printer's table to reach the temperature at which the spiral test sample begins to cool and contract.

Table 3. Experimental results regarding the negative thermal expansion of some polymeric materials.

Time, min	ABS Black		PET G Violet		FLEXIFILL 98A Red		PLA Silver	
	Temperature, °C	Negative Thermal Expansion, mm	Temperature, °C	Negative Thermal Expansion, mm	Temperature, °C	Negative Thermal Expansion, mm	Temperature, °C	Negative Thermal Expansion, mm
0	69.7	0	70	0	71.8	0	71	0
1	64.9	−0.08	62	−0.32	66.7	−0.01	61	−0.132
2	61.5	−0.118	60	−0.514	63.8	−0.022	57.7	−0.24
3	58.8	−0.147	57.2	−0.685	59	−0.028	56.2	−0.332
4	56.8	−0.174	55.6	−0.86	55.8	−0.032	53	−0.432
5	54.7	−0.197	54.2	−1.015	54.9	−0.035	51.6	−0.527
6	52.6	−0.216	52	−1.164	52	−0.039	49.5	−0.617
7	51.3	−0.235	50.2	−1.273	51.4	−0.044	48	−0.71
8	50.2	−0.254	48.8	−1.382	50.3	−0.05	46.5	−0.797
9	47.9	−0.27	47.1	−1.481	48.5	−0.054	45.2	−0.88
10	47	−0.285	45.4	−1.556	45.7	−0.057	43.9	−0.964
11	45.3	−0.297	44.5	−1.652	44.5	−0.064	42.7	−1.03
12	44.4	−0.308	43.4	−1.729	42.5	−0.073	41.6	−1.091
13	43.8	−0.321	42.2	−1.798	41.8	−0.081	40.4	−1.149
14	42.2	−0.335	41	−1.844	40.7	−0.088	39.7	−1.197
15	41.6	−0.343	40.4	−1.92	39.1	−0.097	38.6	−1.238
16	40.7	−0.354	39.3	−1.956	38.6	−0.11	37.6	−1.296
17	39.7	−0.364	38.6	−2.013	38.2	−0.13	37.1	−1.336
18	38.6	−0.372	37.8	−2.053	37.7	−0.14	36.3	−1.376
19	38	−0.381	37	−2.088	36.9	−0.16	35.7	−1.412
20	37	−0.391	36.3	−2.128	36.2	−0.19	35.1	−1.44
21	36.7	−0.396	35.6	−2.166	35.4	−0.2	34.9	−1.462
22	35.8	−0.408	34.9	−2.209	35.1	−0.21	34.5	−1.501
23	35.1	−0.412	34.3	−2.242	34.5	−0.22	33.5	−1.553
24	34.8	−0.42	33.7	−2.267	33.9	−0.23	32.8	−1.582
25	33.8	−0.426	33.1	−2.293	33.3	−0.23	32	−1.592
26	33.6	−0.434	32.8	−2.323	32.8	−0.24	31.3	−1.614
27	33.2	−0.441	32.5	−2.357	32.4	−0.24	30.1	−1.642
28	32.7	−0.448	32	−2.378	31.9	−0.25	29.2	−1.663
29	32.2	−0.454	31.6	−2.398	31.5	−0.26	28.7	−1.679
30	32	−0.461	30.8	−2.424	30.9	−0.27	28.5	−1.698
31	31.5	−0.463	30.2	−2.432	30.4	−0.28	28.4	−1.702
32	31.1	−0.464	29.5	−2.438	29.8	−0.28	28.2	−1.711
33	30.4	−0.465	28.8	−2.441	29.3	−0.29	27.9	−1.712

The results of measurements on the thermal expansion of the previously polymer spiral test sample in the freezer can be seen in Table 2. In contrast, the results of the thermal shrinkage of the polymer spiral test sample previously heated on the table of a 3D printer were included in Table 3.

The values indicated in Table 4 were determined by comparing the maximum values of thermal expansion and negative thermal expansion, respectively, at the temperature variation intervals in the case of experimental research.

For the experimental results in Table 4, which show more pronounced differences in terms of negative thermal expansion for the four materials used in the experimental research, mathematical processing was used by means of specialized software [24], to determine empirical mathematical models able to highlight the influence of temperature on linear negative thermal expansion.

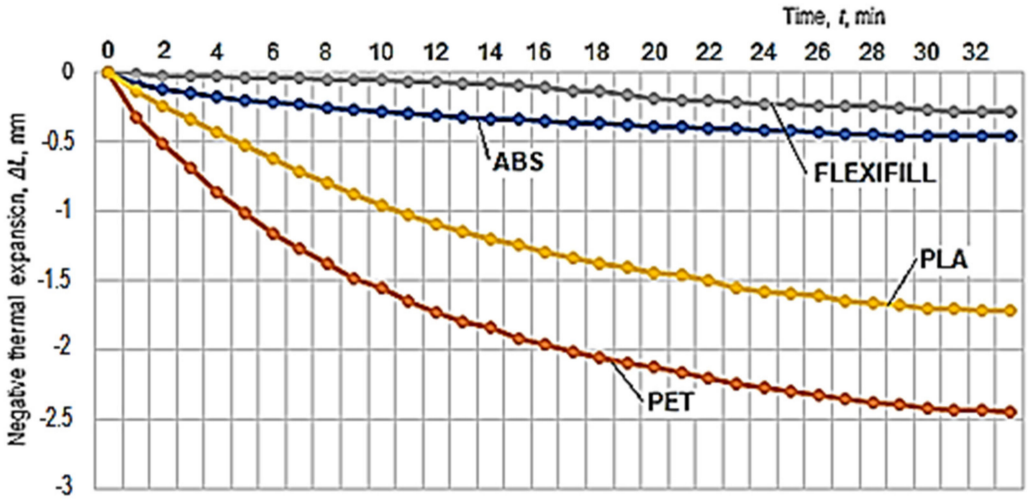

Figure 6. The evolution in time of negative thermal expansion of some spiral specimens made of polymeric materials, there being small differences between the initial temperatures.

Table 4. Calculated values of the thermal and negative thermal expansion coefficients, considering the experimental results presented in Tables 2 and 3.

Material	On Heating			On Cooling		
	The Maximum Value of the Thermal Expansion, ΔL, mm	Temperature Variation, $\Delta\theta$, K	Value of the Coefficient of Thermal Expansion α	The Maximum Value of Negative Thermal Expansion, ΔL, mm	Temperature Variation, $\Delta\theta$, K	Value of the Coefficient of Thermal Negative Expansion α
Column no. 1	**2**	**3**	**4**	**5**	**6**	**7**
ABS (black)	0.092	8.8 + 13.1 = 21.9	$1.25 \cdot 10^{-6}$	0.465	69.7 − 30.4 = 39.3	$3.54 \cdot 10^{-6}$
PET G violet	0.143	11.5 + 13.2 = 24.7	$1.73 \cdot 10^{-6}$	2.441	70 − 28.8 = 41.2	17.7510^{-6}
Flexifill 98A violet	0.081	8.3 + 19.2 = 21.5	$1.12 \cdot 10^{-6}$	0.290	71.8 − 29.3 = 42.5	$2.04 \cdot 10^{-6}$
PLA silver	0.098	9.2 + 13.4 =22.6	$1.31 \cdot 10^{-6}$	1.712	71 − 27.9 = 43.1	$11.90 \cdot 10^{-6}$

The specialized software was generated by taking into account the least squares method. It provides conditions for selecting the most appropriate empirical mathematical model from five such models: the first-degree polynomial, the second-degree polynomial, the power function, the exponential function, and the hyperbolic function. For the selection, the value of the so-called Gauss criterion was used. This value (the Gauss's criterion value) is defined using the sum of the squares of the differences between the ordinate's values determined by the empirical mathematical model considered and the values determined experimentally. The lower the value of the Gauss criterion, the more appropriate the mathematical model is to the experimental results used.

The most appropriate empirical mathematical models determined using specialized software, and the models determined were included in the second column of Table 5.

Table 5. Empirical mathematical models designed to highlight the negative thermal expansion to the temperature decrease, considering the experimental results.

Polymer	The Most Appropriate Empirical Mathematical Model for the Experimental Results and the S_G Value of Gauss's Criterion	Empirical Mathematical Model of the Power Function Type and the S_G Value of Gauss's Criterion
Black ABS	Second-degree polynomial $\Delta L = -0.739 + 0.00757\theta + 0.0000457\theta^2$ $S_G = 1.078667 \cdot 10^{-4}$	$\Delta L = 3074565\theta^{-3.76}$ $S_G = 1.840823 \cdot 10^{-2}$
Violet PET G	Second degree polynomial $\Delta L = 3.805 - 0.0356\theta - 0.000298\theta^2$ $S_G = 2.356737 \cdot 10^{-3}$	$\Delta L = 1672831\theta^{-3.789}$ $S_G = 0.7223308$
Red FLEXIFILL 98A	Exponential function $\Delta L = 6.281 \cdot 0.904^{\theta}$ $S_G = 2.715475 \cdot 10^{-4}$	$\Delta L = 11457241\theta^{-4.468}$ $S_G = 1.078153 \cdot 10^{-3}$
Silver PLA	Second-degree polynomial $\Delta L = 3.658 - 0.0753\theta + 0.000305\theta^2$ $S_G = 3.64125 \cdot 10^{-3}$	$\Delta L = 2463873\theta^{-4.062}$ $S_G = 0.4127897$

4. Discussion

In many situations in manufacturing engineering, empirical mathematical models of the power function type have been determined and used. Such empirical mathematical models are sometimes used to determine the influence of various factors on the cutting speed, the size of the components of the cutting forces, the size of a roughness parameter of the machined surface, etc. [25–27]. An advantage of using empirical mathematical models of power function type derives from the possibility of evaluating the intensity of the influence exerted by a certain factor by analyzing the value of the exponent attached to that factor in the function of power type to the values of exponents attached to other factors. However, empirical mathematical models of the power function type are particularly appropriate when dealing with monotonous evolutions of the output parameter as the value of the input factor increases or decreases in the investigated process. Such a situation, i.e., the lack of minimums or maximums, was confirmed, for example, by the graphical representation in Figure 5, where there is a continuous increase in thermal expansion when the temperature increases by heating the spiral test samples. For this reason, power function empirical mathematical models for the four polymeric materials were also determined, and those models can be seen in the second column of Table 5.

By considering the values of temperatures and thermal expansions or negative thermal expansions in Tables 2 and 3, it was possible to determine the values of the coefficients of thermal expansion corresponding to each of the four materials used to make the spiral test samples. Some aspects of calculating the coefficients of thermal expansion coefficients starting from the experimental values and Equation (3) are presented in Table 5.

The graphical representations in Figures 4 and 6 have been elaborated considering the experimental results in Tables 2 and 3. In the case of the graphical representation in Figure 3, there is a certain reversal of the thermal expansion values in the cases of ABS and PLA polymeric materials for the period from the beginning of heating. Subsequently, with the development of the expansion process, it is found that the thermal expansion of PLA exceeds that of ABS.

A clearer highlight of the differences between the negative thermal expansion of the spiral test samples in the two materials is provided by the content of the graphical representation in Figure 7, which confirms the order defined by the results recorded for longer time intervals than those in the case of the diagram in Figure 4.

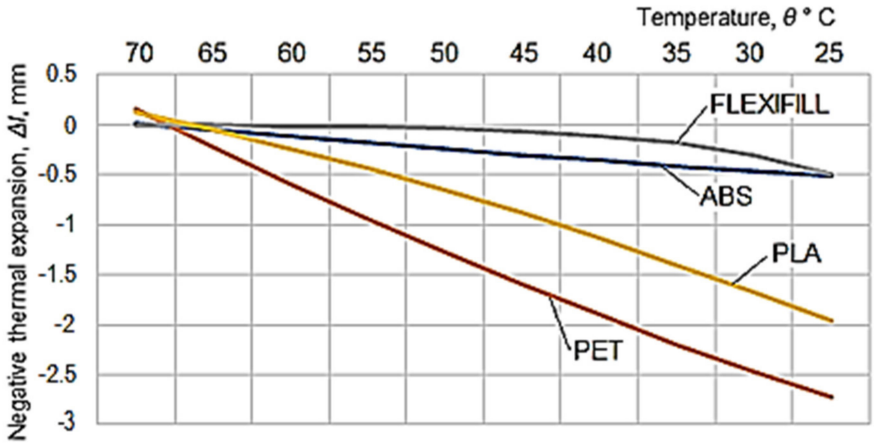

Figure 7. Evolution of negative thermal expansion to the initial temperature, according to the most appropriate empirical mathematical models to the experimental results, for the four polymeric materials.

The most appropriate empirical mathematical models for the experimental results were used to draw the graphical representation in Figure 7. The descending order of the intensity of the influence exerted by the cooling process on the negative thermal expansion can be noticed in this diagram, where polymeric materials are arranged, from this point of view, in the order: polyethylene terephthalate (PET)—polylactic acid (PLA)—styrene-butadiene acrylonitrile (ABS)—thermoplastic polyurethane (Flexfill).

As seen from Table 3, at the beginning of the experiment, heating the aluminum alloy plate and the test samples on the table of the 3D printer, was made on a temperature of 70 °C.

To reduce the friction between the spiral test samples and the spiral groove walls, a thin layer of mineral oil-based lubricant was applied to the support plate before the insertion of the test samples, both when applying the thermal expansion or negative thermal expansion.

In a cross-section, the profile of the spiral test samples made of the four materials has the shape of a rectangle with sides of 1.8 mm and 2.3 mm. The test sample width was 1.8 mm (value measured at a temperature of 22 °C). After the insertion of the spiral test sample in the groove with the shape of an Archimedean spiral, the lateral clearance between the test sample and the groove was about 0.03 mm, at a temperature of 22 °C.

Comparing the maximum values of thermal and negative thermal expansion, respectively, at the temperature variation intervals in the case of experimental research, we reach the values indicated in Table 4.

Comparing the results obtained experimentally with the values indicated in other works shows that the determined coefficients of thermal expansion were lower (Figure 8).

Possible explanations for this could be the following:

- There are, of course, differences between the properties of a part made by 3D printing and the properties of the bulk material. Due to the characteristics of the 3D printing manufacturing process, the material density of the 3D printing test sample may be much lower than in the case of bulk material. This could be the main cause of the relatively large differences between the values of the coefficients of linear thermal expansion indicated by the materials manufacturers or identified in specialized documents and the values determined experimentally using the proposed equipment. It should be noted that the values of the coefficients of thermal expansion determined experimentally were lower than those of the coefficients of linear expansion indicated by the manufacturers of the materials or identified in specialized documents in the case of all four materials;
- The thermal expansion way of the spiral sample is different from that of a strictly linear test sample;

- The relatively small gap between the spiral test sample and the spiral groove in the aluminum alloy plate could lead to frictional forces along the relatively long length of the spiral test sample, and these forces diminish the free expansion of the test sample;
- The existence of roughness resulting from the spiral groove as a result of the spiral groove generation by milling could also contribute to a braking of the free thermal expansion;
- A possible gap at the end of the test sample inside the spiral groove could also reduce the thermal expansion or the negative thermal expansion measured at the end of the segment in the form of a straight line of the spiral test sample.

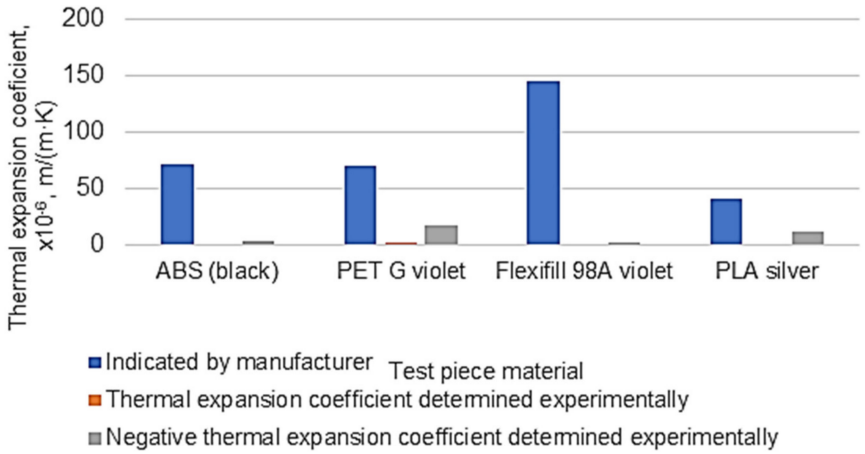

Figure 8. Highlighting the differences between the values of the coefficients of linear thermal expansion indicated by the material manufacturers or identified in specialized documents [20,21] and the values obtained in case of thermal expansion of the spiral test sample.

A certain adjustment of the density of the material of the test sample made by 3D printing is possible by acting on a size that provides some information about the printing process and is called "infill". It must still be taken into account that the density of the test sample material is not uniform, being higher near the outer walls and lower inside the test sample, where there may even be gaps of different sizes. There are, moreover, other print parameters of the printer whose values can change the density of the printed material and therefore can affect the values of the coefficient of thermal expansion. As such, it is expected that there will be a difference between the values of thermal expansion determined using a dilatometer and the proposed equipment, respectively, as long as the dilatometer indicates the value of the linear thermal expansion and the proposed equipment—the thermal expansion along a flat spiral.

Such issues may be further examined in the future to determine their influence on the final results on the values of the coefficients of expansion.

References to the coefficient of linear thermal expansion exist in ASTM E831, ASTM D696, and ISO 11359. These documents describe the test procedure valid for thermomechanical analysis when aiming at linear expansion of the test sample. As this paper aims to expand along a spiral and uses the equipment for such testing, only a few of the provisions included in the above standards could be met, including considering the equipment available for conducting experimental research.

Some aspects that may lead to differences between the results of determining the coefficient of thermal expansion using the proposed equipment and a dilatometer, respectively, have been briefly presented above. In the case of thermomechanical analysis and the use of a dilatometer, the test sample must be 12.7 mm (0.5″) wide and 75 mm (3″) long. The end surfaces of the test sample must be flat. Together with the support on which it is placed, the test sample is introduced into heating equipment and a gradual increase in temperature takes place, with a predetermined heating rate (for example, 10 °C/min) and in a temperature range default (for example, from −30–+30 °C). This ensures conditions for a controlled and as uniform heating as possible of the test sample. In the case of the

proposed equipment, simple and accessible heating sources were used, but which do not allow slow and uniform heating of the spiral test sample. Additionally, the existence of a gap between the spiral test sample and the groove in the aluminum plate could affect to some extent the final result, as the thermal expansion of the aluminum plate exerts a certain influence on the value of the determined coefficient of expansion.

5. Conclusions

For different practical situations, it may be necessary to know the ability of materials used for 3D printing of parts to expand as the temperature rises, and how they shrink when the temperature decreases. A physical quantity used to evaluate this property is the coefficient of thermal expansion. The possibility of determining the size of the coefficient of thermal expansion in the case of four materials used for the manufacture of parts by 3D printing was considered. The materials called acrylonitrile butadiene styrene, polyethylene terephthalate, thermoplastic polyurethane, and polylactic acid were taken into consideration. An experimental device was designed based on an aluminum alloy plate, in which a spiral groove was made by milling. Test samples of the four polymeric materials manufactured by 3D printing were placed in this spiral groove. It was considered that using a spiral test sample would allow an increase in the length of the test sample whose thermal expansion is measured and could provide additional information on the process of thermal expanding or negative thermal expanding of the test sample. Finite element modeling of the heating of the spiral test sample in the spiral groove in the aluminum alloy plate has led to the observation that there is a variation in temperature along the spiral due to cooling at different speeds of the aluminum alloy plate spiral groove is located. In the case of experimental research, the expansion measurement of the outer end of a rectilinear segment of the test sample was performed using an optical microscope. The experimental results were mathematically processed using specialized software based on the least squares method. The specialized software allowed the selection of the most appropriate empirical mathematical models from five mathematical models frequently used in experimental research of different processes in manufacturing technology. The graphical representations elaborated by considering the experimental results and the empirical mathematical models determined by the experimental results showed that, among the materials analyzed, the most intense negative thermal expansion is obtained in the case of polyethylene terephthalate. At the same time, the lowest heat shrinkage was noticed in the case of thermoplastic polyurethane material. In the future, it is intended to expand the experimental research on test samples made of other polymeric materials and deepen the research related to the non-uniform material heating of the test sample in the aluminum alloy plate. Experimental research will also be carried out on changing the thermal expansion or negative thermal expansion coefficients with temperature variation.

Author Contributions: Conceptualization. L.S. and B.R.; methodology. L.S.; software. A.M.M. and B.R.; validation. B.R. and L.S.; formal analysis. O.D. and M.R.; investigation. B.R. and A.M.; resources. G.N.; data curation. A.M.; writing—original draft preparation. L.S.; writing—review and editing. O.D.; visualization. A.H. and M.R.; supervision B.R.; project administration. A.H. and G.N.; funding acquisition. B.R and G.N. All authors have read and agreed to the published version of the manuscript.

Funding: The A.P.C. is funded by the university funding.

Data Availability Statement: Data are available on request from the authors.

Conflicts of Interest: The authors declare no conflict of interest.

References

1. Manufactur3D. The 7 Types of Additive Manufacturing Technologies. 2018. Available online: https://manufactur3dmag.com/7-types-additive-manufacturing-technologies/ (accessed on 5 July 2022).
2. Qu, J.; Kadic, M.; Naber, A.; Wegener, M. Micro-Structured Two-Component 3D Metamaterials with Negative Thermal-Expansion Coefficient from Positive Constituents. *Sci. Rep.* **2017**, *7*, 40643. [CrossRef] [PubMed]
3. Wang, X.; Jiang, M.; Zhou, Z.; Gou, J.; Hui, D. 3D printing of polymer matrix composites: A review and prospective. *Compos. B Eng.* **2017**, *110*, 442–458. [CrossRef]
4. Van de Werken, N.; Tekinalp, H.; Khanbolouki, P.; Ozcan, S.; Williams, A.; Tehrani, M. Additively manufactured carbon fiber-reinforced composites: State of the art and perspective. *Addit. Manuf.* **2020**, *31*, 100962. [CrossRef]
5. Xu, W.; Jambhulkar, S.; Zhu, Y.; Ravichandran, D.; Kakarla, M.; Vernonc, B.; Lott, D.G.; Cornella, J.L.; Shefi, O.; Miquelard-Garnier, G.; et al. 3D printing for polymer/particle-based processing: A review. *Compos. B Eng.* **2021**, *223*, 109102. [CrossRef]
6. Miller, D.J. Material Coefficient of Thermal Expansion Investigation for Use in Additive Manufacturing Fused Deposition Modeling for Composite Tooling. Master's Thesis, University of Southern Mississippi, Hattiesburg, MS, USA, 2015; pp. 31–33. Available online: https://aquila.usm.edu/cgi/viewcontent.cgi?referer=&httpsredir=1&article=1083&context=masters_theses (accessed on 24 July 2022).
7. Nam, R. Additive Manufacturing of Thermoactivated Morphing Materials. Master's Thesis, University of Toronto, Toronto, ON, Canada, 2021; pp. 59–65. Available online: https://tspace.library.utoronto.ca/bitstream/1807/104863/1/Nam_Ryan_202103_MAS_thesis.pdf (accessed on 24 July 2022).
8. Trhlíková, L.; Zmeskal, O.; Psencik, P.; Florian, P. Study of the thermal properties of filaments for 3D printing. *AIP Conf. Proc.* **2016**, *1752*, 040027. [CrossRef]
9. Savu, I.D.; Savu, S.V.; Simion, D.; Sîrbu, N.-A.; Ciornei, M.; Ratiu, S.A. PP in 3D printing—Technical and economic aspects. *Mat. Plast.* **2019**, *56*, 931–936. Available online: https://revmaterialeplastice.ro/pdf/35%2-0SAVU%2-04%2-019.pdf (accessed on 24 July 2022). [CrossRef]
10. Zhang, Z.; Yuan, X. Applications and future of automated and additive manufacturing for power electronics components and converters. *IEEE J. Emerg. Sel. Top. Power Electron.* **2021**. [CrossRef]
11. Wang, L.; Gramlich, W.M.; Gardner, D.J.; Han, Y.; Tajvidi, M. Spray-dried cellulose nanofibril-reinforced polypropylene composites for extrusion-based additive manufacturing: Nonisothermal crystallization kinetics and thermal expansion. *J. Compos. Sci.* **2018**, *2*, 7. [CrossRef]
12. Blanco, I. A brief review of the applications of selected thermal analysis methods to 3D printing. *Thermo* **2022**, *2*, 74–83. [CrossRef]
13. Nath, S.D.; Nilufar, S. An overview of additive manufacturing of polymers and associated composites. *Polymers* **2020**, *12*, 2719. [CrossRef] [PubMed]
14. Huang, Q. 3D Printing Shrinkage Compensation Using Radial and Angular Layer Perimeter Point Information. U.S. Patent 9,886,526, 6 February 2018.
15. Zohdi, N.; Yang, R. Material Anisotropy in Additively Manufactured Polymers and Polymer Composites: A Review. *Polymers* **2021**, *13*, 3368. [CrossRef] [PubMed]
16. Hwang, S.; Reyes, E.I.; Moon, K.-S.; Rumpf, R.C.; Kim, N.S. Thermo-mechanical characterization of metal/polymer composite filaments and printing parameter study for fused deposition modeling in the 3D printing process. *J. Electron. Mater.* **2015**, *44*, 771–777. [CrossRef]
17. Baker, A.M.; Mccoy, J.; Majumdar, B.S.; Rumley-Ouellette, B.; Wahry, J.; Marchi, A.N.; Bernardin, J.D.; Spernjak, D. Measurement and modelling of thermal and mechanical anisotropy of parts additively manufactured using fused deposition modelling (FDM). In Proceedings of the 11th International Workshop on Structural Health Monitoring. Stanford, CA, USA, 12–14 September 2017. [CrossRef]
18. Baron, T.H.K. Generalized theory of thermal expansion of solids. In *Thermal Expansion of Solids*; Ho, C.H., Taylor, R.E., Eds.; ASM International: Metals Park, OH, USA, 1998; pp. 1–2.
19. Rădulescu, B.; Mihalache, A.-M.; Rădulescu, M.; Slătineanu, L.; Hrițuc, A.; Dodun, O.; Nagîț, G.; Coteață, M. Selection of a method for machining an archimedean spiral groove. *Acta Tech. Napoc. Ser. Appl. Math. Mech. Eng.* **2022**, *65*, 231–238. Available online: https://atna-mam.utcluj.ro/index.php/Acta/article/view/1755/1416 (accessed on 24 July 2022).
20. SD3D. ABS Technical Data Sheet. Available online: https://www.sd3d.com/wp-content/uploads/2-015/1-0/MaterialTDS-ABSWeb.pdf (accessed on 10 January 2022).
21. SD3D. PLA Technical Data Sheet. Available online: https://www.sd3d.com/wp-content/uploads/2-017/-06/MaterialTDS-PLA_-01.pdf (accessed on 10 January 2022).
22. Hrituc, A.; Nagîț, G.; Dodun, O.; Slătineanu, L. Measuring the length of a spiral when evaluating the plastic processability by injection molding. *IOP Conf. Ser. Mater. Sci. Eng.* **2019**, *564*, 012025. [CrossRef]
23. Geng, H.; Wang, Y.; Wang, Z.; Zhang, Y. Investigation on contact heating of aluminum alloy sheets in hot stamping process. *Metals* **2019**, *9*, 1341. [CrossRef]
24. Cretu, G. *Fundamentals of Experimental Research. Laboratory Handbook*; "Gheorghe Asachi" Technical University of Iașii: Iași, Romania, 1992. (In Romanian)
25. Groover, M.P. *Fundamentals of Modern Manufacturing*; John Wiley & Sons, Inc.: Hoboken, NJ, USA, 2007; p. 548.
26. Kalpakjian, S.; Schmid, S.R. *Manufacturing Engineering and Technology*, 4th ed.; Prentice Hall: Hoboken, NJ, USA, 2001; pp. 549–578.
27. Danilevsky, N. *Manufacturing Engineering*; Mir Publishers: Moskow, Russia, 1973; pp. 127–128.

polymers

MDPI

Article

Tensile Behavior of Joints of Strip Ends Made of Polymeric Materials

Andrei-Marius Mihalache [1], Vasile Ermolai [1,2], Alexandru Sover [2], Gheorghe Nagîț [1], Marius-Andrei Boca [1,2], Laurențiu Slătineanu [1], Adelina Hrițuc [1,*], Oana Dodun [1] and Marius-Ionuț Rîpanu [1]

[1] Department of Machine Manufacturing Technology, "Gheorghe Asachi" Technical University of Iași, 700050 Iași, Romania
[2] Faculty of Technology, Ansbach University of Applied Science, Residenzstraße 8, 91522 Ansbach, Germany
* Correspondence: adelina.hrituc@student.tuiasi.ro; Tel.: +40-751640117

Abstract: The strength of a joint between the ends of one or more strips can be improved by making the contours of the joint into the shape of either the Greek letter omega or of a dovetail. From the point of view of industrial practice, it is of interest to study the behavior of these joints under stretching demands. The emergence and development of additive manufacturing processes for parts made of polymeric materials has led to the idea of conducting experimental tests to highlight the behavior of omega and dovetail-type joints during the tensile test. For the tensile testing of some test samples in which omega and dovetail joints were used, a Taguchi array of type L18 was employed, with eight independent variables, one variable with a two-level variation, and seven variables with variations on three levels. As independent variables, the type of joint, the couple of polymer materials used to make the two components of the joint, some characteristic dimensions of the joint contours, and some input factors in the 3D printing process were established. The values of average force and average displacement at the peak were considered output parameters. The experimental results were mathematically processed, determining empirical mathematical models of the second-degree polynomial type. These models highlight the influence exerted by the considered input factors on the values of the output parameters.

Keywords: strip end; omega contour; dovetail contour; polymer; tensile; force; displacement; modeling

Citation: Mihalache, A.-M.; Ermolai, V.; Sover, A.; Nagîț, G.; Boca, M.-A.; Slătineanu, L.; Hrițuc, A.; Dodun, O.; Rîpanu, M.-I. Tensile Behavior of Joints of Strip Ends Made of Polymeric Materials. *Polymers* **2022**, *14*, 4990. https://doi.org/10.3390/polym14224990

Academic Editors: Alexander Malkin and Abdel-Hamid I. Mourad

Received: 4 September 2022
Accepted: 14 November 2022
Published: 18 November 2022

1. Introduction

Belt-type strips can be used as transmission belts and in other products' assembly or packaging activities. In this paper, a strip is considered a part where the length is much greater than the width, and the thickness is relatively low compared to the width. The strips are slightly rigid in the case of bending stresses exerted in a perpendicular direction to the surface, in the dimensions corresponding to the length and width of the strip. Most strip parts are subject to tensile stresses.

The development of processes for manufacturing parts made of polymeric materials through 3D printing has facilitated the development of research on how to join strip ends, whether made of the same or of different materials. The strips can be made of metallic or non-metallic materials, the last group being, for example, polymer materials. To increase the strength of the joint between strip ends, it has been possible to introduce an interweaving of several layers belonging to the two strip ends to be joined.

The strength characteristics of the joint of strip ends made by 3D printing depends on the joint's shape and dimensions and the values of some input factors in the 3D printing process.

When using distinct polymer materials for the two strips, additional problems arise as to how they are joined. To obtain a strong joint when using the interweaving solution, a degree of chemical compatibility and a certain bonding of the polymer materials used in the 3D printing process is required. The use of interweaving must be applied in such a way as to avoid, as far as possible, too pronounced porosity or the appearance of cracks.

Problems specific to the behavior of strip end joints or other types of mechanical joints have been addressed by some researchers concerned with obtaining joints with higher mechanical strength.

Thus, Tiwari et al. analyzed the possibilities of making a joint starting from components manufactured by 3D printing from similar/dissimilar thermoplastic parts and using friction stir welding [1]. They focused on the optimization of the behavior of the joint from the point of view of weld strength, elongation, hardness, and desired flatness.

Lopes et al. studied the tensile strength of multi-material test samples made by additive manufacturing from polymeric materials [2]. The obtained results highlighted the importance of the influence of the interface formed upon the contact of some components made of different materials on the value of Young's modulus and the value of the tensile strength of the multi-material test samples.

Chen and Zhang used 70/30 and 30/70 ABS/PETG blends to evaluate notched impact strength [3]. They observed that ABS/PETG (30/70) blends showed an obvious increase in impact strength. The addition of a compatibilizer can result in improved flexural strength.

The problem of the influence exerted by slicing parameters on multi-material adhesion mechanisms in the case of parts manufactured by 3D printing was addressed by [4]. They found that interlocking strategies can compensate for the disadvantages of less favorable thermodynamic and diffusion mechanisms.

Ribeiro and Sousa Carneiro considered the problem of interface geometry in the case of multi-material test samples produced by fused filament fabrication from polymer materials [5]. They used T-shape, U-shape, and dovetail shape joints.

Ando et al. have achieved a stronger horizontal adhesion and a weaker vertical adhesion in the case of the tensile test of some samples made by additive manufacturing of multi-colored polylactic acid materials [6].

Kluczyński et al. [7] used both non-destructive testing methods (laser amplified ultrasonography, microscopic observations) and tensile tests to study the behavior of joints generated by multi-material additive manufacturing. They found that an overlap connection of two parts made of polylactic acid can increase tensile strength by up to 14% and elongation by up to 22%.

Hasanov et al. addressed the problem of additive manufacturing of multi-material parts [8]. They appreciated that to obtain a joint with high mechanical resistance, it is necessary to consider the factors that influence the result of combining the two materials To lessen the negative effect of shrinking adhesion between the components of a joint made of chemically incompatible materials, Kuipers et al. proposed using a so-called interlaced topologically interlocking lattice [9]. They found that in this way, joints with a behavior close to that of dovetail in-interlocking could be obtained.

In this paper, the research results sought to highlight the influence exerted by the shape and dimensions of joints, along with the values of some input factors in the 3D printing process, on the tensile strength of samples made of pairs of distinct polymers. Joints in the form of the Greek letter omega and dovetail joints were considered.

2. Materials and Methods

2.1. Initial Considerations

When the problem of joining the ends of a strip or several strips arises, it is necessary to choose from several possible alternatives approaches. The simplest way to join is along a straight line perpendicular to the parallel edges of the strip. A slightly more complicated alternative, which increases joint strength by increasing the length of the joint area, could be along an inclined line to the parallel edges of the strip. In both cases highlighted previously, it is necessary to glue or weld those surfaces of the strip or strips to make the joint.

An increase in the tensile strength of the joint becomes possible by making a shaped area on one end correspond to the the same shape in reflection on the other strip end to which the first end is to be joined, as in a jigsaw puzzle. As such, several usable solutions have appeared. Two involve a joint along a contour similar to the Greek letter omega (Ω) or,

respectively, along a so-called dovetail contour (Figure 1). Also, in this case, to increase the operational reliability of the joint, it is beneficial to use gluing or welding of the strip ends.

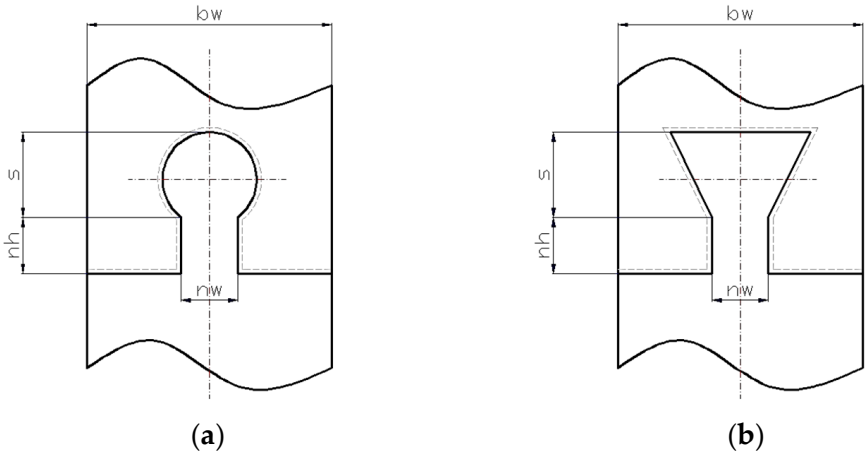

Figure 1. Joints along an outline of the Greek letter omega (**a**) and dovetail (**b**) shape.

For both omega and dovetail-type joints, the mechanical stressing and breaking of the strip ends are affected by the dimensions that characterize these joints.

Thus, if we consider in both cases the presence of a "neck", when the width n_w of the neck is large to the width of the strip, it is expected that the lateral areas of the opposite end will bear an elastic deformation until the free exit of the profile in the form of an arc of a circle or an isosceles trapezoid of the lower end of the strip (Figure 2a); or even to the breaking of the two lateral areas of the upper end (Figure 2b). If the width n_w of the neck is small compared to the width of the strip, it is expected that the strip end break will occur right next to the bottom end neck (Figure 2c).

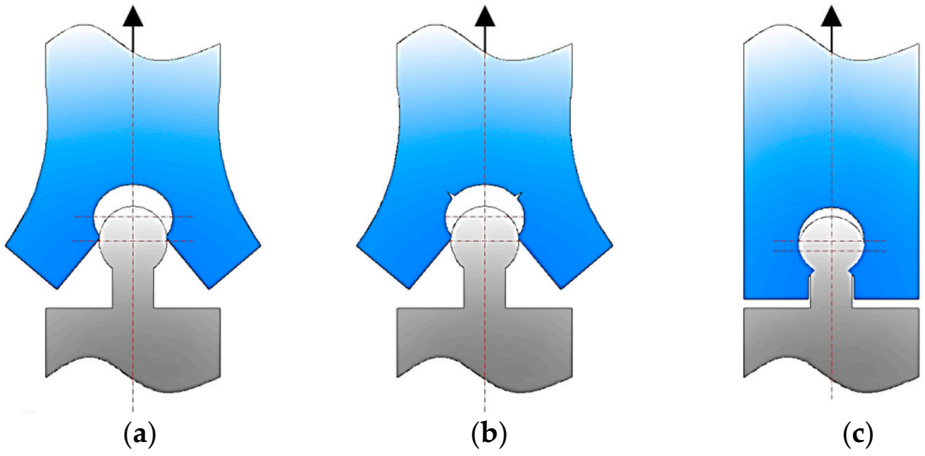

Figure 2. Hypotheses regarding the damage of a joint in the case of an omega-type joint: (**a**) by elastic deformation of some areas of the upper end; (**b**) by deformation until the initiation of cracks in some areas of the upper end; (**c**) by deformation until the initiation of some cracks in the area of the neck on the lower end.

The emergence and development of additive manufacturing processes have increased the number of possible alternatives for joining strip ends. It was possible to interweave some layers of the materials of the two ends of the strip (Figure 3). This situation will lead, on the one hand, to reducing the risk of one end of the strip moving to the other along a direction perpendicular to the strip. On the other hand, increasing the contact surfaces between the two ends of the strip could increase the joint's mechanical strength.

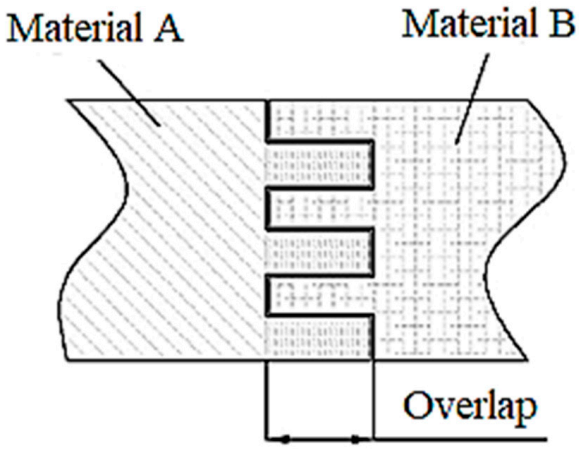

Figure 3. Interlock zone.

An interesting problem is also the behavior of end joints of strips made of different materials when the joints are made by 3D printing. Some aspects of the behavior of such a joint will be considered next.

Multi-material models result from joining two or more bodies of the same part (i.e., meshes). Depending on the model, the joint surfaces have a simple flat or circular arc profile. Since each part has a material associated with it, the printer will only deposit the materials within the mesh boundaries. Depending on the part design, the materials can be deposited side by side, layered, or both [2].

To increase the strength of the bond between materials, slicing tools such as Cura provide a parameter called Merged Meshes Overlap (MMO), which allows materials to cross into each other to interweave, improving joint strength. For this study, the parameter was set to zero to control it via CAD modeling.

2.2. Materials

Three distinct materials were chosen: a blue acrylo-butadiene-styrene from REC, a black polylactic acid PA645 (i.e., a PA6.6-based material) from Taulman3D, and a red Polyethylene terephthalate glycol PETG. These materials were chosen based on their low compatibility and similar melting range. A literature review shows that these pure polymer combinations, ABS-PA645 [8], ABS-PETG [1], and PETG-PA645 [10], have poor bonding. However, research has shown that blends of ABS and PETG have better properties than the base materials [11].

2.3. Experimental Conditions

As is known, when the determination of an empirical mathematical model is intended to highlight the influence of different input factors in the investigated process on some process output parameters, the use of the least squares method may make it necessary to perform a large number of experimental tests to reach an acceptable confidence level for the identified empirical mathematical model.

However, through the so-called design of experiments, it has become possible to significantly reduce the number of experimental trials required so that an empirical mathematical model can be determined through the mathematical processing of the results [12–14]. Ronald Fisher proposed the first principles of using the design of experiment method in 1924. In 1935, Fisher even published a book entitled "Design of experiments".

Starting in the 1950s, Genichi Taguchi identified a series of situations in which the number of experimental tests can be reduced yet further, without significantly affecting the quality of the identified empirical mathematical model [15–17].

An experimental research solution using a relatively small number of experimental trials corresponds, for example, to a Taguchi L18 array with one input factor at two variation levels and seven input factors at three variation levels [18–20]. Such a Taguchi L18 array

will be used to determine an empirical mathematical model capable of highlighting the influence of some input factors in the 3D printing process on the average force at peak and, respectively, on average displacement at peak.

For the design of the experiment, a Taguchi L18 array with one input factor at two levels and seven input factors at three levels was considered.

The input factors are joint shape (j), material pairs (m), neck width (n_w), neck height (n_h), shape height (s), number of walls (no_w), line width (l), and the overlap level (o) of the layers of the two parts being joined.

The values corresponding to the various levels of the input factors can be seen in Table 1. The first variable provides information on the joints' shape, omega, and dovetail. The joint dimensions are defined by the neck width (n_w), neck height (n_h), and shape height (s). As seen in Figure 4, the contact interfaces are constrained symmetrically relative to the mid-plane of the test sample.

Table 1. Experimental conditions and results.

Exp. Run	Input Factors								Output Factors	
	Joint Shape, j	Material Pairs, m	Neck Width, n_w, mm	Neck Height, n_h, mm	Socket Height, s, (mm)	No. of Walls, no_w	Line Width, l, (mm)	Overlap, o, mm	Avg. Force at Peak, F, kN	Avg. Displacement at Peak, L, mm
R1	Omega	ABS-PA645	5	5	8	3	0.4	0	0.288	4.330
R2	Omega	ABS-PA645	8	8	11	4	0.45	2	0.613	4.128
R3	Omega	ABS-PA645	11	11	14	5	0.5	4	0.638	6.363
R4	Omega	ABS-PETG	5	5	11	4	0.5	4	1.628	2.253
R5	Omega	ABS-PETG	8	8	14	5	0.4	0	0.373	0.573
R6	Omega	ABS-PETG	11	11	8	3	0.45	2	1.278	1.640
R7	Omega	PA645-PETG	5	8	8	5	0.45	4	0.555	3.095
R8	Omega	PA645-PETG	8	11	11	3	0.5	0	0.148	4.448
R9	Omega	PA645-PETG	11	5	14	4	0.4	2	0.820	5.200
R10	Dovetail	ABS-PA645	5	11	14	4	0.45	0	0.100	2.860
R11	Dovetail	ABS-PA645	8	5	8	5	0.5	2	0.328	1.660
R12	Dovetail	ABS-PA645	11	8	11	3	0.4	4	0.830	5.758
R13	Dovetail	ABS-PETG	5	8	14	3	0.5	2	0.728	0.975
R14	Dovetail	ABS-PETG	8	11	8	4	0.4	4	1.613	2.273
R15	Dovetail	ABS-PETG	11	5	11	5	0.45	0	0.175	0.810
R16	Dovetail	PA645-PETG	5	11	11	5	0.4	2	0.443	2.123
R17	Dovetail	PA645-PETG	8	5	14	3	0.45	4	0.738	5.070
R18	Dovetail	PA645-PETG	11	8	8	4	0.5	0	0.078	3.530

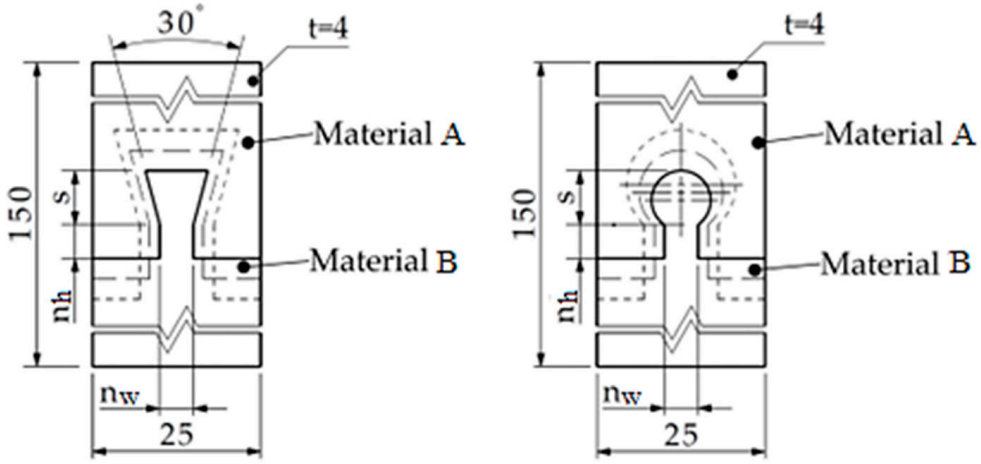

Figure 4. Macroscopic contact interfaces definition on custom samples (design based on type 2 test sample according to ISO 527:3).

The last three input factors consider some characteristics of the 3D printing process of test samples. The number of walls (otherwise known as contours, perimeters, or shells) no_w refers to the number of closed paths deposited along the edge of the part [21]. The line width or the extrusion width (l) is the thickness of an extruded filament that influences the number of passes required to fill a full-density layer. Good results are obtained with line

width between 60% and 150% of the nozzle orifice diameter. Higher values of this ratio can be used, but the results depend on the extrusion subsystem and filament diameter. A wider line width decreases the manufacturing time [22] and increases the tensile strength [23]. However, wider width lines increase the heights of surface asperities generated, due either to larger gaps between filling lines and walls [24] or to under extrusion if the extruder cannot melt the filament and provide a constant material flow.

Tensile tests were performed using an Instron 4411 uniaxial testing machine with a load capacity of 5 kN. All samples were printed using a 3D printer, Ultimaker 3, in an enclosure after reaching 35 °C. Each run covered in the experimental array was printed in four or five replicates. The results of the average tensile strength tests were processed using the statistical tool Minitab 21.1. As a benchmark for the resulting samples, six groups of samples were printed having the following material pairs: ABS-ABS, PA645-PA645, and PETG-PETG, to compare both forms of interconnection. The other parameters were kept at the mid-level values (see Table 2, except for overlap, which was set to zero).

Table 2. Constant process parameters and their levels.

Parameter	Value	Parameter	Value
(1) Layer thickness (mm)	0.2	(11) Initial layer speed (mm/s)	15
(2) No. of top/bottom layers	5	(12) Z Hop height (mm)	1.6
(3) Left extruder seam alignment	Back left	(13) Retraction distance (mm)	7
(4) Right extruder seam alignment	Back right	(14) Retraction speed (mm/s)	35
(5) Infill pattern	Gyroid	(15)[1] Fan speed (%)	10 | *15* | **30**
(6) Infill density (%)	40	(16) Brim	Yes
(7) Printing temperature (°C)	245	(16) Brim width (mm)	3
(8) Bed temperature (°C)	65	(17) Closed environment	Yes
(9) Print speed (mm/s)	30	(18) Alternate mesh removal	Yes

(15)[1] Normal font is associated with ABS, Italic with PA645, and Bold with PETG.

The conditions under which the experimental tests were carried out and the results of these experimental tests are included in Table 1. It is necessary to specify that the values of the output factors in the last two columns of Table 1 are average values for four experimental tests carried out with the same values of input factors. An image regarding the dispersion of the experimental results from the case of experiments no. 2 and 12 can be seen in Figure 5.

The overlap *o* (Figures 3 and 6) between the female and male bodies was adjusted in the sample design stage. Thus, the overlap value of the merged meshes in Cura was set to zero. Alternate mesh removal is another parameter enabled when printing samples. When the meshes are overlapped, the slicer removes a part of the mesh to make space for the other sample's mesh. In this way, the meshes alternate layer by layer, woven like the structure of the materials. An example of the effect of using the 'meshes overlap with alternate mesh removal' function enabled is shown in Figure 6.

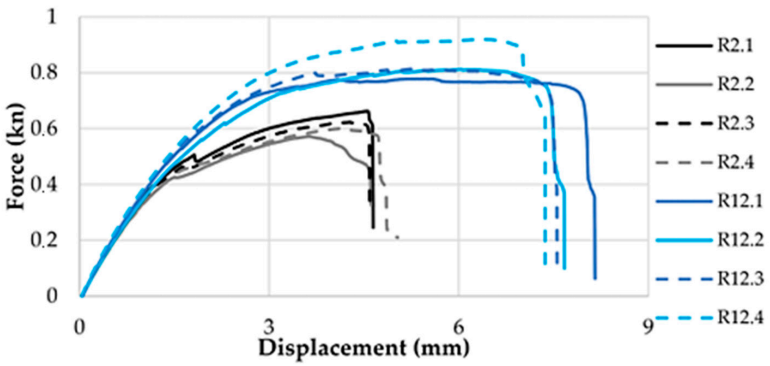

Figure 5. Force-displacement charts for R2 and R12 groups of samples.

As shown in the preview of the g-code, in addition to the interlocking geometry, the materials are also held together by the woven structure created by overlap and alternate mesh removal. It was hypothesized that the frictional force (generated by the stacked layers) would improve the tensile strength of the test pieces.

In this regard, the line width *l* could influence the value of the pulling friction force. As previously mentioned, if the line width *l* is larger, larger voids may occur—either when the lines fuse or due to the possible under-extrusion. This means the second material deposited in the overlapping region will fill the voids formed, creating a mechanical interlock between the layers. The values of the other input factors considered for printing were kept at a constant value and can be seen in Table 2.

The appearance of some damaged test samples as a result of the tensile test is highlighted in Figure 7. In the case of some test samples made from the ABS-PA645 material couple (experiments R1 and R10), the joint damage develops through the elastic deformation of some areas of the two components of the joint. This fact could be justified by the lower mechanical resistance of the materials of the two components. In the case of some test samples made of the ABS-PETG material couple (experiments R4 and R13), damage to the test samples was observed near the interweaving area over the entire width of the test sample.

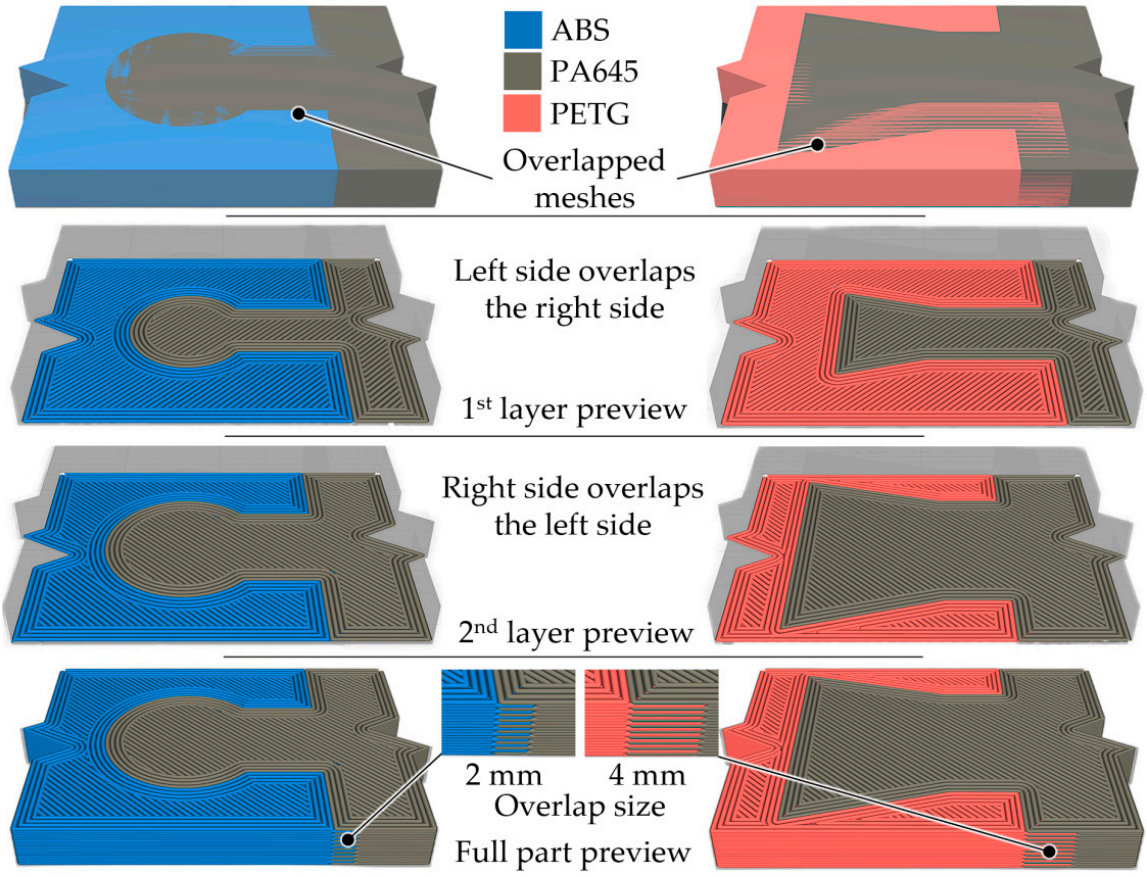

Figure 6. Print preview of the printed samples R2 and R17 experiments from Table 1 using Ultimaker-Cura Arachne Beta 2 engine, with overlap between meshes and alternate mesh removal enabled.

2.4. The Use of the Finite Element Method to Model Some Aspects of the Tensile Behavior of a Joint

Finite element method (FEM) analyses were first considered to highlight stress and strain distribution on selected surfaces of the assemblies. From the 18 samples, two different experiments in terms of shape were selected: experiment R2, corresponding to an omega joint; and experiment R12, corresponding to a dovetail joint. These experiments led to severe damage to the test samples at the end of the tensile tests.

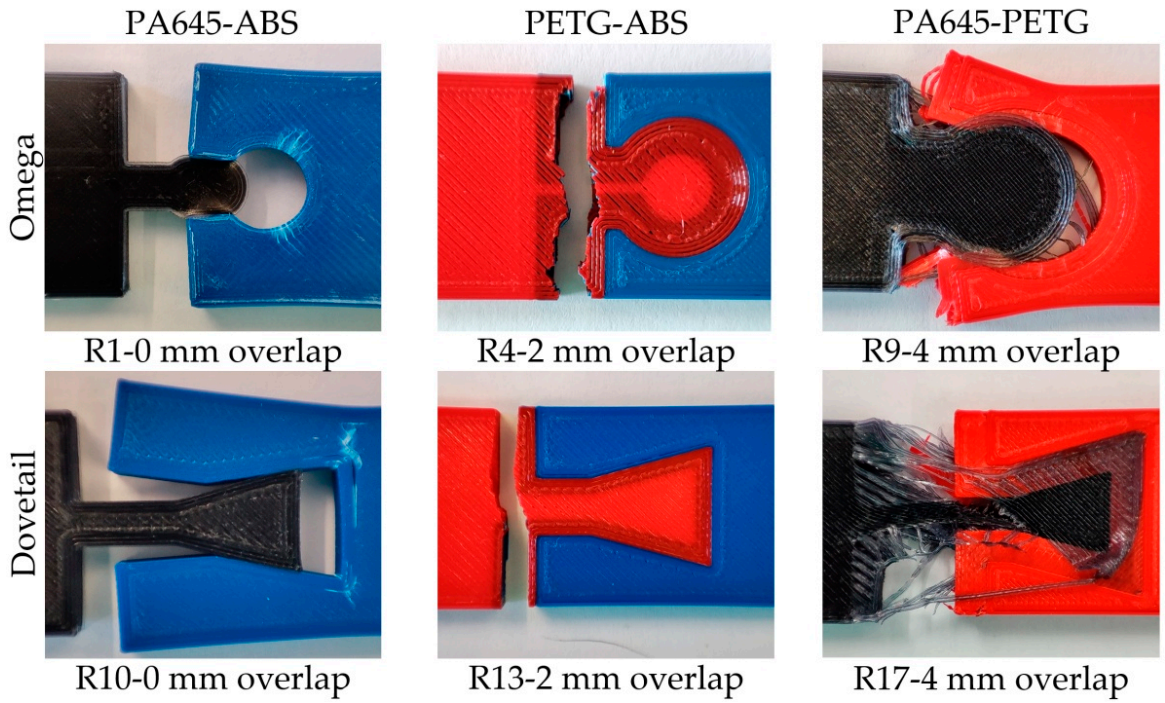

Figure 7. Images of damaged test samples resulting from the tensile test corresponding to experiments R1, R4, R9, R10, R13, and R17.

Some material properties were considered for ABS and generic ABS plastic PA645 and PET plastic. Such properties have been identified in Ansys's Granta. We considered modeling new materials in Ansys's Material Designer module derived from PET plastic with added uniaxial tension test data. That allowed us to design an anisotropic response based on the matrix of the material as mentioned above. The model was set to create a randomized unidirectional composite with default values for volume fraction, seed, and fiber diameter. It used conformal meshing, model set as anisotropic when computing with linear elasticity. Thus, we obtained the stiffness matrix. The results were exported to engineering data where we added the uniaxial tension test data in tabular form, given by the Instron 4411 equipment used for experimental tensile tests. Because both samples cracked, the model aimed to use a method of crack growth assessment to find out if the results matched in terms of direction and shape. Static Crack Growth was used for the possible estimates of the crack growth in case of fracture [25]. In the case of the female component, a quadratic mesh size corresponding to the mesh element of 1 mm was combined with a patch-conforming method based on the use of tetrahedrons, which together took into account the computational limits proposed. The physics preference was set to Nonlinear Mechanical.

The simulations took into account different fixed supports and forces that would be involved in the tensile tests. Since there were different layers, time substeps were used.

The best-case scenario involved different loads and supports for each layer. However, the results are intermediate and should not be used in new research without further refinement due to the designed material's behavior which can be different in terms of fiber reinforcement and additives used by the manufacturer. Only the female part of the two distinct shapes were considered and put to the test by treating each strip end individually. Thus, we imposed supports and loads on each strip end for the omega and dovetail-shaped samples which received pre-modeled V-shaped cracks. Within Ansys Static Structural, we used the Fracture tool with the SMART Crack Growth condition based on Static Crack Growth with Failure Criteria Option set to Stress Intensity Factor with a critical rate of around 100 MPa. All cracks received their Coordinate Systems that were used inside the Pre-Meshed Crack tool with six solution contours. Fracture Controls in Analyses Settings were on, and Stress Intensity Factor enabled. The strip ends that were not

cracked received force loads acting almost normally in the Y direction of the top face of the predesigned crack as the X axis points to the initial crack growth direction. This resulted in an asymmetric response using the Nonlinear Adaptive Region tool with the criterion set to Mesh Quality with the option for Skewness and the Jacobian ratio at default values.

The R2 sample exhibits severe failure, as shown in Figure 8. FEM yields a value of around 0.07 mm/mm for equivalent elastic strain, and each of our five samples of R2 varies from under 0.09 up to 0.13. However, deformed strip ends look slightly different between real-life samples and FEM ones. The difference could come from the linear deformation recorded in the tensile tests versus the total deformation in the FEM that considers all six degrees of freedom.

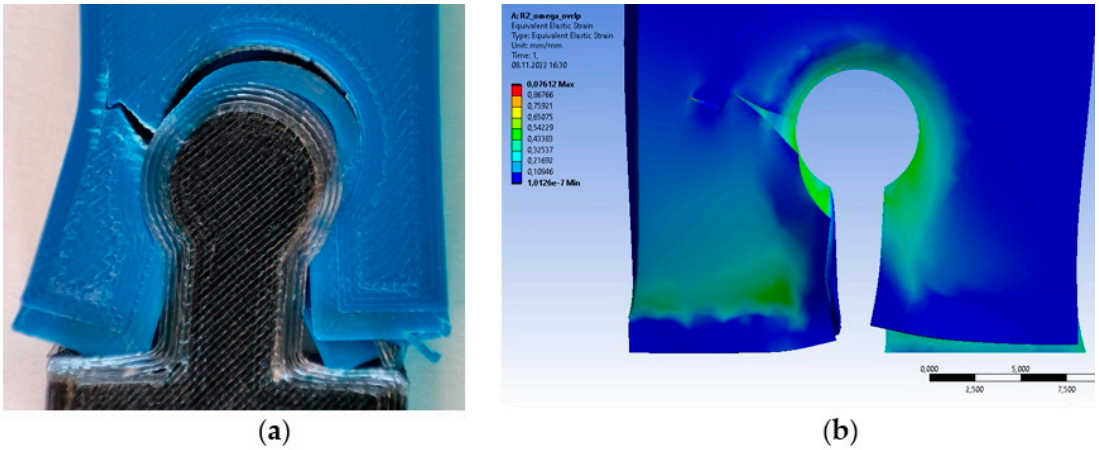

(**a**) (**b**)

Figure 8. Comparison of results for R2 omega-shaped test sample: (**a**) real-life sample after tensile test; (**b**) FEM result when using the equivalent elastic strain distribution.

For the R12 dovetail-shaped test sample, the results are shown in Figure 9. The test sample registers around 0.15 mm/mm for equivalent elastic strain, and each of our five samples of R12 vary from under 0.09 up to 0.16. Real-life samples show more severe damage than FEM ones. A possible explanation could be that FEM stops after failure criteria are met, whereas tensile tests continue.

A certain correspondence between real-life samples and FEM results was achieved regarding deformation and failure. The authors acknowledge that further refinement is mandatory in view of the behavior of the material in our experiments, and FEM setup having focused only on female parts.

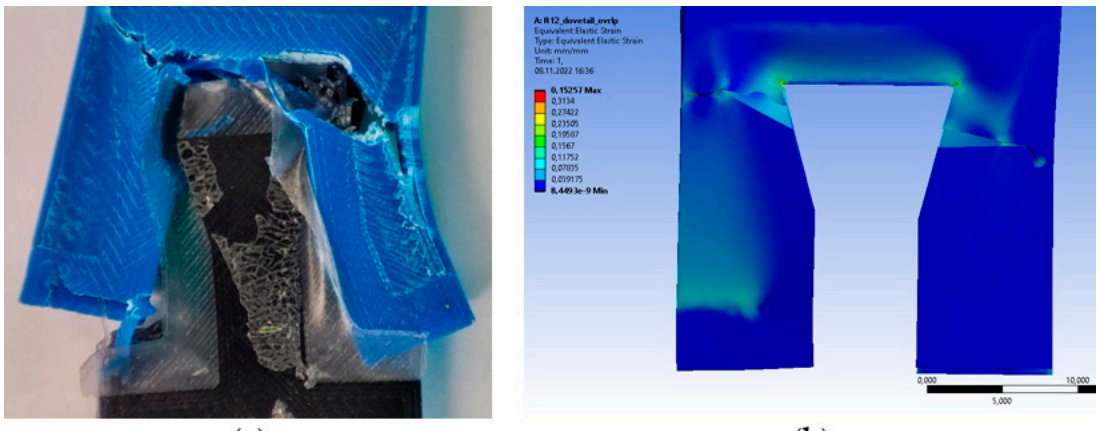

(**a**) (**b**)

Figure 9. Comparison of results for R12 dovetail-shaped sample: (**a**) real-life sample after tensile test; (**b**) FEM result with equivalent elastic strain distribution.

2.5. Using the ANOVA Method to Identify Significant Input Factors

To obtain information on the significance of the factors considered in terms of their influence on the values of the output parameters of the considered process, the ANOVA method was used. Analysis was performed using Minitab software.

Thus, in the case of using the ANOVA method to evaluate the significance of the factors capable of exerting influence on the average force at peak, the results presented synthetically in Table 3 were obtained.

Table 3. Results of analysis of variance for average maximum force.

Source	DF	Seq SS	Adj SS	Adj MS	*F*-Value	*p*-Value
Joint shape, *j*	1	58.07	58.068	58.68	84.65	0.012
Materials pairs, *m*	2	152.32	153.318	76.659	111.76	0.009
Neck width, n_w	2	2.19	2.190	1.095	1.60	0.385
Neck height, n_h	2	6.52	6.524	3.262	4.76	0.174
Socket height, *s*	2	0.32	0.319	0.160	0.23	0.811
Number of walls, no_w	2	24.70	24.701	12.351	18.01	0.053
Line width, *l*	2	58.32	56.324	29.162	42.51	0.023
Overlap, *o*	2	725.99	725.986	362.993	529.18	0.002
Residual error	2	1.37	1.372	0.686		
Total	17	1030.80				

In Table 3, the symbols used have the following meanings: DF—degrees of freedom; Seq SS—Sequential sums of squares; Adj SS—the adjusted sum of squares; Adj MS—adjusted mean squares; *F*-value—value on the *F* distribution; *p*-value—the probability of obtaining the observed results.

The critical value Fcrit of Fisher's criterion for a risk coefficient $\alpha = 5\%$ was determined as follows. Given the number of degrees of freedom $v_1 = N - k - 1 = 18 - 8 - 1 = 9$, and $v_2 = N(n - 1) = 18(8 - 1) = 126$, one can evaluate Fcrit = 2.01 from a table that includes Fisher distribution values [26]. Analyzing the values calculated using the Minitab software for *F*-value, it is found that values higher than the critical value (Fcrit = 2.01) were obtained, depending on the values of the *F*-value criterion for overlap *o* (*F*-value = 529.18), material pairs *m* (*F*-value = 111.76), joint shape *j* (*F*-value = 84.65), line width *l* (*F*-value = 42.51), number of walls no_w (*F*-value = 18.01), neck height n_h (*F*-value = 4.76). This means that the six input factors influence the average displacement value at peak *L*.

Regarding the *p*-value, it can be seen that values lower than 0.05 were determined for the following factors: joint shape j (*p*-value = 0.012), materials pairs m (*p*-value = 0.009), line width *l* (*p*-value = 0.023) and overlap o (*p*-value = 0.002). According to current conventions, for *p*-value < 0.05, it can be considered that there is a statistically significant relationship between the input factors for which the condition for *p*-value is met and the output parameter considered (in the present case, the average displacement at peak *L*).

3. Results

The experimental results were entered in the last two columns of Table 1. To establish some empirical mathematical models that highlight the influence exerted by the values of the input factors in the investigated process on the values of some output parameters of the same process, specialized software was used for the mathematical processing of experimental results [27]. This software is based on the least squares method. It allows the selection of the most appropriate empirical mathematical model from five such models (first-degree polynomial, second-degree polynomial, power type function, exponential function, and hyperbolic function). The selection of the most appropriate empirical mathematical model to the experimental results is performed using the value of Gauss's criterion S_G. The S_G value is determined by taking into account the sum of the squares of the differences between the values of the ordinates determined using the proposed empirical model, on the one hand, and the values of the ordinates corresponding to the experimental tests, on the other—for the same values of the abscissas. The smaller the value of Gauss's criterion, the more appropriate to the experimental results is the empirical mathematical model.

Empirical power function mathematical models have been relatively frequently used in manufacturing processes (for example, to highlight the influence exerted by various factors on the cutting tool life, the size of the cutting forces, the value of some roughness parameters, etc.). Moreover, empirical mathematical power function models can also provide a direct picture of the intensity of influence exerted by a factor on the value of an output parameter by examining the value of the exponent attached to that factor in the power function model. For these reasons, attention was also paid to power functions as empirical mathematical models in the present work. It should be noted that power function-type mathematical models can only be used for a monotonic variation of the output parameter to the values of the input factors. Therefore, it will be assumed that, when pursuing the identification of some power function type mathematical models, and for the various intervals of the values of the input factors, monotonous variations of the two output parameters of the investigated process will then be obtained.

Through the mathematical processing of the experimental results with the help of specialized software, the following empirical mathematical models were arrived at and considered to be the most appropriate for the available experimental results:

For average force at peak:

$$F = -54.794 + 87.207j - 29.115j^2 + 2.003m - 0.501m^2 + 0.0131n_w - 0.000686{n_w}^2 - 0.267n_h + 0.0171{n_h}^2 + 0.00602s - 0.00121s^2 + 1.996no_w - 0.265{no_w}^2 - 31.306l + 33.259l^2 + 0.306o - 0.0261o^2, \quad (1)$$

for which the value of the Gauss's criterion is $S_G = 0.002434847$.

For average displacement at peak:

$$L = -258.788 + 443.982j - 148.243j^2 - 10.630m + 2.625m^2 - 0.169n_w + 0.0239{n_w}^2 - 0.425n_h + 0.0272{n_h}^2 + 0.416s - 0.0132s^2 + 1.794no_w - 0.303{no_w}^2 - 126.527l + 138.649l^2 - 0.482o + 0.206o^2, \quad (2)$$

for which the value of Gauss's criterion is $S_G = 0.1335882$.

It can be seen that from the point of view of the adequacy of the empirical mathematical models to the experimental results, the most convenient of the five models considered is the polynomial one of the second degree.

If this chosen model considers the determination of mathematical models of power-type functions, it obtains:

For average force et peak:

$$F = 0.553j - 0.692m - 0.0351n_w - 0.105n_h - 0.204s - 0.0159no_w - 0.750l - 2.556o^{0.143}, \quad (3)$$

for which the value of Gauss's criterion is $S_G = 0.1720331$.

For average displacement at peak:

$$L = 7.083j - 0.377m - 0.204n_w - 0.295n_h - 0.0853s - 0.0265no_w - 1.054l - 0.0793o^{0.0318}, \quad (4)$$

for which the value of Gauss's criterion is $S_G = 4.216496$.

Using the empirical mathematical models, the diagrams in Figures 10–14 were developed. When generating these diagrams, the empirical mathematical models of the second-degree polynomial type (Equations (1) and (2)) were used, estimating that these models better reflect the actual behavior of the material combinations used to make omega and dovetail joints.

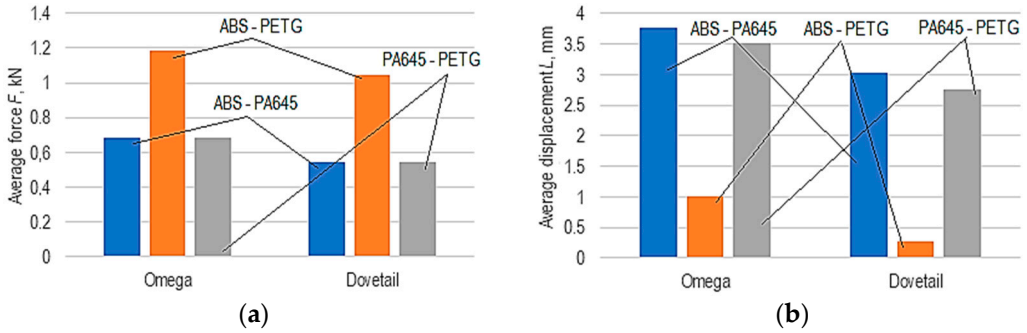

Figure 10. Differences between the corresponding values of: (**a**) average force *F*; (**b**) average displacement *L* for the three types of joints between each of the two materials (n_w = 8 mm, n_h = 8 mm, s = 11 mm, no_w = 4 walls, l = 0.45 mm, o = 2 mm).

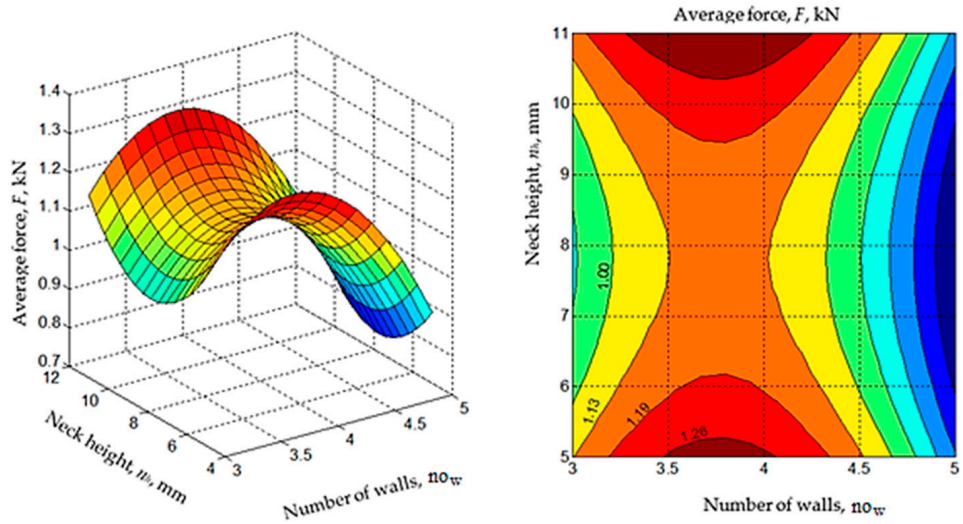

Figure 11. Influence of the neck height n_h and number of walls $\boldsymbol{no}_w$ on the average force *F* (j = 1 for the omega joint, m = 2 for the materials pair ABS-PETG, n_w = 8 mm, s = 11 mm, line width l = 0.45 mm, overlap o = 2 mm; diagrams were made using MATLAB software).

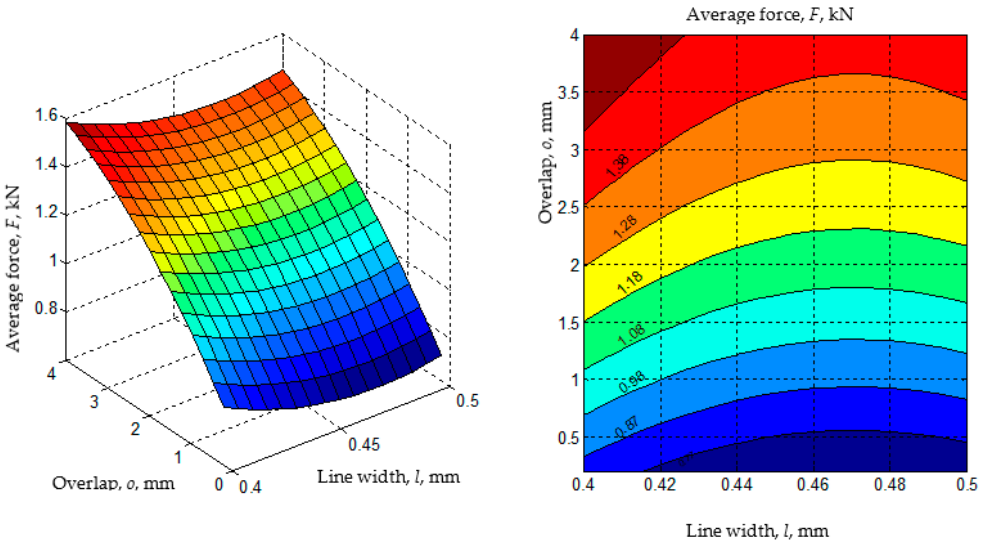

Figure 12. The influence of the line width l and overlap o on the average displacement *L* (j = 1 for the omega joint, m = 2 for the materials pair ABS-PETG, n_w = 8 mm, n_h = 8 mm, s = 11 mm, no_w = 4 walls; diagrams were made using MATLAB software).

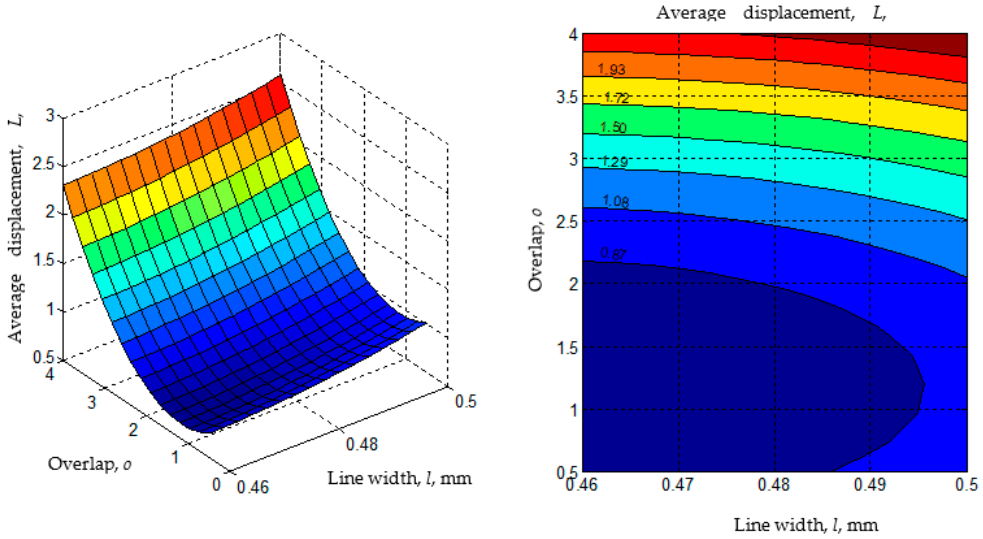

Figure 13. Influence of the overlap o and line width l on the average displacement L (j = 1 for the omega joint, m = 2 for the materials pair ABS-PETG, n_w = 5 mm, n_h = 5 mm, s = 11 mm, no_w = 4 walls; diagrams were made using MATLAB software).

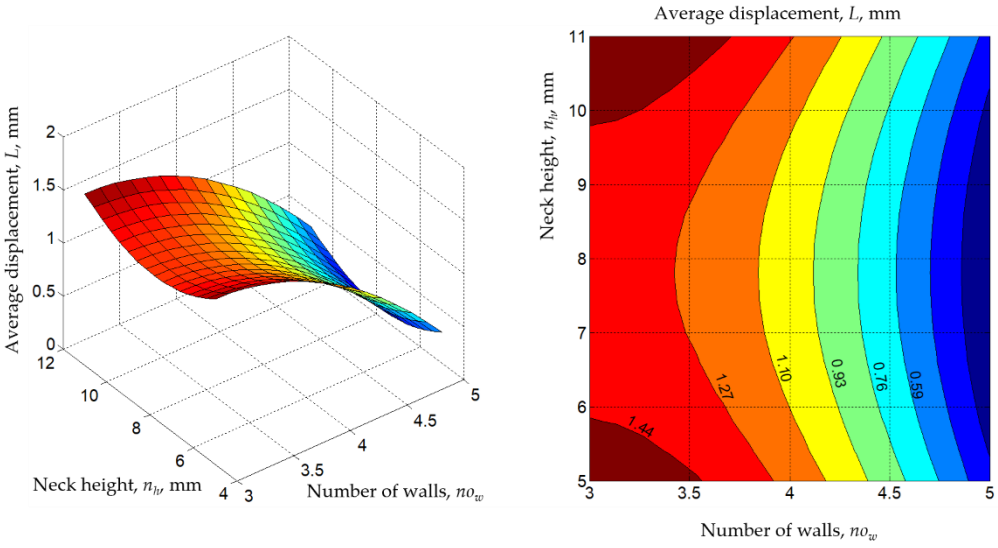

Figure 14. Influence of the number of walls no_w and neck height n_h on the average displacement L (j = 1 for the omega joint, m = 2 for the materials pair ABS-PETG, n_w = 8 mm, s = 11 mm, line width l = 0.45 mm, overlap o = 2 mm; diagrams were made using MATLAB software).

4. Discussion

The analysis of the empirical mathematical models constituted by Equations (1)–(4) and the graphic representations in Figures 10–14 allowed the formulation of the following observations.

It is found that in the mathematical model of the second-degree polynomial corresponding to the output parameter (Equation (1)) of average force F at peak, the lowest values of the coefficients attached to the variables n_w and s also have the lowest values. This means that the input factors related to these variables (neck width n_w and socket height s) practically do not influence the average force F. A similar statement can be made about the influence of the two factors (neck width n_w and socket height s) on average displacement L if the structure of Equation (2) is analyzed. The latter was also highlighted by the results from the ANOVA method.

In the bar diagrams in Figure 10, the values of the average force F and average displacement L were highlighted for the two types of joints (omega and dovetail) and the three combinations of two materials considered. It is found that those combinations of

materials m that lead to a higher value of average force F are found both in the case of the omega-type joint and in the case of the dovetail-type joint (it is the ABS-PETG combination, corresponding to the symbol $m = 2$). The order of material combinations in terms of average force F is the same for both types of joints (omega and dovetail).

It is also observed that omega-type joints lead to higher average forces F at peak than those in the case of dovetail-type joints. A possible explanation of this could be based on the existence, in the case of the dovetail joint, of some areas of jointing of certain surfaces at sharp angles, which would lead to the formation of higher stress concentrators and, therefore could reduce the mechanical strength of the joint.

Considering the average displacement L at peak, it is found that the lowest displacement values correspond to the same combination of materials that also leads to a maximum value of average force F at peak. This is logical because the material that requires the highest value of average force F will also have the lowest average displacement L.

The existence of maxima or minima for the variations of the F and L parameters when variations in the values of the significant input factors occur have been highlighted in the diagrams in Figures 11–14.

The analysis of the empirical mathematical models constituted by Equations (1) and (2) and the graphic representations in Figures 11–14 both highlight the fact that, if we abstract from the type of joint j and the pair of materials m, the strongest influences on the two output parameters (F and L) seem to be exerted by the values of the input factors overlap o, line width l, and the number of walls w. These input factors were assigned larger coefficient values from mathematical models (1) and (2). It was thus expected that an increase in the overlap value o would lead to higher average breaking forces F of the test samples due to the interwoven joining on larger surfaces of the two components of the test samples.

5. Conclusions

The study of the information from the specialized literature and industrial practice highlighted the existence of two possibilities for increasing the strength of strip end joints, namely those based on the use of omega-shaped joints and those based on dovetail-type joints. The finite element method was used to simulate the processes in the joint area. As a result of the increase in tensile force, the deterioration process of at least one of the components of the specimen is initiated. In general, the FEM simulation revealed a faster deterioration of the female component of the test samples. The use of three distinct polymeric materials was considered for the realization of the test samples that were later subjected to tensile tests.

Distinct values were proposed and used for some dimensions that characterize omega and dovetail joints, namely the neck width, the neck height, the socket height, and the overlap that characterized the interweaving of some areas of the ends of the joints. The number of walls and the line width were used as input factors in the 3D printing and defined this process. The experimental tests were carried out following the requirements of a Taguchi L18 factorial experiment with 8 independent variables. The average force at the peak and the average displacement at the peak were used as output parameters. In the case of the average displacement, the ANOVA method allowed the identification of the factors that most significantly influence the output parameter values. The experimental results were then mathematically processed with the help of specialized software, and it was found that empirical mathematical models of the second-degree polynomial type are appropriate for the obtained experimental results. The analysis of the empirical mathematical models and the graphic representations developed based on these empirical models highlighted that the main input factors able to exert influence on the values of the output parameters are primarily the type of joint and, secondly, the material components assembled at the joint. In the future, the intention is to expand this theoretical and experimental research by taking into account other polymeric materials and the variation of other test sample dimensions on the values of the two considered output parameters.

Author Contributions: Conceptualization, V.E. and A.-M.M.; methodology, L.S.; software, V.E. and G.N.; validation, O.D. and A.H.; formal analysis, A.H.; investigation, V.E. and A.-M.M.; resources, A.S.; data curation, M.-I.R.; writing—original draft preparation, V.E.; writing—review and editing, L.S.; visualization, M.-A.B.; supervision, A.S. and L.S.; project administration, O.D.; funding acquisition, A.-M.M. All authors have read and agreed to the published version of the manuscript.

Funding: The A.P.C. is funded by the "Gheorghe Asachi" Technical University funding.

Institutional Review Board Statement: Not applicable.

Informed Consent Statement: Not applicable.

Data Availability Statement: The data presented in this study are available on request from the corresponding author.

Acknowledgments: The authors thank the Plastic Processing Laboratory of the Ansbach University of Applied Science for providing their research facilities.

Conflicts of Interest: The authors declare no conflict of interest.

References

1. Tiwary, V.K.; Ravi, N.; Arunkumar, P.; Shivakumar, S.; Deshpande, A.S.; Malik, V.R. Investigations on friction stir joining of 3D printed parts to overcome bed size limitation and enhance joint quality for unmanned aircraft systems. *Proc. Inst. Mech. Eng. Part C J. Mech. Eng. Sci.* **2020**, *234*, 4857–4871. [CrossRef]
2. Lopes, L.R.; Silva, A.F.; Carneiro, O.S. Multi-material 3D printing: The relevance of materials affinity on the boundary interface performance. *Addit. Manuf. J.* **2018**, *23*, 45–52. [CrossRef]
3. Chen, T.; Zhang, J. Compatibilization of acrylonitrile-butadiene-styrene terpolymer/poly(ethylene glycol-co-1,4-cyclohexanedimethanol terephthalate) blend: Effect on morphology, interface, mechanical properties and hydrophilicity. *Appl. Surf. Sci.* **2018**, *437*, 62–69. [CrossRef]
4. Tamburrino, F.; Graziosi, S.; Bordegoni, M. The influence of slicing parameters on the multi-material adhesion mechanisms of FDM printed parts: An exploratory study. *Virtual. Phys. Prototyp.* **2019**, *14*, 316–332. [CrossRef]
5. Ribeiro, M.; Sousa Carneiro, O. Interface geometries in 3D multi-material prints by fused filament fabrication. *Rapid Prototyp. J.* **2019**, *25*, 38–46. [CrossRef]
6. Andó, M.; Birosz, M.; Jeganmohan, S. Surface bonding of additive manufactured parts from multi-colored PLA materials. *Measurement* **2021**, *169*, 108583. [CrossRef]
7. Kluczyński, J.; Śnieżek, L.; Kravcov, A.; Grzelak, K.; Svoboda, P.; Szachogłuchowicz, I.; Franek, O.; Morozov, N.; Torzewski, J.; Kubeček, P. The examination of restrained joints created in the process of multi-material FFF additive manufacturing technology. *Materials* **2020**, *13*, 903. [CrossRef] [PubMed]
8. Hasanov, S.; Alkunte, S.; Rajeshirke, M.; Gupta, A.; Huseynov, O.; Fidan, I.; Alifui-Segbaya, F.; Rennie, A. Review on additive manufacturing of multi-material parts: Progress and challenges. *J. Manuf. Mater. Process.* **2022**, *6*, 4. [CrossRef]
9. Kuipers, T.; Su, R.; Wu, J.; Wang, C.C.L. Interlaced Topologically Interlocking Lattice for continuous dual-material extrusion. *Addit. Manuf.* **2022**, *50*, 102495. [CrossRef]
10. Acherjee, B. Laser transmission welding of polymers—A review on process fundamentals, material attributes, weldability, and welding techniques. *J. Manuf. Process.* **2020**, *60*, 227–246. [CrossRef]
11. Focke, W.W.; Joseph, S.; Grimbeek, J.; Summers, G.J.; Kretzschmar, B. Mechanical Properties of Ternary Blends of ABS + HIPS + PETG. *Polym. Plast. Technol. Eng.* **2009**, *48*, 814–820. [CrossRef]
12. Fisher, R.A. *The Design of Experiments*; Oliver and Boyd: Edinburgh/London, UK, 1935; Available online: http://tankona.free.fr/fisher1935.pdf (accessed on 23 July 2022).
13. Yates, F. Sir Ronald Fisher and the design of experiments. *Biometrix* **1964**, *20*, 307–321. [CrossRef]
14. Yuangyai, C.; Nembhard, H.B. Design of experiments. In *Emerging Nanotechnologies for Manufacturing*; Ahmed, V., Jakson, M.J., Eds.; Elsevier: Amsterdam, The Netherlands, 2010; pp. 207–234. Available online: https://www.sciencedirect.com/book/9780815515838/emerging-nanotechnologies-for-manufacturing (accessed on 16 August 2022).
15. Pillet, M. *Introduction aux Plans d'expériences par la Méthode Taguchi*, 2nd ed.; Les Éditions d'Organisation: Paris, France, 1992.
16. Ross, P.J. *Taguchi Techniques for Quality Engineering*; McGraw-Hill Companies, Inc.: New York, NY, USA, 1988. [CrossRef]
17. Roy, R.K. *Design of Experiments Using the Taguchi Approach: 16 Steps to Product and Process Improvement*; John Willey & Sons: Hoboken, NJ, USA, 2001.
18. Fraley, S.; Zalewski, J.; Oom, M.; Terrien, B. Design of experiments via Taguchi methods—orthogonal arrays. In *Chemical Process Dynamics and Control*; Woolf, P., Ed.; Libretext: Ann Arbor, MI, USA, 2022; Available online: https://eng.libretexts.org/Bookshelves/Industrial_and_Systems_Engineering/Book%3A_Chemical_Process_Dynamics_and_Controls_ (accessed on 29 September 2022).
19. Kuramochi, N.; Oomuro, Y. Robust design with direct product of the L18 orthogonal arrays. In Proceedings of the 2008 International Symposium on Semiconductor Manufacturing (ISSM), Tokyo, Japan, 27–29 October 2008; pp. 191–194.

20. Kacker, R.N.; Lagergren, E.S.; Filliben, J.J. Taguchi's orthogonal arrays are classical designs of experiments. *J. Res. Natl. Inst. Stand. Technol.* **1991**, *96*, 577–591. [CrossRef] [PubMed]
21. Cao, Y.; Wang, W.; Shen, W.; Cui, X.; Shao, J. A new hybrid phase-field model for modeling mixed-mode cracking process in anisotropic plastic rock-like materials. *Int. J. Plast.* **2022**, *157*, 103395. [CrossRef]
22. Ermolai, V.; Irimia, A. Influence of nozzle parameters in 3D printing under the manufacturing time. *Bull. of the Polytech. Inst. of Iași. Mach. Constr. Sect.* **2021**, *67*, 63–72. [CrossRef]
23. Stavarache, R.C.; Ermolai, V.; Rîpanu, M.A.; Andrușcă, L.; Mareș, M.; Dodun, O. Infill pattern optimization of fused filament fabrication samples for enhanced mechanical properties. *Sci. Bull. Ser. C Fascicle Mech. Tribol. Mach. Manuf. Technol.* **2021**, *35*, 80–85.
24. Ferretti, P.; Leon-Cardenas, C.; Santi, G.M.; Sali, M.; Ciotti, E.; Frizziero, L.; Donnici, G.; Liverani, A. Relationship between FDM 3D Printing Parameters Study: Parameter Optimization for Lower Defects. *Polymers* **2021**, *13*, 2190. [CrossRef] [PubMed]
25. Sangid, M.D. The physics of fatigue crack initiation. *Int. J. Fatigue* **2013**, *57*, 58–72. [CrossRef]
26. Making Sense of Data: A Practical Guide to Exploratory Data Analysis and Data Mining. A.4 F-DISTRIBUTION. 2022. Available online: https://www.oreilly.com/library/view/making-sense-of/9780470074718/appa-sec004.html (accessed on 28 August 2022).
27. Crețu, G. Fundamentals of Experimental Research. In *Laboratory Handbook*; Asachi, G., Ed.; Technical University of Iași: Iași, Romania, 1992. (In Romanian)

medicina

MDPI

Article

Experimental Study on Mechanical Properties of Different Resins Used in Oral Environments

Elena-Raluca Baciu [1,†], Carmen Nicoleta Savin [2,†], Monica Tatarciuc [3,*], Ioana Mârțu [3,*], Oana Maria Butnaru [4], Andra Elena Aungurencei [3], Andrei-Marius Mihalache [5] and Diana Diaconu-Popa [3]

1 Department of Oral Implantology, Discipline of Dental Materials, Faculty of Dental Medicine, University of Medicine and Pharmacy "Grigore T. Popa", 700115 Iași, Romania
2 Department of Surgery, Discipline of Pediatric Dentistry, Faculty of Dental Medicine, University of Medicine and Pharmacy "Grigore T. Popa", 700115 Iași, Romania
3 Department of Oral Implantology, Removable Dentures and Technology, Faculty of Dental Medicine, University of Medicine and Pharmacy "Grigore T. Popa", 700115 Iași, Romania
4 Department of Surgery, Discipline of Basics of Physics and Biophysics in Dental Medicine, Faculty of Dental Medicine, University of Medicine and Pharmacy "Grigore T. Popa", 700115 Iași, Romania
5 Department of Machine Manufacturing Technology, "Gheorghe Asachi" Technical University of Iași, 700050 Iași, Romania; andrei.mihalache@tuiasi.ro
* Correspondence: monica.tatarciuc@umfiasi.ro (M.T.); ioana.martu@umfiasi.ro (I.M.)
† These authors contributed equally to this work.

Abstract: *Background and Objectives*: Acrylic resins remain the materials of choice for removable prosthesis due to their indisputable qualities. The continuous evolution in the field of dental materials offers practitioners today a multitude of therapeutic options. With the development of digital technologies, including both subtractive and additive methods, workflow has been considerably reduced and the precision of prosthetic devices has increased. The superiority of prostheses made by digital methods compared to conventional prostheses is much debated in the literature. Our study's objective was to compare the mechanical and surface properties of three types of resins used in conventional, subtractive, and additive technologies and to determine the optimal material and the most appropriate technology to obtain removable dentures with the highest mechanical longevity over time. *Materials and Methods*: For the mechanical tests, 90 samples were fabricated using the conventional method (heat curing), CAD/CAM milling, and 3D printing technology. The samples were analyzed for hardness, roughness, and tensile tests, and the data were statistically compared using Stata 16.1 software (StataCorp, College Station, TX, USA). A finite element method was used to show the behavior of the experimental samples in terms of the crack shape and its direction of propagation. For this assessment the materials had to be designed inside simulation software that has similar mechanical properties to those used for obtaining specimens for tensile tests. *Results*: The results of this study suggested that CAD/CAM milled samples showed superior surface characteristics and mechanical properties, comparable with conventional heat-cured resin samples. The propagation direction predicted by the finite element analysis (FEA) software was similar to that observed in a real-life specimen subjected to a tensile test. *Conclusions*: Removable dentures made from heat-cured resins remain a clinically acceptable option due to their surface quality, mechanical properties, and affordability. Three-dimensional printing technology can be successfully used as a provisional or emergency therapeutic solution. CAD/CAM milled resins exhibit the best mechanical properties with great surface finishes compared to the other two processing methods.

Keywords: removable dentures; acrylic resins; subtractive methods; additive technologies; finite element analysis

Citation: Baciu, E.-R.; Savin, C.N.; Tatarciuc, M.; Mârțu, I.; Butnaru, O.M.; Aungurencei, A.E.; Mihalache, A.-M.; Diaconu-Popa, D. Experimental Study on Mechanical Properties of Different Resins Used in Oral Environments. *Medicina* **2023**, *59*, 1042. https://doi.org/10.3390/medicina59061042

Academic Editor: Bruno Chrcanovic

Received: 9 May 2023
Revised: 23 May 2023
Accepted: 23 May 2023
Published: 28 May 2023

1. Introduction

Complete and partial edentulism are the most severe and irreversible forms of edentation, which leads to imbalances in all elements of the stomatognathic system. This is why

practitioners and researchers have been continuously concerned over time, seeking to find an optimal therapeutic solution that allows the restoration of all the affected functions.

Acrylic dental resins, especially poly-methyl-methacrylate (PMMA) resin, are commonly used in dentistry as denture base materials due to their advantages, including their relatively high strength, acceptable hardness, color stability, insolubility in the oral cavity, low weight, and low conductivity [1,2]. However, these materials have numerous drawbacks which are frequently reported by practitioners, the most common of which are poor mechanical strength, susceptibility to staining [3], curing shrinkage, and water sorption [3–5].

In the last decade, digital technologies have become an alternative to the conventional fabrication of acrylic removable dentures [6]. These methods substantially reduce workflow, facilitate quick communication between the dentist and the dental technician, and increase patient comfort [7]. Most available systems use subtractive and additive manufacturing to fabricate acrylic-based dentures [8,9]. The materials used in these technologies are industrially produced, so they have superior chemical and volumetric stability and optimal mechanical strength [10–13]. Subtractive systems use pre-polymerized acrylic discs, from which, based on the information received from the CAD unit, the future prosthesis will be milled. Milling strategies allow for obtaining a well-fitted prosthesis with highly accurate surfaces [14–18].

Several 3D printing technologies have been employed in dentistry, including stereolithography (SLA), digital light processing (DLP), selective laser sintering (SLS), selective laser melting (SLM), electron-beam processing (EBM), polyJet photopolymer printing, and fused deposition modeling (FDM). However, the stereolithographic printing of light-cured polymers has gained popularity [19].

Additive methods reduce workflow and the numbers of appointments, allow reproduction of all details, and reduce material waste [20,21].

Printing parameters, such as laser intensity, calibration of the printer and software, resin properties, build direction and angle, layer thickness and numbers, the bond between the layers, the amount of supporting structures, and post-polymerization conditions, play an important role regarding the quality of the final product [22]. It is a huge responsibility for dental staff to fabricate high-quality removable dentures, and it is important to know the details and particularities of each method. Digitalization in the prosthetics field has already activated research and clinical potential and will do significantly more in the near future. Consequently, these systems must be studied to determine their advantages and downsides. A removable denture requires a considerable number of clinical and technological procedures, as well as digital approaches that have the benefit of drastically lowering the amount of work required. On the other hand, the expenses of such a technical line are still rather high, and many experts do not view the procurement of equipment for producing detachable prostheses via additive or subtractive methods as a lucrative investment.

Finite element analysis (FEA) is a computational method that allows for the accurate modeling and analysis of complex structures, making it a valuable tool across a wide range of fields, from engineering to biology. Since Finite Element Analysis (FEA) is a numerical method capable of evaluating the stresses and deformations in structures. It has become a widely accepted and non-invasive approach for studying the biomechanics of biological systems and understanding the impact of mechanical forces on them [23].

Over the last few years, there has been rapid progress in the field of materials used for fabricating removable dentures. Nonetheless, the most recent studies on the mechanical and surface properties of resins do not cover the entire range of commercially available products across all countries. Our study is highly valuable for current practice as it analyzes the most used acrylic resins in our laboratories, replicating the real technological working flow involved in prostheses fabrication. The current research aimed to perform a comparative analysis of the selected mechanical characteristics of three types of resins used in conventional, subtractive, and additive technologies and to determine the optimal material and the most appropriate technology to obtain removable dentures with the highest

mechanical longevity over time. Additionally, for ensuring the precision of the outcomes, we evaluated the ability of the FEA software to predict the direction of crack propagation, as well as provide valuable insights related to stress and strain phenomena.

The null hypothesis was that the mechanical and surface properties of the samples are unaffected by the fabrication process.

2. Materials and Methods

2.1. Study Design

In order to investigate the properties of denture base materials, 90 samples (Figure 1) were manufactured using resins used for conventional and CAD/CAM subtractive- and additive-fabricated dentures. For the experimental tests that were conducted, the resin samples were divided up into three main groups, as shown in Table 1.

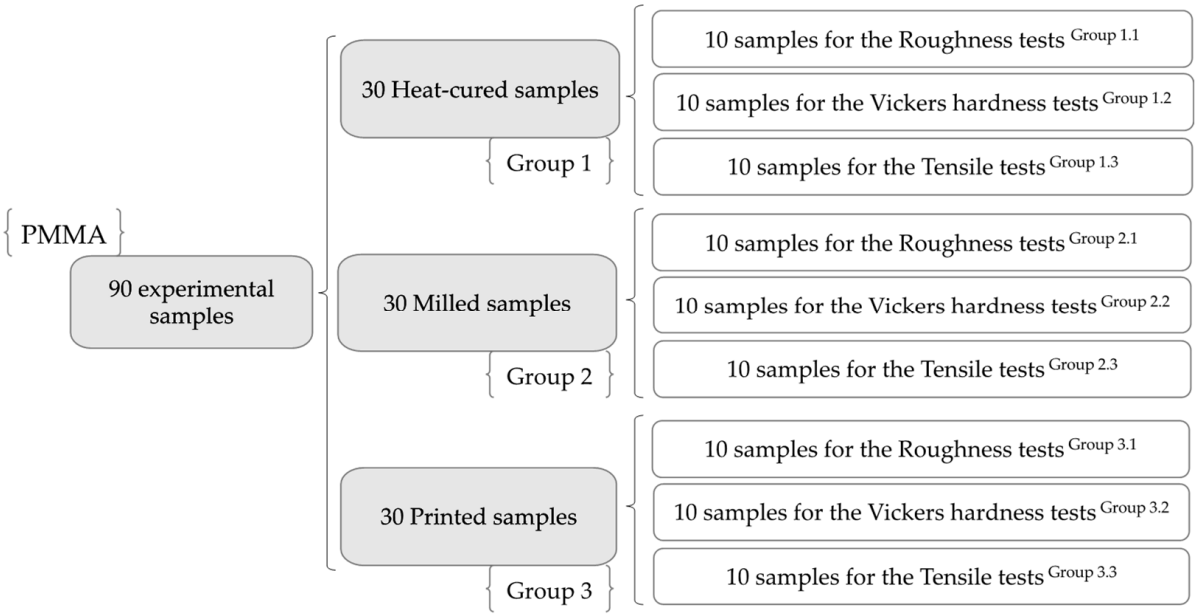

Figure 1. The experimental sample framework.

Table 1. Resin groups with their product information and experimental equipment.

Resin Groups	Resin	Experimental Equipment		
		Surface Roughness	Vickers Hardness	Tensile Tests
Group 1 Heat-cured group	Meliodent Heat Cure (Kulzer GmbH, Hanau, Germany)	Form Talysurf® tester (Taylor Hobson, Leicester, UK)	HVT-1000 (Shanghai Daheng Optics and Fine Mechanics Co., Ltd., Shanghai, China)	Instron 2716-002, Instron, Norwood, MA, US
Group 2 Subtractively manufactured group	Polident (Polident d.o.o, Volja Draga, Slovenia)			
Group 3 Additively manufactured group	Asiga DentaBASE resin (Asiga, Alexandria, NSW, Australia)			

2.2. The Samples Design

For the hardness and roughness tests, rectangular samples with a width of 30 mm, a length of 70 mm, and a thickness of 2 mm were made (Figure 2a).

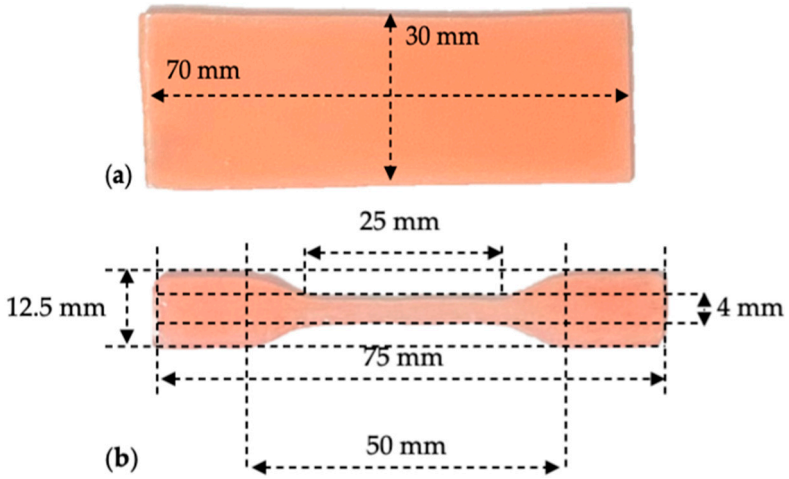

Figure 2. The design of the samples: (**a**) for the hardness and roughness tests; (**b**) for the tensile test.

Dumbbell-shaped samples were used for tensile testing, with dimensions chosen according to ISO 527-2 [24] and ASTM D-638 [25] standards (Figure 2b).

2.3. PMMA Sample Realization

2.3.1. Heat-Cured Samples

For the heat-cured samples, wax patterns were invested in Type 3 dental stones (Moldano, Kulzer GmbH, Hanau, Germany), respecting the manufacturer processing instructions: mixing a ratio of 100 g powder:30 mL water under a vaccum for 30 s.

Then, the metallic flask was immersed in 100 °C water for five minutes, the two sides of the flask were separated, the wax fragments were cleaned, and the mold was isolated using Isodent alginate solution (SpofaDental Inc., Jičín, Czech). The recommended mixing ratio for the resin preparation is 35 g powder to 14 mL liquid. The liquid was added to the mixing beaker along with an appropriate amount of powder, which was then stirred for one minute using a spatula. After 10 min, the Meliodent Heat Cure (Kulzer GmbH, Hanau, Germany) reached a packable consistency and could be manually pressed into the mold. The flask was immersed in boiling water for 15 min, after which the heat source was switched off. According to the manufacturer's recommendations, a short cycle method was used in the polymerization process. The flask was allowed to cool slowly in a water bath after 20 min of boiling. Following polymerization, the specimens were extracted from the mold.

2.3.2. Milled Samples

The wax patterns were scanned with a Swing DOF Scanner (DOF Inc., Seoul, Republic of Korea) and the computer-aided machine automatically milled (VHF K5 Plus, VHF, Ammerbuch, Germany) the experimental samples from CAD/CAM pink denture base resin discs (Polident, Polident d.o.o, Volja Draga, Slovenia), measuring 95 mm in diameter and 25 mm in thickness.

2.3.3. Printed Samples

STL files were submitted to the digital light processing (DLP) printer (Asiga MAX, Asiga, Alexandria, NSW, Australia) for fabrication using Asiga DentaBASE resin (Asiga, Alexandria, NSW, Australia). After the printed samples were removed from the build platform, they were cleaned with 99% isopropyl alcohol and dried with steam.

Finally, a 20 min post-polymerization process was required, which was conducted using the Asiga Flash Post Curing Unit (Asiga, Alexandria, NSW, Australia).

2.3.4. Finishing and Polishing

During the sample processing phase, we utilized the Acrylic Contouring & Finishing Kit HP (Shofu Dental GmbH, Ratingen, Germany) for denture finishing and polishing.

Initially, a dark gray AcryPoint coarse-grit BP1 tool (Shofu Dental GmbH, Ratingen, Germany) was utilized for 60 s (in dry conditions). Then, a brown AcryPoint medium-grit BP1 tool (Shofu Dental GmbH, Ratingen, Germany) was used for the same duration. The instruments' rotational speed was rather modest at 10,000 rpm.

A light gray AcryPoints tool (Shofu Dental GmbH, Ratingen, Germany) and a gentle circular goat hair brush were employed at an even slower speed of 4000 rpm (60 s in dry conditions) for fine finishing.

For polishing, a Pala Polish Polishing paste (Kulzer GmbH, Hanau, Germany) was applied first to the samples, and then the procedure was carried out with a rag wheel (Kulzer GmbH, Hanau, Germany) three times for 60 s in order to achieve a flawless sheen.

2.4. Experimental Tests

2.4.1. Roughness Tests

For each sample, six measurements (three records before and three records after finishing and polishing) were taken at the level of the examined surface using a contact-type roughness tester Form Talysurf® (Taylor Hobson, Leicester, UK).

Based on the determined roughness parameter values, the influence of finishing on the micrometric profile of each surface (ΔR_a) was calculated as follows:

$$\Delta R_a = R_{a\ \text{before finishing}} - R_{a\ \text{after finishing}}$$

R_a—the arithmetic mean roughness.

2.4.2. Vickers Hardness Tests

The Vickers tests were performed using a HVT-1000 automatic tester (Shanghai Daheng Optics and Fine Mechanics Co., Ltd., Shanghai, China) with a 50 gf load force for 10 s. On each sample, five determinations were made.

The Vickers hardness (HV) was calculated using the following formula:

$$HV = 1854.4\ L/d^2$$

L—the load force in gf; d—the average diagonal in μm.

2.4.3. Tensile Tests

Standard tensile tests were conducted at room temperature in accordance with ISO 527-1: 2000 [25], and computer-controlled testing equipment was used for the direct strain measurements (Instron 2716-002, Instron, Norwood, MA, USA).

Young's modulus and the tensile stress at yield were determined using a 1 mm/min crosshead speed.

Young's modulus (E) was calculated according to Hook's law:

$$E = \sigma/\varepsilon$$

σ—tensile stress (the amount of force applied per unit area, $\sigma = F/A$); ε—tensile strain (the extension per unit length, $\varepsilon = dL/L$).

2.4.4. Finite Element Method (FEM)

The finite element method (FEM) goal was to model a fracture similar to the ones obtained after tensile tests that would give us stress and strain distributions, which are otherwise very difficult to measure. Our choice of software was Ansys (Ansys, Canonsburg, USA). First, we had to design the materials with mechanical properties similar to the ones used in our research. None of the three resins were available as a library source that

could be used inside the simulation. Therefore, we used a specific tool -Ansys- as Material Designer. Poly-methyl-methacrylate (PMMA) resins are most commonly used for denture applications. We aimed to design materials similar to those used for mechanical testing [26]. For this purpose, we accessed the software library containing various types of materials, named Engineering Data. From the composite materials section we added a Polyamide resin and Epoxy E-Glass [27] for designing a materials similar to PMMA. In order to create this material, the software first requires a matrix and a binder and it was selected the resin as matrix and particles of epoxy as binder. The next step consisted of selecting a geometry for the inner arrangement at a macromolecular level. We chose a random particle distribution with default values of 15430 seed, a 0.3 particle volume fraction, and a 10 µm particle diameter. The diameter distribution was set to be constant. The resulting particle arrangement, and the mentioned settings, can be observed in Figure 3.

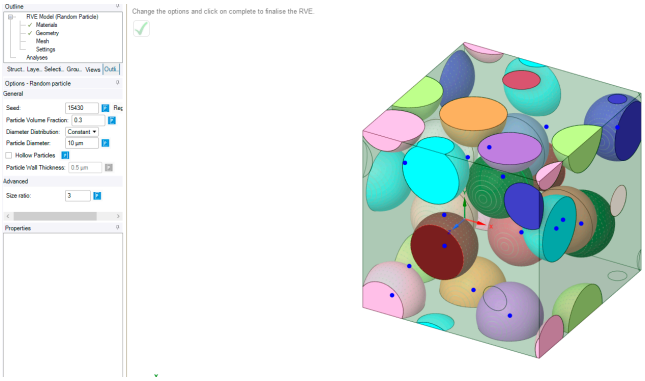

Figure 3. Material designer setup with graphical representations of the 3D view of the random particle type of arrangement with unprojected connections represented by blue dots.

Mesh-wise, we chose a conformal and periodic meshing without imposing a maximum size for its elements. Our choice for anisotropy was orthotropic and we computed a linear elasticity property without the need for coefficients of thermal expansion or thermal conductivity. We used the periodic boundary conditions option for our analyses and chose a constant material type of solver, which we generically named PMMA. The software computed a Young's modulus of 3255.3 MPa on XY, 2725.4 MPa on YZ, and 2718.2 MPa on XZ. We obtained a Poisson's ratio of 0.38701 in XY, 0.39117 in YZ, and 0.41716 in XZ. The density was reported as 1.4066×10^{-9} t mm^{-3} (Figure 4).

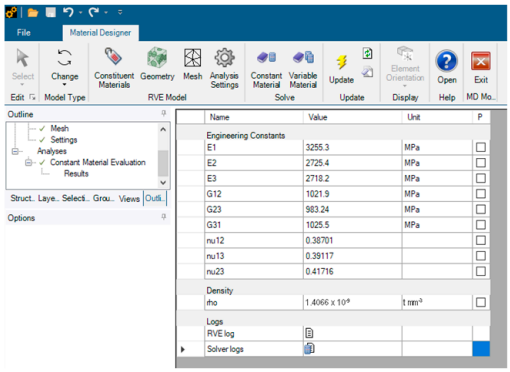

Figure 4. Material designer setup with graphical representations of the view of results that were obtained.

The newly designed material needed for finite element analyses was imported into the Engineering Data section of a Static Structural type of analysis. In order to obtain a fracture direction, the sample was designed with the same geometric dimensions as the ones specified by standards in a 3D software solution (Siemens SolidEdge academic,

Siemens, Munich, Germany) and used inside experimental tensile tests. Based on the results of the tensile tests, we designed a pre-crack about the same height as the area where the fracture appeared after tensile testing. The 3D model was later translated into a Parasolid file that was easily interpreted by the software.

By reading the internal library, namely Engineering Data, we were able to assign the newly created material to the imported geometry. Because of the complexity of this process, we used a virtual topology tool based on an edge mapping type of behavior. Our choice for predicting a crack direction was to use the SMART crack growth tool available in Ansys. This was suitable for our setup because crack growth simulation expands in homogenous environments, which was the case for our specimen. The criterion is in fact a rate of energy release type of method, which uses stress intensity factors (SIFs) for assessments. We chose a static crack type of growth, which calculates the extension of each front node of the crack. We had to generate a new coordinate system specific to the crack itself, where the X points to the direction of propagation and the Y sits almost normal to its upper face. Mesh-wise, we imposed a patch conforming method that uses quadratic element orders and a face meshing method for both of the crack's faces with an element size of just 0.25 mm, as the mesh general settings were set to 0.5 mm with an aggressive mechanical type of error limits assessment. That resulted in 9590 elements and 18,210 nodes (Figure 3). The fracture tool included a pre-meshed crack with six solution contours and the SMART crack growth tool was set to be static. The chosen option for failure criteria was a stress intensity factor with a critical rate of 100 MPa·mm$^{(0.5)}$. The analysis settings received a 0.001 sec end time defined by ten sub-steps. Conditions were set in the form of a fixed support on the lower face of the sample and a force solicitation on the upper face (Figure 4).

Equivalent elastic strain registers showed values a little over 0.008 mm/mm (Figure 5a), as the propagation direction was similar to the one observed in our tested samples and the equivalent stress, evaluated by means of von Mises criteria, reached 1634.8 MPa along the fracture line (see Figure 5b). The analysis was stopped just before the body was separated.

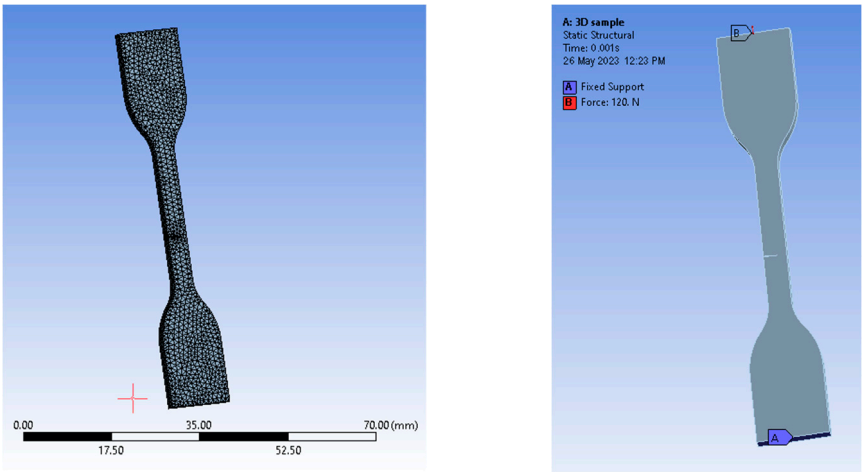

(**a**) (**b**)

Figure 5. Setup with graphical representations of the (**a**) 3D view of the meshed body and (**b**) 3D view with supports and conditions applied on the sample body.

2.5. The Statistical Analysis

For the statistical data analysis, Stata 16.1 software (StataCorp, College Station, TX, USA) was used. The one-way ANOVA analysis was employed to check if there were statistical differences in terms of surface roughness, hardness, and tensile parameters across the three types of resins used. Furthermore, the Bonferroni multiple comparison test was used to check where the statistically significant difference lay by zooming in on each of the possible paired samples. The statistical analysis was carried out with a significance level of $p < 0.05$.

3. Results

3.1. Evaluation of the Roughness Parameters

The findings from the statistical analysis for the compared roughness parameters are shown in Table 2.

Table 2. The roughness parameter values for the studied samples.

Group	Number of Samples	Mean Values ± Standard Deviation		
		Ra before Finishing and Polishing [µm]	Ra after Finishing and Polishing [µm]	ΔRa [µm]
Heat cured	10	0.239 ± 0.024	0.037 ± 0.008	0.201 ± 0.022
CAD/CAM milled	10	0.267 ± 0.044	0.046 ± 0.011	0.221 ± 0.035
3D printed	10	0.494 ± 0.028	0.050 ± 0.007	0.445 ± 0.027
F(df)		177.24 (2,27)	5.33 (2.27)	224.11 (2.27)
p-value		0.000	0.0112	0.000

A one-way ANOVA was used. The significance level was established at 5%.

The results of the roughness coefficients before finishing and polishing revealed a statistically significant difference between the three groups ($p < 0.001$). However, the Bonferroni multiple comparison test indicated that only the 3D printed samples were, on average, different compared to the other two groups ($p < 0.001$). As is also displayed in Figure 6, on average, the heat-cured sample displayed the lowest roughness coefficients.

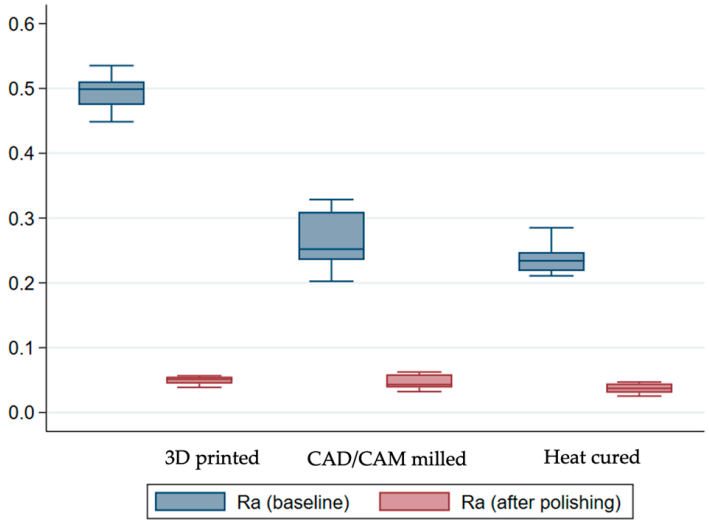

Figure 6. Box plot of surface roughness by resin before/after polishing.

As expected, after polishing and finishing, the average roughness coefficients dropped in all three methods, with the heat-cured sample still reporting, on average, the lowest coefficients. The ANOVA confirmed that there was still a statistically significant difference in roughness between the groups ($p = 0.0112$). Nonetheless, the difference is only significant between the 3D printed and the heat-cured samples, as indicated by the Bonferroni test ($p = 0.011$). Finally, when investigating the differences in terms of averages across the study groups, the results confirmed a significant difference between them ($p < 0.001$).

3.2. Evaluation of the Vickers Hardness

At a magnification of 400:1, Figure 7a–c illustrates the indentations produced by the indenter on the surface of the samples subjected to Vickers hardness analyses.

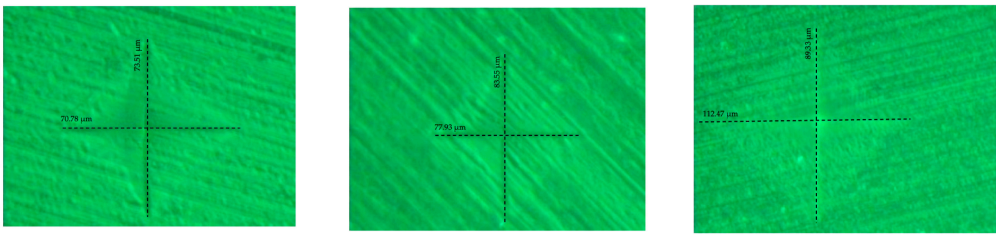

Figure 7. The impressions of the penetrator on the surface of the samples: (**a**) Group 1.2—Sample 3 heat-cured; (**b**) Group 2.2—Sample 2 CAD/CAM milled; (**c**) Group 3.2—Sample 8 3D printed.

The average values of the determinations are presented in Table 3, with the 3D printed sample reporting, on average, the smallest HV coefficients.

Table 3. Vickers hardness values for the studied samples.

Group	Number of Samples	Mean Values ± Standard Deviation
		Vickers Hardness HV
Heat cured	10	20.257 ± 0.854
CAD/CAM milled	10	22.301 ± 1.115
3D printed	10	13.853 ± 0.586
F(df)		251.63(2.27)
p-value		0.000

A one-way ANOVA was used. The significance level was established at 5%.

When looking at the distribution of our samples, the CAD/CAM milled sample clearly displays, on average, the highest Vickers. At the other end lies the 3D printed sample, with the lowest values (Figure 8).

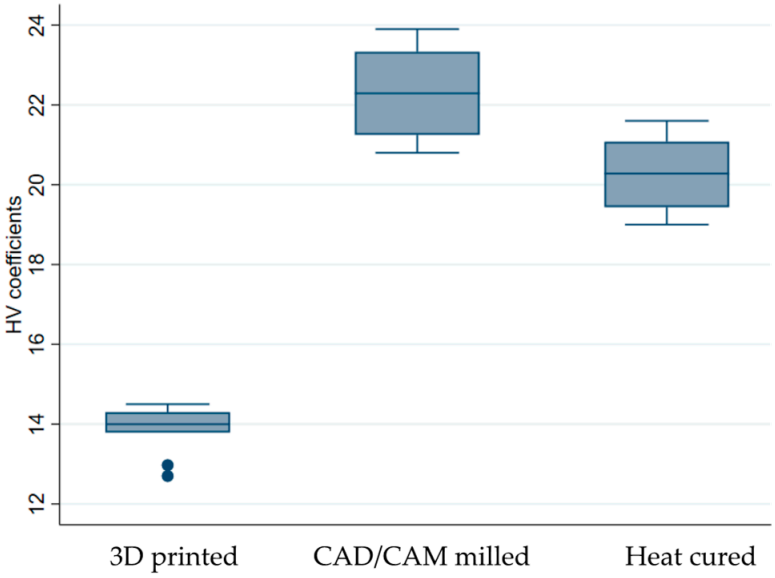

Figure 8. Box plot of Vickers hardness values by resin used.

The one-way ANOVA test revealed that the surface hardness depends on the type of resin used determine [F(2.27) = 251.63, $p < 0.001$]. According to the Bonferroni multiple comparison test, there was a statistically significant difference in the mean values of the HV coefficients for all potentially matched samples ($p < 0.001$).

3.3. Evaluation of the Tensile Parameters

The average values of the modulus and tensile stress at yield obtained by the tensile test are shown in Table 4.

Table 4. The average values of the mechanical characteristics of the experimental samples obtained by tensile tests.

Group	Number of Samples	Mean Values ± Standard Deviation	
		Modulus (Segment 0.0005–0.0025 mm/mm) [MPa]	Tensile Stress at Yield (Offset 0.5%) [MPa]
Heat cured	10	2805.779 ± 245.604	37.575 ± 1.272
CAD/CAM milled	10	2930.298 ± 32.013	41.188 ± 3.449
3D printed	10	2106.551 ± 16.663	30.642 ± 1.501
F(df)		95.98(2.27)	54.66(2.27)
p-value		0.000	0.000

A one-way ANOVA was used. The significance level was established at 5%.

According to the descriptive results, the CAD/CAM samples group displayed greater modulus coefficients, as well as higher tensile stress parameters (Table 4 and Figure 9).

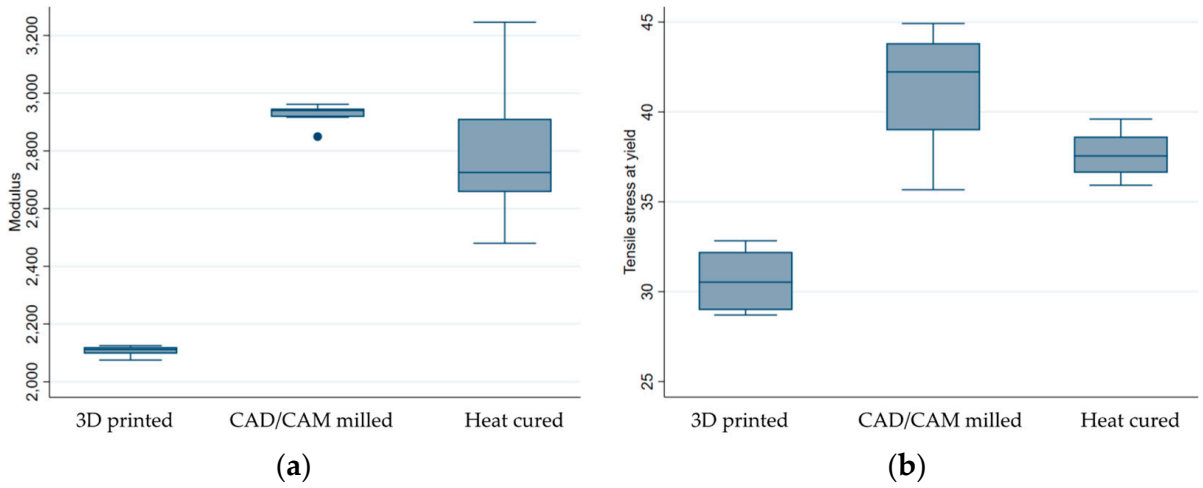

Figure 9. Box plot of mechanical characteristics obtained by tensile tests by resin used: (**a**) modulus and (**b**) tensile stress at yield.

The one-way ANOVA also revealed a significant difference ($p < 0.001$) in the mechanical characteristics between the three groups ($p < 0.001$). Zooming in to each of the possible pairs, the Bonferroni test revealed that, when it comes to the modulus coefficient, only the 3D printed samples were, on average, different from the other two samples ($p < 0.0001$). However, when looking at the tensile strength parameter, a statistically significant difference between the mean values was confirmed for all three possible paired samples.

3.4. Finite Element Method (FEM) Analysis

The contours of the samples showed that the critical points were at the ends of the fracture line and all along its length as the crack propagated. This type of result (Figure 10 a,b) is similar to the one observed in a real-life specimen that was subjected to a tensile test.

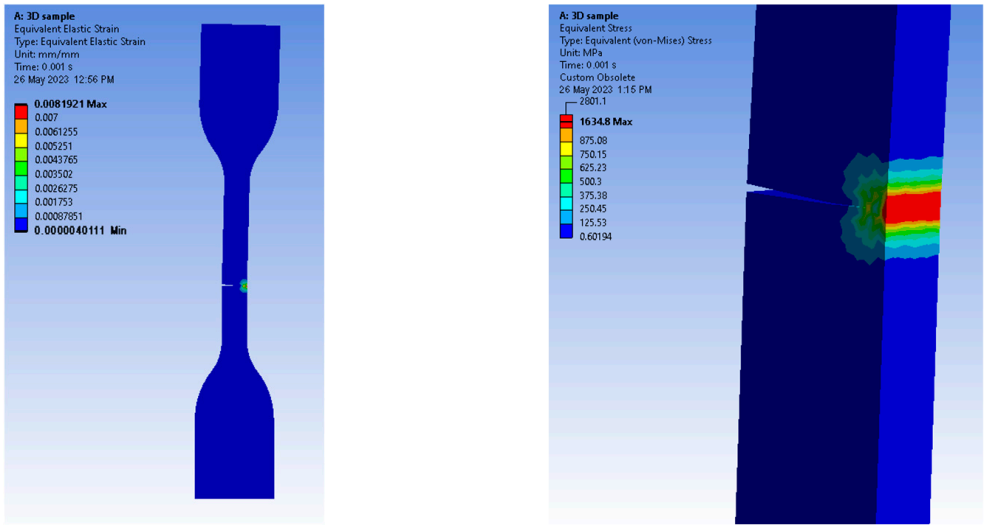

(**a**) (**b**)

Figure 10. Graphical representations of FEM results: (**a**) front view of the equivalent elastic strain distribution along the fracture line and (**b**) semi-side view of the equivalent (von Mises) stress distribution along the fracture line.

4. Discussion

Based on the findings of this research, there were significant differences between the sample groups for all the characteristics investigated, indicating that the study's null hypothesis was rejected. Although 3D-printed samples recorded the highest surface roughness, heat-cured samples and CAD/CAM milled samples showed the lowest Ra coefficients, both before and after polishing. This discrepancy could be related to the manufacturing process of pre-polymerized resin blocks in subtractive technologies, as well as the reduced degree of polymerization in 3D printing.

Similar results were obtained by Helal et al. [28], who found significant differences between the tested denture base resins (3D-printed, CAD/CAM milled resin, and polyamide flexible resins). These findings are also supported by those obtained by the authors Zeidan et al. [29]. In contrast, Srinivasan et al. [18] demonstrated that the surface roughness of milled and rapidly prototyped resins was similar.

Srinivasan et al. [4] conducted a study in which the surface roughness of CAD/CAM milled and rapidly prototyped/3D-printed resins utilized in the fabrication of complete dentures was evaluated using a high-resolution white light non-contact laser profilometer (CyberSCAN CT 100, Cyber technologies, Eching-Dietersheim, Germany). Based on their findings, the authors concluded that both types of resins exhibited similar levels of surface roughness.

Contact testers, such as stylus profilometers, directly measure the height of surface irregularities and can provide highly accurate results. However, they can cause damage to delicate surfaces, are sensitive to vibrations, and require a high level of operator skill to use properly. On the other hand, non-contact testers, such as laser and optical profilometers, are non-invasive, can measure surface roughness at high speeds, are able to measure smaller asperity than contact types, allow for simultaneous observations of surface images and height profiles (microscope type), and are able to acquire high-definition, fully focused images that rival those of SEMs (color 3D laser microscopes) [30]. However, they can be more expensive, require complex alignment procedures, the measurement area is limited, and they are used for in-situ measurements [31].

The most significant effect of finishing on the micrometric profile was observed on 3D-printed ($\Delta Ra = 0.445 \pm 0.027$ µm) sample surfaces, whereas the impact was comparable in the CAD/CAM milled and heat-cured samples. Even though polishing improved the samples, they remained in the same order, with the 3D sample having the highest coefficients.

In research conducted by Freitas et al. [32], the surface properties of milled dentures were found to be comparable to those of heat-polymerized denture base resins, but with reduced *Candida albicans* adhesion. According to other authors, even after proper finishing and polishing and long-term thermocyclic aging, traditional complete dentures were associated with greater *Candida* adhesion than CAD/CAM milled prostheses.

Al Moaleem et al. [33] and Ramage et al. [34] reached the conclusion that superior denture surface characteristics, such as porosity and surface roughness, contribute to a reduction in microbial *Candida* adherence, lowering the incidence of denture stomatitis.

In their research, Paolone et al. [35] emphasize the importance of denture surface quality in reducing bacterial plaque adherence and determining superior esthetics and excellent clinical results.

Regarding the mechanical parameter of hardness and tensile parameters, there were statistically significant differences between the groups.

Vickers hardness measurements revealed elevated values for the CAD/CAM milled experimental samples and the lowest values for the 3D-printed samples. The conventional heat-cured resin group recorded an average hardness value. Comparable findings were revealed in recent studies [6,36].

The one-way ANOVA revealed a significant *p*-value when examining the statistical differences between the mean modulus and tensile stress values of the three groups (p 0.001). Comparing each of the potential pairs, the Bonferroni test revealed that, in terms of the modulus coefficient, only the 3D-printed samples differed from the other two on average (p 0.0001). However, when examining tensile stress, a statistically significant difference between the mean values was confirmed for all three potential matched samples.

The internal structures of materials determine their mechanical qualities, such as hardness and flexural strength [33]. CAD/CAM milled polymers have a higher flexural strength than denture bases that are manufactured with compression molding, according to studies [30].

According to Srinivasan et al. [8], milled resins have a higher ultimate strength, toughness, and elastic modulus than printed resins, whereas Al-Dwairi et al. [11] found that CAD/CAM milled denture base resins have a considerable advantage in surface wettability, surface roughness, and surface hardness.

Many studies have indicated that milled removable dentures demonstrate greater flexural strength, flexural modulus, and impact strength than typical heat-cured groups [37–42], as well as superior surface qualities compared to 3D-printed and conventional ones.

Acrylic resins for rapidly prototyped removable dentures have a poor double-bond conversion compared to standard heat-curing resins, which can impact their mechanical qualities. Unlike CAD/CAM milled resins, high pressure promotes the creation of longer polymer chains and can decide a greater degree of monomer conversion [37–44]. The lower characteristics of 3D-printed resin may also be attributed to the processing technique used, such as light polymerization and printing methods (e.g., the layering technique and printing orientation) and parameters.

Steinmassl et al. [45] obtained contradictory results, indicating that digital dentures do not generally have a higher fracture resistance compared to conventional prostheses made of self-curing or heat-curing resins. All CAD/CAM milled denture base resins have greater elastic moduli than heat- or self-curing resins. The fracture surface analyses imply that the microstructure of the resin, as opposed to the polymer chain length, which would be affected by the curing technique, may be accountable for the differing mechanical properties. They believe the changes in mechanical properties are due to the composition of the resin rather than the industrial procedure used [46].

According to the literature, CAD/CAM milled dentures have a superior fit and greater surface qualities and mechanical properties compared to traditional heat-polymerized dentures. Nonetheless, removable dentures that are fabricated with heat-cured resins remain a viable alternative since the mechanical characteristics and surface quality of these materials allow the manufacture of clinically well-tolerated prostheses. Being in direct

contact with the oral tissues, all the new materials must be accurately tuned to fit the requirements and usage conditions [47].

The FEA software predicted the correct propagation direction and offered valuable information in a graphical manner, which can be used for future research. However, the authors acknowledge the need for further refinement since our material mechanical properties may be different depending on the producer's manufacturing process.

Due to the lack of proper understanding regarding the biomechanical principles of the materials involved in restorative procedures, many detrimental effects resulted, causing restorative failures. Therefore, in order to know the behavior of the materials and dental tissues, biomechanical studies are very crucial [6,7].

The limitations of the current research were the lack of denture base materials, the absence of oral condition simulations, and that the samples were not aged by thermocycling. Given these constraints, further in vitro and in vivo studies are required.

5. Conclusions

The study was based on three different groups of specimens which gave us 90 samples to test. Every ten samples had two more that were used for validation purposes. Each sample proved consistent within limits, thus proving our results. Out of the three samples, the 3D-printed samples experienced the lowest surface quality in terms of surface finishing and structural integrity. CAD-CAM milled and heat-cured resins have comparable roughness parameters; however, the milled samples exhibited better mechanical properties than conventional and 3D-printed resins.

Finite element analyses predicted similar behaviors in terms of crack propagation, as real-life samples showed similar results if the concentrator was placed in the same area. Statistically, ANOVA highlighted different values for the 3D-printed samples, on average, compared to the others. Despite the advantages of CAD/CAM milling technology, heat-cured resins continue to be a feasible option since their surface quality and mechanical properties allow the fabrication of satisfactorily removable dentures with long-term durability.

Although 3D-printed removable dentures can be successfully used as a provisional or emergency therapeutic solutions, further refinement is still required in order to make them suitable for prosthetic constructions with great longevity over time. The authors acknowledge the need for further refinement of the results and a wider research base.

Author Contributions: Conceptualization, D.D.-P. and I.M.; methodology, E.-R.B.; software, A.E.A. and A.-M.M.; validation, C.N.S. and O.M.B.; formal analysis, D.D.-P.; investigation, E.-R.B. and A.-M.M.; resources, M.T.; data curation, C.N.S.; writing—original draft preparation, D.D.-P. and I.M.; writing—review and editing, E.-R.B.; visualization, D.D.-P.; supervision, M.T. All authors have read and agreed to the published version of the manuscript.

Funding: This research received no external funding.

Institutional Review Board Statement: Not applicable.

Informed Consent Statement: Not applicable.

Data Availability Statement: Not applicable.

Conflicts of Interest: The authors declare no conflict of interest.

References

1. Martori, E.; Ayuso-Montero, R.; Martinez-Gomis, J.; Viñas, M.; Peraire, M. Risk factors for denture-related oral mucosal lesions in a geriatric population. *J. Prosthet. Dent.* **2014**, *111*, 273–279. [CrossRef] [PubMed]
2. Al-Fouzan, A.F.; Al-Mejrad, L.A.; Albarrag, A.M. Adherence of Candida to complete denture surfaces in vitro: A comparison of conventional and CAD/CAM complete dentures. *J. Adv. Prosthodont.* **2017**, *9*, 402–408. [CrossRef]
3. Diaconu-Popa, D.; Sedze, J.P.; Vitalariu, A.; Luca, O.; Aungurencei, O.; Holban-Cioloca, C.; Tatarciuc, M. Technological Aspects In Aesthetic Rehabilitation of Full Dentures. *Rom. J. Oral Rehabil.* **2021**, *12*, 176–182.

4. Srinivasan, M.; Kamnoedboon, P.; McKenna, G.; Angst, L.; Schimmel, M.; Özcan, M.; Müller, F. CAD-CAM removable complete dentures: A systematic review and meta-analysis of trueness of fit, biocompatibility, mechanical properties, surface characteristics, color stability, time-cost analysis, clinical and patient-reported outcomes. *J. Dent.* **2021**, *113*, 103777. [CrossRef]
5. Vitalariu, A.; Tatarciuc, M.; Luca, O.; Cioloca, C.H.; Bulancea, B.; Aungurencei, A.; Aungurencei, O.; Raftu, G.; Diaconu-Popa, D. Structural and Thermal Changes in Dental Resins Enriched with Silver Nanoparticles. *Rev. Chim.* **2019**, *70*, 591–595. [CrossRef]
6. Prpić, V.; Schauperl, Z.; Ćatić, A.; Dulčić, N.; Čimić, S. Comparison of Mechanical Properties of 3D-Printed, CAD/CAM, and Conventional Denture Base Materials. *J. Prosthodont.* **2020**, *29*, 524–528. [CrossRef] [PubMed]
7. Diaconu-Popa, D.; Vitalariu, A.; Martu, I.; Luchian, I.; Luca, O.; Tatarciuc, M. Full dentures realization-conventional vs digital technologies. *Rom. J. Oral Rehab.* **2021**, *13*, 160–173.
8. Srinivasan, M.; Gjengedal, H.; Cattani-Lorente, M.; Moussa, M.; Durual, S.; Schimmel, M.; Müller, F. CAD/CAM Milled Complete Removable Dental Prostheses: An in Vitro Evaluation of Biocompatibility, Mechanical Properties, and Surface Roughness. *Dent. Mater. J.* **2018**, *37*, 526–533. [CrossRef]
9. Abualsaud, R.; Gad, M.M. Flexural Strength of CAD/CAM Denture Base Materials: Systematic Review and Meta-analysis of In-vitro Studies. *J. Int. Soc. Prev. Community Dent.* **2022**, *1*, 160–170. [CrossRef]
10. Perea-Lowery, L.; Minja, I.K.; Lassila, L.; Ramakrishnaiah, R.; Vallittu, P.K. Assessment of CAD-CAM Polymers for Digitally Fabricated Complete Dentures. *J. Prosthet. Dent.* **2021**, *125*, 175–181. [CrossRef]
11. Al-Dwairi, Z.N.; Tahboub, K.Y.; Baba, N.Z.; Goodacre, C.J.; Özcan, M. A Comparison of the Surface Properties of CAD/CAM and Conventional Polymethylmethacrylate (PMMA). *J. Prosthodont.* **2019**, *28*, 452–457. [CrossRef] [PubMed]
12. de Oliveira Limírio, J.P.J.; Gomes, J.M.L.; Alves Rezende, M.C.R.; Lemos, C.A.A.; Rosa, C.D.D.R.D.; Pellizzer, E.P. Mechanical properties of polymethyl methacrylate as a denture base: Conventional versus CAD-CAM resin—A systematic review and meta-analysis of in vitro studies. *J. Prosthet. Dent.* **2022**, *128*, 1221–1229. [CrossRef]
13. Steinmassl, O.; Dumfahrt, H.; Grunert, I.; Steinmassl, P.-A. Influence of CAD/CAM Fabrication on Denture Surface Properties. *J. Oral Rehabil.* **2018**, *45*, 406–413. [CrossRef] [PubMed]
14. Hsu, C.-Y.; Yang, T.-C.; Wang, T.-M.; Lin, L.-D. Efects of fabrication techniques on denture base adaptation: An in vitro study. *J. Prosthet. Dent.* **2020**, *124*, 740–747. [CrossRef]
15. Masri, G.; Mortada, R.; Ounsi, H.; Alharbi, N.; Boulos, P.; Salameh, Z. Adaptation of Complete Denture Base Fabricated by Conventional, Milling, and 3-D Printing Techniques: An In Vitro Study. *J. Contemp. Dent. Pract.* **2020**, *21*, 367–371.
16. Kalberer, N.; Mehl, A.; Schimmel, M.; Müller, F.; Srinivasan, M. CAD-CAM milled versus rapidly prototyped (3D-printed) complete dentures: An in vitro evaluation of trueness. *J. Prosthet. Dent.* **2019**, *121*, 637–643. [CrossRef]
17. Goodacre, B.J.; Goodacre, C.J.; Baba, N.Z.; Kattadiyil, M.T. Comparison of denture tooth movement between CAD-CAM and conventional fabrication techniques. *J. Prosthet. Dent.* **2018**, *119*, 108–115. [CrossRef] [PubMed]
18. Srinivasan, M.; Kalberer, N.; Kamnoedboon, P.; Mekki, M.; Durual, S.; Özcan, M.; Müller, F. CAD-CAM complete denture resins: An evaluation of biocompatibility, mechanical properties, and surface characteristics. *J. Dent.* **2021**, *114*, 103785. [CrossRef] [PubMed]
19. Baciu, E.-R.; Budală, D.G.; Vasluianu, R.-I.; Lupu, C.I.; Murariu, A.; Geleţu, G.L.; Zetu, I.N.; Diaconu-Popa, D.; Tatarciuc, M.; Nichitean, G.; et al. A Comparative Analysis of Dental Measurements in Physical and Digital Orthodontic Case Study Models. *Medicina* **2022**, *58*, 1230. [CrossRef]
20. AlHelal, A.; AlRumaih, H.S.; Kattadiyil, M.T.; Baba, N.Z.; Goodacre, C.J. Comparison of retention between maxillary milled and conventional denture bases: A clinical study. *J. Prosthet. Dent.* **2017**, *117*, 233–238. [CrossRef]
21. Javaid, M.; Haleem, A. Current status and applications of additive manufacturing in dentistry: A literature-based review. *J. Oral Biol. Craniofac. Res.* **2019**, *9*, 179–185. [CrossRef] [PubMed]
22. Katheng, A.; Kanazawa, M.; Iwaki, M.; Minakuchi, S. Evaluation of dimensional accuracy and degree of polymerization of stereolithography photopolymer resin under diferent postpolymerization conditions: An in vitro study. *J. Prosthet. Dent.* **2021**, *125*, 695–702. [CrossRef] [PubMed]
23. Tatarciuc, M.; Vitalariu, A.; Luca, O.; Aungurencei, A.; Aungurencei, O.; Diaconu-Popa, D. The influence of food consistency on the abutment teeth in fixed prostheses- a FEA study. *Rev. Chim.* **2018**, *69*, 407–412. [CrossRef]
24. *ISO 527-2:2012*; Plastics—Determination of Tensile Properties—Part 2: Test Conditions for Molding and Extrusion Plastics. International Organization for Standardization: Geneva, Switzerland, 2012.
25. U.S. Department of Defense. Decision on Principles for the Development of International Standards, Guides and Recommendations Issued by the World Trade Organization Technical Barriers to Trade (TBT) Committee of Plastics. In *Standard Test Method for Tensile Properties*; U.S. Department of Defense: Washington, DC, USA, 15 December 2014.
26. Ucar, Y.; Akoa, T.; Aysan, I. Mechanical properties of Polyamide versus different PMMA denture base materials. *J. Prosthet. Dent.* **2012**, *21*, 157–254. [CrossRef] [PubMed]
27. Safwat, E.M.; Khate, A.G.A.; Abd-Elsatar, A.G.; Khater, G.A. Glass fiber-reinforced composites in dentistry. *Bull. Natl. Res. Cent.* **2021**, *45*, 190. [CrossRef]
28. *ISO 527-1:2020*; Plastics—Determination of Tensile Properties—Part 1: General Principles. International Organization for Standardization: Geneva, Switzerland, 2019.

29. Helal, M.A.; Fadl-Alah, A.; Baraka, Y.M.; Gad, M.M.; Emam, A.M. In-vitro Comparative Evaluation for the Surface Properties and Impact Strength of CAD/CAM Milled, 3D Printed, and Polyamide Denture Base Resins. *J. Int. Soc. Prev. Community Dent.* **2022**, *12*, 126–131.
30. Zeidan, A.A.E.; Abd Elrahim, R.A.; Abd El Hakim, A.F.; Harby, N.M.; Helal, M.A. Evaluation of Surface Properties and Elastic Modulus of CAD-CAM Milled, 3D Printed, and Compression Moulded Denture Base Resins: An In Vitro Study. *J. Int. Soc. Prev. Community Dent.* **2022**, *12*, 630–637.
31. Fu, S.; Cheng, F.; Tjahjowidodo, T.; Zhou, Y.; Butler, D. A Non-Contact Measuring System for In-Situ Surface Characterization Based on Laser Confocal Microscopy. *Sensors* **2018**, *18*, 2657. [CrossRef]
32. Freitas, R.F.C.P.; Duarte, S.; Feitosa, S.; Dutra, V.; Lin, W.S.; Panariello, B.H.D.; Carreiro, A.D.F.P. Physical, Mechanical, and Anti-Biofilm Formation Properties of CAD-CAM Milled or 3D Printed Denture Base Resins: In Vitro Analysis. *J. Prosthodont.* 2022; *Online ahead of print*.
33. Al Moaleem, M.M.; Porwal, A.; Alahmari, N.; Shariff, M. Oral Biofilm on Dental Materials Among Khat Chewers. *Curr. Pharm. Biotechnol.* **2020**, *21*, 964–972. [CrossRef]
34. Ramage, G.; Coco, B.; Sherry, L.; Bagg, J.; Lappin, D.F. In vitro Candida albicans biofilm induced proteinase activity and SAP8 expression correlates with in vivo denture stomatitis severity. *Mycopathologia* **2012**, *174*, 11–19. [CrossRef]
35. Paolone, G.; Moratti, E.; Goracci, C.; Gherlone, E.; Vichi, A. Effect of Finishing Systems on Surface Roughness and Gloss of Full-Body Bulk-Fill Resin Composites. *Materials* **2020**, *13*, 5657. [CrossRef]
36. Al-Dharrab, A. The residual monomer content and mechanical properties of CAD\CAM resins used in the fabrication of complete dentures as compared to heat cured resins. *Electron. Phys.* **2017**, *9*, 4766–4772.
37. Baba, N.Z.; Goodacre, B.J.; Goodacre, C.J.; Müller, F.; Wagner, S. CAD/CAM Complete Denture Systems and Physical Properties: A Review of the Literature. *J. Prosthodont.* **2021**, *30*, 113–124. [CrossRef]
38. Mubaraki, M.Q.; Moaleem, M.M.A.; Alzahrani, A.H.; Shariff, M.; Alqahtani, S.M.; Porwal, A.; Al-Sanabani, F.A.; Bhandi, S.; Tribst, J.P.M.; Heboyan, A.; et al. Assessment of Conventionally and Digitally Fabricated Complete Dentures: A Comprehensive Review. *Materials* **2022**, *15*, 3868. [CrossRef]
39. Choi, J.J.E.; Uy, C.E.; Plaksina, P.; Ramani, R.S.; Ganjigatti, R.; Waddell, J.N. Bond Strength of Denture Teeth to Heat-Cured, CAD/CAM and 3D Printed Denture Acrylics. *J. Prosthodont.* **2020**, *29*, 415–421. [CrossRef]
40. Zeidan, A.A.E.; Sherif, A.F.; Baraka, Y.; Abualsaud, R.; Abdelrahim, R.A.; Gad, M.M.; Helal, M.A. Evaluation of the Effect of Different Construction Techniques of CAD-CAM Milled, 3D-Printed, and Polyamide Denture Base Resins on Flexural Strength: An In Vitro Comparative Study. *J. Prosthodont.* **2023**, *32*, 77–82. [CrossRef] [PubMed]
41. Fouda, S.M.; Gad, M.M.; Abualsaud, R.; Ellakany, P.; AlRumaih, H.S.; Khan, S.Q.; Akhtar, S.; Al-Qarni, F.D.; Al-Harbi, F.A. Flexural Properties and Hardness of CAD-CAM Denture Base Materials. *J. Prosthodont.* 2022; *Online ahead of print*.
42. Steinmassl, O.; Offermanns, V.; Stöckl, W.; Dumfahrt, H.; Grunert, I.; Steinmassl, P.-A. In Vitro Analysis of the Fracture Resistance of CAD/CAM Denture Base Resins. *Materials* **2018**, *11*, 401. [CrossRef] [PubMed]
43. Al-Dwairi, Z.N.; Tahboub, K.Y.; Baba, N.Z.; Goodacre, C.J. A Comparison of the Flexural and Impact Strengths and Flexural Modulus of CAD/CAM and Conventional Heat-Cured Polymethyl Methacrylate (PMMA). *J. Prosthodont.* **2020**, *29*, 341–349. [CrossRef]
44. Pacquet, W.; Benoit, A.; Hatège-Kimana, C.; Wulfman, C. Mechanical properties of CAD/CAM denture base resins. *Int. J. Prosthodont.* **2019**, *32*, 104–106. [CrossRef]
45. Steinmassl, O.; Dumfahrt, H.; Grunert, I.; Steinmassl, P.A. CAD/CAM produces dentures with improved fit. *Clin. Oral Investig.* **2018**, *22*, 2829–2835. [CrossRef] [PubMed]
46. Spagnuolo, G.; Sorrentino, R. The Role of Digital Devices in Dentistry: Clinical Trends and Scientific Evidences. *J. Clin. Med.* **2020**, *9*, 1692. [CrossRef] [PubMed]
47. Drobota, M.; Vlad, S.; Gradinaru, L.M.; Bargan, A.; Radu, I.; Butnaru, M.; Rîmbu, C.M.; Ciobanu, R.C.; Aflori, M. Composite Materials Based on Gelatin and Iron Oxide Nanoparticles for MRI Accuracy. *Materials* **2022**, *15*, 3479. [CrossRef] [PubMed]

polymers

MDPI

Article

Tensile Behavior of Chain Links Made of Polymeric Materials Manufactured by 3D Printing

Bruno Rădulescu [1], Andrei Marius Mihalache [2], Emilian Păduraru [1], Adelina Hriţuc [2,*], Mara Cristina Rădulescu [1], Laurenţiu Slătineanu [2] and Vasile Ermolai [2]

[1] Department of Digital Production Systems, "Gheorghe Asachi" Technical University of Iași, 700050 Iași, Romania; bruno.radulescu@academic.tuiasi.ro (B.R.); emilian.paduraru@academic.tuiasi.ro (E.P.); mara.radulescu@academic.tuiasi.ro (M.C.R.)

[2] Department of Machine Manufacturing Technology, "Gheorghe Asachi" Technical University of Iași, 700050 Iași, Romania; marius-andrei.mihalache@academic.tuiasi.ro (A.M.M.); slati@tcm.tuiasi.ro (L.S.); vasile.ermolai@student.tuiasi.ro (V.E.)

* Correspondence: adelina.hrituc@student.tuiasi.ro; Tel.: +40-751640117

Abstract: For reduced mechanical stress, some chains with links made of metallic materials could be replaced by chains made of polymeric materials. A lower weight and a higher corrosion resistance would characterize such chains. From this point of view, research on the behavior of chain links made of polymeric materials under the action of tensile stresses can become important. Modeling by the finite element method highlighted some specific aspects of the behavior of a chain link subjected to tensile stresses. Later, we resorted to the manufacture by 3D printing of some chain links from four distinct polymeric materials, with the modification of the size of the chain link and, respectively, of the values of some of the input factors in the 3D printing process. The tensile strength of the chain links was determined using specialized equipment. The experimental results were processed mathematically to determine some empirical mathematical models that highlight the influence of the values of the input factors in the 3D printing process on the tensile strength of the samples in the form of chain links. It thus became possible to compare the results obtained for the four polymeric materials considered and identify the polymeric material that provides the highest tensile strength of the sample in the form of a chain link. The results of the experimental research showed that the highest mechanical resistance was obtained in the case of the links made of polyethylene terephthalate glycol (PETG). According to experimental results, when tested under identical conditions, PETG links can break for a force value of 40.9 N. In comparison, polylactic acid links will break for a force value of 4.70 N. Links printed in the horizontal position were almost 9-fold stronger than those printed in the vertical position. Under the same test conditions, according to the determined empirical mathematical models, PETG links printed in a horizontal position will break for a force of 300.8 N, while links printed in a vertical position will break for force values of 35.8 N.

Keywords: chain link; polymers; tensile testing; influence factors; empirical mathematical models

Citation: Rădulescu, B.; Mihalache, A.M.; Păduraru, E.; Hriţuc, A.; Rădulescu, M.C.; Slătineanu, L.; Ermolai, V. Tensile Behavior of Chain Links Made of Polymeric Materials Manufactured by 3D Printing. *Polymers* **2023**, *15*, 3178. https://doi.org/10.3390/polym15153178

Academic Editor: Chin-San Wu

Received: 30 April 2023
Revised: 12 July 2023
Accepted: 14 July 2023
Published: 26 July 2023

1. Introduction

The chain link is a component of the chain. In turn, the chain is a string of links assembled consecutively between them and which is used to materialize some tying, suspension, tensile, etc., operations. The previous definition of a chain also highlights its main possibilities of use or the stress it is subjected to.

In its simplest form, a chain link is shaped similar to a ring deformed to reduce the width of the chain link and, thus, of the chain. The material and dimensions of a chain link in a cross-section are usually determined considering the mechanical stresses to which the chain composed of links will be subjected.

The classification of chain links can be carried out taking into account the shape of the chain links (circular or oval), the destination of the chain (for limiting the movements of

an object or animal, for suspending or towing an object or an assembly/subassembly, for increasing the towing capacity of tires (in the case of anti-skid chains)), etc.

Given the chains' relatively high tensile stress values, their links are made of metallic materials, mainly steel. The need to reduce the chains' weight, especially when the mechanical stresses are somewhat lower, has led to the research and use of chain links made of plastic or composite materials.

Plastic materials are non-metallic materials with an amorphous structure obtained by melting together several constituents, such as resins, plasticizers, dyes, lubricants, fillers, or auxiliary materials. These materials are characterized by the possibility of being easily shaped, thanks to good plasticity, at temperatures usually between 140 and 180 °C. On the other hand, composite materials include a metallic or non-metallic mass and are reinforced with resistance elements from the category of short or very short fibers, long fibers, fabrics, felt, etc.

Plastic or polymer matrix composite chain links are lighter than metal chain links and have higher corrosion resistance. Consistent with the general properties of plastics, such materials are thermally and electrically insulating [1,2].

Suppose the production of chain links from metallic materials is based on bending a workpiece originally as a bar or wire. In that case, the chain links from plastic or composite materials can be obtained through specific processes, such as injection and 3D printing.

The expansion in the last decades of 3D printing processes has facilitated the development of some research on the properties required by the uses of chains with chain links made of plastic materials or composite materials with polymer matrix made even by 3D printing.

Thus, the possibilities of direct manufacturing through 3D printing of interconnected moving parts in the category of which interconnected chain links are also highlighted by researchers [3–5].

Chains with links having more complicated shapes were made by 3D printing (SLM) and studied by Venes et al. [6]. The material of the chain links was an alloy containing titanium, aluminum, and vanadium. It was found that it is possible to ensure a clearance between two moving surfaces of 150 μm.

Wójcicki et al. designed and built a stand for the wear testing of the chain links of the scraper conveyor [7]. A simplified stand prototype was materialized using 3D printing of its components.

The possibility of making chain links from lightweight material through additive manufacturing was highlighted [5,8]. Chains of this type can be used in the mining industry to reduce the weight of some equipment.

A theoretical and experimental analysis of the stress generated in metal chain links under different operating conditions was carried out by Mešić et al. [9]. They considered stress analysis for different chain link positions during mechanical loading.

The possibilities of manufacturing some objects from ceramic materials with polymeric matrix and including some chain links from such materials were investigated by Román-Manso et al. They resorted to 3D printing with microwave-activated polymerization [10].

3D printing of polymer link chains for dog harnesses was addressed by Woodman [11]. He produced a report outlining the possibilities of using 3D printing to create objects that could improve the living conditions of pets or laboratory animals. He thus analyzed the situation of the use of chain links made of plastic materials, appreciating that the plastic material of the links must be hard enough so that the animals do not swallow the particles detached from the links as a result of use and harm their health.

The finite element method was used by Noguchi et al. for a static stress study in the case of a link plate of a roller chain [12]. The study also aimed at identifying some possibilities for reducing the weight of the chain.

Researching the behavior of ship mooring chains on shore has been an important objective for different groups of researchers [13–26]. The static, dynamic, and fatigue stresses occurring in the chain links for different operating conditions were thus highlighted.

The values of some input factors in the additive manufacturing process are expected to influence the physical-mechanical properties of the materials of the parts manufactured by such processes [8,9,27].

The problem of manufacturing chain links from polymeric materials was an objective also addressed in various invention patents [28–30].

From those mentioned above, it can be seen that until now, the research related to the chain links made of metallic and non-metallic materials has focused on the establishment of the dimensions of these chain links [1,7,31–33], the efforts generated in the chain links during operation [8,18,25,26,31], the modeling by the finite element method or by other methods of the stresses and deformations from chain links during their mechanical loading [9,12–15,18,19], investigating the fatigue behavior of chain links [20–22].

It was found that there is relatively little information on the behavior of chain links from polymeric materials manufactured by 3D printing when these chain links are subjected to tensile stress. It is necessary to mention that in the category of chains made of metallic materials that could be replaced by links made of polymers or chains with links made of polymeric materials, some chains for ornaments of monuments, chains for suspending some objects of religious worship, chains of ornaments, chains for leashes used to tie dogs, etc.

The authors of this paper are unaware of results obtained by other researchers regarding the influence exerted by the dimensions of polymer material beads and the factors that characterize the manufacturing conditions of beads by 3D printing on the tensile strength of beads. For low mechanical loads, link chains made of polymeric materials could be characterized by lower mass and superior corrosion resistance. Such chains could be made directly by 3D printing without the need for an assembly operation of separately manufactured chain links.

The finite element method was used to obtain additional information regarding the behavior of the chain links during their tensile testing. In the framework of this paper, the main aspects related to oval-shaped rings manufactured by 3D printing processes from polymeric materials will be briefly analyzed. The conditions for conducting the tensile tests of the 3D printed polymer materials and the obtained experimental results will be presented in the next chapter. Afterward, the emphasis will be on the mathematical processing of the experimental results and the identification, as such, of some empirical mathematical models that characterize the tensile behavior of chain links made of polymeric materials and, respectively, of a composite material with a polymeric matrix. The analysis of the empirical mathematical models will have to allow the formulation of some observations regarding the meaning of variation and the intensity of the influence exerted on the maximum force supported by the chain links when the sizes of the input factors in the investigated process change.

2. Materials and Methods

2.1. The Mechanical Loading of a Chain Link

As mentioned, the chain link is shaped similar to an ovalized ring, with a cross-section through the ring usually revealing a circular shape. During operation, static or dynamic stretching, compression, bending, and torsional stresses can occur in different areas of the chain link.

From the point of view of most uses of the chain link, its tensile strength is of particular interest. However, even during a tensile test, different areas of the chain link may be affected by other categories of stress.

In principle, the tensile testing of the chain link involves using hooks or bolts whose ends are inserted into the gap of the chain link and through which tensile stress is generated in the lateral areas (Figure 1).

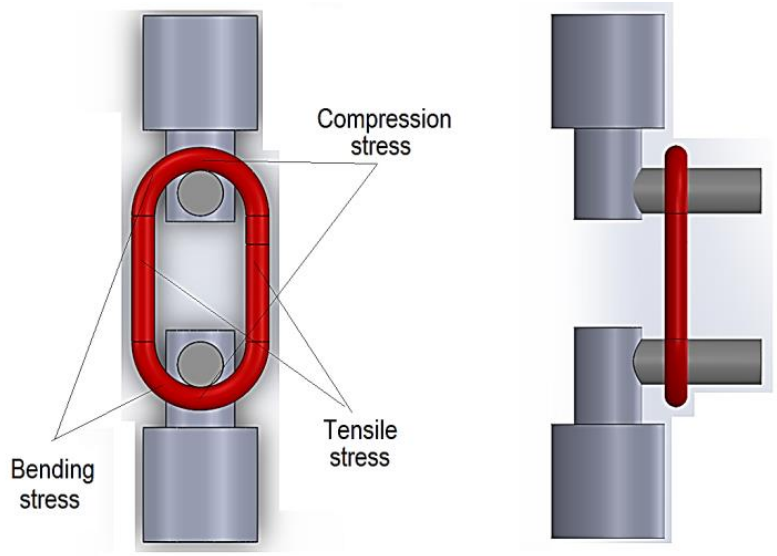

Figure 1. Way to clamp the chain link on the tensile test machine, using two bolts.

The mentioned stress can have a static character. Compressive and crushing stress occurs in the contact areas of the chain link with the two bolts. Bending efforts occur near the contact between the chain link and the bolts through which the chain links are subjected to mechanical stresses. Torsional stresses will still appear in chain links if a twisted chain is considered. Still, there are situations when the loading can also be cyclical, which requires some research on the fatigue resistance of the chain links.

The manufacture of chains from oval-shaped metal chain links may involve operations of cutting straight segments from wire or bar, heating, and descaling, and one or more bending operations, with the eventual joining of chain links, butt welding, shot blasting, marking, thermal treatment, application of surface protection operations, etc. [26]. Chain manufacturing technology also includes some operations to inspect and test the quality of products in different phases of the manufacturing process. Stretch testing and impact testing are such chain quality control operations.

Chain links can be made of polymer or matrix composite materials for low or moderate loads. Thus, chain links can be manufactured by injection molding. As mentioned, the expansion in the last decades of 3D printing processes led, among other results, to ensure the conditions for manufacturing chain links from polymer materials or composite materials with a polymer matrix through additive manufacturing processes. The possibility of changing the values of some parameters specific to the manufacturing conditions of the chain links through 3D printing processes facilitates a deeper investigation of the factors capable of influencing the behavior of the chain link during their operation.

Fused deposition modeling is one of the most widespread groups of techniques that can be used to manufacture parts from polymer materials through 3D printing. In this case, the material of a polymer wire is melted and then deposited to make up the successive layers of material of a particular part. Let us note that fused deposition modeling or 3D printing, in general, can provide conditions for manufacturing the assembled chain links from the beginning so that the chain can be directly obtained.

An improvement in the behavior of chains made of non-metallic materials becomes possible through composite materials with a polymer matrix, in which case the use of certain reinforcement materials could contribute to a significant improvement in the behavior of the chains during their exploitation.

Suppose the manufacture of chain links by fused deposition modeling is considered. In that case, the main groups of factors capable of affecting the behavior of the chain links or chains during their use are the following:

- The sizes and shapes of the chain links;
- The nature and physical-mechanical properties of the polymer material or the composite material with a polymer matrix;
- Some parameters that characterize the conditions for carrying out the 3D printing process;
- The way to load chain links, the nature of these loads, etc.

It is interesting to study the extent to which some of the previously mentioned factors or groups of factors influence the mechanical strength characteristics of chain links made of polymer materials or polymer matrix composite materials.

2.2. Finite Element Modeling of the Behavior of a Plastic or Composite Chain Link

A chain link with the shape and dimensions indicated in Figure 2 was considered. One criterion considered when determining the geometry and dimensions of the 3D printed and tensile-tested chain links was to approximate the dimensions and geometry of existing chain links in practice. Since it was also intended to highlight the influence exerted by the size of the diameter of the za element on the tensile behavior, we resorted to the use of two such diameters, with values close to those existing in the case of some chains encountered in practice.

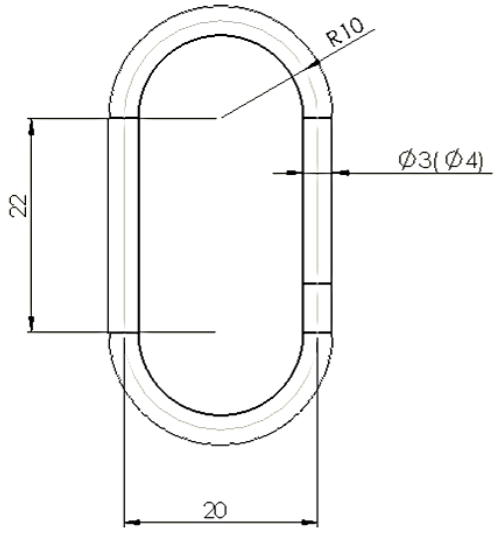

Figure 2. Dimensions of the chain link proposed to be tested.

As a matter of choice, the finite element method (FEM) is to obtain a similar crack pattern as one from the experimental tests. This would give insight into stress distribution just before the crack extends on the whole part length and the fracture occurs. For this purpose, it had to design a similar model with one of the eight test samples used in the experimental tests. It had chosen sample 1 with a 30% infill (see Figure 3a). This option is because sample 1 is printed vertically (see Table 2), making it more difficult to print and analyze than its horizontal peers. The E-moduli obtained using the fused deposition modeling (FDM) printing process is lower than that provided by the manufacturer and depends on the printing direction. Six samples of Ultrafuse ABS-type filament manufactured by BASF (Ludwigshafen, Germany) on Instron 4411 equipment were printed for analyses to be as accurate as possible and tested. It carries a 5 kN load cell with a 5 mm/sec testing speed. The room temperature was 22 °C with a 60% humidity level. It resulted in an E-modulus mean value of 558 MPa. The manufacturer lists in the filament's technical data sheet (TDS) 1608 MPa on ZX direction of printing [34], whereas the Ansys library uses 1628 MPa. The measured value was used inside Engineering Data, Ansys's library of materials. The infill model was replicated in a 3D model and later translated into a Parasolid file for analysis (see Figure 3b).

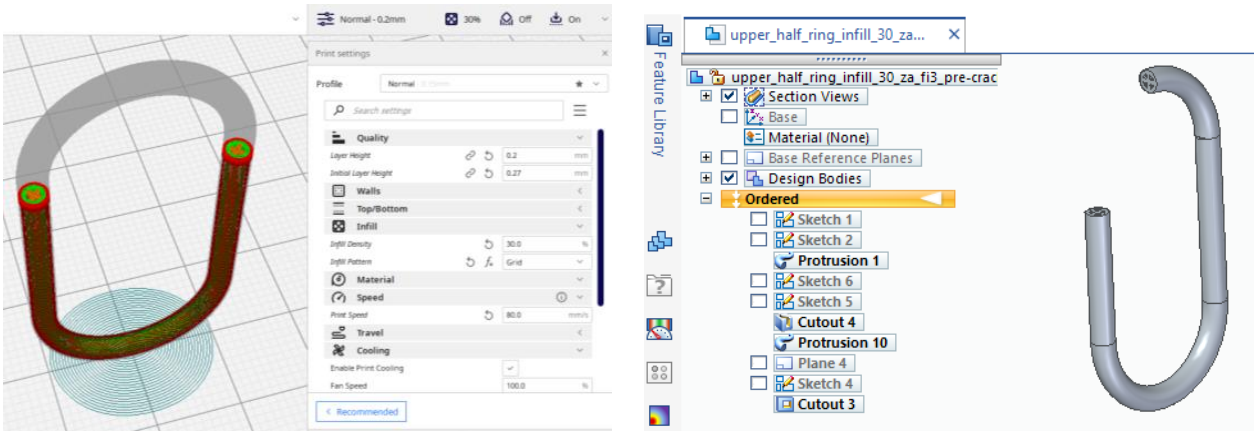

(**a**) (**b**)

Figure 3. Models of the chain link: (**a**)—intermediate step from the preview of the 3D printing process; (**b**)—section view of the 3D model with a 30% infill pattern.

The 3D model also received a crack initiation model because the FEM analyses are based on the prediction of crack propagation using Ansys's SMART Crack Growth, which relies on the energy release rate method. It has opted for the stress intensity factor as the desired fracture criterion inside a static crack growth mechanism. This one predicts a pre-existing crack growth when certain loading conditions are met. The algorithm calculates the maximum stress intensity factor of the crack's front nodes, and if it exceeds the specified criterion, the crack is set to grow. The critical rate was set to 100 MPa $mm^{1/2}$, which will not stop on maximum crack extension. The body was assigned an ABS type of material retrieved from the software's library. It has imposed a virtual topology that uses the edges-only type of behavior. Mesh controls use a patch-conforming method with quadratic element order set for the entire chain link body and a face sizing of 0.15 mm for the two faces of the pre-existing designed crack. Element size was set to 0.25 mm for the entire mesh, with an aggressive mechanical method set for whenever error limits are encountered during analyses. That gave almost 80.000 elements and more than 140,000 nodes (see Figure 4a). The pre-meshed crack was designed to occur before the infill pattern, thus giving us the opportunity to set the front, top and bottom nodes using named selection. As experimental tests revealed in the case of sample 1 the crack initiates at the beginning of the semi-circular top section of the chain link. After several trial and error attempts, it has chosen 6 solution contours and imposed a new Coordinate System set for the crack only for the algorithm to work properly. This system has the X axis set in the direction of the crack extension as the Y sits almost normal on its geometry (see Figure 4b). Conditions use a fixed support for the lower section of the chain link and a force value imposed on the upper section of the chain link in the Z+ direction of the Global Coordinate System (see Figure 4c). Analyses settings are set to 0.00001 sec end step time divided into ten sub-steps.

Just before separation, the value of force required by the software to generate crack growth was 54 N which is close to that registered in the case of sample 1 made of ABS. (Table 2). The difference may come from the fact that the 3D model uses an ideal type of homogeneity, whereas the printed sample suffers from this perspective. It has resulted in 15.025 MPa registered for the equivalent stress evaluated using Von-Mises criteria. The graphical representation shows a distribution along the fracture line with its ends colored in red (see Figure 5a). Equivalent elastic strain peaks at 0.042454 mm/mm, showing that the chain link takes the force solicitation and tries to overcome it by distributing it along its length (see Figure 5b). Finally, it has attached a real-life photo of cracked sample 1 after the experimental test. It can observe a similar direction of propagation as that obtained for the pre-designed crack (Figure 5c).

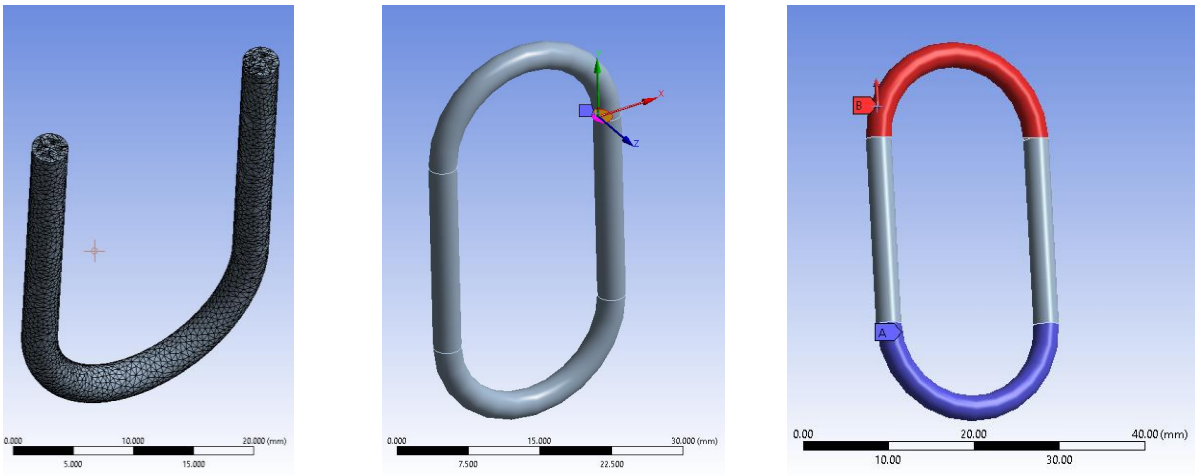

(**a**) (**b**) (**c**)

Figure 4. FEM setup: (**a**)—section view of the meshed model with a 30% infill patterns; (**b**)—view of the pre-meshed crack setup with its coordinate systems; (**c**)—setup conditions inside analyses settings.

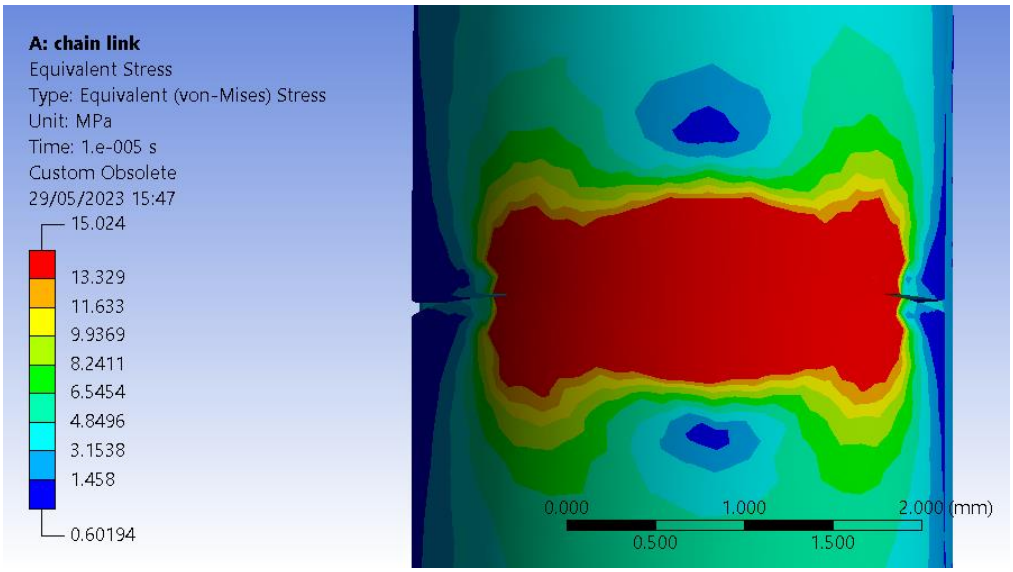

(**a**)

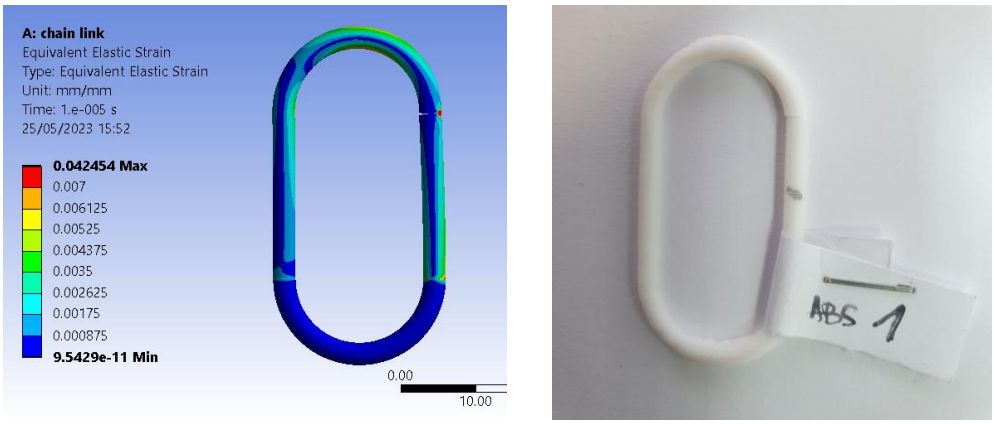

(**b**) (**c**)

Figure 5. Results of FEM and experimental test: (**a**)—side view of the distribution of equivalent (von Mises) stress type of result; (**b**)—front view of the distribution of equivalent elastic strain type of result; (**c**)—front view of the real-life cracked sample 1 made of ABS.

SMART crack growth produces a result similar to that obtained using experimental tests. Before the body gets separated, stress and strain distribution is very useful information for future research, which would consider optimization using 3D printing setup and design. However, results should be used carefully. Further refinement is necessary, considering a finer mesh, more contour plots, or another type of crack growth assessment with an arbitrary or surface-based crack.

2.3. Experimental Conditions

The objective pursued through the experimental research was to highlight the influence exerted by the nature of some polymer materials used for manufacturing chain links, some dimensions of the chain links, and some factors that characterize the conditions of 3D printing of chain links.

Four materials were considered, namely: acrylonitrile butadiene styrene (ABS, Kimya, Nantes, France), acrylonitrile butadiene styrene-Kevlar composite material (ABS-K), polylactic acid (PLA), and polyethylene terephthalate glycol (PETG) (Prusa, Prague, Czech Republic). Information on some of the properties of these materials has been listed in Table 1.

Table 1. Some properties of the materials used in the case of tensile-tested beams.

Properties	ABS	ABS-Kevlar	PLA	PETG
Tensile modulus [GPa]	1.6815 (ISO 527)	1.775 (ISO 527)	2.3 (ASTM D638—Type V)	1.6 ± 0.1 (ISO 527-1—vertical XZ)
Tensile strength [GPa]	0.0436 (ISO 527—at yield)	0.0311 (ISO 527—at yield)	0.0359 (ASTM D638—Type V—at yield)	0.05 (ISO 527-1—vertical XZ)
Elongation	3.5 % (ISO 527—at yield)	2.3 % (ISO 527—tensile strength)	2 % (ASTM D638—Type V—at yield)	5.1 % (ISO 527-1—at yield)
Hardness	97 (Shore A)	65.2 (Shore D)	95 (Shore D)	74 (Shore D)

The chain links were manufactured by 3D printing on a Prusa i3MK3S equipment made in the Czech Republic. The values of some input factors in the 3D printing process have been established, as shown next. The values of the printing speed v, the thickness t of the deposited layer, and those of the infill density i were entered into the 3D printing program. As far as possible, consideration was given to the use of the same input factor values for the experiments performed on each of the four materials from which the chain links test samples were manufactured. Instead, for the printer plate temperature θ_p and the extrusion temperature θ_e, a rewrite of the 3D printing program was required.

The equipment used to determine the mechanical strength of the beads was a tensile testing machine type LRX Plus (Lloyd Instrument Ltd., An AMETEK Company, Hampshire, UK). It uses XLC-5000-Al type of load cell up to 5 kN with a precision of 0.5% according to ASTM E4 and DIN 1221. Data acquisition was made by using equipment's NEXIGEN Data Analysis software (ver. 3.0) solution.

The components involved in the experimental research can be seen in Figure 6.

Table 2. Conditions for performing experimental tests and results of tensile tests.

Part/ Exp no.	Values of the Input Factors							Values of the Output Parameter (Maximum Force F, N)			
	Chain Link Diameter, d, mm	Printing Speed, v, mm/s	Layer Thickness, t, mm	Infill Density, i, %	Temperature Build Plate, θ_p, °C	Extrusion Temperature, θ_e, °C	Printing Position, p	ABS	ABS-K	PLA	PETG
1	3	80	0.2	30	90	245	1	53.809	51.415	4.7005	40.96
2	3	80	0.2	60	110	265	2	350.23	216.41	235.7	414.93

Table 2. *Cont.*

Part/ Exp no.	Values of the Input Factors							Values of the Output Parameter (Maximum Force *F*, N)			
	Chain Link Diameter, *d*, mm	Printing Speed, *v*, mm/s	Layer Thickness, *t*, mm	Infill Density, *i*, %	Temperature Build Plate, θ_p, °C	Extrusion Temperature, θ_e, °C	Printing Position, *p*	ABS	ABS-K	PLA	PETG
3	3	120	0.3	30	90	265	2	459.45	94.09	252.02	414.3
4	3	120	0.3	60	110	245	1	54.519	47.876	302.2	16.923
5	4	80	0.3	30	110	245	2	435.48	208.47	403.73	273.56
6	4	80	0.3	60	90	265	1	120.03	124.44	121.78	80.394
7	4	120	0.2	30	110	265	1	150.47	113.51	141.96	103.43
8	4	120	0.2	60	90	245	2	289.04	233.66	257.23	612.66

Printing position: $p = 1$ for vertical position; $p = 2$ for horizontal position.

Figure 6. Components of equipment used for tensile testing of chain links.

Clamping of the bars to the tensile testing machine was carried out using 2 bolts (Figure 7).

Figure 7. Clamping the chain link on the tensile testing machine.

The deformation rate of the specimens during the tensile test was 6 mm/min. The LRX Plus Universal Tensile Testing Machine can obtain the force–deformation diagram and all related numerical information directly.

To obtain as complete information as possible regarding the factors that influence the tensile behavior of the chain links manufactured by 3D printing, they resorted to using a Taguchi fractional factorial experiment of type L8 (2^{8-1}), with 7 input factors at two variation levels. Each type of material received an additional sample for testing purposes to proof our L8-1 plan. Such an experimental program also ensures a certain reduction

in the number of experimental tests necessary to be performed without the precision of the established empirical mathematical model being significantly affected [35,36].

The 7 input factors considered were the chain link diameter (d_{min} = 3 mm, d_{max} = 4 mm), printing speed (v_{min} = 80 mm/s, v_{max} = 120 mm/s), layer thickness (t_{min} = 0.2 mm, t_{max} = 0.3 mm), infill density (i_{min} = 30%, i_{max} = 60%), build plate temperature (θ_{pmin} = 90°, θ_{pmax} = 110°), extrusion temperature (θ_{emin} = 25 °C, θ_{emax} = 265 °C and, respectively, the way of specimen placement during the 3D printing process (code 1 for vertical printing and code 2 for horizontal printing).

Experimental research has shown that the duration of the printing process of a vertically placed specimen is approximately 50% longer than that corresponding to printing the specimen in a horizontal position. An image made as a screenshot and related to the vertical or horizontal placement of the chain link in the 3D printing process is shown in Figure 8. In this image, the support elements generated by the slicer were highlighted using green color.

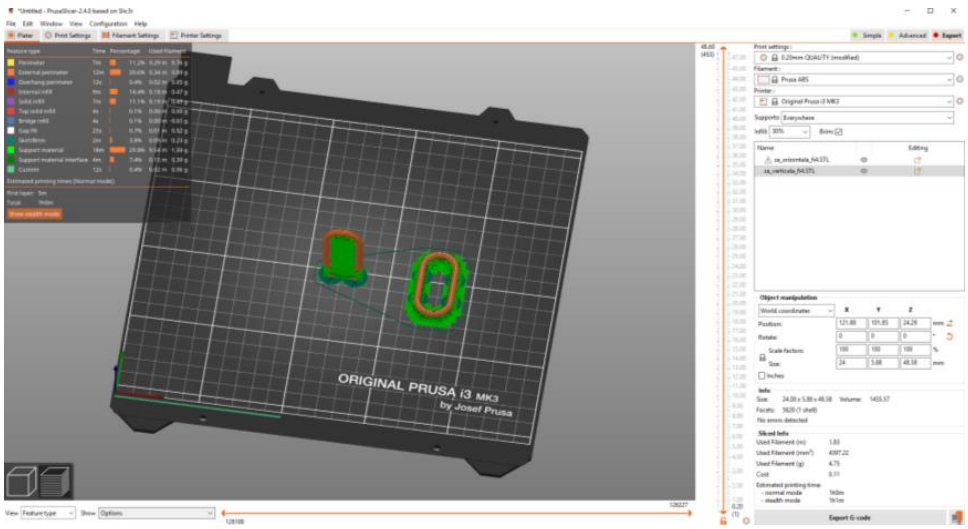

Figure 8. Screenshot showing how to place the printed chain link vertically or horizontally.

The value of the maximum force F at which the initiation of the sample damage process is highlighted was used as the output parameter. The values of the F forces for each material and experimental test were determined by analyzing the force–deformation diagrams generated by the computer program used by the tensile testing machine.

In Figure 9, the aspect of a chain link can be observed before being subjected to the tensile test and, respectively, after stopping the tensile test.

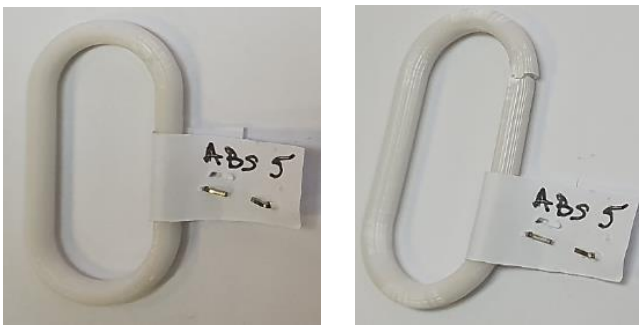

Figure 9. The appearance of a chain link made of ABS polymer material before (**left**) and after (**right**) breaking, respectively.

In Figure 10, the 32 specimens manufactured by 3D printing from different polymer materials can be observed after their rupture by the tensile test.

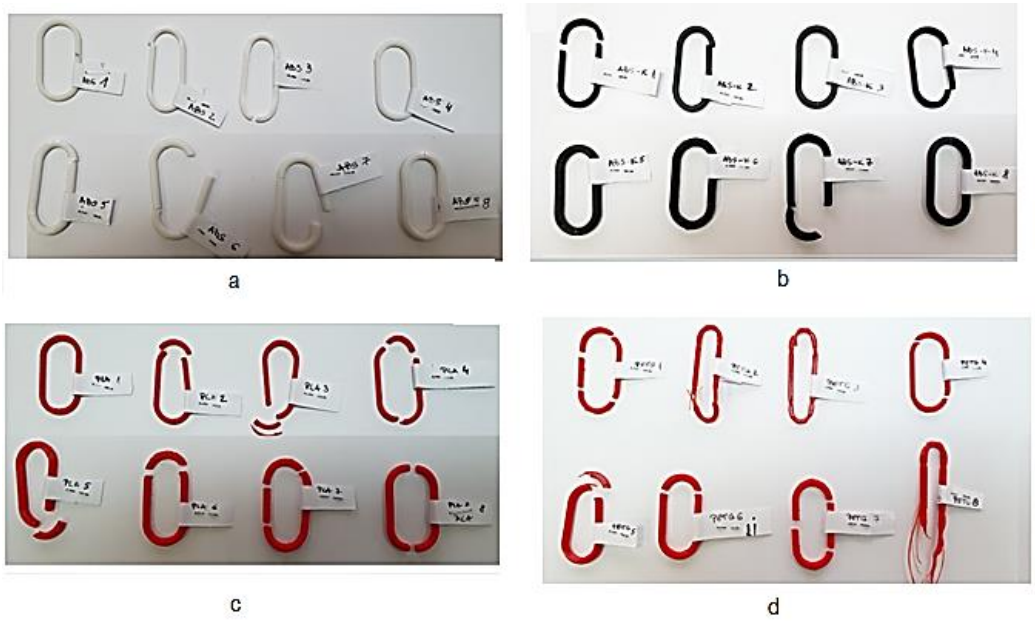

Figure 10. Images of the 32 links manufactured by 3D printing from 4 different polymer materials, after breaking them by the tensile test ((**a**)—ABS links; (**b**)—ABS-K links; (**c**)—PLA links; (**d**)—PETG links).

Some examples of force–deformation curves made under the conditions of testing the specimen made of ABS polymer material can be seen in Figure 11.

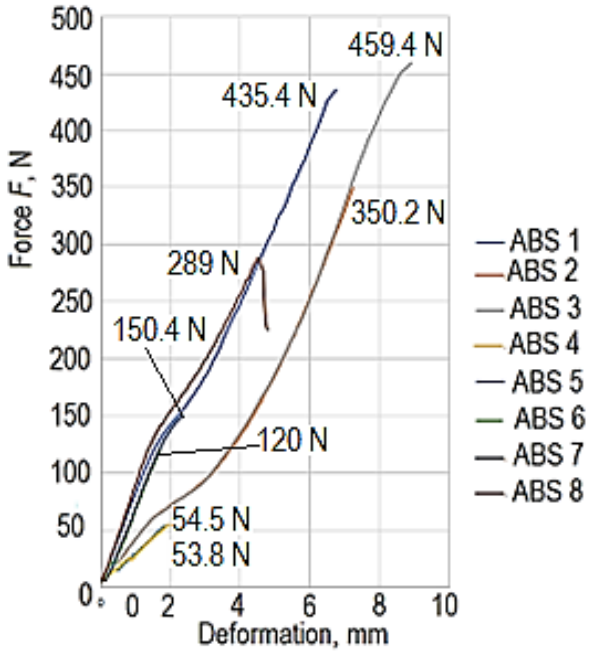

Figure 11. Examples of force–deformation curves in the case of links made of ABS polymer material, corresponding to the 8 experimental tests.

The influence of the diameter d on the magnitude of the maximum force F that determines the damage of a chain link made of different materials can be seen in Figure 12.

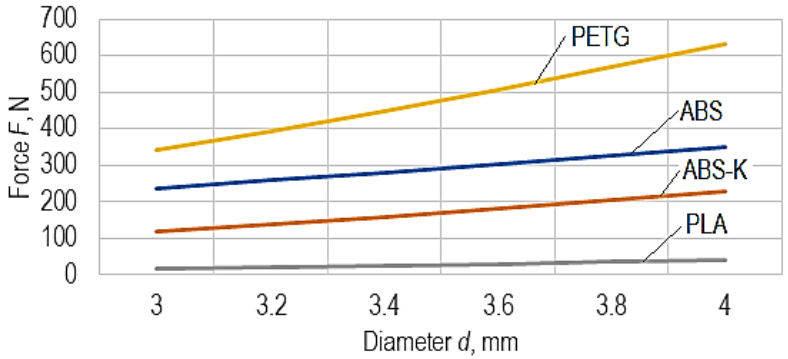

Figure 12. The influence of the diameter d on the magnitude of the maximum force F that determines the damage of a chain link made of different materials (v = 80 mm/min, t = 0.2 mm, I = 30%, θ_p = 90°, θ_e = 245°, p = 2, corresponding to manufacturing in horizontal position).

The conditions for performing the experimental tests were those mentioned in Table 2. Each experimental trial was performed only once, so the experimental trials were not repeated with the same values of the input factors in the 3D printing process. It is mentioned that the design of the experiment method (used to design the experimental trials whose experimental results were included in Table 2) was introduced and used to allow obtaining the maximum information with a minimum of trials [37–40].

The values of the force F determined by analyzing the diagrams corresponding to each chain link made of the 4 materials considered were entered in the last 4 columns of Table 2.

The experimental results were processed using a computer program based on the least squares method [41]. The computer program can select the most appropriate empirical mathematical model from among five models (first-degree polynomial, second-degree polynomial, power-type function, exponential-type function, hyperbolic-type function).

The selection is made by using Gauss's criterion value [41,42]. This value of Gauss's criterion is determined by taking into account, first of all, the sum of the squares of the differences between the values of the ordinates corresponding to the use of the proposed mathematical model and, respectively, the values of the ordinates related to the experimental results, for the same values of the abscissas. The sum of the squares of the mentioned differences is related to the difference between the number of experimental trials and the number of constants in the dependence relationship [41,42]. A lower value of Gauss's criterion characterizes a better approximation of the experimental results to those calculated using a certain empirical mathematical model.

Among the 5 empirical mathematical models that can be determined using the mentioned computer program, the power-type function was preferred, given its use for the characterization of other processes or sizes specific to machine manufacturing (for example, for determining the tool life, cutting force components, and roughness parameters of the machined surfaces). It is necessary to note that power-type functions are preferred when it is considered that there is a monotonous variation in the pursued output parameter to the variation in the input factors in the investigated process. It will be assumed, as such, that in the situations presented in this paper and for the variation intervals considered, the seven input factors do not determine the occurrence of maxima or minima of the value of the force F, and they lead to a monotonous variation in the output parameter. The selection of a factorial experiment of type L8-2^7 to arrive at empirical mathematical models that highlight the influence of different factors on the force F was carried out, taking into account the simplification of the calculations necessary to identify empirical mathematical models [43–46].

A monotonic variation, at least for certain ranges of variation in the values of the input factors in the 3D printing process, was highlighted by the experimental results obtained by other researchers. Thus, Vanaei et al. considered that changes in the crystallization mode could explain the variation in ultimate strength of the liquefier temperature and,

therefore, the material's microstructure in the sample [47]. For a temperature variation between 200 and 220 °C, they found an increase in ultimate strength in the case of samples made of polylactic acid. Similar explanations were formulated by Vanaei et al. regarding the influence exerted on ultimate strength by print speed, support temperature, and layer height. The influence of different input factors in the 3D printing process on ultimate strength was investigated by Jackson et al. [48]. They thus considered that increasing the ultimate strength by modifying the deposition angle could be connected with the retraction speed. The 3D printed parts with higher retraction speed presented higher values of the ultimate strength, which means a monotonous variation in the ultimate strength when the retraction speed is increased. Meram and Sözen appreciated that lower layer thickness values lead to higher ultimate strength values, ensuring better adhesion between layers [49]. This means that the two researchers thought there was a monotonous variation in the ultimate strength when changing the value of the thickness of the deposited material layer. A contrary result was obtained by Cho et al., which shows that the higher the thickness of the deposited layer, the higher the mechanical strength of the deposited material [50]. They, therefore, accept a monotonous variation in the mechanical resistance of the material of the specimen made by 3D printing by the thickness of the deposited layer. Müller et al. observed a monotonic variation (an increase) in tensile strength when the infill density increases [51].

An advantage of using empirical mathematical power-type function models is that such models provide direct information on the intensity of influence exerted by an input factor by comparing the value of the exponent attached to that factor in the mathematical power-type function with the values of other exponents. At the same time, a positive value of the exponent in question means that for the range of variation investigated, an increase in the size of the input factor will lead to an increase in the value of the output parameter. In contrast, a negative value of the exponent will cause a decreasing the size of the output parameter.

The mathematical relationships corresponding to the force F and the values of Gauss's coefficients are mentioned next.

Thus, in the case of ABS material, the mathematical relationship was determined: the value of Gauss' criterion being $S_G = 0.115262$.

$$F = 9.436 \cdot 10^{-16} d^{1.366} v^{0.0622} t^{0.288}{}_{\mathrm{i}}{}^{-0.322} \theta_p{}^{0.471} \theta_e{}^{6.588} p^{2.144} \quad (1)$$

The empirical mathematical model determined for the ABS-K material has the form:

$$F = 5.166 \cdot 10^{-8} d^{2.276} v^{-0.543} t^{-0.571} i^{0.349} \theta_p{}^{0.692} \theta_e{}^{2.795} p^{1.208} \quad (2)$$

in this case, Gauss's criterion being $S_G = 8.626843 \cdot 10^{-3}$.

For the PLA material, the following form of the empirical mathematical model was arrived at:

$$F = 3.973 \cdot 10^{-32} d^{2.656} v^{2.424} \mathrm{t}^{2.791} i^{1.259} \theta_p{}^{5.856} \theta_e{}^{6.209} p^{1.993} \quad (3)$$

the Gauss criterion having, in this case, the value $S_G = 0.28817645$.

For the PETG material, the empirical mathematical model is of the form:

$$F = 1.158 \cdot 10^{-16} d^{2.137} v^{0.106} t^{-1.118} i^{-0.118} \theta_p{}^{-1.787} \theta_e{}^{8.017} p^{3.071} \quad (4)$$

the Gauss criterion having, in this case, the value $S_G = 0.2780781$.

3. Discussion

The graphical representations in Figures 12 and 13 were developed using empirical mathematical models.

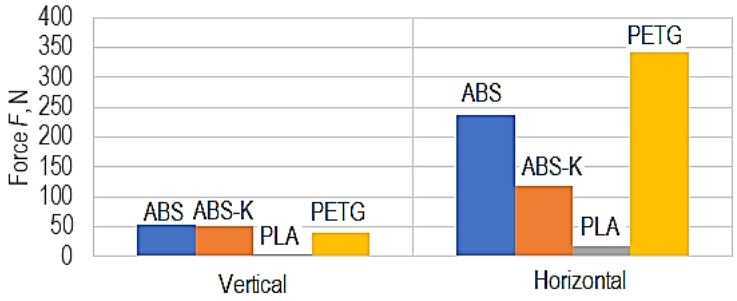

Figure 13. Differences between the maximum force values for the four polymeric materials considered in the case of manufacture in vertical and horizontal positions, respectively (d = 3 mm, v = 80 mm/min, t = 0.2 mm, i = 30%, θ_p = 90 °C, θ_e = 245 °C).

The analysis of the experimental results, the empirical mathematical models, and the graphic representations elaborated on their basis allowed the formulation of the observations mentioned below.

Examining the empirical mathematical models (Equations (1)–(4)) reveals maintenance of the same direction of force magnitude variation only when considering the corresponding diameter d of a cross-section through the chain link and, respectively, the position in which the chain link was manufactured by 3D printing on the printer table.

As expected, an increase in the diameter d of the cross-section through the chain link increases the maximum force F (Figure 11). Still, following the initial hypothesis, manufacturing the chain link in a horizontal position leads to a higher strength of the chain link and a higher value of the maximum force F. This fact can be explained by the better behavior of the applied material layers to the stretching stress right along the main stress direction on the chain link during the tensile test. The continuity of the layers formed by the gradual deposition of the wire of melted polymeric material leads to an increase in the tensile strength of the polymer material.

Less expected results were obtained in the case of chain links made of ABS material with Kevlar when a decrease in the mechanical resistance of the chain links reinforced with one of the most resistant plastic materials (Kevlar) was observed. The analysis of the appearance of the broken test samples as a result of tensile stress reveals a certain separation of the ABS polymer from the Kevlar fibers due to a reduced adhesion between the two materials. Since the Kevlar fibers are not continuous, it is possible that the low adhesion between the materials incorporated in the chain link and the discontinuity of the Kevlar fiber led to the decrease in the mechanical strength of the ABS-K material chain links, compared to the mechanical strength of the chain links made of ABS material only. It was also observed that under the conditions considered for the 3D printing process, the ABS-K type material became brittle, which led to the destruction of the tensile chain link at the appearance of the first cracks. The lower mechanical strength of the chain links made from PLA may be due to the 3D printing conditions. The results of the experimental research showed that the highest mechanical resistance was obtained in the case of the links made of polyethylene terephthalate glycol (PETG). According to the experimental results, when tested under identical experimental conditions (experiment no. 1 in Table 2), PETG links can break for a force value of 40.9 N. In comparison, polylactic acid links will break for a force value of 4.70 N. Links printed in the horizontal position were almost 9-fold stronger than those printed in the vertical position. Under the same test conditions (d = 3 mm, v = 80 mm/s, t = 0.2 mm, I = 30%, θ_p = 90 °C, θ_e = 245 °C, according to the determined empirical mathematical models, PETG links printed in a horizontal position will break for a force of 300.8 N, while links printed in a vertical position will break for force values of 35.8 N.

The chemical compositions of the four polymer materials from which the chain links were fabricated by 3D printing were different. They involved using different input factor values in the 3D printing process. To compare the results obtained in the case of using

these different polymer materials, the chain links need to be printed under the conditions of using the same values of the input factors in the 3D printing process. In this way, it was possible that the used values of some of the input factors in the 3D printing process were not the most suitable for making links with high tensile strength. This aspect could be, for example, a cause of the relatively low value of the tensile strength determined in the case of gels made of polylactic acid. These printing conditions were the same for all the polymer materials from which the plates were made, being established in such a way that, as far as possible, they corresponded, to a greater or lesser extent, to the valid recommendations for the manufacture of parts from the respective polymer materials.

According to the determined empirical mathematical models, except for one material (PETG), the values of the maximum force F increase with the increase in the temperature θ_p of the plate on which the chain links were generated. A possible explanation of this situation could be based on a better adhesion of successively deposited material layers when the plate temperature θ_p increases.

It is also found that, except for the ABS-K material, increasing the velocity v leads to an increase in the maximum force F. It is possible that with increasing the velocity v, more favorable heat transfer conditions specific to the cooling of the specimen material are reached and, under these conditions, to achieve better adhesion of successively deposited layers of material, so at a higher value of the magnitude of the maximum force F.

According to the determined empirical mathematical models, a high influence on the magnitude of the maximum force F is exerted by the extrusion temperature θ_e. In all empirical mathematical models, it was found that the exponents attached to the temperature in the extrusion nozzle have large and positive values. This means an increase in the extrusion temperature θ_e will significantly increase the magnitude of the maximum force F. The findings can be explained by the fact that when the extrusion temperature θ_e is increased, there is an increase in the fluidity of the material to be deposited and, as such, a better connection between layers of material added successively.

A validation test of the determined empirical mathematical models was possible by conducting experimental tests for other combinations of the values of some input factors in the 3D printing process. Some such results led to maximum force values close to values determined using empirical mathematical models.

Some of the results determined in the manner previously described were as follows:

- For an ABS chain link, where the variables took the values d = 4 mm, v = 80 mm/s, t = 0.2 mm, i = 60%, θ_p = 90 °C, θ_e = 265°, p = 2 (printing in horizontal position), the maximum force F values were 460.84 N for the experimental test and 469 N when the empirical mathematical model was used. The difference between the two values is 1.9%.
- For a chain link made of ABS-K, where the variables took the values d = 4 mm, v = 80 mm/s, t = 0.2 mm, i = 30%, θ_p = 90 °C, θ_e = 245°, p = 2 (printing in horizontal position), the values of the maximum force F were 192.66 N for the experimental test and 284.21 N when the empirical mathematical model was used. The difference between the two values is 32.2%.
- For a chain link made of PETG, where the variables took the values d = 4 mm, v = 80 mm/s, t = 0.2 mm, i = 30%, θ_p = 90 °C, θ_e = 245°, p = 2 (printing in horizontal position), the maximum force F values were 564.53 N for the experimental test and 556.36 N when the empirical mathematical model was used. The difference between the two values is 1.46%.

Even larger differences were found for other sets of input factor values in the case of additional experimental tests performed. These differences could be explained by a rather large dispersion of the experimental results due, for example, to the variation and other input factors in the 3D printing process and whose values were not followed during the experimental trials. Large differences between the experimental results and those obtained using the empirical mathematical model were also observed in the case of chain links made

of PLA. Such differences could also be generated by the fact that the values of some of the input factors in the 3D printing process were not suitable for the PLA material.

The highest value of the maximum force F was recorded in the case of the chain link made of PETG material. It should be noted that the value of the maximum force F is almost 7-fold higher when the chain link is made in a horizontal position compared to that made in a vertical position. A possible explanation for this was mentioned earlier. PETG polymer material also has the highest tensile strength, as seen in Table 1.

4. Conclusions

The problem of replacing parts made of metallic materials with parts made of plastic materials manufactured by 3D printing can also be formulated in the case of chain links. For reduced mechanical stress, link chains made of polymeric materials have a lower weight and better corrosion resistance than chains made of metallic materials. It should be noted that such chains made of polymer materials could be manufactured directly by 3D printing without assembling separately manufactured chain links. The consultation of specialized literature highlighted research concerns in such a direction. The research presented in this article aimed to highlight the influence exerted by some input factors in the 3D printing process of chain links from four different materials on the tensile behavior of the respective chain links. The four materials from which the chain links were made were acrylonitrile butadiene styrene (ABS), the composite material acrylonitrile butadiene styrene-Kevlar (ABS-K), polylactic acid (PLA) and polyethylene terephthalate glycol (PETG). The experimental tests were conducted according to the requirements of a fractional factorial experiment with seven input factors at two levels of variation. The chain link diameter in a cross-section, printing speed, layer thickness, infill density, the temperature of the printer table, extrusion temperature, and test sample placement during 3D printing were considered input factors. Through the mathematical processing of the experimental results, empirical mathematical power-type function models were determined. These empirical mathematical models provide information on the direction of variation and the intensity of the influence exerted by the input factors considered on the maximum force at which damage to the chain links occurs. The analysis of the experimental results highlighted the fact that the same directions of action of the input factors were recorded only in the case of the diameter of the chain link rod and the way of positioning the sample during printing. As expected, printing the chain link horizontally ensured superior mechanical strength due to the stress development along the deposited layers, thus characterized by a certain continuity. The results of the experimental research showed that chain links printed in a horizontal position are almost 9-fold stronger than chain links printed in a vertical position. Under the same test conditions, according to the determined empirical mathematical models, PETG links printed horizontally will break for a force of 300.8 N. In comparison, links printed in a vertical position will break for force values of 35.8 N. Polyethylene terephthalate glycol (PETG) links have proven the highest mechanical resistance among the materials used. Under the same test conditions, the PETG links broke for a force of 40.6 N, while the polylactic acid rings broke for values of 4.70 N. In the future, it is intended to continue the research by considering other materials for the chain links and identifying more appropriate mathematical and empirical models to illustrate the tensile behavior of some plastic materials incorporated in the chain links. Another research direction could be to directly manufacture complete chains with polymer links assembled by the 3D printing process itself, eliminating the need for an additional operation of assembling separately manufactured links.

Author Contributions: Conceptualization, B.R. and L.S.; methodology, L.S.; software, A.M.M.; validation, E.P. and A.H.; formal analysis, A.H.; investigation, E.P. and V.E.; resources, B.R.; data curation, A.H.; writing—original draft preparation, L.S.; writing—review and editing, A.H.; visualization, A.H., M.C.R.; supervision, L.S.; project administration, B.R.; funding acquisition, B.R. All authors have read and agreed to the published version of the manuscript.

Funding: This research received no external funding.

Institutional Review Board Statement: Not applicable.

Data Availability Statement: The data presented in this study are available on request from the corresponding author. The data are not publicly available due to privacy.

Conflicts of Interest: The authors declare no conflict of interest.

References

1. Fafenrot, S.; Grimmelsmann, N.; Wortmann, M.; Ehrmann, A. Three-dimensional (3D) printing of polymer-metal hybrid materials by fused deposition modeling. *Materials* **2017**, *10*, 1199. [CrossRef]
2. Abdalla, A.; Patel, B.A. 3D Printed Electrochemical Sensors. *Annu. Rev. Anal. Chem.* **2021**, *14*, 47–63. [CrossRef]
3. Kalva, R.S. 3D Printing—The future of manufacturing (the next industrial revolution). *Int. J. Innov. Eng. Technol.* **2015**, *5*, 185–190.
4. Mareș, M. Additive manufacturing technologies. A concise introduction. *Bul. Institutului Politeh. Din Iaşi. Secţia Construcţii De Maşini* **2018**, *64*, 27–57.
5. Wang, L.; Alexander, C.A. Additive manufacturing and big data. *Int. J. Math. Eng. Manag. Sci.* **2016**, *1*, 107–121. [CrossRef]
6. Veness, R.; Andreazza, W.; Gudkov, D.; Miarnau Marin, A.; Samuelsson, S. Metal 3D Additive Machining for in-Vacuum Beam Instrumentation. In Proceedings of the 10th Mechanical Engineering Design of Synchrotron Radiation Equipment and Instrumentation Conference, Paris, France, 25–29 June 2018; pp. 121–124. [CrossRef]
7. Wójcicki, M.; Wieczorek, A.N.; Głuszek, G. Concept of the facility for testing the wear of chain links in the aspect of synergism of environmental factors. *Min. Mach.* **2021**, *39*, 71–81. [CrossRef]
8. Aliakbari, M. Additive Manufacturing: State-of-the-Art, Capabilities, and Sample Applications with Cost Analysis. Master's Thesis, KTH Royal Institute of Technology, Stockholm, Sweden, 2012. Available online: https://www.diva-portal.org/smash/get/diva2:560827/FULLTEXT02.pdf (accessed on 15 May 2023).
9. Mešić, A.; Čolić, M.; Mešić, E.; Pervan, N. Stress analysis of chain links in different operating conditions. *Int. J. Eng. Sci. Invention* **2016**, *5*, 43–49.
10. Román-Manso, B.; Weeks, R.D.; Truby, R.L.; Lewis, J.A. Embedded 3D printing of architected ceramics via microwave-activated polymerization. *Adv. Mater.* **2023**, *35*, 2209270. [CrossRef]
11. Woodman, C. *3D Printing for Animal Welfare. A Report for the Animal Welfare Institute*; Texas A&M University: College Station, TX, USA, 2021; p. 17. Available online: https://awionline.org/sites/default/files/uploads/documents/3d-printing-animal-welfare.pdf (accessed on 15 May 2023).
12. Noguchi, S.; Nagasaki, K.; Nakayama, S.; Kanda, T.; Nishino, T.; Ohtani, T. Static stress analysis of link plate of roller chain using finite element method and some design proposals for weight saving. *J. Adv. Mech. Des. Syst. Manuf.* **2009**, *3*, 159–170. [CrossRef]
13. Das, N. Models to Explain out-of-Plane Bending Mechanism in Mooring Chain Links. Master's Thesis, Delft University of Technology, Delft, The Nederlands, 2016. Available online: http://resolver.tudelft.nl/uuid:f387281a-1365-4121-a2cf-3f0b59448f67 (accessed on 15 May 2023).
14. Berthelsen, K. Out of Plane Bending of Mooring Chains Finite Element. Analysis of a 7-link model. Master's Thesis, Norwegian University of Science and Technology, Trondheim, Norway, 2017. Available online: https://ntnuopen.ntnu.no/ntnu-xmlui/handle/11250/2453087 (accessed on 15 May 2023).
15. Kim, S.; Won, D.-H. Bending behavior of the mooring chain links subjected to high tensile forces. *J. Korean Soc. Steel Const.* **2017**, *29*, 99–110. [CrossRef]
16. Choung, J.; Lee, J.B.; Kim, Y.H. Out-of-plane bending stiffnesses in offshore mooring chain links based on conventional and advanced numerical simulation techniques. *J. Ocean Eng. Technol.* **2018**, *32*, 297–309. [CrossRef]
17. Chung, W.; Kang, H.; Kim, M. Multi-scale approach for chain-mooring OPB-induced failure considering time-varying interlink bending stiffness and fairlead condition. *Appl. Ocean Res.* **2020**, *98*, 102128. [CrossRef]
18. Chung, W.C.; Kim, M.H. Effects of various fairlead-connection parameters on chain-mooring OPB-induced failure. *Mar. Struct.* **2021**, *76*, 102926. [CrossRef]
19. Chung, W.C.; Kang, H.Y.; Kim, M.H. Numerical study on OPB/IPB interlink angle with underwater chain stopper system. In Proceedings of the SNAME 24th Offshore Symposium, Houston, TX, USA, 20 February 2019.
20. Perez, I.M.; Constantinescu, A.; Bastid, P.; Zhang, Y.H.; Venugopal, V. Computational fatigue assessment of mooring chains under tension loading. *Eng. Fail. Anal.* **2019**, *106*, 104043. [CrossRef]
21. Zarandi, E.P. Multiaxial Fatigue Analysis of Offshore Mooring Chains, Considering the Effects of Residual Stresses and Corrosion Pits. Ph.D. Thesis, Norwegian University of Science and Technology, Trondheim, Norway, 2020. Available online: https://www.researchgate.net/publication/348200873_Multiaxial_fatigue_analysis_of_offshore_mooring_chains_considering_the_effects_of_residual_stresses_and_corrosion_pits (accessed on 15 May 2023).
22. Zarandi, E.P.; Skallerud, B.H. Experimental and numerical study of mooring chain residual stresses and implications for fatigue life. *Int. J. Fatigue* **2020**, *135*, 105530. [CrossRef]
23. Zarandi, E.P.; Lee, T.L.; Skallerud, B.H. Data on residual stresses of mooring chains measured by neutron diffraction and hole drilling techniques. *Data Br.* **2020**, *30*, 105587. [CrossRef]

24. Xue, X.; Chen, N.-Z. Fracture mechanics analysis for a mooring system subjected to tension and out-of-plane bending. In Proceedings of the First Conference of Computational Methods in Offshore Technology (COTech2017), Stavanger, Norway, 30 November–1 December 2017; Volume 276, p. 012036. [CrossRef]
25. Xue, X.; Chen, N.-Z.; Pu, Y.; Chen, L.; Wang, L. Fracture mechanics assessment for mooring chain links tensioned over a curved surface. *Appl. Ocean Res.* **2021**, *117*, 102900. [CrossRef]
26. Takeuchi, T.; Utsunomiya, T.; Gotoh, K.; Sato, I. Development of interlink wear estimation method for mooring chain of floating structures: Validation and new approach using three-dimensional contact response. *Mar. Struct.* **2021**, *77*, 102927. [CrossRef]
27. Vanaei, H.R.; Magri, A.E.; Rastak, M.A.; Vanaei, S.; Vaudreuil, S.; Tcharkhtchi, A. Numerical-experimental analysis toward the strain rate sensitivity of 3D-printed nylon reinforced by short carbon fiber. *Materials* **2022**, *15*, 8722. [CrossRef]
28. Egli, E. Link Chain for Transmitting a Mechanical Load. U.K. Patent GB1191225A, 13 May 1970. Available online: https://patents.google.com/patent/GB1191225A/en?oq=GB1191225A (accessed on 15 May 2023).
29. Dietrich, W.; Roelof, M.; Bergsma, O.; Gruber, J.M.; Mehdi, H.; Licup, A.J.; Van Keulen, A.; Van Rijssel, J.; Yalcin, A.O.; Van Eden, G.G.; et al. Polymeric Chain Link. Canada Patent CA2984062A1, 1 December 2016. Available online: https://patents.google.com/patent/CA2984062A1/en?oq=CA2984062A1 (accessed on 15 May 2023).
30. Van Loon, M.A.Y. Chain Link Formed of Polymeric Material. European Patent EP0404224A1 (B1), 27 December 1990. Available online: https://patents.google.com/patent/EP0404224A1/en?oq=EP0404224A1 (accessed on 15 May 2023).
31. Bastid, P.; Smith, S.D. Numerical analysis of contact stresses between mooring chain links and potential consequences for fatigue damage. Paper OMAE2013-11360. In Proceedings of the 32nd International Conference on Ocean, Offshore and Arctic Engineering, Nantes, France, 9–15 June 2013. Available online: https://www.twi-global.com/technical-knowledge/published-papers/numerical-analysis-of-contact-stresses-between-mooring-chain-links-and-potential-consequences-for-fatigue-damage (accessed on 15 May 2023).
32. Hamanaka Group. Chain Manufacturing Process Outline Drawing. Available online: http://www.hamanaka-chain.co.jp/en/products/products3/ (accessed on 16 April 2023).
33. Jha, N.K.; Avinash, G.; Siddharth, V. Design and structural analysis of plastic chain link with polypropylene and polyoxymethylene material. *Mater. Today Proc.* **2021**, *38*, 3066–3076. [CrossRef]
34. Technical Data Sheet. Ultrafuse ABS. Available online: https://www.ultrafusefff.com/wp-content/uploads/2016/05/Ultrafuse_ABS_TDS_EN_v5.2.pdf (accessed on 5 June 2023).
35. Pillet, M. *Introduction Aux Plans D'expériences par la Méthode Taguchi*; Les Éditions d'Organisation: Paris, France, 1992.
36. Chauveau, J.-C.; Chassaing, J.-P. Introduction à la Methode des Plans D'expériences par la Méthode Taguchi. Available online: https://eduscol.education.fr/sti/sites/eduscol.education.fr.sti/files/ressources/techniques/3870/3870-introtaguchi-cned.pdfamanaka-chain.co.jp/en/products/products3/ (accessed on 27 May 2023).
37. Torii, D.; Nagahara, T.; Okihara, T. Suppression of the Secondary Flow in a Suction Channel of a Large Centrifugal Pump. *IOP Conf. Ser. Mater. Sci. Eng.* **2013**, *52*, 032005.
38. Donnelly, T. Efficient simulation using design of experiments (DOE). Available online: https://community.jmp.com (accessed on 27 May 2023).
39. Lakshminarayanan, A.K.; Annamalai, V.E.; Elangovan, K. Identification of optimum friction stir spot welding process parameters controlling the properties of low carbon automotive steel joints. *J. Mater. Res. Technol.* **2015**, *4*, 262–272. [CrossRef]
40. Tinsson, W. *Plans d'expérience: Constructions et analyses statistiques. Mathématiques et Applications*; Springer: Berlin/Heidelberg, Germany, 2010; Volume 67. Available online: https://link.springer.com/book/10.1007/978-3-642-11472-4 (accessed on 27 May 2023). (In French)
41. Crețu, G.; Varvara, G. *Methods of Experimental Research in Machine Manufacturing*; Publishing House Junimea: Iași, România, 1999. (In Romanian)
42. Worthing, A.G.; Geffner, J. *Processing the Experimental Data*; Technical Publishing House: Bucharest, Romania, 1959. (In Romanian)
43. Agarwal, S.; Tyagi, I.; Gupta, V.K.; Jafari, M.; Edrissi, M.; Javadian, H. Taguchi L_8 orthogonal array design method for the optimization of synthesis conditions of manganese phosphate ($Mn_3(PO_4)_2$) nanoparticles using water-in-oil microemulsion method. *J. Mol. Liq.* **2016**, *219*, 1131–1136. [CrossRef]
44. Krishnaiah, K.; Shahabudeen, P. *Applied Design of Experiments and TAGUCHI Methods*; Ghosh, A.K., Ed.; PHI Learning Pvt. Ltd.: New Delhi, India, 2012. Available online: https://eko.staff.uns.ac.id/files/2014/09/Buku-Alternatif.pdf (accessed on 27 May 2023).
45. Mohamed, H.; Lee, M.H.; Sanugi, B.; Sarahintu, M. Taguchi approach for performance evaluation of routing protocols in mobile ad hoc networks. *J. Stat. Modeling Anal.* **2010**, *1*, 10–18.
46. Limon-Romero, J.; Tlapa, D.; Baez-Lopez, Y.; Maldonado-Macias, A.; Rivera-Cadavid, L. Application of the Taguchi method to improve a medical device cutting process. *Int. J. Adv. Manuf. Technol.* **2016**, *87*, 3569–3577. [CrossRef]
47. Vanaei, H.; Shirinbayan, M.; Deligant, M.; Raissi, K.; Fitoussi, J.; Khelladi, S.; Tcharkhtchi, A. Influence of process parameters on thermal andmechanical properties of polylactic acid fabricated by fused filament fabrication. *Polym. Eng. Sci.* **2020**, *60*, 1822–1831.
48. Jackson, B.; Fouladi, K.; Eslami, B. Multi-parameter optimization of 3D printing condition for enhanced quality and strength. *Polymers* **2022**, *14*, 1586. [CrossRef]
49. Meram, A.; Sözen, B. Investigation on the manufacturing variants influential on the strength of 3D printed products. *Res. Eng. Struct. Mater.* **2020**, *6*, 293–313. [CrossRef]

50. Cho, E.E.; Hein, H.H.; Lynn, Z.; Hla, S.; Saw, J.; Tran, T. Investigation on influence of infill pattern and layer thickness on mechanical strength of PLA material in 3D printing technology. *J. Eng. Sci. Res.* **2019**, *3*, 27–37. [CrossRef]
51. Müller, M.; Jirků, P.; Šleger, V.; Mishra, R.K.; Hromasová, M.; Novotný, J. Effect of infill density in FDM 3D printing on low-cycle stress of bamboo-filled PLA-based material. *Polymers* **2022**, *14*, 4930. [CrossRef]

A.2.1.47_polymers-16-00005

polymers

MDPI

Article

Propagation of Sounds through Small Panels Made of Polymer Materials by 3D Printing

Adelina Hrițuc [1,*], Andrei Marius Mihalache [1], Oana Dodun [1], Gheorghe Nagîț [1], Irina Beșliu-Băncescu [2], Bruno Rădulescu [3] and Laurențiu Slătineanu [1]

[1] Department of Machine Manufacturing Technology, "Gheorghe Asachi" Technical University of Iași, 700050 Iasi, Romania; andrei.mihalache@tuiasi.ro (A.M.M.); oanad@tcm.tuiasi.ro (O.D.); nagit@tcm.tuiasi.ro (G.N.); slati@tcm.tuiasi.ro (L.S.)

[2] Faculty of Mechanical Engineering, Automotive, and Robotics, "Stefan cel Mare" University, 720229 Suceava, Romania; irina.besliu@usm.ro

[3] Department of Machine Tools, "Gheorghe Asachi" Technical University of Iași, 700050 Iasi, Romania; bruno.radulescu@academic.tuiasi.ro

* Correspondence: adelina.hrituc@student.tuiasi.ro; Tel.: +40-751640117

Abstract: To evaluate the sound insulation capacity of small panels made of polymeric materials by 3D printing, a Taguchi L18-type factorial experiment with eight independent variables was designed and materialized. The independent variables were the panel thickness, polymer material type, 3D printing speed, infill percent, infill pattern, layer thickness, frequency, and sound volume. Empirical mathematical models were determined through the mathematical processing of the experimental results using specialized software. These empirical mathematical models highlight the meaning and intensity of the influence exerted by the input factors in the process on the acoustic pressure level of the energy absorbed after the passage of sounds through the small panels manufactured by 3D printing from polylactic acid and polyethylene terephthalate glycol. The factor with the strongest influence was the frequency of the sounds, with a maximum of the sound pressure level for a frequency of 13,000 Hz. A polylactic acid panel between the sound source and the sound-receiving sensor reduces the sound pressure level by about 45% from 95.8 to 65.8 dB. The power function type mathematical model in the case of the energy absorbed by the panel highlights the fact that the highest values of the exponents are those attached to the sound frequency (exponent equal to 1.616) and, respectively, to the thickness of the panel (exponent equal to −0.121).

Keywords: sound propagation; polymeric material; small panel; factorial experiment; influencing factors; empirical mathematical model

Citation: Hrițuc, A.; Mihalache, A.M.; Dodun, O.; Nagîț, G.; Beșliu-Băncescu, I.; Rădulescu, B.; Slătineanu, L. Propagation of Sounds through Small Panels Made of Polymer Materials by 3D Printing. *Polymers* **2024**, *16*, 5. https://doi.org/10.3390/polym16010005

Academic Editor: Francesco Mollica

Received: 6 November 2023
Revised: 11 December 2023
Accepted: 12 December 2023
Published: 19 December 2023

1. Introduction

Sounds are vibrations that travel through an elastic medium and can be sensed by the human ear. This means that the vibrations corresponding to the sounds must have a certain intensity and, respectively, a certain frequency that makes it possible to sense them via a membrane in the human ear. Intensity and frequency are two essential characteristics of sounds, to which, from a musical point of view, duration and timbre are added. Unlike vibrations co-responsive to sounds, noises are vibrations less desired or agreed upon by human beings.

In general, sounds have a frequency between 16 Hz and 20 kHz, but it is also possible for some people to perceive frequencies slightly lower than 16 Hz, just as other people can perceive sounds with frequencies slightly higher than 20 kHz. With age, the ability of the human ear to detect sounds characterized by high frequencies decreases.

Using sounds, people can communicate. They can detect the proximity of vehicles, the presence of other beings, or natural or artificial systems capable of generating or reflecting sounds.

It is normal for sounds to be absorbed by different media, as there may be situations where sounds are amplified.

It is known that sounds propagate at speeds that differ from the constitution of the environment they travel through. Thus, the sound propagation speed can have distinct values in different environments. If sounds propagate in the air with speeds of 330–350 m/s, in water, the sound propagation speed can be 1–4 m/s, while in a steel piece, the sound speed can have values of 5100 to 5900 m/s. In parts made of solid materials, sounds propagate through successive elongations and contractions of some areas of the part (Figure 1).

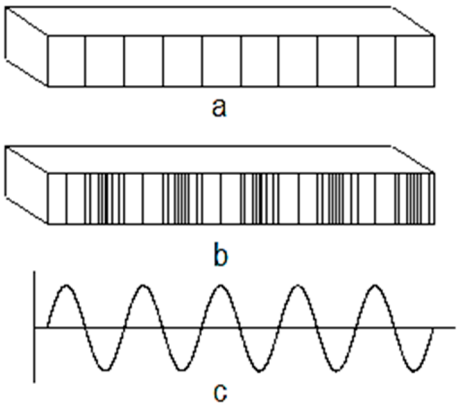

Figure 1. Propagation of sounds through a bar with a square section of solid material, highlighted by the time displacement of some elongations and contractions: (**a**) bar unaffected by sound propagation; (**b**) bar through which elongations and contractions corresponding to the sound are propagated; (**c**) time variation of elongations and contractions.

The situation in which the absorption of sound energy by the environment is necessary occurs mainly when the problem of so-called sound insulation is raised, when technical measures are taken that are mainly aimed at reducing the intensity of sounds. In such a case, the problem of identifying and determining the characteristics of materials with sound insulation properties arises.

The emergence of 3D printing processes has led, among other things, to the need to evaluate the ability of materials from 3D printed parts to be used as insulating materials from a sound point of view, and such a problem has been addressed by researchers in the field of manufacturing parts from polymeric materials by 3D printing.

Thus, Alfarisi et al. (2021) investigated the problem of improving the quality of sounds in the case of a music box for which some components were made by 3D printing [1]. They used the finite element method to identify possibilities for improving the materials' ability to transmit sounds.

King et al. have addressed the problem of studying the ability of some panels made by 3D printing to absorb noise using a sound impedance tube [2]. They found that a model characterized by a micro-perforated design can absorb noises characterized by a frequency between 100 and 6400 Hz.

Vasina et al. studied the sound absorption properties of open-porous acrylonitrile butadiene styrene structures manufactured by 3D printing technologies [3]. One of their conclusions was that the sound absorption properties of the samples made from the investigated material could be significantly influenced by the type of 3D printing process, the structure of the material, the frequency of excitation, the thickness of the sample, and the size of the interstice in the back of the absorbent material panel.

Hrițuc et al. proposed using equipment to study sound propagation through small panels manufactured by 3D printing [4,5]. They researched the influence of different factors on the sound pressure level after passing sounds through such panels.

The experimental research carried out has shown that the main factors or groups of factors able to influence the sound propagation capacity of some materials incorporated in parts manufactured by 3D printing are the following:

- The nature of the sample material [3,6–8];
- The proportion of different materials in the sample [6];
- The structure corresponding to the arrangement of the material in parts [2,3,9–20];
- Imperfections in the sample material [14,17];
- The size of the so-called "throat effect" (the throat is the smallest aperture in a series of interconnected pores) [9,10,21];
- Test sample manufacturing technology [7,14,17];
- The shape of the cavity in which the testing is performed [22];
- The frequency of sounds that pass through parts manufactured by 3D printing [3,5,6,8, 9,12,14,15,20,22];
- The acoustic pressure level [5];
- The distance from the test sample to the sound receiver [3,12,15];
- Sample thickness [3,5,13,15,23];
- The parameters corresponding to the 3D printing process [5,7], etc.

Sounds are generated by operating various categories of equipment, by a loudspeaker or by the voice boxes of humans or other animals, by the rubbing of wings by some insects, etc. For example, the operation of a crank-rod mechanism, an internal combustion engine, an electric motor, a percussive hammer, etc., is accompanied by the generation of vibrations that, if they have a certain intensity and a frequency within certain limits, can be perceived by the ear of the human being. If sounds can be produced by moving or striking parts in the case of some mechanical equipment, there are also structural transformations of certain metallic materials associated with generating sounds.

Objectives deriving from communication or entertainment equipment led to the appearance of audio speakers. Such loudspeakers convert electrical energy into mechanical energy that manifests in vibrations with characteristics corresponding to the sound field. Such loudspeakers have a fixed magnet near a coil through which an electric current flows, characterized by a variation in the intensity of the electric current in the audio frequency range. The electromagnet is solidarized with a flexible cone that is intended to amplify and direct the sounds. The interaction between the fields generated by the fixed magnet and the movable electromagnet drives the flexible material cone into motion, thus producing sounds.

As a rule, the passage of sounds through test samples made of different materials is studied using the so-called sound impedance tubes [18,24]. Indications regarding the measurement of sound absorption level when passing through different media have been included in two main standards regarding this field of research [25,26].

The equipment used to determine the sound absorption coefficient requires small samples in the form of discs inserted into the tube through which the sounds reflected by the walls of the cylindrical glass enclosure will also pass. A variant of the tube impedance is used in the two-microphone impedance method [12]. Maroo and Wright appreciated that the common impedance tube could not be used to determine sound transmission loss in the case of samples manufactured by 3D printing, especially in the case of high frequencies. For this reason, a small reverberation room was used [19]. Shtrepi and Prato showed that the currently used methods for studying the absorption of sounds by different materials have some disadvantages. For example, the impedance tube is less suitable for 3D systems, and a real reverberation chamber requires test pieces of large dimensions [27]. The research results completed through a doctoral thesis on designing a new reverberation chamber usable for characterizing sound transmission loss in the case of multi-material samples manufactured by 3D printing were published in 2021 by Maroo [28]. A reverberation chamber has been used by Peng et al. for the research of sound transmission loss in the case of some aircraft composite panels of large dimensions, which were not manufactured by 3D printing [29].

The content of this article is intended to highlight the behavior of small panels made of two polymeric materials by 3D printing when such panels are used as sound insulating materials. A finite element modeling was used to theoretically investigate the process of sound propagation through polymer panels. Later, using the results of some experimental research, empirical mathematical models were determined, and such models highlight the influence exerted by different factors on the acoustic pressure level of the sounds that passed through small panels made of 3D-printed polymer materials.

2. Materials and Methods

2.1. Propagation of Sounds through Panels Made of Polymeric Materials

In the research framework, the results of which are presented in this paper, an audio mini speaker was used to generate sounds with variable frequencies and amplitudes (Figure 2). This audio mini speaker is model Bass, from Andowl, China, being a mini portable wireless speaker. The sounds generated by the audio mini speaker pass through a small panel made of polymer material. The polymer material panel was manufactured by 3D printing. Later, the sounds reach the sensor of a sound level meter, which will provide information about the characteristics of the sounds that have passed through the polymer material panel. The sound level meter is a digital instrument from Ckinnfon, model HY1361, Mainland, China. The three main components (the audio mini speaker, the polymer material panel, and the sound level meter) were placed in enclosures lined on the inside with a material capable of absorbing the energy of sound vibrations.

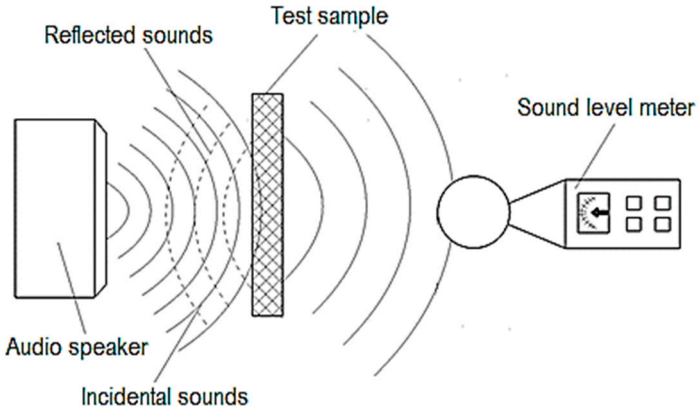

Figure 2. Evaluation of the characteristics of sounds after passing through a panel of polymeric material manufactured by 3D printing.

In principle, the velocity v_g of sound in gases is considered to correspond to a shape relation:

$$v_g = \sqrt{\frac{K}{\rho}}, \quad (1)$$

where K is the bulk modulus and ρ is the gas density.

In the case of solid materials, the sound propagation speed can be evaluated using a shape relationship:

$$v_s = \sqrt{\frac{E}{\rho}}, \quad (2)$$

where E is the Young's modulus and ρ is the density of the solid material.

In the case of macroporous polymers, the presence of the compressible air-filled pores contributes to a reduction of the longitudinal sound speed v_l, reaching [30] values consistent with the equation:

$$v_l = \sqrt{\frac{M}{\rho}}, \quad (3)$$

where M is the longitudinal modulus, and ρ is the mass density of the porous material.

The speed of sounds in a body made of polymeric material can have different values, for example, from 1950 m/s in the case of polyethylene of low density to 2270 m/s in the case of polycarbonate and 2430 m/s in the case of polyethylene of high density.

Equations (1)–(3) highlight the fact that elements characterizing the nature and properties of the medium through which the sound waves propagate are capable of exerting an important influence on the energy carried by these waves and that measuring the sound energy can provide information on the capacity of different media to absorb, to a greater or lesser extent, the energy of the sound waves.

2.2. Experimental Conditions

The experimental research aimed to highlight the influence exerted by some factors on the reduction of the sound intensity level after passing the sounds through some small panels made of polymer materials by 3D printing.

In the case of the present research, we resorted to using equipment made up of several distinct compartments (Figure 2). It can be seen that there is a compartment in which the audio mini speaker was fixed. A second compartment allowed for the locating and clamping of the polymer sample through which the sound waves pass. Another compartment was where the sensor of a sound level meter was located. An intermediate compartment was provided to include the development of some experimental research on the influence of the distance between the audio mini speaker and the sensor of the sound level meter. The four compartments are made of wooden boards and assembled using wooden pins. To reduce the risk of the wooden walls of the premises influencing the intensity of sounds received by the sound level meter sensor, the interior surfaces of the compartments with wooden walls were covered with a porous polymeric material characterized by a high capacity of sound absorption.

An audio mini speaker type Andowl M10 was used (Figures 3 and 4). The application use for phone control (using Bluetooth) of the mini audio speaker was the Frequency Generator built by LuxdeLux, being an online resource, specifically, an Android app, available on Play Store from Google.

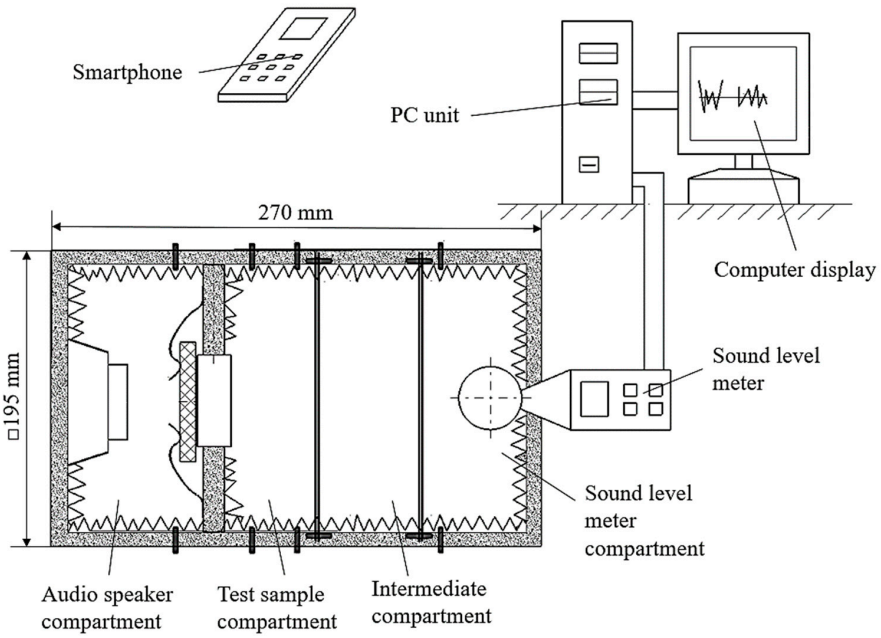

Figure 3. Schematic representation of the equipment used to highlight the intensity of the influence exerted by different factors on the sound pressure level after passing sounds through a panel of polymeric material manufactured by 3D printing.

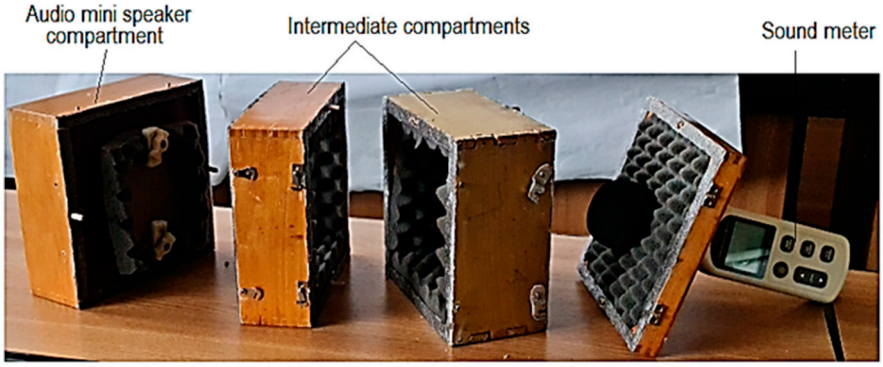

Figure 4. The appearance of some equipment components used to highlight the intensity of the influence exerted by different factors on the acoustic pressure level after the passage of sound waves through a panel of polymeric material manufactured by 3D printing.

The intensity of the influence exerted by different factors on an output parameter corresponding to the process of passing sounds through a small panel manufactured by 3D printing is dependent on the nature of the panel material, the thickness of its wall, some characteristics of the materials embedded in the panel that depends on the 3D printing conditions, the level of acoustic pressure and the frequency of the sound generated by a certain voltage source, etc.

Polylactic acid (PLA, produced by Filamentum, Fillamentum Manufacturing Czech s.r.o., Nám. Míru 1217, 768 24 Hulín, Czech Republic), high-impact polystyrene (HIPS, produced by Formfutura as EasyFil HIPS, Tarweweg 3, 6534 AM Nijmegen. The Netherlands), and polyethylene terephthalate glycol (PETG, produced by PrimaSelect as PrimaSelect™ PETG, PrimaCreator, Kantyxegatan 25 F, 213 76 Malmö, Sweden) were used as materials for the small panels. Some properties of the three materials are presented in Table 1. The three polymeric materials were chosen to be easily accessible and present different physical–mechanical properties. It was assumed that such materials would also have different sound insulation properties.

Table 1. Initial properties of materials used for the 3D printing of small panels.

Material	Properties		
	Density, ρ, kg/m^3	Tensile Strength, *Rm*, MPa	Printing Temperature, °C
Polylactic acid (PLA)	1250	32.9	180–220
High-impact polystyrene (HIPS)	1040	42	220–240
Polyethylene terephthalate glycol (PETG)	1230	31.9	220–260

During the experimental tests, we noted some characteristics of the small panels (thickness and type of material), some parameters specific to the 3D printing process (being selected, in the present case, printing speed v_p, infill percent i, infill pattern i_p, and the thickness of the deposited layer t), and also some characteristics of the sounds generated by the audio mini speaker (frequency f and sound volume s).

The design of the experimental tests was carried out by considering an L18-type Taguchi factorial experiment, with seven input factors having three-level variance values and one input factor with two-level variation values. For the selection of the input factor with a two-level variation, it was assumed that an increase in the thickness t of the small panel would lead to a monotonous decrease (hence, one without maxima or minima) of the sound intensity, which would make it more appropriate to use only two levels of variation for the input factor (independent variable) mentioned.

Thus, the thickness t of the small panels (t_1 = 1 mm and t_2 = 5 mm) was selected as an input factor with values on two levels. The small panels had a surface with an area of 100 × 100 mm^2. An Ultimaker 3 printer (Eindhoven, The Netherlands) was used for the 3D printing of panels from different polymer materials.

In the case of factors with values on three levels of variation, the nature of the material from the small panel (three distinct materials, these being the polylactic acid, which was assigned the value of m_{PLA} = 1; high impact polystyrene HIPS, which was taken into account considering m_{HIPS} = 2; and, respectively, polyethylene terephthalate glycol PETG, for which a symbol with the value m_{PETG} = 3 was used), along with 3D printing speed (v_{p1} = 20 mm/s, v_{p2} = 40 mm/s, v_{p3} = 60 m/s), infill percentage i (i_1 = 18%, i_2 = 48%, i_3 = 78%), infill pattern (i_{p1} for grid, i_{p2} for cubic, i_{p3} for gyroid), the thickness of the deposited layer (t_1 = 0.05 mm, t_2 = 0.1 mm, t_3 = 0.15 mm), sound frequency (f_1 = 5000 Hz, f_2 = 10,000 Hz, f_3 = 15,000 Hz), and sound volume s, expressed as a percentage of the maximum sound volume generated by the micro audio speaker used (s_1 = 30%, s_2 = 50%, s_3 = 100%), were accounted for.

As output parameters from the analyzed process, the sound pressure level or sound pressure (this being a measure of the sound energy emitted by a sound source) was used. The unit of measure for evaluating the sound pressure level is the decibel, and it is the decimal logarithm of the ratio between the measured sound pressure and the reference sound pressure p_o = 2 × 10^{-5} Pa (the pressure that can be sensed by the human being, corresponding to a frequency of 1 kHz).

It is relatively common to measure acoustic pressure with the help of sound level meters.

The present research measured the acoustic pressure level using a sound level meter that can be connected to a computer. The use of specialized software allows us to highlight on the computer screen the evolution over time of the acoustic pressure level of the sound received under different conditions.

The values of the input factors (of the independent variables) were included in Table 2. For each input factor in the investigated process, the coded value according to the Taguchi methodology for an L18-type factorial experiment and the actual value of that factor were included. Also, control samples have been 3D printed considering the infill percentage parameter; it has been 6% and 96%, with the default type of infill assigned per percentage value. Each group of materials received two control samples. The results were consistent with the ones presented for the 18 samples.

Table 2. Values of input factors considered and experimental results.

Exp. No.	Input Factors																A-Coustic Pressure Level without Panel, I_0, dB	A-Coustic Pressure Level When Using Polymer Panel, I_p, dB	Difference in A-Coustic Pressure Level, Δp_{ac}, dB
	Panel Thickness, t		Material Type, m		Printing Speed, v		Infill Percent, i		Infill Pattern, i_p		Layer Thickness, l		Sound Frequency, f		Sound Volume, s				
	Coded Value	Real Value, mm	Coded Value	Real Value	Coded Value	Real Value, mm/s	Coded Value	Real Value, %	Coded Value	Real Value	Coded Value	Real Value, mm	Coded Value	Real Value, Hz	Coded Value	Real Value, %			
Column No. 1	2	3	4	5	6	7	8	9	10	11	12	13	14	15	16	17	18	19	20
R1	1	1	1	PLA	1	20	1	18	1	Grid	1	0.06	1	5000	1	30	77.7	72.8	4.9
R2	1	1	1	PLA	2	40	2	48	2	Cubic	2	0.1	2	10,000	2	50	95.8	65.8	30
R3	1	1	1	PLA	3	60	3	78	3	Gyroid	3	0.15	3	15,000	3	100	103.6	74.6	29
R4	1	1	2	HIPS	1	20	1	18	2	Cubic	2	0.1	3	15,000	3	100	103.6	75.7	28.4
R5	1	1	2	HIPS	2	40	2	48	3	Gyroid	3	0.15	1	5000	1	30	77.7	73.0	4.7
R6	1	1	2	HIPS	3	60	3	78	1	Grid	1	0.06	2	10,000	2	50	95.8	67.7	28.1
R7	1	1	3	PETG	1	20	2	48	1	Grid	3	0.15	2	10,000	3	100	115.5	88.9	26.6
R8	1	1	3	PETG	2	40	3	78	2	Cubic	1	0.06	3	15,000	1	30	58.5	38.6	19.9
R9	1	1	3	PETG	3	60	1	18	3	Gyroid	2	0.1	1	5000	2	50	95.9	91.8	4.1
R10	2	5	1	PLA	1	20	3	78	3	Gyroid	2	0.1	2	10,000	1	30	77.7	61.5	16.2
R11	2	5	1	PLA	2	40	1	18	1	Grid	3	0.15	3	15,000	2	50	78.1	52.1	26
R12	2	5	1	PLA	3	60	2	48	2	Cubic	1	0.06	1	5000	3	100	114.5	110.5	4
R13	2	5	2	HIPS	1	20	2	48	3	Gyroid	1	0.06	3	15,000	2	50	78.1	51.8	26.3
R14	2	5	2	HIPS	2	40	3	78	1	Grid	2	0.1	1	5000	3	100	114.5	110.2	4.3
R15	2	5	2	HIPS	3	60	1	18	2	Cubic	3	0.15	2	10,000	1	30	77.7	58.7	19
R16	2	5	3	PETG	1	20	3	78	2	Cubic	3	0.15	1	5000	2	50	95.9	90.7	5.2
R17	2	5	3	PETG	2	40	1	18	3	Gyroid	1	0.06	2	10,000	3	100	115.5	98.7	16.8
R18	2	5	3	PETG	3	60	2	48	1	Grid	2	0.1	3	15,000	1	30	58.5	39.5	19

3. Results

3.1. Modeling Sound Propagation through Polymer Panels Using the Finite Element Method

The finite element method (FEM) offers a perspective on the way the polymeric panel deflects the sound and how it is propagated inside a closed enclosure. It needed the same infill pattern and thickness to provide accurate results as the analyzed 3D-printed panels. For that matter, the SolidEdge teacher edition was used to model two panels with different patterns, grids, and gyroid of 5 mm thick. They correspond to the R7 and R17 samples of 3D-printed parts for the experiments, having received the same infill percentage and shape (Figure 5). Each panel was later added to an assembly, including a speaker box and the panel itself at the same distance as the one from the experimental setup.

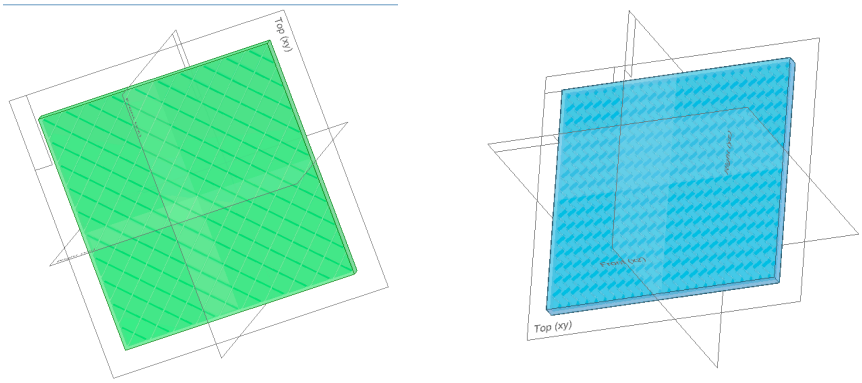

(**a**) (**b**)

Figure 5. Graphical representations of designed polymeric panels: (**a**) panel with grid infill pattern; (**b**) panel with gyroid infill pattern.

Ansys 2023 R2 (researcher license), as the preferred software was chosen for FEM, with its module named Harmonic Acoustics, because of its ability to highlight a linear structure's response to sinusoidal loads, which vary in time. That means that each boundary condition determines the frequency applied using its amplitude and phase. Different loads can be applied, from which the mass source was selected as the primary excitation method. It was necessary to model the acoustic medium surrounding each speaker with a panel type of assembly because this is the one computational domain (CD) in which acoustic waves propagate (Figure 6).

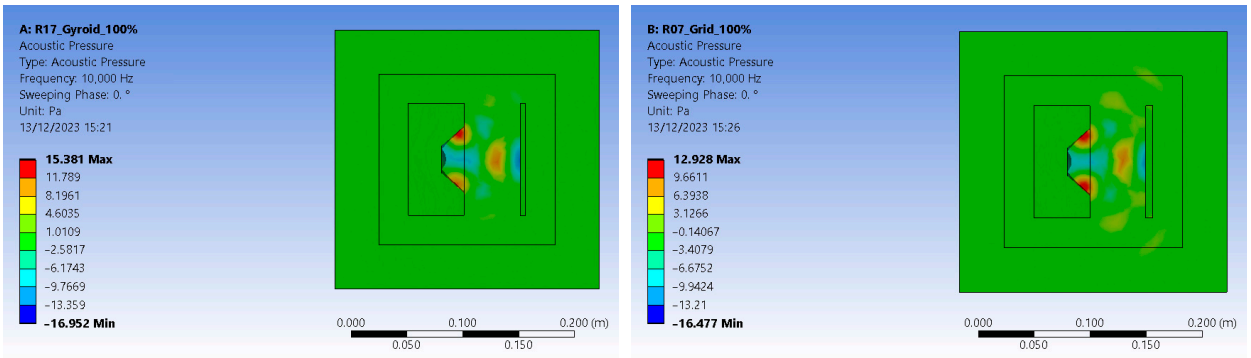

(**a**) (**b**)

Figure 6. Graphical representations of acoustic pressure distribution: (**a**) setup with gyroid infill pattern; (**b**) setup with grid infill pattern.

The authors acknowledge that further refinement may be needed and recommend using the information carefully.

3.2. Experimental Results

The experimental results were entered in the last columns of Table 2. Thus, in column no. 18, the values of the sound intensity level were mentioned when between the sound source (audio mini speaker) and the sensor of the sound meter level, which was not placed on a panel of polymeric material; and in column no. 19, the values were received by the sensor of the sound level meter when a panel of polymeric material with certain characteristics, obtained through the 3D printing process, was placed between the sound source and the sensor. In column no. 20, the differences between the values entered in the two previous columns were included. These values (from column no. 20) provide information on the extent to which the sound pressure level was affected by the presence of a polymeric material panel between the sound source and the sound-receiving sensor.

The experimental results were mathematically processed using specialized software based on the least squares method [31]. The software allows for the selection of a certain empirical mathematical model from among five such models (first-degree polynomial, second-degree polynomial, power-type function, exponential function, and hyperbolic function, respectively). The adequacy of a certain empirical mathematical model to the experimental results can be assessed using the value of the so-called Gauss criterion [32,33]. In principle, the value of Gauss's criterion is determined as a ratio in which the numerator is a sum of the squares of the differences between the values determined by using the proposed empirical mathematical model and, respectively, the values of the ordinates corresponding to the experimental results, for the same values of the abscissas. The ratio's denominator represents the difference between the number of experimental trials and the number of constants in the proposed empirical mathematical model. It is considered that the lower the value of Gauss's criterion, the more appropriate the considered mathematical model is for the set of experimental results obtained. According to this observation, it can be appreciated that when several empirical mathematical models are proposed, the most appropriate model will be the one for which the value of Gauss's criterion is the lowest.

Through the mathematical processing of the experimental results, it was found that the most appropriate empirical mathematical models for the sets of experimental results are the following:

- For the absolute values determined in the case of the sound pressure level, it is a polynomial function of the second degree:

$$\begin{aligned} p_{ac} &= 61.589 + 12.355t - 1.944t^2 - 2.859m + 0.941m^2 - 0.117v \\ &+0.00153v^2 - 0.321i + 0.00315i^2 + 0.815i_p + 0.216i_p^2 \\ &+89.372l - 444.032l^2 + 0.00853f - 4.351 \cdot 10^{-9} f^2 \\ &+0.825s - 0.00241s^2, \end{aligned}$$

  for which the value of Gauss's criterion is S_G = 0.3702504;
- For the sound pressure level corresponding to the energy absorbed primarily by the panel material manufactured by 3D printing, calculated as a difference between the values entered in columns 18 and 19 of Table 2, the most appropriate empirical mathematical model is like a polynomial function of the second degree:

$$\begin{aligned} \Delta p_{ac} = \; & 169.745 - 263.917t + 43.719t^2 + \\ & 5.097m - 1.639m^2 - 0.141v + 0.00153v^2 + \\ & 0.180i - 0.00177i^2 + 1.311i_p - 0.571i_p^2 - \\ & 27.377l + 222.774l^2 + 0.00853f - 3.253 \cdot 10^{-7} \cdot f^2 + \\ & 0.685s - 0.00480s^2, \end{aligned}$$

  the value of Gauss's criterion being, in this case, S_G = 0.4655038.

On the other hand, in manufacturing engineering, empirical mathematical models of the power function type have been used for a relatively long time. Such models are used, for example, to highlight the influence of the cutting parameters on the size of the cutting

tool life, the sizes of the cutting forces, the value of the roughness parameters, etc. It is considered that by simply examining the values of the exponents attached to the independent variables in a power-type function mathematical model, some first information is obtained relatively quickly regarding the intensity and sense of the influence exerted by the action of the input factors (consider as independent variables) in the process investigated on a magnitude of interest. By resorting also in the present case to such empirical mathematical models of the power function type, the following relations were determined:

- For the absolute values of the acoustic pressure level (values entered in column no. 19 of Table 2):

$$p_{ac} = 1198.755 t^{-0.000324} m^{-0.0175} v^{-0.0314} i^{-0.0348} i_p^{0.0654} l^{0.0406} f^{-0.460} s^{0.419},$$

  the value of Gauss's criterion being higher than that of the most appropriate model, namely, $S_G = 28.49857$.
- For the acoustic pressure level corresponding to the energy absorbed by the panel material:

$$\Delta p_{ac} = 6.726 \cdot 10^{-6} t^{-0.121} m^{-0.0904} i^{0.0322} i_p^{-0.0939} l^{0.113} f^{1.618} s^{0.102},$$

  for which the value of Gauss's criterion has value $S_G = 56.99927$.

  The graphical representations in Figures 7–9 were drawn using Equation (5).

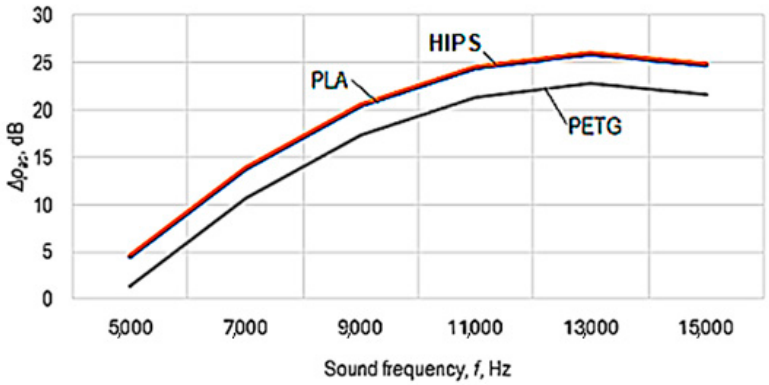

Figure 7. The influence exerted by the frequency f of the sounds and by the type m of the panel material of polymer material manufactured by 3D printing on the difference in acoustic pressure Δp_{ac} (panel thickness t = 5 mm; printing speed v = 60 mm/s; infill percent i = 48%; infill pattern: cubic (i_p = 2); layer thickness l = 0.06 mm; sound volume s = 100%).

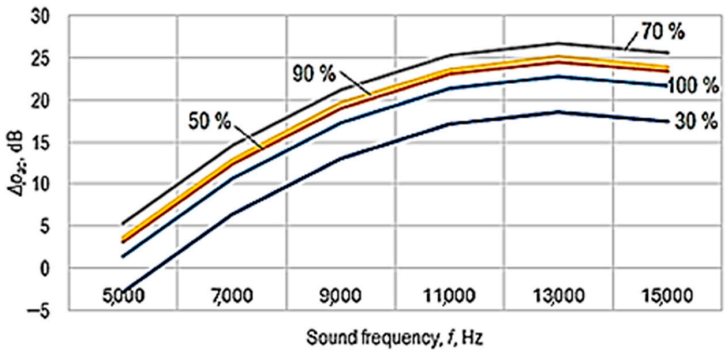

Figure 8. The influence of sound frequency f on the difference in acoustic pressure for different sound volume values (panel thickness t = 5 mm; test piece material: PETG (m = 3); printing speed v = 60 mm/s; infill percent i = 48%; infill pattern: cubic (i_p = 2); layer thickness l = 0.06 mm; empirical mathematical model of the second degree polynomial type).

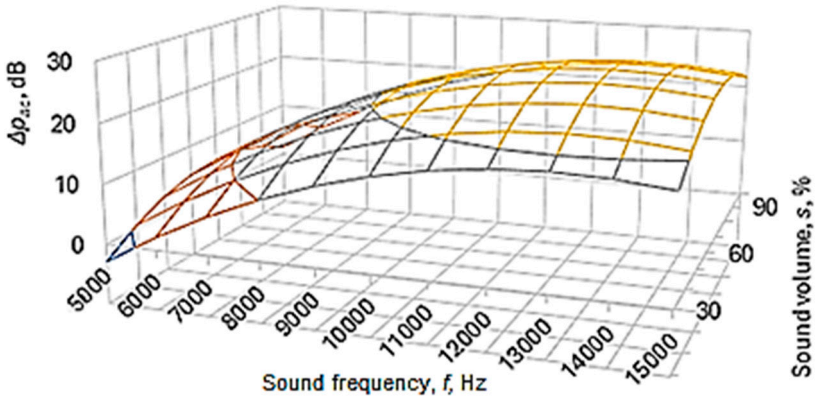

Figure 9. The influence of sound frequency f and sound volume on the difference in acoustic pressure Δp_{ac} (test piece material PETG (m = 3); printing speed v = 60 mm/s; infill percent i = 48%; infill pattern: cubic (i_p = 2); layer thickness l = 0.06 mm; empirical mathematical model of the second-degree polynomial type).

4. Discussion

The validation of the empirical mathematical model proposed by Equation (5) can be performed by making an additional experimental test using for one independent variable or for several independent variables, other values different from those used to generate the empirical mathematical models, by processing the experimental results. In the case of the mathematical model represented by Equation (5), an additional experimental test was performed. Experiment no. 18 from Table 2 was taken into account. The following values of the independent variables were used: t = 5 mm; m = 3 (corresponding to PETG material); v = 60 mm/s; i = 48%; i_p = grid; l = 0.1 mm; f = 8000 Hz; and s = 7500 Hz. It can be seen that the last two independent variables (f și s) had values other than those used to determine the empirical mathematical model corresponding to Equation (5) in the case of experiment no. 18.

For these independent variables' values, the Δp_{ac} parameter value, determined using the empirical mathematical model (5), was 17.31 dB. Through the experimental test, the values I_0 = 117.5 dB were obtained without the panel and, respectively, I_p = 101.2 dB when the PETG panel was placed between the mini audio speaker and the sensor of the sound level meter. The difference between the two measured values leads to a value of Δp_{ac} = 16.3 dB. It is thus possible to determine a percentage difference between the value determined using the identified empirical mathematical model and the value obtained using the experimental result of the additional test $\Delta = (17.31 - 16.3) \times 100/17.31 = 5.83\%$. It can thus be appreciated that the proposed empirical mathematical model can be considered validated.

The analysis of Equations (6) and (7)—and, respectively, of the graphic representations in Figures 7–9—facilitated the formulation of the following findings.

From the analysis of the power-function-type mathematical models (Equations (6) and (7)), it is found that the greatest influences on the values of the acoustic pressure level p_{ac}—and, respectively, on the sound energy absorption highlighted by the acoustic pressure difference Δp_{ac}—correspond to the factors frequency f and sound volume s, as these factors are associated, in Equations (6) and (7), with relatively high absolute values of exponents (in Equation (7), the two magnitudes are associated with exponent values of 1.618 in the case of frequency f and, respectively, 0.102 in the case of sound volume s).

The empirical mathematical model of power function type defined by Equation (7) highlights the strong influence of frequency f and sound volume s on the sound energy absorbed by the sample material.

Using mathematical models of the second-degree polynomial type, the graphic representations in Figures 7–9 highlight the existence of maxima of the value of the acoustic pressure difference Δp_{ac}. The more pronounced influence of the frequency f of the sounds

exerted on the difference in acoustic pressure level can be more clearly observed in the graphic representation in Figure 9.

For the conditions in which the experimental research was carried out, from Figures 7–9, it can be seen that there is a maximum of the acoustic pressure difference for a frequency of about 13,000 Hz. It is worth noting that different researchers have observed maximum sound absorption values by panels made of different materials for certain frequency values. These maximum values differ depending on the nature of the panel material and other conditions in which the measurements were made. Thus, it was found the existence of a maximum absorption coefficient for a frequency of approximately 2000 Hz in the case of a panel made of 20% polyester resin and 80% PET pellets [6]. Others highlighted the existence of two maxima of the sound absorption coefficient for frequencies with approximate values of 2500–4000 Hz and, respectively, of approximately 7500–9500 Hz in the case of panels made of porous solid fiber structures [9].

As mentioned in the introduction, there is an influence exerted on the sound absorption capacity in the case of some panels of polymeric materials by some input factors in the experimental investigation process, such as the sound frequency [6,8,9,12,14,15,20,22], the nature of the materials from which the samples were made [3,6–9], the acoustic pressure level of the incident sound radiation [5], the thickness of the panels [3,5,13,15,23], the structure corresponding to the arrangement of the material in samples [2,3,9–20] etc. However, the values that characterize the sound energy absorption by the samples have values between wide limits due to the differences corresponding to the conditions involved in making the measurements. Through the experimental results presented in this paper, as expected, it is confirmed that an increase in the thickness t of the panel will lead to the absorption of a greater amount of the energy of the sounds emitted by the source.

Figure 10 shows the reduction of the sound level when a panel made of polymeric material manufactured by 3D printing was placed between the sound source and the sensor of the equipment under the conditions valid for experiment no. 2. As expected, the presence of the polymer panel contributes to a decrease in the sound level received by the device's sensor. It can be noted that the panel made of polymer material absorbs energy corresponding to a difference in acoustic pressure of about 35 dB. This means that the presence of the polylactic acid panel leads to a reduction of about 45% in the sound pressure level.

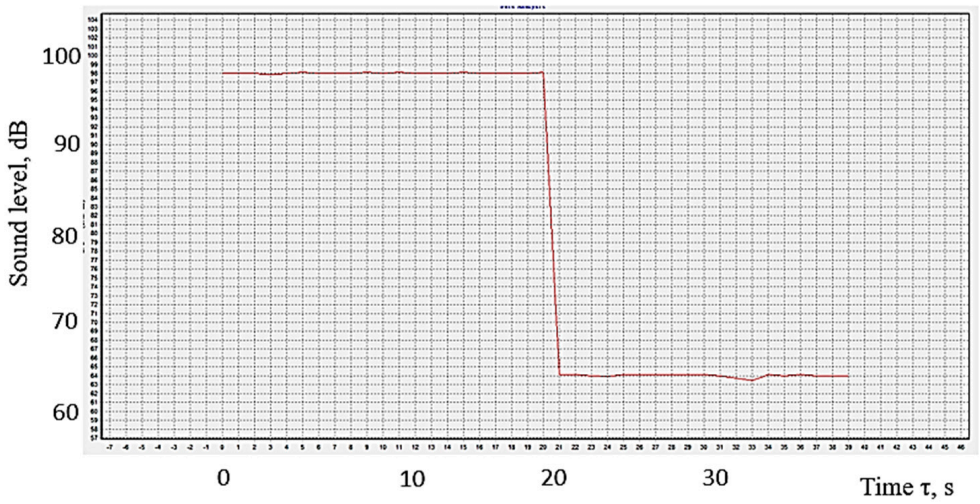

Figure 10. The difference in sound level (acoustic pressure) in the case of the absence of the panel and the presence of the polymer panel manufactured by 3D printing for experiment no. 2.

The graphic representation in Figure 11 sought to highlight the time variation of the sound level reaching the sound level meter sensor. The graph corresponds to the use of the conditions corresponding to experiment no. 18. The sound level meter transmits the values

to the computer software, which determines a mean sound level value after one-second intervals. Such mean values were considered when the computer software developed the diagram in Figure 11. It can be seen that the sound level reaching the sound level meter sensor after passing through the polymer material panel is not constant. For the conditions of the experimental tests, the sound level registers a variation between relatively close limits, namely, between 38.7 dB and 39.6 dB.

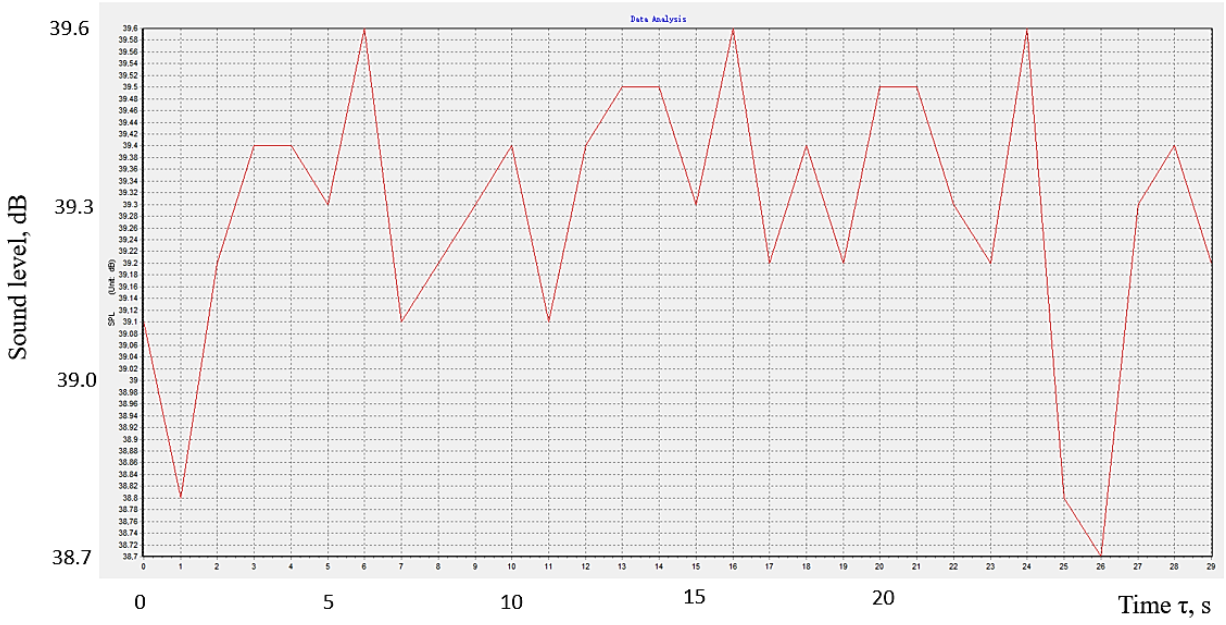

Figure 11. The time variation of the sound level when using the panel made of polymeric material manufactured by 3D printing in experiment no. 18 (the points correspond to the mean values of the sound level recorded for a duration of one second).

To simulate a perfect insulation environment, another medium had to be modeled as a perfectly matched layer (PML) which absorbs bouncing waves without reflecting them. In the Ansys Space Claim module, the boxed type of enclosure was chosen was for both media—computational domain (CD) and the perfectly matched layer (PML)—which were later imported in the analysis's module (Figure 12a). The entire geometry shares its topology among its components. Because the aim is to obtain acoustic pressure distribution results, air was added as the propagation medium and assigned as the default material for both enclosures. Mesh-wise, a face-sizing method was added to capture all facets of the newly designed assembly by suppressing the initial setup containing the speaker and the polymeric panel. That made the assignation of materials for the two-suppressed components irrelevant. Mesh resulted in 60,553 nodes and 38,745 elements. The mass excitation source was applied to the speaker's membrane (Figure 12b). When applied to a surface, one can divide the mass flow rate by the area on which it is applied. After this step, the speaker and polymeric panel are suppressed to mesh the entire geometry.

The analysis settings received a linear frequency spacing varying from zero to 10,000 Hz. The acoustic region is set to the DM enclosure, and a newly added physics region is added and assigned to the PML enclosure. This ensures that pressure builds up inside as acoustic waves do not escape the setup and are not reflected by its outer boundaries. The solution requires a sound pressure level and an acoustic pressure distribution. For the R17 experiment, the gyroid 18% infilled sample at 100% sound intensity level resulted in 119.66 dB (Figure 12b). For the R7 experiment, the grid 48% infilled sample at 100% sound intensity level resulted in 119.01 dB (Figure 12b). The values are greater than the ones recorded in experimental tests since Ansys uses a perfectly isolated medium.

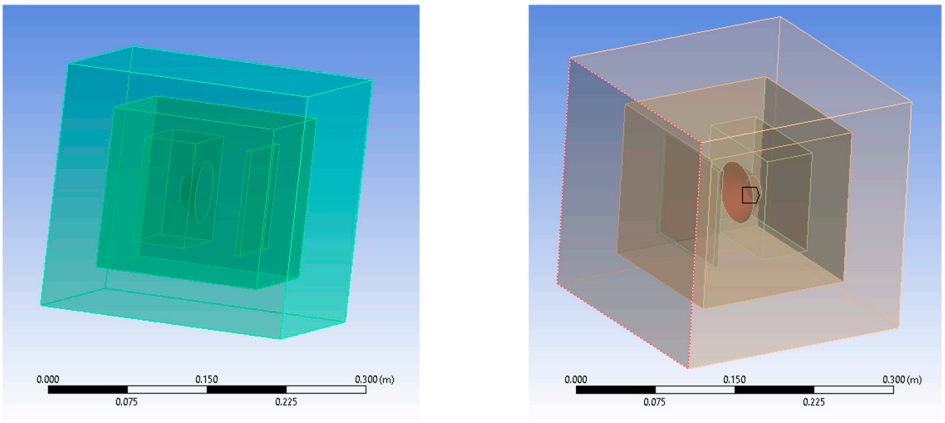

(**a**) (**b**)

Figure 12. Graphical representations setup with two enclosures: (**a**) general view of resulted geometry; (**b**) mass source excitation applied to the speaker's membrane.

Acoustic pressure builds up inside the computational domain (CD) and extends to the limits of PML enclosure. The R17 experiment setup peaks at 15.381 Pa, and the R7 experiment reaches 12.928 Pa (Figure 13). Results show that gyroid infill better deflects the sound waves. They are consistent with experimental results that revealed a 26.6 dB loss in sound pressure level for the R7 experiment gyroid-infilled sample instead of just 16.8 dB for the R17 experiment grid-infilled one.

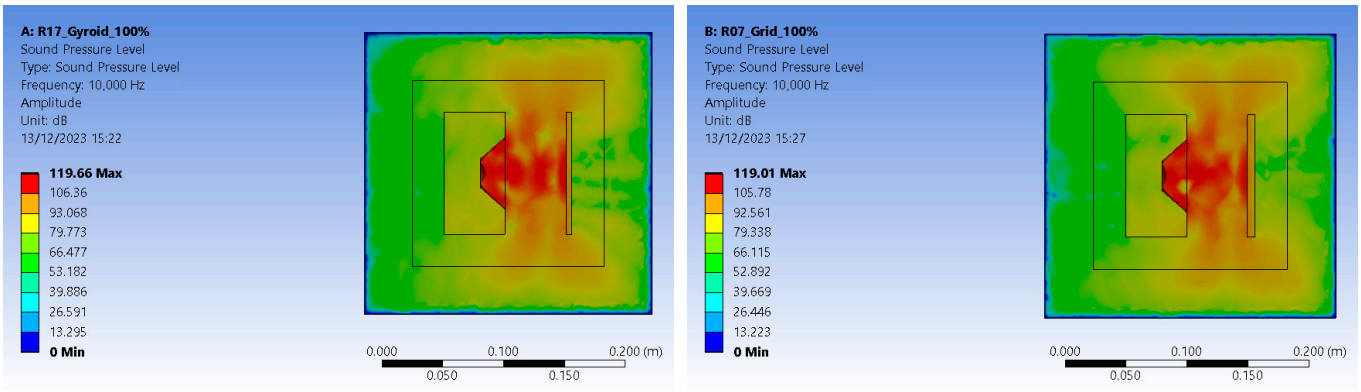

(**a**) (**b**)

Figure 13. Graphical representations of sound pressure levels: (**a**) setup with gyroid infill pattern; (**b**) setup with grid infill pattern.

5. Conclusions

In some situations, reducing the intensity of sounds in certain spaces is necessary. In such situations, panels made of polymeric materials can be used to allow for the sound insulation of the respective spaces. For this reason, it is useful to know some information about the ability of some polymeric materials to absorb sound energy. On the other hand, the expansion of the use of parts made of polymeric materials through 3D printing has opened up new possibilities for modification, including the ability of some polymeric materials to absorb the energy of sound vibrations. The finite element method was employed to obtain initial information on the behavior of small polymeric-med panels. Later, experimental research was carried out, starting with a Taguchi L18-type factorial experiment. The experiment considered eight independent variables, of which one variable (the thickness of the polymer material panel) received values on two levels of variation. The other seven independent variables had values on three levels of variation. The input factors were the thickness of the panel, the nature of the polymer material of the panel, the 3D printing

speed, the infill percentage, the infill pattern, the layer thickness, the frequency, and the sound volume. The output parameters taken into account as dependent variables were the acoustic pressure level of the sound wave after passing through the polymer material panel and, respectively, the acoustic pressure level corresponding to the energy absorbed by the panel. The experimental research was carried out using a sound-insulated enclosure. In this enclosure, in separate compartments, a mini audio speaker, a supporting wall of the sample in the form of a small panel, and, respectively, the sensor of a sound level meter were placed. Panels with an area of 100 × 100 mm^2 and 5 mm thicknesses were manufactured by 3D printing from polylactic acid and polyethylene terephthalate glycol, respectively. The experimental results were mathematically processed using specialized software. Empirical mathematical models of the second-degree polynomial and power function were obtained in this way. The last type of function directly highlights the means and intensity of the influences exerted by the input factors on the values of the output parameters. As expected, it was found that an increase in the thickness of the polymer material panel leads to a decrease in the sound pressure level after sound passes through the polymer material panel. The strongest influence on the difference in acoustic pressure is due to the energy the panel absorbs, which is exerted by the frequency of the sounds. For the polymer materials used to make the small panels and for the conditions of the experimental tests, the variation of the acoustic pressure difference due to the change in the frequency of the sounds led to a maximum corresponding to a frequency of about 13,000 Hz. In the future, research is intended to continue considering the possible influence exerted by other factors that characterize the 3D printing process. Another direction for experimental research could consider panels manufactured by 3D printing from other materials.

Author Contributions: Conceptualization, A.H. and L.S.; methodology, A.H.; software, A.M.M.; validation, O.D. and G.N.; formal analysis, I.B.-B. and B.R.; investigation, A.H. and B.R.; resources, A.M.M.; data curation, I.B.-B.; writing—original draft preparation, L.S. and A.H.; writing—review and editing, A.H.; project administration, O.D. All authors have read and agreed to the published version of the manuscript.

Funding: This research received no external funding.

Data Availability Statement: All information necessary to understand the authors' considerations has been included in the article. Other information will be provided by the authors of the article at the request of those interested in such other information.

Conflicts of Interest: The authors declare no conflict of interest.

References

1. Alfarisi, N.A.S.; Santos, G.N.C.; Norcahyo, R.; Sentanuhady, J.; Azizah, N. Model optimization and performance evaluation of hand cranked music box base structure manufactured via 3D printing. *Heliyon* **2021**, *7*, e08432. [CrossRef] [PubMed]
2. King, Y.-J.; Teo, K.-K. Application of 3D printed structured materials as the sound absorption panels. *IOP Conf. Ser. Earth Environ.* **2020**, *463*, 012032. [CrossRef]
3. Vasina, M.; Monkova, K.; Monka, P.P.; Kozak, D.; Tkac, J. Study of the Sound Absorption Properties of 3D-Printed Open-Porous ABS Material Structures. *Polymers* **2020**, *12*, 1062. [CrossRef] [PubMed]
4. Hrițuc, A.; Dodun, O.; Mihalache, A.; Nagîț, G. Equipment Requirements for the Investigation of Sound Insulation Properties of 3D Printed Polymeric Materials. *Acta Tech. Napoc. Ser. Appl. Math.* **2022**, *65*, 1186–1192. Available online: https://atna-mam.utcluj.ro/index.php/Acta/article/view/2046 (accessed on 18 October 2023).
5. Hrițuc, A.; Dodun, O.; Mihalache, A.M.; Slătineanu, L.; Nagîț, G. The Sound Insulation Capacity of Some Panels Made of Polymeric Materials Manufactured by 3D Printing. *Mater. Res. Proc.* **2023**, *28*, 1719–1728. [CrossRef]
6. Bratu, M.; Ropotă, I.; Vasile, O.; Dumitrescu, O.; Muntean, M. Research on the absorbing properties of some new type of composite materials. *Rom. J. Mater.* **2011**, *44*, 147–154.
7. Johnston, W.; Sharma, B. Additive Manufacturing of Fibrous Sound Absorbers. *Addit. Manuf.* **2021**, *41*, 101984. Available online: https://www.sciencedirect.com/science/article/pii/S2214860421001494 (accessed on 18 October 2023). [CrossRef]
8. Maroo, T.; Wright, A. Sound transmission loss improvement using additively manufactured multimaterial. *Proc. Meet. Acoust.* **2022**, *46*, 030001. [CrossRef]
9. Perrot, C.; Chevillotte, F.; Panneton, R. Optimal sound absorbing and manufacturable two-dimensional, hexagonal-like porous structure. *Proc. Mtgs. Acoust.* **2008**, *4*, 045004.

10. Perrot, C.; Chevillotte, F.; Panneton, R. Bottom-up approach for microstructure optimization of sound absorbing materials. *J. Acoust. Soc. Am.* **2008**, *124*, 940–948. [CrossRef]
11. Perrot, C.; Hoang, M.T.; Chevillotte, F. An overview of microstructural approaches for modelling and improving sound proofing properties of cellular foams: Developments and prospects. In Proceedings of the 10th International Styrian Noise, Vibration & Harshness Congress: The European Automotive Noise Conference, Graz, Austria, 20–22 June 2018. [CrossRef]
12. Gao, N.; Hou, H. Sound absorption characteristic of micro-helix metamaterial by 3D printing. *Theor. App. Mech* **2018**, *8*, 63–67. [CrossRef]
13. Wen, G.; Zhang, Y.; Liu, J. Sound insulation properties of sandwich structure with hemispheric shell cores: Numerical and experimental studies. *Appl. Acoust.* **2020**, *162*, 107209. [CrossRef]
14. Zieliński, T.; Opiela, K.; Pawlowski, P.; Dauchez, N.; Boutin, T.; Kennedy, J.; Trimblec, D.; Rice, H.; Van Damme, B.; Hannema, G.; et al. Reproducibility of sound-absorbing periodic porous materials using additive manufacturing technologies: Round robin study. *Addit. Manuf.* **2020**, *36*, 101564. [CrossRef]
15. Yang, W.; Bai, X.; Zhu, W.; Kiran, R.; An, J.; Chua, C.K.; Zhou, K. 3D Printing of Polymeric Multi-Layer Micro-Perforated Panels for Tunable Wideband Sound Absorption. *Polymers* **2020**, *12*, 360. [CrossRef] [PubMed]
16. Du, Y.; Wu, W.; Chen, W.; Lin, Y.; Chi, Q. Control the structure to optimize the performance of sound absorption of acoustic metamaterial: A review. *AIP Adv.* **2021**, *11*, 060701. [CrossRef]
17. Zieliński, T.G.; Dauchez, N.; Boutin, T.; Leturia, M.; Wilkinson, A.; Chevillotte, F.; Bécot, F.-X.; Venegas, R. Taking advantage of a 3D printing imperfection in the development of sound-absorbing materials. *Appl. Acoust.* **2022**, *197*, 108941. [CrossRef]
18. Opiela, K.C.; Zieliński, T.G.; Attenborough, K. Limitations on validating slitted sound absorber designs through budget additive manufacturing. *Mater. Des.* **2022**, *218*, 110703. [CrossRef]
19. Maroo, T.; Wright, A. Design of multi-material sound transmission blocker using additive manufacturing. *J. Acoust. Soc. Am.* **2022**, *151*, A179–A180. [CrossRef]
20. Zahiruddin, S.K.; Yarlagadda, J. Experimental investigation of sound absorption properties of 3d printed PETG absorbers. *Eur. Chem. Bull.* **2023**, *12*, 5400–5407. [CrossRef]
21. Perrot, C.; Chevillotte, F.; Jaouen, L.; Hoang, M.T. Acoustics properties and applications. In *Metallic Foams: Fundamentals and Applications*; Dukhan, N., Ed.; DesTech Publications: Lancaster, PA, USA, 2013; pp. 285–316. Available online: https://hal-upec-upem.archives-ouvertes.fr/hal-00811700 (accessed on 19 October 2023).
22. Setaki, F.; Tenpierik, M.; van Timmeren, A.; Turrin, M. Sound absorption and additive manufacturing. In Proceedings of the Inter-Noise, International Conference Inter-Noise and Noise-Con Congress and Conference Proceedings, Chiba, Japan, 9–12 August 2015; Volume 250, pp. 5023–5032. [CrossRef]
23. Chevillotte, F.; Perrot, C. Effect of the three-dimensional microstructure on the sound absorption of foams: A parametric study. *J. Acoust. Soc. Am.* **2017**, *142*, 1130–1140. [CrossRef] [PubMed]
24. Lin, C.; Wen, G.; Yin, H.; Wang, Z.-P.; Liu, J.; Xie, Y.M. Revealing the sound insulation capacities of TPMS sandwich panels. *J. Sound Vib.* **2022**, *540*, 117303. [CrossRef]
25. *ISO 10534-1*; Acoustics. Determination of Sound Absorption Coefficient and Impedance in Impedance Tubes. Part 1: Method Using Standing Wave Ratio. ISO: Geneva, Switzerland, 2022.
26. *ISO 10534-2*; Acoustics. Determination of Sound Absorption Coefficient and Impedance in Impedance Tubes. Part 2: Transfer Function Method. ISO: Geneva, Switzerland, 2023.
27. Shtrepi, L.; Prato, A. Towards a sustainable approach for sound absorption assessment of building materials: Validation of small-scale reverberation room measurements. *Appl. Acoust.* **2020**, *165*, 107304. [CrossRef]
28. Maroo, T.D. Design and Characterization of a Novel Reverberation Chamber for Measuring Sound Transmission Loss in 3D Printed Multimaterials. Ph.D. Dissertation, University of Arkansas at Little Rock, Little Rock, AR, USA, 2021. Available online: https://www.proquest.com/openview/00dbd7eed57b54795faf5b70bbe884ad/1?pq-origsite=gscholar&cbl=18750&diss=y (accessed on 19 October 2023).
29. Peng, T.; Dong, N.; Yan, Q. Analysis of sound transmission loss characteristics of aircraft composite panel under variable temperature environment. *J. Low Freq. Noise Vib. Act. Control* **2022**, *41*, 1044–1065. [CrossRef]
30. Kovalenko, A.; Fauquignon, M.; Brunet, T.; Mondain-Monval, O. Tuning the sound speed in microporous polymers with a hard or soft matrix. *Soft Matter* **2017**, *13*, 4526–4532. [CrossRef]
31. Cretu, G. *Fundamentals of Experimental Research. Laboratory Handbook*; "Gheorghe Asachi" Technical University of Iași: Iași, Romania, 1992. (In Romanian)
32. Worthing, A.G.; Geffner, J. *Treatment of Experimental Data*; Editura Tehnică: Bucharest, Romania, 1959. (In Romanian)
33. Crețu, G.; Varvara, G. *Experimental Research Methods in Machine Manufacturing*; Publishing House Junimea: Iași, Romania, 1999. (In Romanian)

sensors

MDPI

Article

A Proposed System for Temperature Measurement During Tensile Testing

Marius Andrei Mihalache [1], Vasile Merticaru [1,*], Vasile Ermolai [1], Liviu Andrusca [2], Nicanor Cimpoesu [3] and Florin Negoescu [1]

[1] Department of Machine Manufacturing Technology, Gheorghe Asachi Technical University of Iasi, 700050 Iasi, Romania; marius-andrei.mihalache@academic.tuiasi.ro (M.A.M.); vasile.ermolai@academic.tuiasi.ro (V.E.); florin.negoescu@academic.tuiasi.ro (F.N.)
[2] Department of Mechanical Engineering, Mechatronics and Robotics, Gheorghe Asachi Technical University of Iasi, 700050 Iasi, Romania; liviu.andrusca@academic.tuiasi.ro
[3] Department of Materials Science and Engineering, Gheorghe Asachi Technical University of Iasi, 700050 Iasi, Romania; nicanor.cimpoesu@academic.tuiasi.ro
* Correspondence: vasile.merticaru@academic.tuiasi.ro; Tel.: +40-723940041

Abstract

Integration of thermographic imaging with in situ scanning electron microscopy (SEM) analysis may aid in quantifying thermal–mechanical behavior during tensile testing of 3D-printed polymers, which gives information about fracture mechanics, including the associated thermal phenomena. Upon fracture, samples exhibit changes in the thermal field, which is interesting because temperature fluctuations can affect material integrity. The paper introduces printing parameters to demonstrate a thermal measurement system's sensitivity in detecting variations in mechanical response due to controlled changes in the process. Employing scientific methods, one can extrapolate results to a wider class of materials such as thermoplastics. Analysis of variance (ANOVA) is key in the design of experiments (DOE) if one wants to analyze the effect of factors and interactions. It has been used with the purpose of reducing the risk of type I errors (i.e., false positives). The finite element method (FEM) highlights temperature distribution in the area of interest and confirms recorded data. The particularly developed research experiments are carried out in a laboratory environment. Different samples are subjected to tensile tests under the evaluation of changes in the thermal field. SEM analysis is also widely used in fracture analysis to understand failure modes (ductile vs. brittle, crazing, delamination, and others). Thus, the paper aims to present a custom setup comprised a thermal camera pointed at samples during tensile testing that would serve as a reliable assessment system that accounts for the substitution of a sensor-based environment but is still fully capable of validating the measurement approach.

Keywords: thermal imaging; 3D printing; tensile testing; ANOVA; FEM; SEM

Academic Editor: Guillermo Villanueva

Received: 1 May 2025
Revised: 10 August 2025
Accepted: 26 August 2025
Published: 4 September 2025

Citation: Mihalache, M.A.; Merticaru, V.; Ermolai, V.; Andrusca, L.; Cimpoesu, N.; Negoescu, F. A Proposed System for Temperature Measurement During Tensile Testing. *Sensors* **2025**, *25*, 5494. https://doi.org/10.3390/s25175494

1. Introduction

The combination of thermal imaging and in situ observation, aligned with mechanical testing, offers a coherent measurement system for comprehensive material evaluation. It is generally accepted that printing parameters have a great influence on the final part's mechanical integrity and toughness. Hamidi et al. have studied the influence of printing parameters of thermoplastic polymers. By blending two filaments they were able to detect how various ratios impact final products by means of differential scanning calorimetry

(DSC) and thermogravimetric analysis (TGA). Not only printing procedures are responsible, but also different blends that, in their case, accounted for a reduced cold crystallization temperature among others, which gave 64% reduced strength but better ductility. By using different strain rates for tensile tests, the authors have found a relation to the rate-dependent properties of the PLA/TPU polymer [1].

Jin et al. have studied the thermal properties of some 3D-printed monofilaments. At a certain value of the monofilament diameter, they have found that the tensile strength reaches a maximum of 48.3 MPa in the case of carbon fiber-reinforced polylactic acid (CF-PLA) and as CF amount is increased up to 8 vol%, a high thermal stability is achieved. A single PLA-based board shows numerous fusion interfaces, which may account for a tensile strength of just 22.1 MPa, which is half the strength of CF-based ones. Thermogravimetry revealed that the thermal conductivity of the CF-based monofilament is higher than the average PLA one. However, if the threshold of 8 vol% is exceeded, thermal stability is affected by favoring the appearance of more cracks [2].

Švantner et al. tackled the problem of thermographic devices that exhibit limited accuracy, often rendering them inadequate for certain applications. They propose a built-in active reference element that leads to enhanced measurements, thus obtaining pertinent results in a given range. It shows the potential for commercial devices to be used in precision-based applications by successfully substituting more expensive equipment [3].

Researchers have strived to find ways for suitable thermal management. Analyses of thermal performance were carried out by Pei et al. on 3D-printed polymer vacuum insulation panels known for their low thermal conductivity. Their thermal insulation performance derives directly from thermal conductivity, as it was found that it is very sensitive to the emissivity of the solid material when the pressure levels are low. However, PLA for example, exhibits higher emissivity in the infrared region, which explains the behavior of samples under temperature fluctuations. There is a reason why researchers are aiming for lower values for thermal conductivity, as it opens the path for other methods for increasing strength of printed parts [4].

Researchers have addressed different types of tests to assess the strength of materials, among which are tensile ones under thermal cycling conditions. By varying temperature conditions, Kang et al. were able to correlate material strength with temperature variations. They have used the Matsuoka model and achieved up to 90% more strength for their polymethyl methacrylate (PMMA) samples because the polymers react upon heating beyond the glass transition temperature (Tg) but were able to maintain a consistent elastic modulus for the studied samples batch [5].

By deploying thermal data augmentation techniques, Khoshkbary-Rezayiye et al. have managed to combat limited datasets. Their approach, which uses deep learning, aims at the automation of defect detection processes. By generating synthetic sub-surface defects by means of finite element modelling (FEM), one could obtain synthetic thermal images, that when overlapped onto reals ones, may be used for training the learning algorithm. This method shows the potential of thermal imaging in the detection of defects in pipes but may be extended to others as well [6].

Other researchers have used scientific methods like ANOVA, Taguchi, and grey relational analysis (GRA) to find ways to improve the mechanical performance of 3D-printed samples through thermal annealing. These methods also produce optimal results in in form of tensile strength, flexural strength, compressive strength, and impact resistance. Kahya et al. found a significant effect of annealing temperature and time on the tensile properties of their PLA-based samples which exhibited approximately a 25% increase in strength after 200 min of annealing at 90 °C, thus facilitating beneficial phase transition. ANOVA revealed that temperature was the primary factor, accounting for 94.46% of the variance

almost independent of time. By employing differential scanning calorimetry (DSC) results, it was confirmed that the process of annealing enhances and promotes molecular alignment, which gives more stable crystalline regions. This type of research may be very well continued by assessing the influence of temperature fluctuations in 3D-printed models [7].

Fujita et al. are evaluating fatigue damage of carbon-fiber-reinforced plastic (CFRP) structures by taking into account thermal diffusivity and specific heat capacity retrieved by lock-in thermography. After numerous fatigue cycles, which produced microstructures changes and degradation, values of thermal diffusivity decreased and triggered an increased volumetric heat capacity under fatigue loading [8]. Thus, thermal evolution may be captured and assessed as one of the main output factors of certain mechanical processes. Demarbaix et al. have also studied defect detection by using active thermography. They have established two benchmarks that set a detectability threshold and look for defects as a result of 3D printing. Successful detection is achieved through reflection and transmission modes as reflection avoidance is not necessary. It shows the potential of using thermal equipment for early detection [9].

Roudný et al. have reviewed FDM-ready composites that are thermal conductive (TC). It is pointed out that, regularly, anisotropy may be present as TC being higher in the print direction. Even though manageable by 3D printing, oriented fibers are not preserved after process completion due to their inability to maintain molecular orientation after filament reheat, which often occurs when the polymer that is molten stretches under stress-induced conditions to form macromolecules. It has been found that it is possible to achieve a certain TC in a given time interval that is comparable to drawn fibers' molecular orientation by 3D printing at high speeds. Of course, the addition of conductive fillers helps in the sense that smaller particles form a denser network with improved TC. One of the solutions is to build a segregated structure by using coextrusion that would allow a shell cover to be created. However, there are limitations, as adhesion between the network structure and polymer matrix must be improved [10].

Interlayer adhesion was also studied by Nguyen et al., which revealed that it also depends on polymeric chain mobility because as soon as thermal energy accumulates that will determine when layers fuse and bond. Another interesting approach focuses on the post-processing of parts obtained by means of 3D printing by introducing an additional thermal treatment that further strengthens their mechanical toughness through interlayer interaction. Others have built custom chambers that allowed envelope temperatures to be controlled, which led to enhanced neck growth and improved strength of the interlayers. By employing a time–temperature superposition (TTS), they have investigated the creep modulus of their samples, which exhibited a greater value than that of the untreated specimens that might be explained by good local relaxation and greater polymer chain flexibility. That translates into less visible interfacial voids and porosity on treated specimens and also impacts tensile strength [11].

Castillo et al. tackled the relationship between temperature profiles and ultimate tensile strength (UTS) by using a cyber–physical production system (CPPS) that analyzed certain thermal parameters, such as layer thickness, printing speed, extrusion temperature, and bed temperature. The first one was found to be the most influential as UTS registered a 17% increase. The study revealed that good mechanical strength is possible through optimal thermal transition between deposition, adhesion, and layer solidification [12].

The present study aims to present a functional setup that may substitute dedicated, highly expensive, sensor-based systems for the assessment of thermal evolution of 3D-printed samples that were subjected to tensile tests. Video files were recorded for each sample in order to capture peak values and temperature evolution, in time, in such a manner that it would encompass a monitoring system. Statistical methods were employed

that highlight tendencies, depending on input parameters. Scanning electron microscopy (SEM) was used, as well as numerical simulations based on finite element analyses (FEA), that revealed stress distribution as tensile testing was carried out. The proposed setup, which includes the thermal imaging equipment, may account for a sensor-based system used for monitoring anisotropy and mechanical strength in FDM printing systems and is susceptible to system capability analysis. The results confirm initial assumptions and allow statistical analysis with valuable insights. Improvements in terms of printing parameters may overcome defects revealed by fracture analysis. Limitations are present due to equipment capabilities. The authors acknowledge that there may be a research gap because by studying similar work we aim to demonstrate the diversity of scientific approaches and experimental frameworks that address similar concerns in the field while using a custom evaluation system.

2. Materials and Methods

The methodological framework is designed to be replicable by researchers in related fields of mechanical engineering and others, offering a structured approach that integrates both the experimental setup and several analyses that are used as part of the evaluation system as a whole. By documenting these stages, the paper aims to prove reproducibility and transparency, enabling others to adopt or adapt the system according to their specific investigative needs. The proposed workflow can be observed in Figure 1.

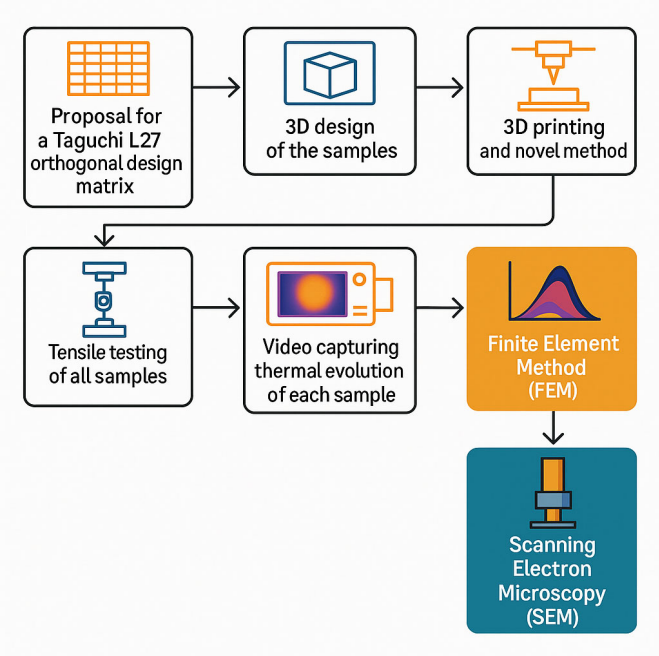

Figure 1. Workflow schematics of experimental testing setups and methods.

2.1. Experimental Testing Setup

The proposed setup involves the HTI HT-18 thermal imaging camera, manufactured by Dongguan Xintai Instrument Co., Ltd. (Dongguan, China), the People's Republic of China, mounted on a tripod. It has a vanadium oxide uncooled infrared focal plane detector with a resolution of 256 × 192 and a cell size of 12 µm. Measurement accuracy varies from −15 °C to 550 °C with ±2% error and a temperature measurement resolution of 0.1 °C. Calibration involved adjusting the emissivity value to match the object being measured, thus for matte surfaces a default of 0.95 was used.

The equipment was placed in front of the universal mechanical testing machine, WDW 50, manufactured by Jinan Hensgrand Instrument Co., Ltd. (Jinan, China), the People's Republic of China (see Figure 2a), used for tensile testing of specimens and structures of various shapes, including cables, profiled bars, plates, springs, and others. The machine is driven by an AD800 closed-loop automated measurement and control system. The driving software (i.e., WinWdw Electronic Universal Testing Machine Measure and Control System, version 2.15.P.E) automatically calculates and stores tensile experimental data such as strength, yield strength, modulus of elasticity, or elongation at break. It has a 50 kN load cell with a 600 × 600 mm^2 testing area. The measurement scale ranges from 0.4% up to 100% full scale (FS). Speed control allows increments of 0.02–100% (FS/min), with the equipment being able to move at rates of 0.005~500 (mm/min).

It used the ISO 527-2:2012 type 1B standard for sample preparation [13]. The 3D models were designed in 3D CAD type of software (i.e., Solid Edge 2023, teacher licensed, version 2210). Scanning electron microscopy was carried out using a SEM VegaTescan LMH II, manufactured by Tescan Orsay Holding, Brno, Czech Republic (see Figure 2b).

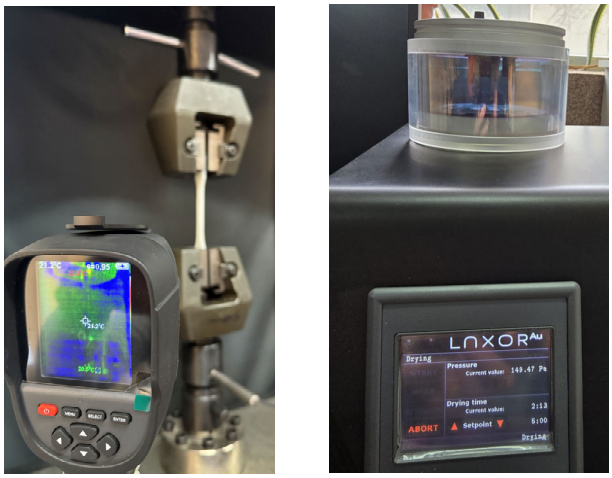

(**a**) (**b**)

Figure 2. Setup of different stages: (**a**) image taken in the laboratory premises for tensile testing and (**b**) image taken in the laboratory premises for scanning electron microscopy.

The aim of this study was to use additive manufacturing to obtain 3D-printed samples that will be subjected to tensile testing. The process requires layer-by-layer deposition to build a part directly from a digital model, with minimal material waste. The fabrication method is favored because several process-related factors exhibit great influence. Material selection affects strength, ductility, and thermal resistance. Poor interlayer bonding leads to weaker mechanical strength as print orientation and path significantly affect anisotropic properties. Process parameters could affect porosity, warping, residual stresses, and surface finish, and uneven cooling can cause internal stresses or cracks.

The authors have tested multiple infill patterns for the 3D-printed specimens with their aim to achieve ones that would exhibit enough temperature variation to be captured by the thermal imagining equipment. It was found that neither produced satisfactory results as fracture occurred too rapidly without any significant burst of thermal behavior. Thus, the present study proposes a printing strategy that would compensate for that.

Specimens were 3D-printed on a Prusa Mk3s+ type of 3D printing equipment and the slicer used was an Orca slicer 2.3.0-beta, which is an open-source type of software. The above-mentioned strategy involves printing concentric walls as opposed to an infill pattern, as observed in Figure 3. The grip area was extended from 17.5 mm to 30 mm for a

better grip, as it was found that the proposed printing strategy allows fractures only in the calibrated area of the specimen since each one exhibited the same behavior during testing.

This type of printing creates layer voids that behave differently depending on the type of material chosen and does account for the brittleness or ductility of the test specimens. It is expected that fibers upon fracture should elongate or even curve as the specimen turns ductile in opposition to brittle ones that should exhibit a sudden, clean cut.

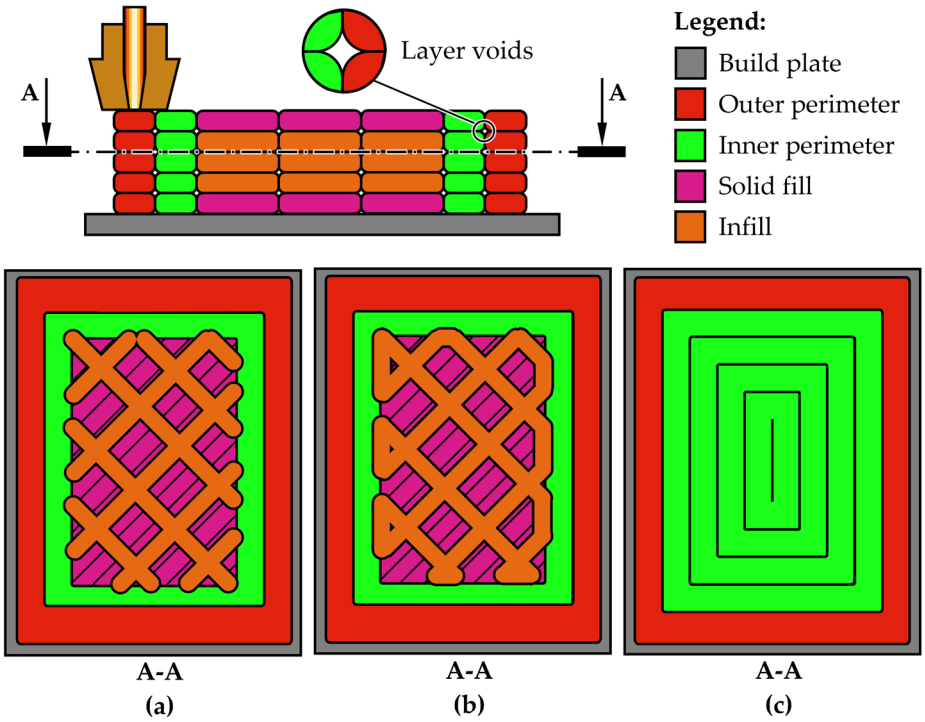

Figure 3. Snapshot from the slicer with the proposed printing strategy: (**a**) standard infill; (**b**) infill with connecting lines; and (**c**) infill with walls.

The first type of infill shows the way the slicer commands the 3D printer to layout each layer. One can see that when the infill pattern meets the inner walls depicted in green, there is a piercing by a tiny fraction, thus creating weak points that will act as stress concentrators (see Figure 3a). This is the reason why the samples prematurely fail. The slicer shows that it enters the wall structure with about 0.1 to 0.2 mm out of the wall's 0.4 m thickness, to allow a steady fusion. The second graphical representation proposes that the infill would take advantage of connecting lines instead of points of intersection (see Figure 3b). This allows a diminishment of the stress concentrators effect but still fails to achieve this study goal of capturing thermal burst upon fracture. The third strategy does not use infill but favors concentrically printing walls with offset (see Figure 3c). This produces layer voids when viewed in section as scanning electron microscopy will reveal. The approximate shape is presented in detail in Figure 3. This strategy offers the benefits of improved toughness along the fiber, because the printed sample is essentially a package of very long, stacked filament.

The design of experiments (DOE) followed a Taguchi L27 orthogonal array, incorporating five input factors, each at three levels of variation. The selected parameters for the 3D-printed samples included: material type, raster height, raster width, material flow rate, and pulling speed during tensile testing, as detailed in Table 1.

Table 1. Taguchi L27 orthogonal design matrix.

Run Ord.	Material	Raster Height (mm)	Raster Width (mm)	Material Flow (%)	Test Speed (m/s) (mm/min)	Avg. Fracture Temp. (°C)	Avg. Load (N)	Avg. Displace-ment (mm)
1	ABS	0.15	0.5	100	50	37.66	37.663	45.165
2					100	50.16	50.163	60.165
3					200	75.16	75.163	90.165
4		0.25	0.6	105	50	38.96	38.963	46.705
5					100	51.46	51.463	61.705
6					200	76.46	76.463	91.705
7		0.35	0.7	110	50	40.26	40.263	48.245
8					100	52.76	52.763	63.245
9					200	77.76	77.763	93.245
10	ASA	0.15	0.6	110	50	40.19	40.188	48.195
11					100	52.69	52.688	63.195
12					200	77.69	77.688	93.195
13		0.25	0.7	100	50	37.74	37.738	45.235
14					100	50.24	50.238	60.235
15					200	75.24	75.238	90.235
16		0.35	0.5	105	50	38.96	38.963	46.685
17					100	51.46	51.463	61.685
18					200	76.46	76.463	91.685
19	rPETG	0.15	0.7	105	50	38.96	38.963	46.725
20					100	51.46	51.463	61.725
21					200	76.46	76.463	91.725
22		0.25	0.5	110	50	40.19	40.188	48.175
23					100	52.69	52.688	63.175
24					200	77.69	77.688	93.175
25		0.35	0.6	100	50	37.74	37.738	45.215
26					100	50.24	50.238	60.215
27					200	75.24	75.238	90.215

The study utilizes three different materials: a white acrylonitrile butadiene styrene (ABS) filament from the company BASF, Emmen, Germany, a red acrylonitrile styrene acrylate (ASA) filament from the company FormFutura, Amsterdam, The Netherlands, and a black recycled polyethylene terephthalate glycol-modified (rPETG) filament also from FormFutura, Tarweweg, the Netherlands. Before printing, all filaments were dried at 70 °C for six hours. During the printing process, the filaments remained in a silica-conditioned enclosure to prevent moisture absorption. The printing parameters adhered strictly to the manufacturers' specifications. For the 3D printer parameters, the raster height varied at 0.15 mm, 0.25 mm, and 0.35 mm, while the raster width levels were set at 0.4 mm, 0.6 mm, and 0.7 mm. These parameters controlled the cross-sectional dimensions of the extruded filaments [14]. The material flow rate was adjusted to 100%,

105%, and 110% of the nominal volumetric flow rate, based on the hypothesis that increased flow rates would reduce internal voids between filament layers. Specimens followed a modified version of the ISO 527-2:2012 type 1B standard, incorporating a 30 mm grip zone. For each parameter combination, five dog bone-shaped specimens were printed using a Prusa Mk3s+ enclosed 3D printer (Prague, Czech Republic), equipped with a 0.6 mm nozzle. After conditioning for 24 h in a controlled laboratory environment (20 °C and 50% relative humidity), the specimens were subjected to tensile testing at three pulling speeds: 50 mm/min, 100 mm/min, and 200 mm/min. It was found that at those values there are results that can be captured by the thermal camera. The mechanical tests were carried out on the WDW 50 [15]. The three above-mentioned types of filaments were chosen among others for their intrinsic thermal properties such as heat capacity (Cp), thermal conductivity (k), and thermal diffusivity ($\alpha = k/\rho \cdot Cp$), where (ρ) stands for density. Approximate values are presented in Table 2.

Table 2. Filament material comparisons.

Property	ABS	ASA	rPETG
Cp [J/g·K]	1.3–1.6	1.4	1.0–1.20
k [W/m·K]	0.128–0.187	0.2	0.24–0.3
α [mm^2/s]	0.11–0.17	0.13–0.18	0.12–0.18

Each of these polymers exhibits distinct thermal behavior. The properties of ABS, an amorphous thermoplastic, offer balanced thermal insulation and dimensional stability during printing [16,17]. The attributes of ASA not only allow for similar processability as ABS but also impart improved resistance to weathering and UV degradation, thus extending its use to outdoor applications where thermal and environmental stability are required [17,18]. On the other hand, recycled PET, a semi-crystalline thermoplastic, exhibits a more thermally complex behavior. Due to post-processing and thermal history, rPETG demonstrates a wide variability in its crystallinity (20–35%), which influences its thermal response during manufacturing and end-use [16,18,19].

2.2. Setup for Thermal Variation Assessment of the Tensile Test Using Finite Element Method (FEM)

The use of the finite element method (FEM) was aimed at replicating experimental tests when fracture of a test specimen occurs. For that purpose, an Ansys researcher license was used. By simulating the entire experimental test, one could obtain similar results by means of finite element analyses (FEA) that would thus be validated. Furthermore, stress and strain distributions may be revealed so that conclusions may be formulated regarding the thermal behavior of specimens under given conditions that otherwise would be difficult to assess.

The present study uses samples obtained by a 3D printing process manipulation in the form of a multiple concentric walls internal layout that favors increased toughness of each specimen inside the calibrated zone during the tensile tests (see Figure 4a).

The 3D model was imported to the Ansys Explicit Dynamics module in Parasolid format. The reason that this module was first used is that FEM aims to replicate one tensile test, including thermal assessment. This is made possible by importing the results of the above-mentioned module into another one, namely Steady-State Thermal module.

It was chosen to use ABS from the software library, which was assigned a non-linear behavior. The material exhibits isotropy, thus transforming the analysis into an ideal setup. An anisotropic type of ABS would predict failure along weaker planes, such as inter-layer boundaries in fused deposition modelling (FDM) printed parts. This makes results prone

to overestimate ductility. To overcome this, the solution was to implement a direction-dependent material model in FEM in the form of an orthotropic material definition, which is based on experimental stress–strain data in different orientations retrieved from previous research [20]. Future endeavors will also use anisotropic failure criteria like Tsai-Wu, Hashin, or maximum stress theory in FEM to capture directional weaknesses.

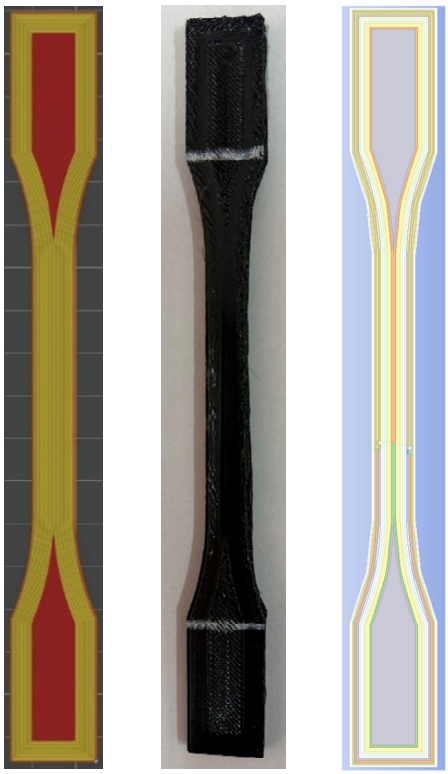

(**a**) (**b**) (**c**)

Figure 4. Specimen model: (**a**) plot of 3D printing process manipulation; (**b**) 3D intermediate printed sample made of ABS; and (**c**) 3D CAD model replica of the wall infill pattern.

The connection branch uses no contacts or body interactions since the 3D model is interpreted as a single body.

Mesh wise, there were several software tools used.

It was assumed that failure would occur in the calibrated area because boundary conditions were set in such a manner that would favor it. Experimental tests revealed that the fracture area is slightly elongated and very abruptly shaped, with leftovers that are irregular and randomly distributed, leading to the conclusion that the triangle type of finite elements must be used for the simulation to succeed.

The body sizing method, in combination with patch conforming that uses both quadratic and triangle-shaped elements, was first imposed. It led to inaccurate results since it was obvious that there was a need for higher-order types of finite elements. Thus, the Hex-dominant method that forces all quads was used. That produced hexagonal elements with eight nodes (Hex8) and wedge-shaped ones with six nodes (Wed6), with acceptable orthogonal quality in the calibrated zone, as can be observed in Figure 5a. Skewness assessment showed that the areas affected are outside the calibrated zone, as can be seen in Figure 5b. The process of meshing produced 19,482 nodes and 6676 elements.

Boundary conditions include a force type-of-load that received the same value as one that has been recorded in experimental testing and a fixed support that holds the sample in place. Thus, tensile testing conditions are met. However, because of the skewness that the mesh quality inquiry has revealed, additional conditions were imposed. Displacements of

zero value on the *Z* axis were introduced for the top and bottom faces, as well as on the *Y* axis, for the lateral faces of the model, as can be observed in Figure 6.

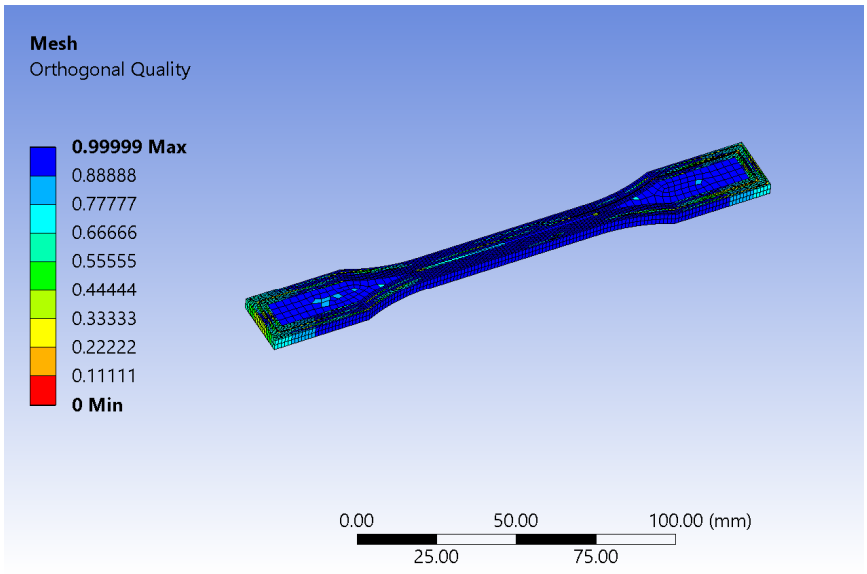

(**a**)

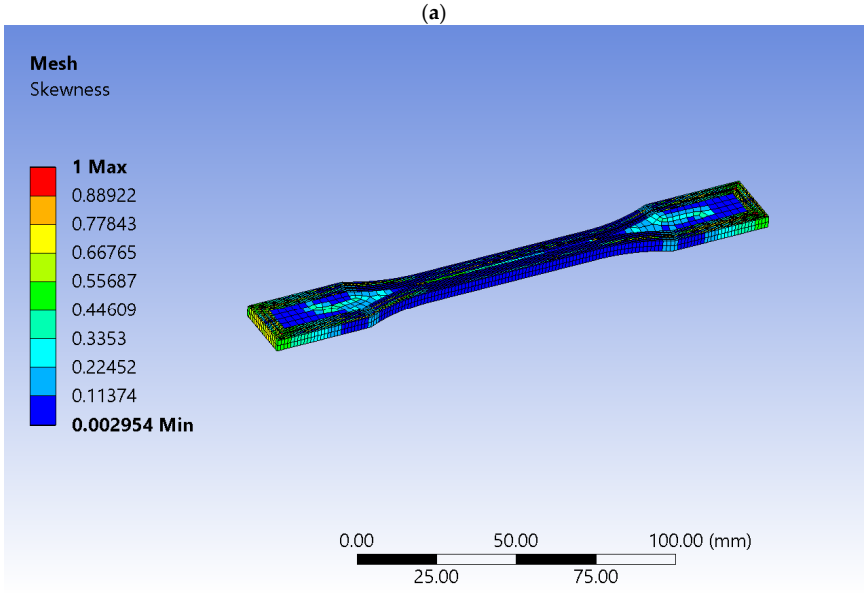

(**b**)

Figure 5. Mesh quality assessment: (**a**) orthogonal and (**b**) skewness.

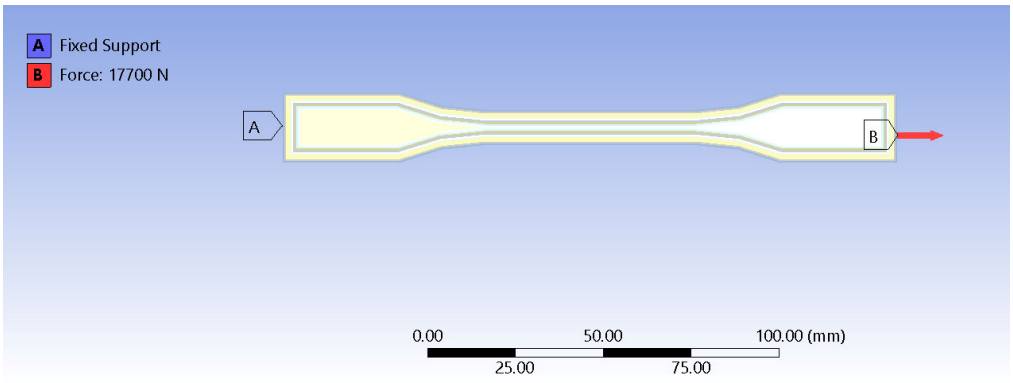

(**a**)

Figure 6. *Cont.*

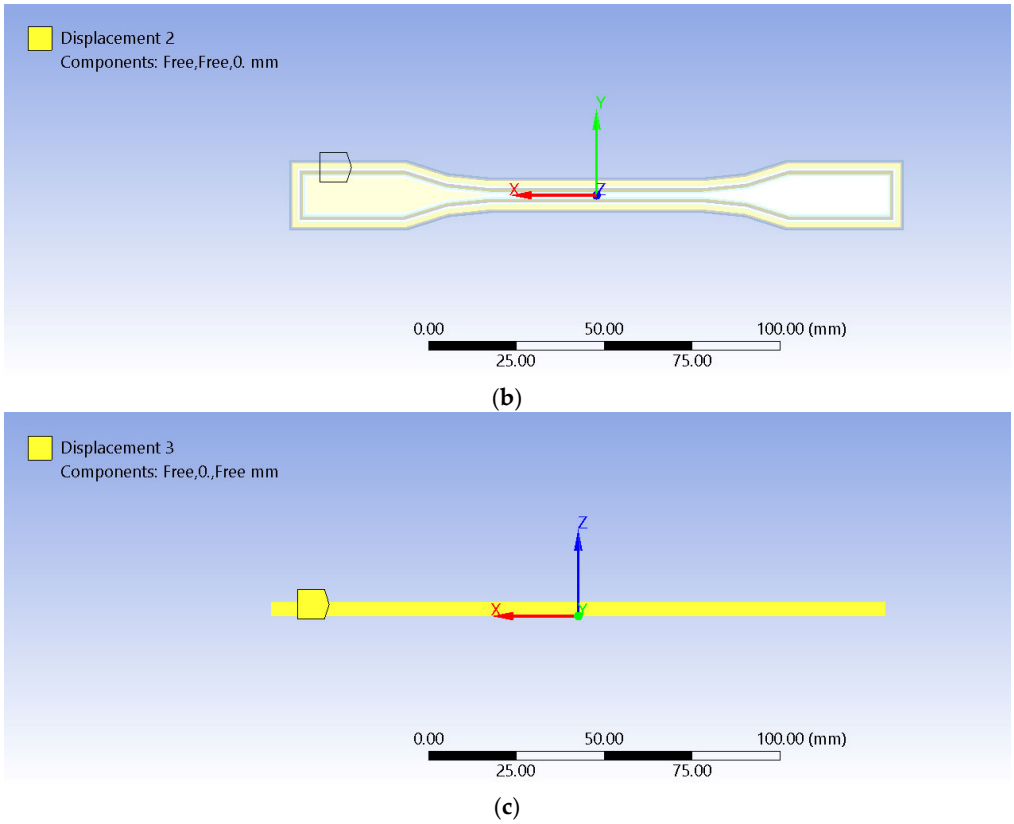

Figure 6. Boundary conditions: (**a**) force type-of-load and fixed support applied at both ends; (**b**) zero displacement on the *Z* axis for upper and bottom faces; and (**c**) zero displacement for lateral faces.

Analysis settings had no automatic mass scaling and a limit of one for the geometric strain limit, which corresponds to 100%. Because FEM aimed to achieve readings as accurately as possible regarding thermal variation, all experimental tensile tests were performed in a laboratory room with temperatures that varied from 19.6 °C to 20.4 °C. Thus, for the randomly chosen test for replication, the temperature reading was of 20.1 °C, which was inputted as an initial condition.

FEM is considered valuable because it allows the assessment of potential failure points that might not be captured in traditional statistical analysis by the identification of stress concentrations. Enhancing statistical models with physical insight often relies on statistical variation of outputs (e.g., stress, displacement). In this regard, FEM allows for the simulation of a wide range of input parameter variations and the incorporation of physics-based constraints into statistical analysis, thus making it more robust.

2.3. Setup for Scanning Electron Microscopy (SEM)

The 3D-printed samples after breakage were analyzed microscopically and macroscopically using a stereomicroscope and a scanning electron microscope (VegaTescan-LMHII, SEM, VegaScan, Brno-Kohoutovice, Czech Republic, SE detector, 10 kV gun power supply) with the software solution VegaTC version 3.5.0.0.

For scanning electron microscopy, the samples were coated with a 7 nm gold layer using Luxor Au plasma deposition equipment produced by Luxor Tech, Nazareth, Belgium, after preliminary vacuuming of the enclosure. Images of the setup from the laboratory are presented in Figure 7.

The analysis followed a standardized protocol: images were converted to 8-bit grayscale, the scale was set based on the magnification (0.2 mm or 0.02 mm), and regions of interest were cropped to sizes of 0.12 × 0.12 mm^2 and 1.25 × 1.25 mm^2, respectively.

Thresholding was applied using the Otsu method, followed by particle analysis to quantify surface porosity. Higher magnification images (500× and 1000×) were used to evaluate micro-void distribution, while lower magnification images (typically 100×) were employed to estimate the percentage of surface area occupied by interlayer voids.

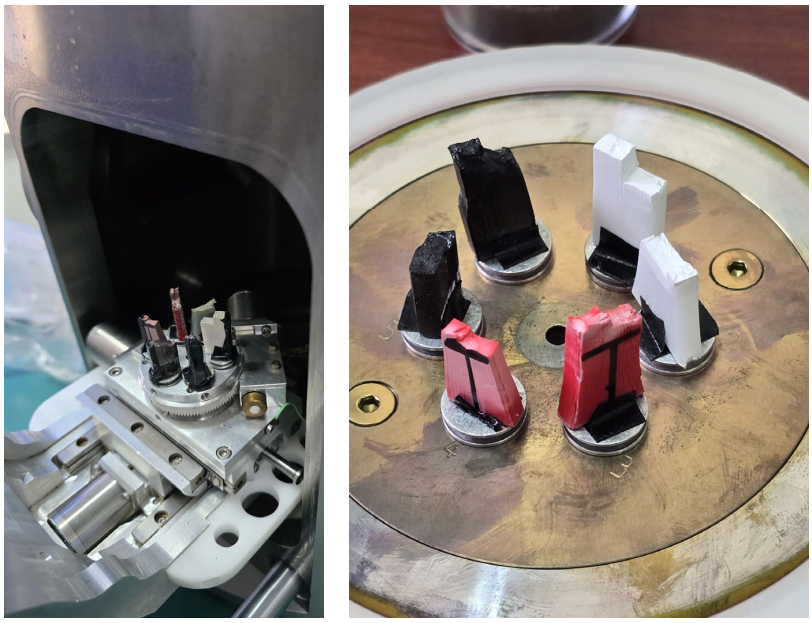

(**a**) (**b**)

Figure 7. Preliminary steps for SEM analyses: (**a**) view of setup and (**b**) sample fixing procedure.

3. Results

Results from tensile tests were recorded and used for a clear view of each type of filament used, as can be observed in Figure 8, as plots were designed for all 27 samples.

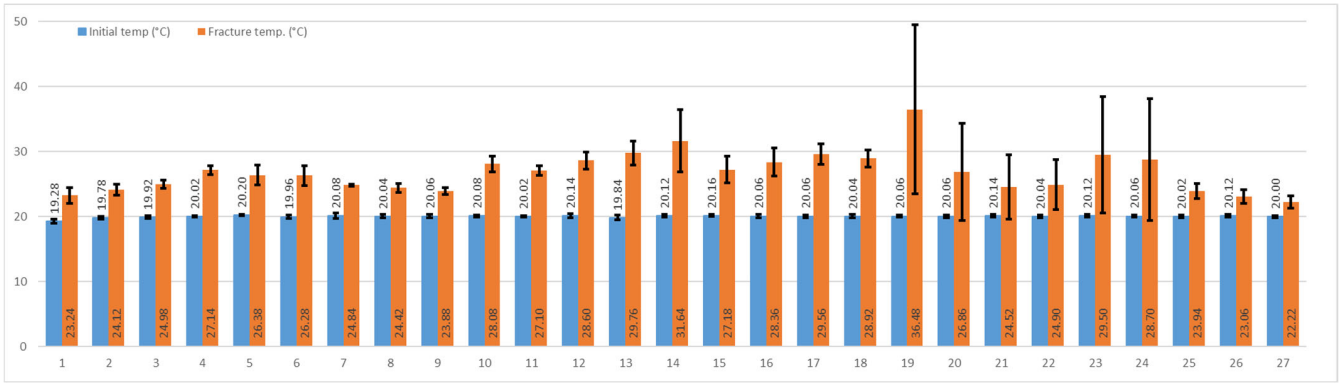

(**a**)

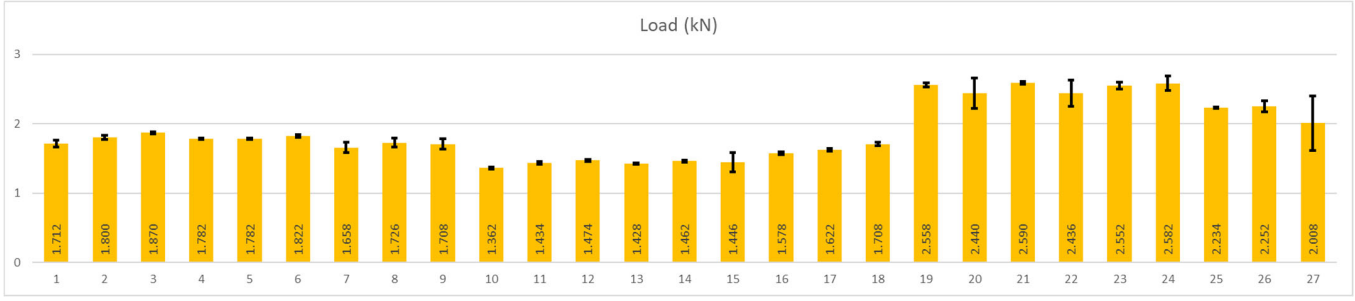

(**b**)

Figure 8. *Cont.*

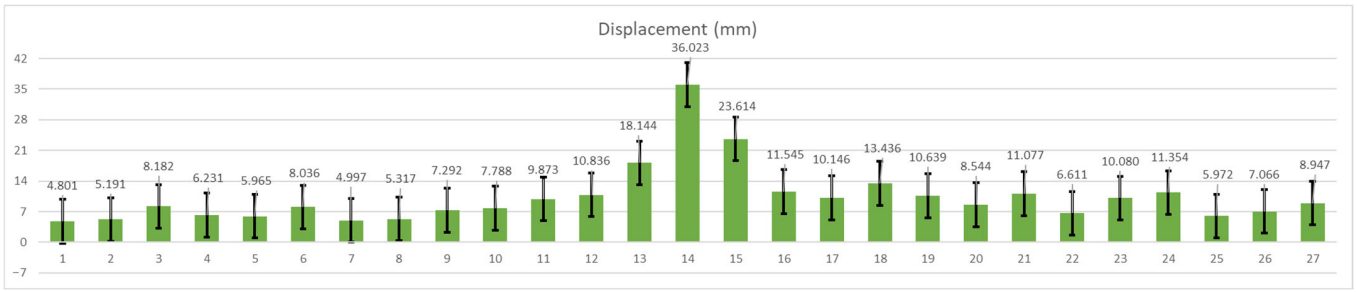

(**c**)

Figure 8. Plots: (**a**) temperature variation; (**b**) load; and (**c**) displacement.

3.1. Statistical Analysis Results

Data evaluation was performed using Minitab 20 software. Analysis of variance (ANOVA) was conducted at a significance level of $\alpha = 0.05$. To enable comparison across different units and variable types, all variables were standardized by subtracting the mean and dividing by the standard deviation. The Taguchi L27 orthogonal design was used because the study aims at statistical relevance, which can be achieved by a wider array of tested specimens. Beginning with the fracture temperature response, the Pareto chart from Figure 9 indicates that material type exerts the most significant influence [21]. The material flow directly influences the raster width and, consequently, the contact area at the interface level in the way that a slight increase results in an additional volume of molten material, which tends to fill the voids between adjacent rasters. This surplus partially overlaps the previously deposited ones, thereby enhancing interlayer adhesion and contributing to increased tensile yield and strength. It is highlighted that the interaction between raster height and raster width plays a critical role in determining the tensile properties, as it affects the cross-sectional geometry of the rasters.

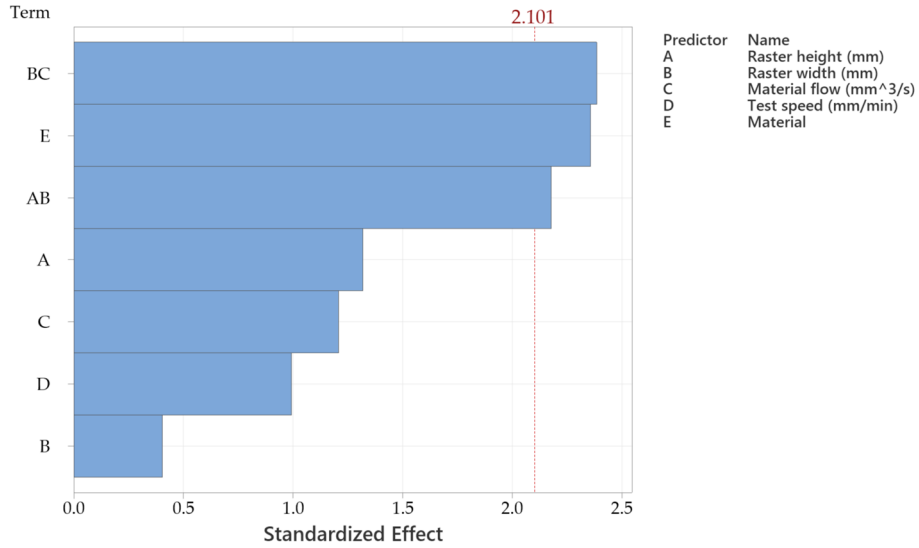

Figure 9. Pareto chart of the standardized variable effects for the samples' temperature at fracture.

As shown in Table 3, the material parameter achieved an F-value of 4.29 and a *p*-value of 0.03. Although the other main factors also affected the temperature response, their individual effects were less significant than certain interaction effects. In particular, the raster width × material flow and raster height × raster width interactions demonstrated statistically significant contributions to fracture temperature variation [22].

Table 3. Analysis of variance of the sample's temperature at fracture.

Source	DF	Seq SS	Contribution	Adj SS	Adj MS	F-Value	*p*-Value
Regression	8	121.530	64.50%	121.530	15.1912	4.09	0.006
Raster height (mm)	1	6.456	3.43%	6.456	6.4560	1.74	0.204
Raster width (mm)	1	0.605	0.32%	0.605	0.6050	0.16	0.691
Material flow (%)	1	5.423	2.88%	5.423	5.4230	1.46	0.243
Test speed (mm/min)	1	3.661	1.94%	3.661	3.6610	0.99	0.334
Material	2	66.641	35.37%	31.860	15.9300	4.29	0.030
Raster height × Raster width	1	17.613	9.35%	17.613	17.6131	4.74	0.043
Raster width × Material flow	1	21.131	11.22%	21.131	21.1313	5.69	0.028
Error	18	66.877	35.50%	66.877	3.7154		
Total	26	188.407	100.00%				

The factorial plots in Figure 10 reveal that the highest fracture temperature occurred in ASA samples printed with a raster height of 0.25 mm, a raster width of 0.7 mm, a material flow of 105%, and pulled at a speed between 50 and 100 mm/min.

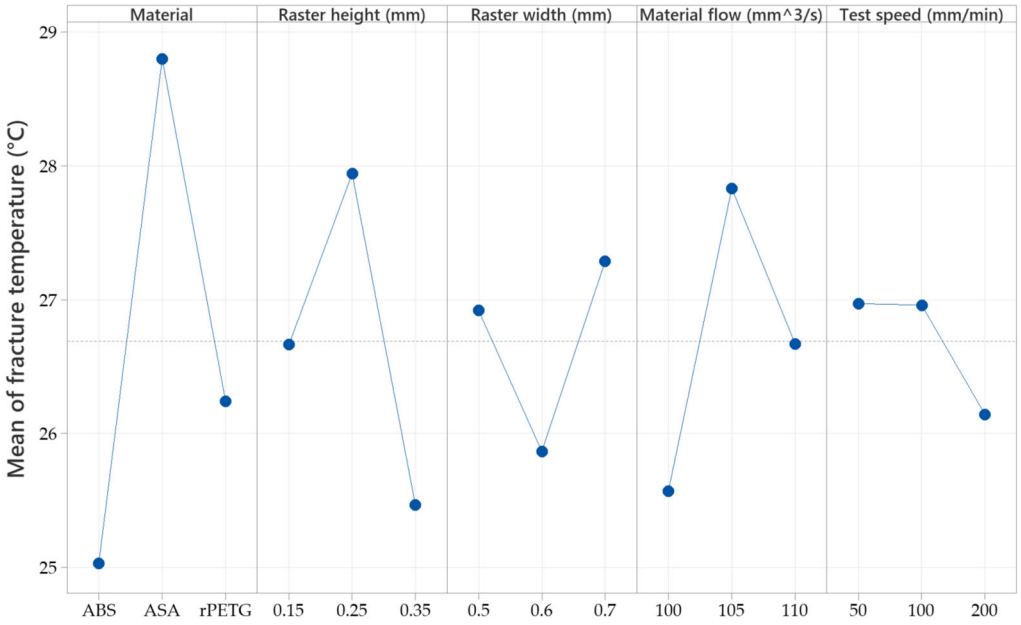

Figure 10. Factorial plots for the samples' temperature at fracture.

Regarding the load capacity response, the Pareto chart from Figure 11 confirms that material type again plays a dominant role, with an F-value of 334.31 and a *p*-value below 0.001.

In this case, additional main effects also contributed significantly, specifically raster width, raster height, and material flow, in descending order of influence [23]. Pulling speed did not show a statistically significant effect. Furthermore, the raster height × raster width and raster height × material flow interactions significantly influenced the load-bearing capacity, as shown in Table 4.

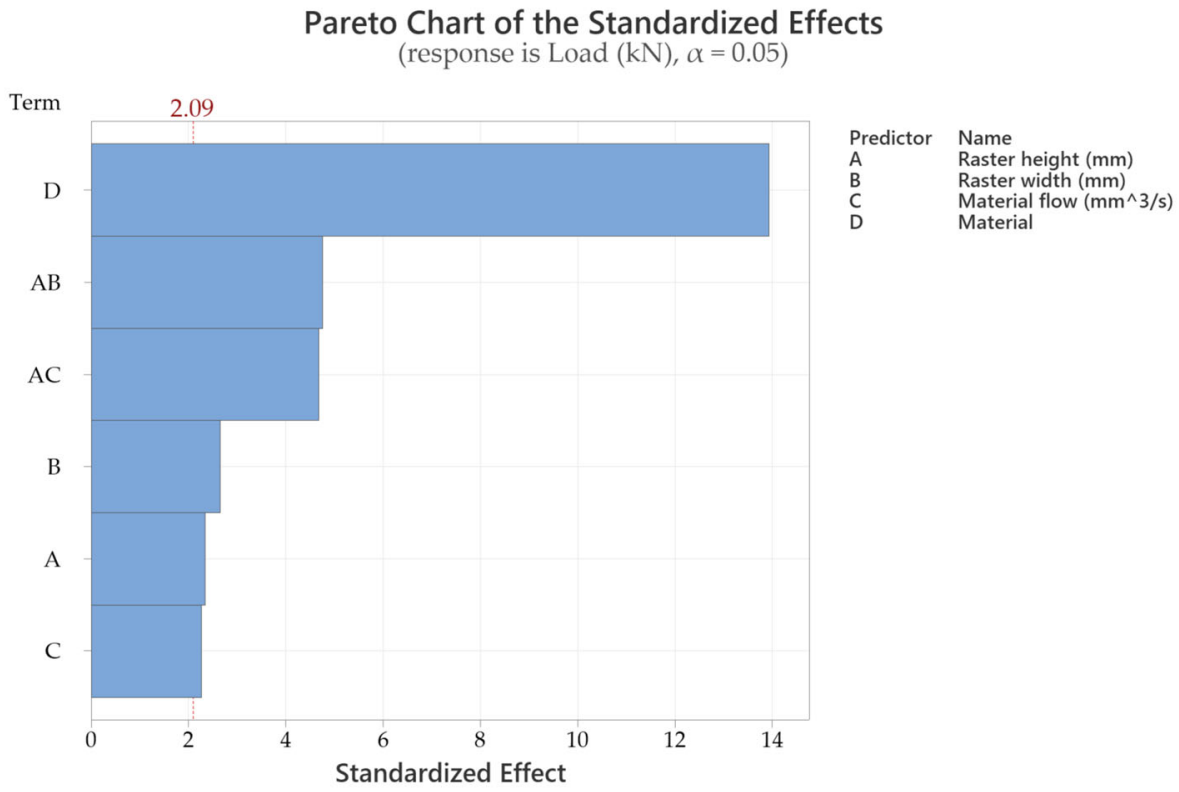

Figure 11. Pareto chart of the variable standardized effects for the tensile load.

Table 4. Analysis of variance of the samples' tensile load (kN) at peak.

Source	DF	Seq SS	Contribution	Adj SS	Adj MS	F-Value	*p*-Value
Regression	7	4.24848	97.55%	4.24848	0.60693	108.19	0.000
Raster height (mm)	1	0.03092	0.71%	0.03092	0.03092	5.51	0.030
Raster width (mm)	1	0.03957	0.91%	0.03957	0.03957	7.05	0.016
Material flow (%)	1	0.02880	0.66%	0.02880	0.02880	5.13	0.035
Material	2	3.89919	89.53%	3.75072	1.87536	334.31	0.000
Raster height × Raster width	1	0.12712	2.92%	0.12712	0.12712	22.66	0.000
Raster height × Material flow	1	0.12288	2.82%	0.12288	0.12288	21.91	0.000
Error	19	0.10658	2.45%	0.10658	0.00561		
Lack-of-Fit	1	0.01338	0.31%	0.01338	0.01338	2.58	0.125
Pure Error	18	0.09320	2.14%	0.09320	0.00518		
Total	26	4.35506	100.00%				

The factorial plots in Figure 12 indicate that the highest load capacity was achieved in rPETG samples printed with a raster height of 0.25 mm, a raster width of 0.5 mm, and a material flow rate of 105%.

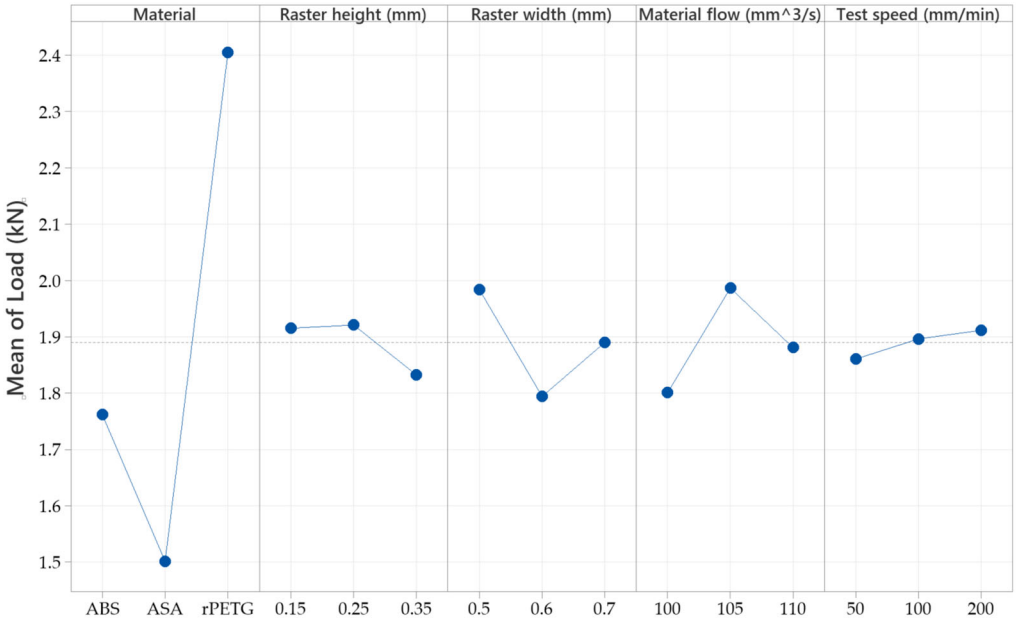

Figure 12. Factorial plots of the samples' tensile load at peak.

3.2. Finite Element Analysis (FEM) Results

Belgen et al. have pioneered measurements of thermal infrared radiation as a valuable tool in the assessment of mechanical properties through their stress pattern analysis by measurement of thermal emission (STATE) proposal [24]. Others have followed and have established a ground basis for future research [25,26].

Results were requested as equivalent stress evaluated under von Mises criteria. We know that the force F measured in a uniaxial tensile test is used to compute the nominal stress σ by the following:

$$\sigma = \frac{F}{A_0} \tag{1}$$

where A_0 is the cross-sectional area of the specimen.

Under uniaxial loading, the von Mises stress σ_v is given by the following:

$$\sigma_v = \sigma \tag{2}$$

However, in a general 3D stress state, the von Mises stress is calculated as follows:

$$\sigma_v = \sqrt{\frac{1}{2}\left[(\sigma_1 - \sigma_2)^2 + (\sigma_2 - \sigma_3)^2 + (\sigma_3 - \sigma_1)^2\right]} \tag{3}$$

For a uniaxial tensile test, the principal stresses are the following:
$\sigma_1 = \sigma$, which is applied stress in the tensile direction;
$\sigma_2 = 0$, assuming no lateral stress in transverse directions;
$\sigma_3 = 0$, assuming no lateral stress in the thickness direction.
Substituting these into the von Mises equation,

$$\sigma_v = \sqrt{\frac{1}{2}\left[(\sigma - 0)^2 + (0 - 0)^2 + (0 - \sigma)^2\right]} \tag{4}$$

we get

$$\sigma_v = \sqrt{\frac{1}{2}[\sigma^2 + \sigma^2]} \tag{5}$$

It results in the following:

$$\sigma_v = \sqrt{\frac{2\sigma^2}{2}} = \sigma \tag{6}$$

The von Mises stress simplifies to the following:

$$\sigma_v = \sigma = \frac{F}{A} \tag{7}$$

Thus, in simple uniaxial tension, the von Mises stress is equal to the applied tensile stress, which is directly proportional to the force registered in the tensile test [27].

FEM shows a maximum value of 33.152 MPa (see Figure 13a) and averages for the mentioned value at 1.7474 MPa. Given that if we are to obtain direct proportionality, we would expect $\sigma_v = k \cdot F$, that would result in 1.02 for the k constant, which is consistent with the mathematical model given that this is an ideal simulation setup. Fracture shape and size are considered consistent between FEM and experimental tests in terms of visual conformance, as can be observed when compared to the image from Figure 13b.

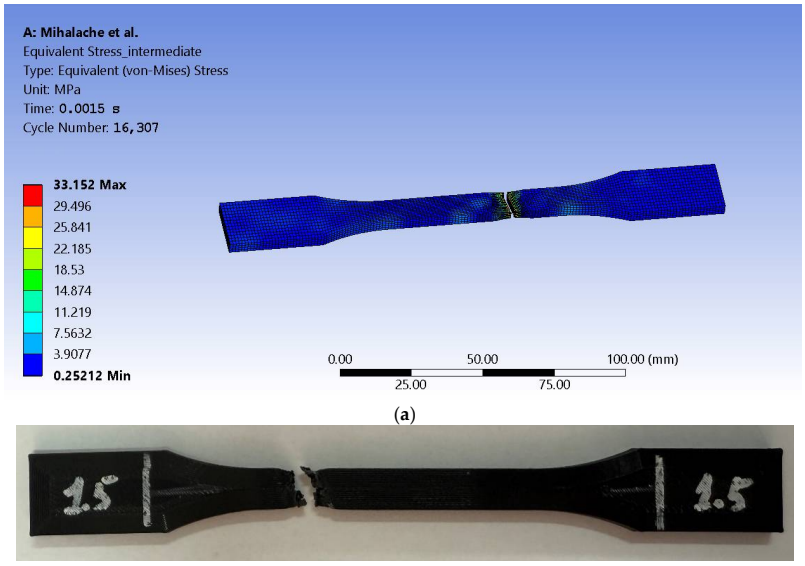

Figure 13. Graphical representation of a specimen: (**a**) simulation given equivalent (von Mises) stress distribution and (**b**) intermediate sample after the tensile test.

By further exporting obtained results to the Steady-State Thermal module of Ansys, it was aimed to highlight thermal variation and distribution up to the necking stage. As it is known, fracture in a tensile test occurs after the material has exceeded its ultimate tensile strength (UTS). Out of the four stages it undergoes (i.e., elastic deformation, plastic deformation, necking, and fracture), FEM resulted in temperature values that were retrieved upon initiation of the third stage, whereas ultimate tensile strength is reached, the material reaches its maximum load capacity. That is because after necking, as the cross-section reduces, stress concentrates in the necked region.

The 20.1 °C temperature value was maintained and assigned to the entire body. The results show a similar distribution as the one recorded by the thermal camera in the experimental test sessions. The simulation peak at 27.043 °C is close to the 27.3 °C recorded by the thermal capture equipment (see Figure 14). The difference between values is explained by quantifying the margin of error. First, it starts by computing the absolute difference between the presented values:

$$\text{Margin of Error } = |27.3 - 27.043| = 0.257\ ^\circ\text{C} \tag{8}$$

The resulting value gives the possibility to compute relative error as follows:

$$\text{Relative Error} = \left(\frac{0.257}{27.3}\right) \times 100 \approx 0.94\% \quad (9)$$

The computed deviation is less than 1%, which is typically found acceptable in thermal simulations. One has to take into account experimental uncertainties such as the precision of the sensor with ±2% error, ambient conditions, which may include uncontrolled airflow or heat losses, and even a slight spatial deviation when placing the probes from the modelled location. FEA modelling assumptions include material properties and possible mesh resolution.

The image in Figure 14b shows a screen capture from a video file and therefore is not at high resolution. Because the camera captures the evolution of temperature during tensile tests, it shows multiple values such as the ones for spot measuring at a specific moment in time as well as the last significant value recorded during the process.

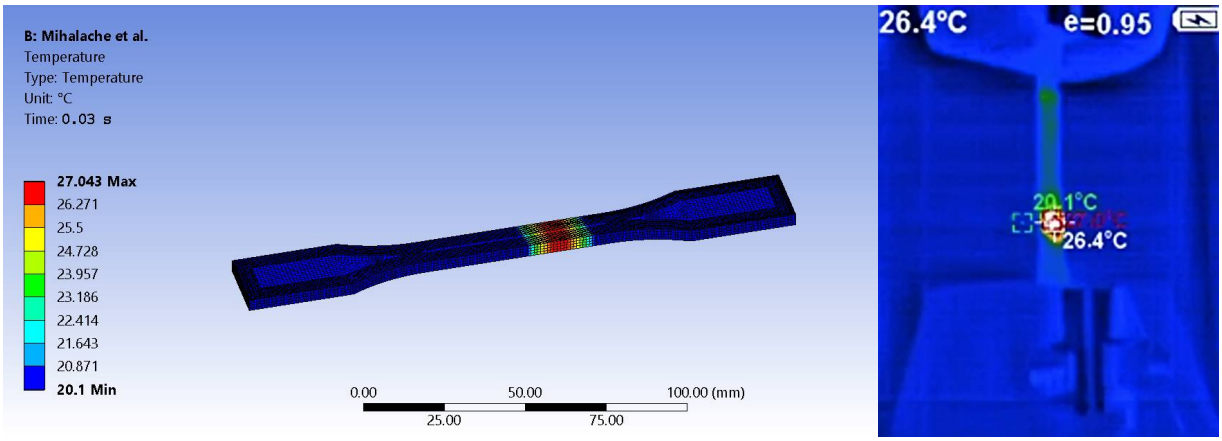

(**a**) (**b**)

Figure 14. Graphical representation of thermal distribution: (**a**) according to FEM and (**b**) recorded live by thermal camera.

The results show that as a material deforms, mechanical work is converted into heat due to plastic deformation and internal friction. The temperature rises due to the strain rate because if we achieve a faster deformation than more heat accumulation will occur as it is in the present case. Again, given the four stages of tensile tests that the specimen undergoes, one may conclude that, after yield strength, the temperature starts to increase, with the mention that higher strain rates lead to a more pronounced rise. Before fracture, localized temperature spikes in the necking region occur as thermal softening may accelerate failure by reducing local material strength. This phenomenon has been captured by FEM. As expected for the ABS, under load, the material shows a rather sharp temperature increase before fracture, which suggests significant plastic work absorption.

By corroborating simulation results with those obtained during experimental tests, one may observe the benefits of using thermal capture equipment in the form of the design of materials for high-temperature environments or high-strain-rate applications (e.g., aerospace and automotive), as well as being useful in fracture mechanics modelling, which may lead to improved failure predictions.

Authors recommend treating results with care since FEM uses an ideal model. Future analyses may take into account that some materials may exhibit slight cooling due to thermoelastic effects, which are interpreted as entropy changes. In addition, the material's thermal conductivity may be assessed by means of thermal imagining, which would capture how quickly heat dissipates.

3.3. Scanning Electron Microscopy (SEM) Results

From a macroscopic point of view, all samples showed, in the middle area and especially on the edges, whitening of the material during the tensile test, until breaking, and afterward, it persisted (Figure 15).

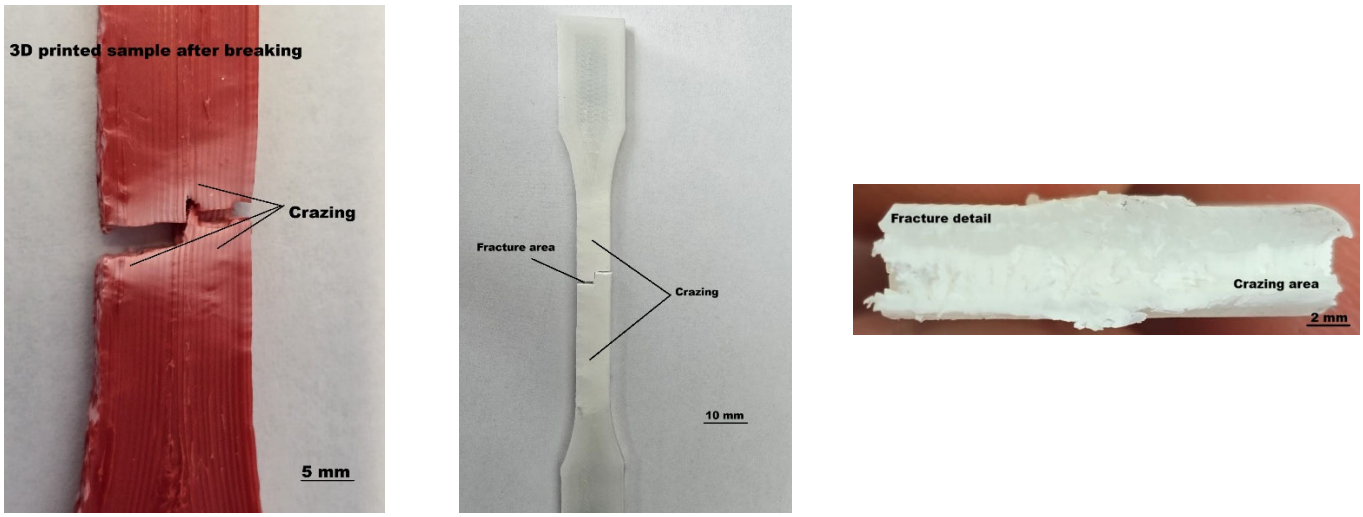

(**a**) (**b**) (**c**)

Figure 15. Snapshots of optical insights of various fractured samples: (**a**) ASA fractured sample; (**b**) ABS fractured sample; and (**c**) detail of the ABS fractured sample.

When 3D-printed plastic samples turn white at the break area after a mechanical test, it is usually due to plastic deformation and microstructural changes in the material. The whitening is primarily caused by light scattering from internal damage (crazes, cracks, and voids) or changes in material structure caused by mechanical stress.

Under mechanical stress, microscopic voids and fibrils form in the polymer matrix—this is known as crazing. A more detailed explanation states that crazing is a stress-induced phenomenon in thermoplastics, where localized areas of plastic undergo microcrack formation. These microcracks are often filled with oriented polymer fibrils that can still carry load, making crazing a precursor to cracking, but not yet full structural failure, and they appear as white, hazy lines or zones, typically perpendicular to the direction of stress. Is common in amorphous thermoplastics like PLA, ABS, and PETG [28].

A different factor that can influence color change is plastic deformation through local yielding that leads to morphological changes in the polymer matrix. Commonly, crazing can manifest in 3D-printed samples due to residual stresses, material choice, environmental exposure, and processing conditions.

This whitening phenomenon originates at the center (highest stress concentration zone) and spreads toward the edges, especially being noticeable at surface layers where deformation is the most visible. It persists after fracture, which is an indication of permanent structural changes, as well as of ductile-to-brittle transition under certain raster angles or loading conditions [29].

First, we have analyzed SEM images (five for each sample) to determine the porosity and layer voids area of the samples using the ImageJ 1.54g (Wayne Rasband and contributors National Institutes of Health, Bethesda, MD, USA) image analysis software. For porosity, areas of 0.12×0.12 mm^2 were analyzed and the results showed a higher porosity for samples 4.4, 5.5, and 12.3 (with values of 4.1%, 2.83%, and 2.09%, respectively), while samples 14.5, 22.2, and 23.2 had lower porosities below 1%: 0.9%, 0.3%, and 0.5%, respectively.

Regarding the analysis of layer voids and their distribution on the surface of the samples, five determinations were also performed; analyses on a surface of 1.56 mm^2 and the following average values were obtained: for sample 4.4, 2.4%, for sample 5.5, 1%, sample 12.3, 6.9%, sample 14.5, 4.8%, sample 22.2, 1.1%, and sample 23.2, 3.1%.

Two SEM samples of each material were chosen to be presented. Graphical images were obtained at different magnification factors. It was chosen to present instances of both macro- and micro-scale with different topology and distribution of fractures so that for each material differences would be highlighted (see Figure 16).

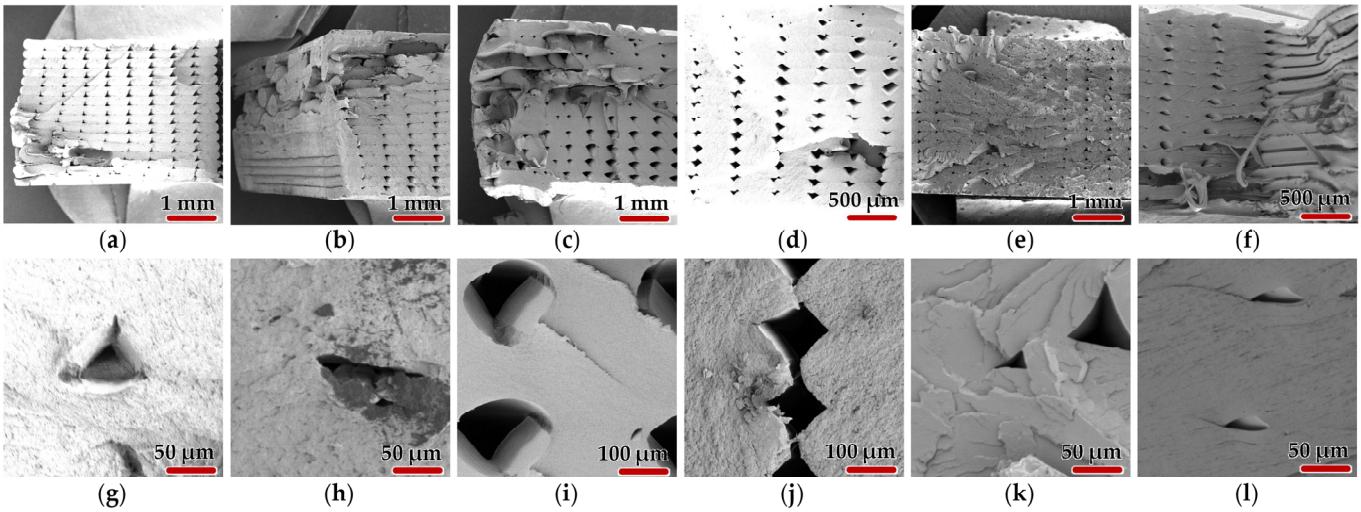

Figure 16. SEM related images of 3D-printed fractured samples at different magnification factors: (**a**) ABS 25x, sample 4.4; (**b**) ABS 25x, sample 5.5; (**c**) ASA 25x, sample 12.3; (**d**) ASA 50x, sample 14.5; (**e**) rPETG 25x, sample 22.2; (**f**) rPETG 50x, sample 23.2; (**g**) ABS 500x, sample 4.4; (**h**) ABS 500x, sample 5.5; (**i**) ASA 250x, sample 12.3; (**j**) ASA 250x, sample 14.5; (**k**) rPETG 500x, sample 22.2; and (**l**) rPETG 500x, sample 23.2.

It can be observed that each material is behaving differently. The results confirm the general knowledge about the three materials: the most ductile is recycled PETG, which typically has high elongation at break, often 20–30% or more; ASA comes next with a typical elongation at break around 10–20%; and ABS being the less ductile among the three, with elongation at break, usually around 5–15% [30]. In the case of ABS, one may observe that layer voids are in a straight line because of sudden fracture, and at the macro-level, the void keeps it shape as it elongates very little. In addition, on edges, one may observe the stacking of fibers, thus confirming the hypothesis of the proposed printing strategy. With ASA, layer voids are beginning to flatten as debonding occurs within the tested specimens (see Figure 16j). It makes fibrils break away and stack upon each other as voids begin to derail from straight lines. rPETG samples suffer the most, as full detachment is present between the layers as voids get flattened out towards the margins of the specimen. Some break away and form thin filiform threads (see Figure 16f).

The formation of flakes is also notable in the case of rPETG. It refers to thin, shard-like fragments that peel or splinter off from the fracture surface during or after the failure of a tensile specimen that are not smooth or ductile tears but rather brittle, lamellar separations or delaminated fragments from the fracture plane. Their formation may be caused by the fact that recycled PETG's often consist of a mix of degraded polymer chains, contaminants, or additive residues. In this case, thermal evolution has a significant influence as molecular weight reduction from thermal history leads to temporal loss of ductility. Of course, one must take into account the fact that the proposed strategy of printing using rPETG is layer-by-layer, which leads to anisotropic strength that under stress delaminates, producing

flake-like fracture patterns, especially along layer lines or flow lines (see Figure 16k). Repeated melting during recycling may also create heterogeneous crystallinity, which amplifies flaking.

4. Conclusions

When assessing thermal evolution, implications during tensile fracture refer to material intrinsic properties: ABS and ASA both have low *Cp* and *k*, which leads to more pronounced local temperature rise where it is presumed that heat remains localized, potentially softening the fracture zone. rPETG has a slightly higher *Cp* and *k*, therefore allowing for more thermal buffering and less localized heating but slower temperature spikes. One may conclude that the temperature rise during fracture is affected by how well the material absorbs (*Cp*) and dissipates (*k*, *α*) the heat generated during deformation. Tensile testing-wise, under smaller loads, ASA samples showed greater displacements. ABS samples need sustained loads, generally greater than ASA but do show cleaner, sharp fractures. The rPETG samples require the greatest loads among all but show displacements similar to ABS in values.

The present study focused on evaluating material behavior under quasi-static loading conditions using fixed strain rates. While this approach provides valuable insights into baseline mechanical performance, it is recognized that real-world applications often involve dynamic or impact loading with variable strain rates. Future work will aim to address these conditions to offer a more comprehensive understanding of the material response under practical service environments.

Scanning electron microscopy revealed that fracture surfaces of ASA material samples exhibit the smallest dispersion in fracture shape. Flakes are more pronounced in the case of rPETG given its modified form. Poor thermal bonding or oxidation may further weaken polymer chain entanglement as under an SEM microscope; fibrillar pull-out and voids between flakes may be observed. ABS samples are the cleanest ones in terms of fracture because of sustained loads and small displacements after tensile testing.

The combination of 3D-printed specimens, tailored process parameters, controlled testing conditions, and thermal imaging has proven effective in establishing a coherent thermal measurement system. The proposed approach demonstrated sufficient sensitivity in detecting variations in mechanical response in tensile testing. This unified methodology represents a viable alternative to conventional sensor-based systems, offering a non-intrusive, flexible, and cost-effective solution for real-time thermal evaluation in experimental and applied research contexts.

Author Contributions: Conceptualization, M.A.M. and V.M.; methodology, M.A.M., L.A. and N.C.; software, V.E. and M.A.M.; validation, V.E., M.A.M. and N.C.; formal analysis, V.M., F.N. and N.C.; investigation, V.E., M.A.M., L.A. and N.C.; resources, V.M. and F.N.; data curation, F.N.; writing—original draft preparation, M.A.M.; writing—review and editing, V.M.; visualization, M.A.M. and N.C.; supervision, V.M.; and project administration, V.M. All authors have read and agreed to the published version of the manuscript.

Funding: This research received no external funding.

Data Availability Statement: Information supporting the reported results can be obtained upon request to the authors.

Conflicts of Interest: The authors declare no conflicts of interest.

Abbreviations

The following abbreviations are used in this manuscript:

ANOVA	analysis of variance
DOE	design of experiments
FEM	finite element method
SEM	scanning electron microscopy
DSC	differential scanning calorimetry
TGA	thermogravimetric analysis
PLA	polylactic acid
TPU	thermoplastic polyurethane
CF-PLA	carbon fiber-reinforced polylactic acid
PMMA	polymethyl methacrylate
Tg	glass transition temperature
GRA	grey relational analysis
TC	thermal conductive
TTS	time–temperature superposition
UTS	ultimate tensile strength
CPPS	cyber–physical production system
FEA	finite element analyses
FDM	fused deposition modelling
ABS	acrylonitrile butadiene styrene
ASA	acrylonitrile styrene acrylate
rPETG	recycled polyethylene terephthalate glycol-modified
PET	polyethylene terephthalate

References

1. Hamidi, M.N.; Abdullah, J.; Mahmud, A.S.; Hassan, M.H.; Zainoddin, A.Y. Influence of thermoplastic polyurethane (TPU) and printing parameters on the thermal and mechanical performance of polylactic acid (PLA)/thermoplastic polyurethane (TPU) polymer. *Polym. Test.* **2025**, *143*, 108697. [CrossRef]
2. Jin, P.; Pan, T.; Li, Y.; Zhong, T.; Jiang, J.; Pu, C.; Ma, C. Performance and thermal properties of 3D printed CF-reinforced PLA monofilaments. *Coatings* **2024**, *14*, 1479. [CrossRef]
3. Švantner, M.; Lang, V.; Skála, J.; Kohlschütter, T.; Šroub, J.; Muzika, L.; Klepáček, J.; Honner, M. Compact thermographic device with built-in active reference element for increased measurement accuracy. *Eng. Proc.* **2023**, *51*, 17.
4. Pei, Y.; Shen, Z.; Zhou, J.; Yang, B. Experimental and theoretical thermal performance analysis of additively manufactured polymer vacuum insulation panels. *Appl. Therm. Eng.* **2024**, *256*, 123957. [CrossRef]
5. Kang, C.; Peng, L.; Li, Y.; Zong, J. Mechanical performance of structural polymethyl methacrylate joints at different temperatures. *Polymers* **2024**, *16*, 3243. [CrossRef]
6. Rezayiye, R.K.; Laurent, K.; Nooralishahi, P.; Ibarra-Castanedo, C.; Maldague, X. Thermal data augmentation approach for the detection of corrosion in pipes using deep learning and finite element modelling. *Eng. Proc.* **2023**, *51*, 20.
7. Kahya, C.; Tunçel, O.; Çavuşoğlu, O.; Tüfekci, K. Thermal annealing optimization for improved mechanical performance of PLA parts produced via 3D printing. *Polym. Test.* **2025**, *144*, 108735. [CrossRef]
8. Fujita, R.; Kudo, N.; Abe, S.; Mohammad Fikry, M.J.; Koyanagi, J.; Ogihara, S.; Nagano, H. Non-destructive fatigue evaluation through thermophysical properties using lock-in thermography. *Eng. Proc.* **2023**, *51*, 34.
9. Demarbaix, A.; Juste, E.; Verlaine, T.; Strazzeri, I.; Quinten, J.; Notebaert, A. Investigating defect detection in advanced ceramic additive manufacturing using active thermography. *NDT* **2024**, *2*, 504–518. [CrossRef]
10. Roudný, P.; Syrový, T. Thermal conductive composites for FDM 3D printing: A review, opportunities and obstacles, future directions. *J. Manuf. Process.* **2022**, *83*, 667–677. [CrossRef]
11. Nguyen, K.Q.; Vuillaume, P.Y.; Hu, L.; Vachon, A.; Diouf-Lewis, A.; Marcoux, P.L.; Robert, M.; Elkoun, S. Effect of in situ thermal treatment on interlayer adhesion of 3D printed polyetherimide (PEI) parts produced by fused deposition modeling (FDM). *Mater. Today Commun.* **2024**, *39*, 108588. [CrossRef]
12. Castillo, M.; Monroy, R.; Ahmad, R. Design of experiments to compare the mechanical properties of polylactic acid using material extrusion three-dimensional-printing thermal parameters based on a cyber–physical production system. *Sensors* **2023**, *23*, 9833. [CrossRef]

13. *ISO 527-1:2019*; Plastics—Determination of Tensile Properties—Part 1: General Principles. International Organization for Standardization: Geneva, Switzerland, 2019.
14. Sajjadi, S.A.; Ghasemi, F.A.; Rajaee, P.; Fasihi, M. Evaluation of fracture properties of 3D printed high impact polystyrene according to essential work of fracture: Effect of raster angle. *Addit. Manuf.* **2022**, *59*, 103191. [CrossRef]
15. Cantrell, J.; Rohde, S.; Damiani, D.; Gurnani, R.; DiSandro, L.; Anton, J.; Young, A.; Jerez, A.; Steinbach, D.; Kroese, K.; et al. Experimental characterization of the mechanical properties of 3D printed ABS and Polycarbonate parts, Chapter 11. In *Advancement of Optical Methods in Experimental Mechanics*; Springer: Berlin/Heidelberg, Germany, 2016; Volume 3, pp. 89–105.
16. Wypych, G. *Handbook of Polymers*, 2nd ed.; ChemTec Publishing: Toronto, ON, Canada, 2016.
17. NETZSCH Analyzing & Testing. Thermal Characterization of Polymers: Thermoplastics, Thermoplastic Elastomers, Elastomers and Thermosets. 2020. Available online: https://analyzing-testing.netzsch.com (accessed on 17 June 2025).
18. Paesano, A. *Handbook of Sustainable Polymers for Additive Manufacturing*; CRC Press: Boca Raton, FL, USA, 2022.
19. NETZSCH Group. *Thermal Analysis and Rheology in Polymer Additive Manufacturing*, 1st ed.; Netzsch Buch: Selb, Germany, 2023.
20. Mihalache, A.M.; Ermolai, V.; Sover, A.; Nagît, G.; Boca, M.A.; Slatineanu, L.; Hrituc, A.; Dodun, O.; Rîpanu, M.I. Tensile behavior of joints of strip ends made of polymeric materials. *Polymers* **2022**, *14*, 4990. [CrossRef]
21. Galeja, M.; Hejna, A.; Kosmela, P.; Kulawik, A. Static and dynamic mechanical properties of 3D printed ABS as a function of raster angle. *Materials* **2020**, *13*, 297. [CrossRef] [PubMed]
22. Zhang, Y.; Ye, H.; Yuan, L.; Luo, C.; Ren, X.; Yu, Q.; Chen, J.; Gao, Q.; Lei, Y.; Cheng, Y.; et al. The effect of weak interface on the fracture behavior of material extrusion 3D-printed polyetherimide. *Appl. Mater. Today* **2023**, *34*, 101905. [CrossRef]
23. Ayatollahia, M.R.; Nabavi-Kivia, A.; Bahramia, B.; Yahyab, M.Y.; Khosravani, M.R. The influence of in-plane raster angle on tensile and fracture strengths of 3D-printed PLA specimens. *Eng. Fract. Mech.* **2020**, *237*, 10722. [CrossRef]
24. Belgen, M.H. Structural stress measurements with an infrared radiometer. *ISA Trans.* **1967**, *6*, 49–53.
25. Wong, A.K.; Sparrow, J.G.; Dunn, S.A. On the revised theory of the thermoelastic effect. *J. Phys. Chem. Solids* **1988**, *49*, 395–400. [CrossRef]
26. Pron, H.; Bissieux, C. 3-D thermal modelling applied to stress-induced anisotropy of thermal conductivity. *Int. J. Therm. Sci.* **2004**, *43*, 1161–1169. [CrossRef]
27. Alarifi, I.M. Mechanical properties and numerical simulation of FDM 3D printed PETG/carbon composite unit structures. *J. Mater. Res. Technol.* **2023**, *23*, 656–669. [CrossRef]
28. Torrado Perez, A.R.; Roberson, D.A.; Wicker, R.B. Fracture surface analysis of 3D-printed tensile specimens of novel ABS-based materials. *J. Fail. Anal. Preven.* **2014**, *14*, 343–353. [CrossRef]
29. Cahyadi, W. Mechanical Properties of 3D Printed Acrylonitrile Styrene Acrylate. Master's Thesis, South Dakota State University, Brookings, SD, USA, 2019.
30. Sedlak, J.; Joska, Z.; Jansky, J.; Zouhar, J.; Kolomy, S.; Slany, M.; Svasta, A.; Jirousek, J. Analysis of the mechanical properties of 3D-printed plastic samples subjected to selected degradation effects. *Materials* **2023**, *16*, 3268. [CrossRef] [PubMed]

Wiley
International Journal of Polymer Science
Volume 2026, Article ID 3357501, 11 pages
https://doi.org/10.1155/ijps/3357501

WILEY

Research Article

Geometrical and Dimensional Accuracy of Pine-Based Polymer Composites Produced by FDM

Irina Beşliu,[1] **Ioan Tamaşag**,[1] **and Andrei Mihalache**[2]

[1]*Mechanical and Technology Department, Stefan cel Mare University of Suceava, Suceava, Romania*
[2]*Department of Machine Manufacturing Technology, "Gheorghe Asachi" Technical University of Iaşi, Iaşi, Romania*

Correspondence should be addressed to Irina Beşliu; irina.besliu@usm.ro

Received 29 July 2025; Revised 12 October 2025; Accepted 8 December 2025

Academic Editor: Renhui Qiu

Fused deposition modeling (FDM) is the most widely used additive manufacturing technology due to its simplicity and undeniable advantages. In the current context, marked by the orientation towards a sustainable bioeconomy, research focuses on the development and use of biodegradable materials, of which wood-polymer composites (WPC) have gained increased interest in recent years. The purpose of this work is to investigate the dimensional and shape accuracy of parts made by FDM technology from a wood-based polymer, with an emphasis on the accuracy of the holes and the quality of the surfaces obtained. The research methodology is based on a complete factorial plan, analyzing the influence of some process parameters on the performance of the parts. The results are compared with those obtained for similar parts made of PLA under the same printing conditions. The findings highlight the critical factors that influence geometric accuracy and surface appearance, highlighting the advantages and limitations of using sustainable materials in additive manufacturing.

Keywords: dimensional accuracy; FDM; hole accuracy; PLA; shape accuracy; wood-polymer composite

1. Introduction

Additive manufacturing (AM) is a technology in full ascension and development. The rapid growth of this technology is mostly related to its high potential. AM can help improve the efficiency of manufacturing by reducing the manufacturing time and production costs. Fused deposition modeling (FDM) belongs to the material extrusion (MEX) family of AM processes, as defined by ISO/ASTM standards [1].and is one of the most commonly known and widely used techniques of the AM. FDM has prevailed due to its simplicity and accessibility, being used both in prototype applications and in the production of functional parts. However, parts obtained through FDM often present challenges related to dimensional and shape accuracy, as well as surface quality, critical aspects of mechanical components. Also, most of the materials that are used in 3D printing have high costs and raise a series of problems related to environmental sustainability.

In parallel, current sustainability requirements have directed research towards biodegradable materials and bio-based composites, such as polymer–wood composites. WPC is the acronym usually used when referring to wood-based polymers or wood-plastic composites. These materials are composite materials obtained by a polymeric matrix and wood particles that typically result from industrial waste such as sawdust, wood shavings, or reclaimed wood. The use of recycled materials helps reduce the environmental impact, promotes sustainable resource use, and lowers the amount of waste going to landfills. The European bioeconomy strategy highlights the use of wood as one of the cornerstones for sustainable economic growth [2, 3].

Even if these materials offer promising opportunities, they raise additional difficulties in controlling dimensional deviations and geometric quality of printed parts.

Wood-polymer composites can be used to create a wide variety of parts and products in various industries, from furniture and construction parts to automotive components

such as interior panels, trunk liners, and flooring. The main advantages of these materials are durability, weather resistance, and flexibility in design. In addition, WPC parts combine some of the environmental advantages of wood with the durability of polymers, resulting in materials that are more resistant to moisture and biological degradation and generally require less maintenance than natural wood in certain applications. However, the incorporation of wood fibers or particles into a polymer matrix presents several challenges, such as particle agglomeration, void formation, poor adhesion between fibers and matrix, printer nozzle clogging due to filler inclusions, longer curing time, and additional stresses in the material [4].

AM with wood composites faces challenges such as processing difficulties in extrusion and part production, especially concerning the dimensional stability of components and the material's brittleness based on the wood content's loading level, along with impacts on the polymer's crystallization behavior during processing. In some instances, the mechanical and physical characteristics of printed parts may come close to the property range of traditional wood composites like particleboard, fiberboard, and wood-thermoplastic composites [5].

Findings indicate that FDM manufacturing at various printing speeds significantly influences the surface color, surface roughness, density, and compressive characteristics of the WPC part produced by FDM printing [6]. Another study [7] indicates that fill density is the most critical factor affecting tensile strength, with building orientation and layer height next in significance, whereas printing speed appears to have no considerable impact on the mechanical properties investigated.

In addition to offering excellent mechanical characteristics, the wood-polymer composite material has been reported by Mazlan et al. [8] to enhance dimensional accuracy by ensuring stability throughout the printing process of thin-walled parts. The study also showed that wood-based polylactic acid (PLA) aids in minimizing the warping effects commonly seen in thermoplastic materials. Good accuracy for the 3D printed wood-based polymer composite parts had also been outlined by Cekic et al. [9]. They demonstrated that through optimization of the significant process parameters small variations in the dimensions and form of the 3D printed part along with improved product quality can be achieved.

The research carried out in the field of 3D printing PLA-wood composites is rather recent and is mainly concentrating on their mechanical properties.

This study is aimed at analyzing the influence of some 3D printing parameters on the dimensional and form accuracy of holes in pine-based wood-polymer composite FDM parts. When printing composites with wood fibers, there may be some limitations in terms of detail fineness and dimensional accuracy. Also, uneven distribution of fibers in the filament can lead to inconsistencies in extrusion.

There are several aspects that must be taken into consideration when printing parts with holes if certain accuracies must be obtained [10–15]. Besides the usual discussed machining parameters—the printing speed, printing temperature, layer height—there are also other factors like the nozzle dimension, infill pattern, infill density, printing direction, wall thickness, and number of wall loops that can influence the 3D printed hole accuracy.

Popescu et al. [10] showed that the most relevant process parameters affecting the holes' dimensional accuracy of 3D printed PLA parts are the layer thickness and the number of shells around the holes. Another study carried out by Petruse et al. [11] reported that when 3D printing, holes' dimensional deviations were significantly influenced by the size of the nozzle and the height of the layers, and that surface roughness parameters Ra and Rz are also strongly influenced by the print speed and nozzle size, indicating that reduced speeds and smaller nozzles produce better finishes. Boca et al. had investigated the dimensional accuracy of plastic parts by testing five polymer-based materials (PLA, ABS, PP, PA, and PET). They concluded that the best hole dimensional accuracy from the materials used was obtained for the PLA 3D printed parts. The literature review shows that most of the existing studies on WPC parts obtained by FDM have focused on mechanical characterization and general surface properties.

In a study published by Jayakumar et al. [16], it was demonstrated that the Taguchi L9 method can be efficiently applied to optimize FDM printing parameters, with the infill pattern and layer height exerting the greatest influence, thereby ensuring high dimensional and geometric precision in PLA samples.

Factors such as bed and nozzle temperature, nozzle diameter, print speed, fill density and angle, as well as layer height, have been shown to significantly affect the dimensions of FDM fabricated screws and nuts. By adjusting these parameters, variations of up to 4% were obtained for bolt diameters and 7% for nut diameters [17]. These findings emphasize the importance of parameter optimization, including the interactions between them, to obtain complex parts with increased precision.

There are studies that evaluate the dimensional accuracy of FDM parts through indirect measurements such as weighing. The experimental results in the case of PLA parts revealed a variation of approximately 8% from the designed dimensional values [18]. This highlights the need to optimize the printing parameters to improve the geometric fidelity of the components.

Results reported in another study demonstrated that material type and layer thickness are the most important factors, contributing 49.25% and 17.97%, respectively, to the dimensional accuracy of circular geometries, which underlines the sensitivity of FDM printing in making holes and other round contoured shapes [19]. Scanning electron microscopy analysis revealed significant differences in surface morphology depending on printer and print parameters, providing practical guidance for selecting optimal settings to achieve superior surface quality and hole accuracy in FDM parts [20].

Studies have shown that for parts made of WPC, dimensional accuracy and surface quality decrease as the wood content increases, indicating a greater sensitivity of these parts to variations in printing parameters [21].

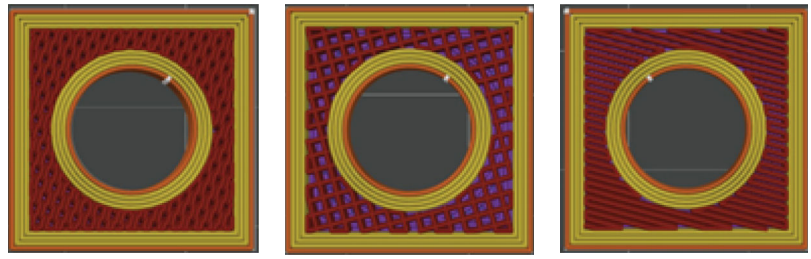

(a) (b) (c)

Figure 1: Infill pattern used: (a) honeycomb; (b) grid; (c) aligned rectilinear.

The holes obtained by 3D printing expose several downsides, such as the seam lines between layers, material shrinkage, and warping phenomenon that compromise the dimensional accuracy of the printed part. Things get even more difficult when 3D printing wood-fiber polymer composites. Wood fibers can make the composite more abrasive, leading to loss of precision. Also, fibers can cause clusters leading to uneven deposition. From the shrinkage point of view, the wood-based polymers offer some advantages. Wood fibers can provide dimensional stability, reducing shrinkage during cooling. This can help maintain the shape of the printed part. Although a good mixture between fibers and matrix can reduce shrinkage, poor compatibility can lead to deformations.

However, there is little research that addresses in detail the dimensional and shape accuracy of geometric elements such as holes, especially in relation to the influence of nonconventional process parameters such as fill type or rasterization angles. This gap highlights the need for dedicated studies that provide a deeper understanding of how these parameters affect the performance of parts made from sustainable materials. In this context, the objective of the present study is to systematically investigate the accuracy and surface quality of holes made from a polymer–wood composite, compared with PLA, by using a full factorial design. The results contribute both to the foundation of knowledge on the behavior of WPC in AM and to the expansion of the use of bio-based materials in industrial applications.

2. Materials and Methods

The paper analyzes the influence of some nontraditional 3D printing parameters: the infill pattern, the raster angle, and number of wall loops on the accuracy of 3D printed holes. Two types of filaments were used in the tests—a PLA wood-based polymer and PLA. A different set of experiments were carried out for the two types of filaments. The wood-based composite filament used was a commercially available produced by AzureFilm, from Slovakia—PLA wood pine with 1.75 mm diameter [22, 23]. The filaments compound contains a mix of 60% PLA, with 40% recycled wood. In order to properly determine the printing capabilities for the WPC filament, a set of experiments using the same printing conditions was also performed for a 100% PLA filament. The PLA filament used in the second set of experiments was premium PLA—Frosty White, produced by FormFutura, from Netherlands [24, 25].

Three different infill patterns were considered for the experiments Figure 1. The type of infill will determine to some extent the expansion and contraction during printing. It is desirable for the infill to provide a rigid structure, which can help maintain the shape of the part and prevent warping. The types of infill chosen in this investigation were: grid, honeycomb, and aligned rectilinear. Each type of infill has specific geometric characteristics that influence the structural performance and accuracy of printed parts. The geometry of the grid infill contains lines that are arranged in two perpendicular directions forming a grid of squares or rectangles. Honeycomb infill mimics the structure of honeycomb cells, having a hexagonal pattern. The hexagonal cells interconnect to form a dense, structurally efficient network. The aligned rectilinear infill is composed of parallel lines that are aligned in one direction, without forming a grid. The lines are arranged in layers, with each layer oriented in a single direction. These structures exhibit distinct mechanical and thermal behaviors, influencing the material distribution, contractions and deformations of the parts. Their choice allows the investigation of the effect of the infill pattern on the dimensional accuracy and geometric deviations, providing useful information for the optimization of the FDM process.

The second input factor is the raster angle, Figure 2. This 3D printing parameter refers to the angle at which extrusion lines are laid during 3D printing, especially in infill types or in the part's support structure. An optimized raster angle can help evenly distribute forces and ensure adhesion between layers acting on the part, reducing the risk of deformation. The 90° raster angle was omitted because preliminary studies and existing literature indicate that it has similar effects to other angles in combination with these fill types and does not bring additional information relevant to the purpose of the analysis.

The third controlled parameter selected in the research is the number of wall loops (wall layers). An increased number of wall loops increases the walls' thickness of the part, which improves strength and durability and provides better support for the inner layers and infill.

A full factorial design of experiments with three factors each at three levels was considered for each filament type. Table 1 presents the input factors chosen in the experiments and their levels of variation.

To conclude, the choice of these parameters was made because: infill pattern affects the way the material is distributed inside the piece, and implicitly, contractions and

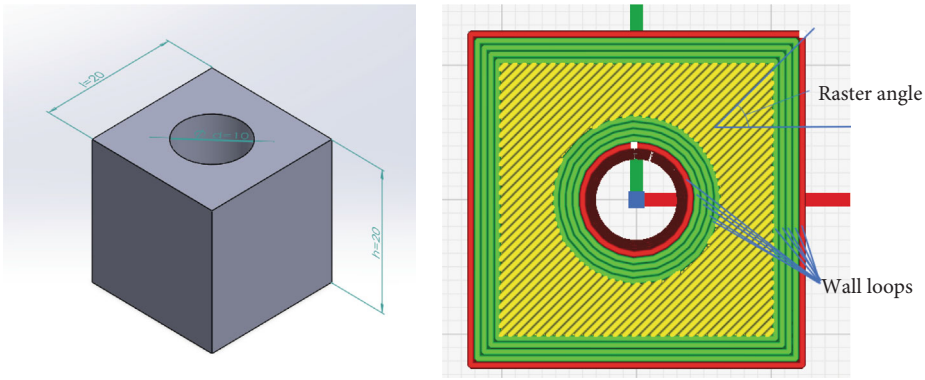

(a) (b)

FIGURE 2: (a) Part geometry; (b) controlled parameters: raster angle and wall loops.

TABLE 1: Input factors of the factorial design.

Level	Factor		
	Infill pattern	Raster angle (°)	Wall loops
1	Grid	0	4
2	Honeycomb	15	5
3	Aligned rectilinear	45	6

TABLE 2: Printing conditions.

Printing temperature	215°C
Bed temperature	60°C
Infill	70%
Layer height	0.2 mm
Printing speed inner wall	300 m/min
Printing speed outer wall	200 m/min
Travel speed	500 m/min
Nozzle diameter	0.4 mm

deformations; raster angle influences the anisotropy of parts and dimensional deviations in certain directions; the number of wall loops determines the thickness of the wall and the stability of the external geometry, having a direct impact on the accuracy of critical dimensions, such as holes.

The FDM printing was carried out on a Bambu Lab X1 from Austin, Texas, United States desktop printer. The printing conditions used in the experiments are presented in Table 2.

The hole dimensional and form accuracy were measured using a coordinate measuring machine (CMM) Type Wenzel LH87, produced by WENZEL Group GmbH & Co. KG from Germany. The Wenzel LH87 is a high-quality measuring machine, ideal for industrial applications requiring high precision (up to 0.8 μm). The least square computing method was used for the measurements. After preprobing, the measurement was carried out automatically, thus eliminating possible human errors. Automatic measurement was configured to take four evenly distributed points to ensure complete coverage of the shape, on the circumferences of three circles arranged at distances of 4 mm between them and 5 mm from the upper plane, as it can be seen in Figure 3.

To evaluate the holes, four points on each circle and three circles distributed over the height of the part were used, according to the principles defined in ISO 1101:2017 and ISO 12181, this approach ensuring a compromise between measurement accuracy and experimental feasibility.

Besides the hole inspection, also the other dimensions were measured and analyzed. In order to fully establish the printed part accuracy, the part height and width were also measured. A profilometer with confocal microscopy and interferometry produced by Mahr GmbH, Germany type CWM100 was used to analyze the surface texture and determine the surface roughness. For a more concise analysis, an area surface parameter was chosen. The investigate surface roughness parameter was Sa (μm)—the arithmetical mean height that measures the average of the absolute values of the deviations of each point on a surface from a reference plane (the mean plane). Sa is the 3D equivalent of the linear parameter Ra, but it considers an entire surface, not just a single profile. After measurements, all the experimental data was processed by using a specialized statistic software Minitab 20.

3. Results and Discussion

In the case of 3D printing, the type of filament turned out to have an extremely pronounced influence on the quality of the surfaces obtained. The roughness parameters obtained when printing the polymer composite filament with wood fibers were on average up to 123.91% higher than the roughness parameters Sa obtained for surfaces printed with PLA filament.

Figure 4 exposes the differences of surface textures of the PLA printed parts and the ones printed with PLA wood pine filament obtained by using the same printing conditions.

The analysis of the topography of the surfaces revealed significant differences between the parts made with different filaments. The surface of the part obtained with WPC

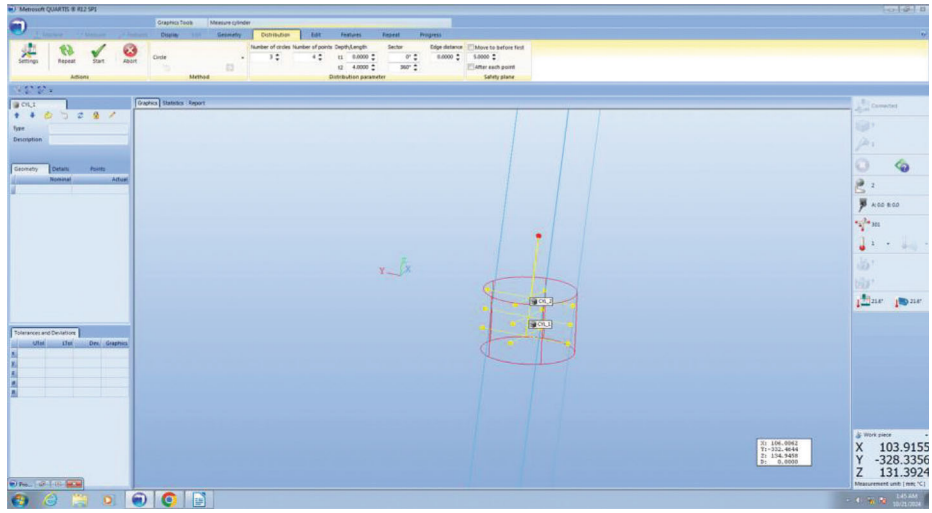

Figure 3: Hole dimensional and shape accuracy measurement.

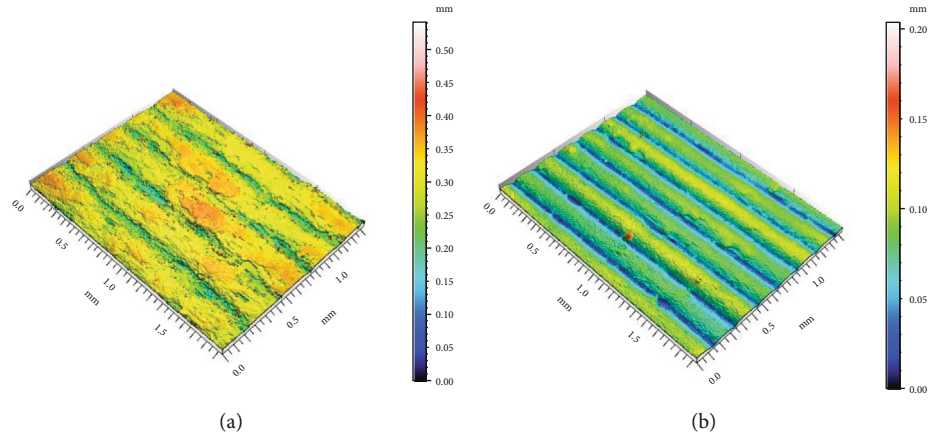

(a) (b)

Figure 4: The lateral surface texture: (a) WPC filament; (b) PLA filament.

filament shows increased roughness and irregular texture, indicating a decline in surface quality compared with PLA. In contrast, the surface of the part printed with PLA filament has a much more uniform profile with reduced height variations, characteristic of a print with homogeneous and stable material. These differences have a direct impact on the behavior of the parts in functional, esthetic applications and can also affect part geometrical accuracy. Although the layer height was kept constant for both filament types, the obvious differences in deposition width observed in profilometry are explained by the different behavior of the materials during deposition. Filaments with high viscosity or inhomogeneous composition tend to create more diffuse bands with a more flattened relief, whereas homogeneous and fluid materials, as PLA, maintain a well-defined pitch, generating a more regular and rhythmic texture.

For parts printed with composite filament, inconsistent surface texture such as under-extrusion and voids was observed microscopically in certain isolated areas. These errors were mainly caused by clogging as it can be seen in Figure 5. Stringing and artifacts were also observed in certain cases revealing instabilities in the printing process.

Figure 6 presents the main effects plots obtained after processing the experimental data for the area surface roughness parameter, Sa.

By analyzing the main effect plots, we can observe that in the case of WPC filament printed parts, the raster angle significantly influences the surface quality due to the anisotropic nature of the material and the tendency of the wood fibers to align in the extrusion direction. In contrast, for the PLA printed parts, the infill pattern has a more pronounced influence, given the homogeneous behavior of the material and the way in which the internal structure influences the geometric stability and stress dissipation during cooling.

As shown in Figure 6, increasing the raster angle improves the surface quality of both PLA and WPC specimens by promoting better alignment of deposition lines and reducing visible layer steps. Additionally, the infill pattern affects internal material distribution and layer uniformity, whereas the number of wall loops influences the thickness and continuity of external walls, directly impacting surface roughness. These observations highlight the combined effect of process parameters on surface quality.

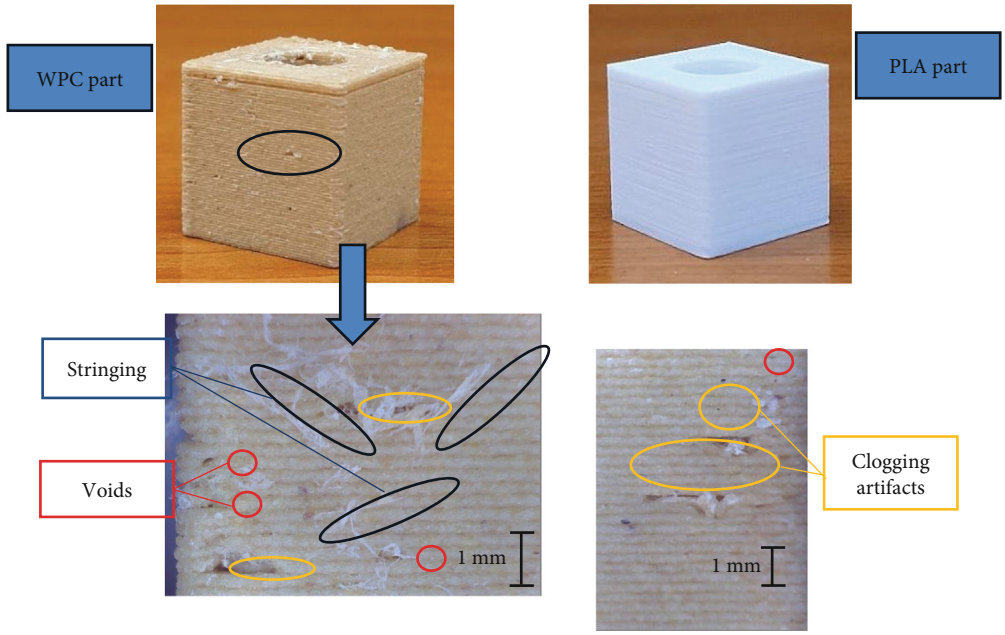

Figure 5: Microscopic images of sample surfaces with inconsistent surface texture.

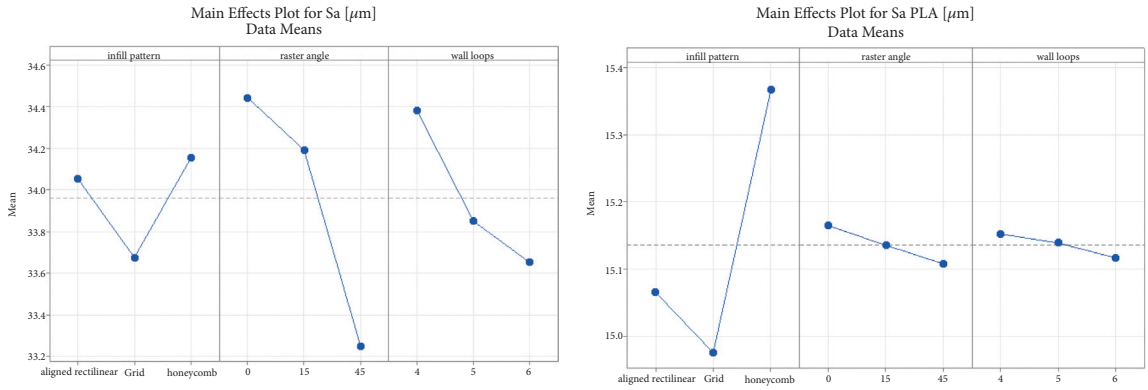

(a) (b)

Figure 6: Main effects plots for area surface roughness parameter Sa (μm) of parts printed with (a) pine wood—PLA composite filament; (b) PLA filament.

The interaction plots for Sa PLA indicate that the effects of raster angle and wall loops depend on the type of infill; for example, rectilinear aligned shows a more pronounced increase in roughness for the 45° angle compared with other fill patterns, highlighting the importance of considering interactions in optimizing printing parameters, Figure 7.

Parts printed with pine-PLA WPC filament have a significantly rougher surface, and the control of the raster angle becomes more important to reduce roughness. Raster angle has the greatest influence on roughness: for both PLA and WPC printed parts, the 15° angle generates the highest Sa values, whereas the 45° angle leads to smoother surfaces. To obtain the smoothest possible surface, it is recommended to print PLA with grid type infill and a raster angle of 0°–45°, and for WPC-PLA to use the angle of 45° and 5–6 wall loops.

In Figure 8 the main effect plots for the values obtained for the hole diameter deviation, ε_d (mm) after measuring the hole diameter on the coordinate measuring machine are presented.

In the case of PLA printed parts, a higher number of wall loops can assure a better dimensional accuracy of the holes. This is due to the fact that as the material tends to shrink slightly when cooling, holes result with smaller diameters than the one desired. By contrast, results show that for the WPC composite filament printed parts, the wood fibers assure better stability and therefore fewer wall loops are necessary to maintain the designed geometry. Too many wall loops in the case of wood-polymer composites conducts to the local accumulation of material and reduce accuracies. The infill type influences the printed hole accuracy due to the number of contact points between the infill pattern and wall loops. Small raster angles (0°, 15°) are disadvantageous for materials with high viscosity such as wood fiber–polymer composites, as they favor the accumulation of material

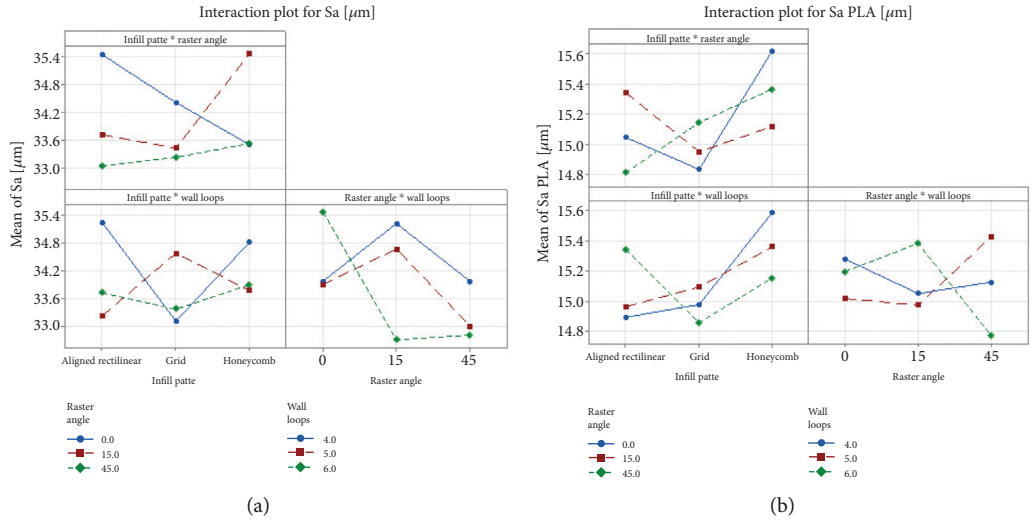

(a) (b)

FIGURE 7: Interaction plots for area surface roughness parameter Sa (μm) of parts printed with: (a) pine wood—PLA composite filament; (b) PLA filament.

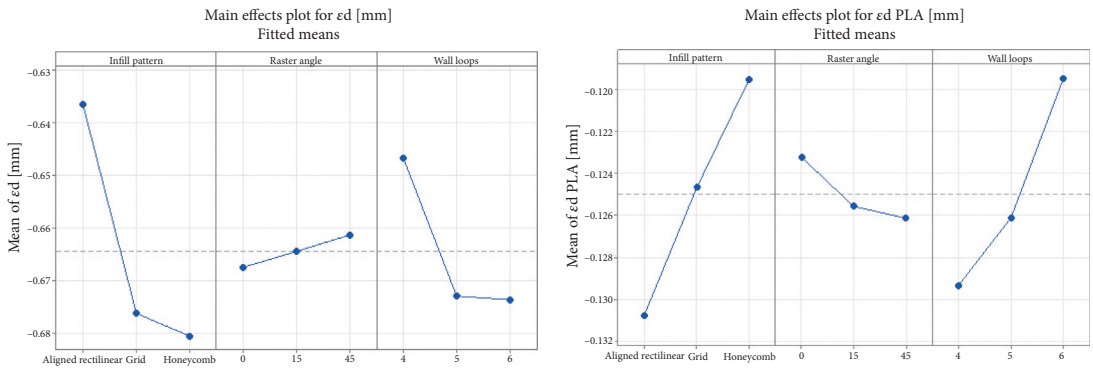

(a) (b)

FIGURE 8: Main effects plots for diameter deviations of parts printed with (a) pine wood—PLA composite filament; (b)PLA filament.

towards the interior. At the same time, composite fibers tend to align along the direction of the print path, and when the path involves changes in direction at a small angle, the fibers do not have enough deflection to reorient themselves, which can lead to: local accumulations of material in the bend areas or even surface defects due to uneven layer overlap.

When the raster is oriented at a small angle, the material lines intersect the hole contour more often, thus ensuring better structure stability in the case of materials such as PLA that exhibit shrinkage at cooling. This may explain why lower diameter deviations were obtained when the prints were carried out with the 0° raster angles.

The reduction in hole diameter accuracy observed with an excessive number of wall loops in WPC parts is due to the higher local infill density in the wall regions. As more wall loops are added, material accumulates in these areas, affecting the geometry of adjacent features. This effect highlights the interaction between wall design and infill on dimensional precision.

In the analysis of hole accuracy, it was observed that the type of infill influences the interaction with wall loops not only through contact points but also through linear contacts, which determines a larger or smaller contact area between the infill layer and the part wall. Contact area is a more relevant indicator for assessing structural accuracy, and experimental data show that a larger contact area contributes to structural stability and reduced hole dimensional deviations for both PLA and WPC.

Figure 9 presents the main influences exhibited by the investigated input factors: infill pattern, raster angle and wall loops over the shape accuracy of the printed holes. For both types of filaments, the shape accuracy of the printed holes was better in the case of the grid infill patterns. The interaction between infill and wall loops involves both point and line contacts. The contact area between infill and wall loops represents a more relevant indicator for the evaluation of structural accuracy, and experimental observations show that a larger contact area contributes to structural stability and to the reduction of dimensional deviations of the holes. Also, the larger raster angle (45°) contributes to better geometric stability and uniform deposition in curved areas assuring improved shape accuracies. The bigger number of wall loops can improve the strength and integrity of the part, conducting to better shape accuracies for the PLA and pine

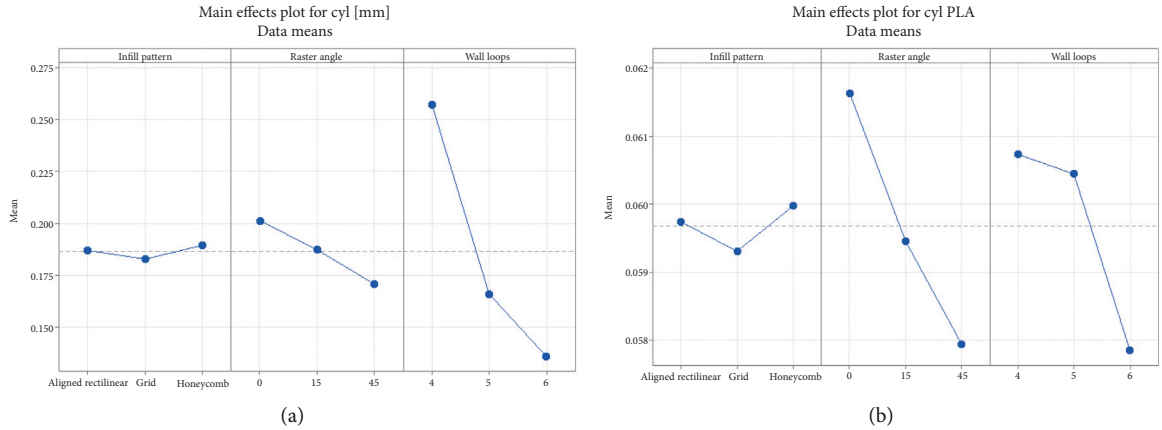

(a) (b)

FIGURE 9: Main effects plots for the hole shape accuracy (cylindricity) of parts printed with: (a) pine wood—PLA composite filament; (b) PLA filament.

fiber-PLA composite. PLA parts printed at 0° show the weakest cylindricity. These results highlight that raster angle influences cylindricity deviations in a more complex way and depend on the interaction with other printing parameters.

Regarding the raster angles, the analysis of the cylindricity of the PLA parts (Figure 8) reveals that the values corresponding to the 0° raster show the weakest cylindricity, contradicting the initial claim that small angles would increase structural stability. These results indicate that the effect of raster angle on cylindricity deviations is complex and depends on the interaction with other printing parameters. In conclusion, experimental observations suggest that optimizing the accuracy of PLA and WPC 3D parts requires a combined approach, which takes into account both the type of infill, the number of wall loops, and the raster angles, in order to achieve superior structural stability and dimensional accuracy.

Also, the results showed that better hole dimensional accuracy was obtained for the PLA printed parts when honeycomb infill was used. This could be because this type of infill is based on hexagonal cells, which provides a uniform distribution of mechanical forces, high stability and more uniform cooling of the part.

The better hole dimensional accuracy of the pine fiber composite printed parts with aligned rectilinear infill can be explained by the fact that compared with the other two types of infill, this infill assures fewer intersections with the hole walls.

Analysis of variance, presented in Table 3, shows that only the number of wall loops has a significant effect on the deviation from cylindricity ($F = 6.94$, $p = 0.005$). The parameters infill pattern and raster angle do not significantly influence the shape of the holes ($p > 0.05$). This suggests that an increase in the number of wall layers contributes to better geometric stability of the inner contour and a reduction in circular distortions.

The improvement in cylindricity observed for certain infill patterns can be attributed to a more uniform distribution of contacts between the internal structure and the hole wall. Although a quantitative characterization of the contact uniformity for each infill pattern was not performed in this study, the experimental observations suggest that patterns with more evenly distributed contacts contribute to higher structural stability and reduced dimensional deviations. Future work could focus on quantifying this uniformity to provide a more precise correlation between infill design and hole accuracy.

TABLE 3: Analysis of variance for the linear model of the cylindricity of WPC printed parts.

Source	DF	Adj SS	Adj MS	*F* value	*p* value
Infill pattern	2	0.000203	0.000102	0.02	0.981
Raster angle	2	0.004189	0.002095	0.41	0.672
Wall loops	2	0.071617	0.035809	6.94	0.005
Error	20	0.103181	0.005159		
Total	26	0.179191			

Figures 10 and 11 expose the main effects plots for the linear dimensional deviations measured for the part height—ε_h (mm), and width—ε_l (mm). Being a material with high contraction, PLA printed parts resulted in negative deviations, that is, values slightly lower than the ones designed. In general, fibers in the WPC composition can help reduce shrinkage and deformation of the part during cooling. Pine is a softwood and therefore, the pine wood—-PLA composite is expected to tend to be more elastic with greater dimensional fluctuations during cooling and solidification, and the dimensions of printed parts resulted in positive deviation.

For linear dimensions the higher raster angle assured the best accuracy for the 3D printed parts made of pine WPC filament. Contrary to the trends identified in the specialized literature [14] in the experiments carried out on the Bambu Lab printer, the 0° raster angle led to superior dimensional accuracy in both linear directions and circular features. This difference can be attributed to a combination of the mechanical rigidity of the printer, the accuracy of the *x*-axis (primary in the 0° raster), the lack of frequent repositioning, but also the stability of the flow of the PLA material on rectilinear trajectories.

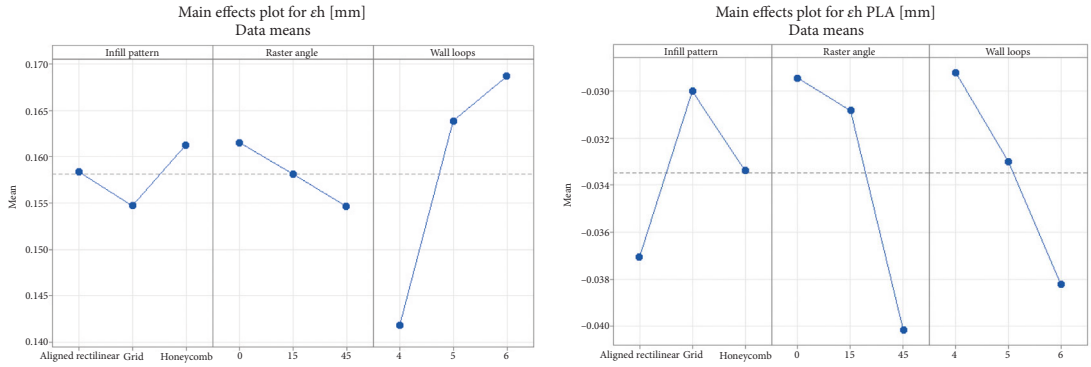

(a) (b)

FIGURE 10: Main effects plots for the height deviations of parts printed with: (a) pine wood—PLA composite filament; (b) PLA filament.

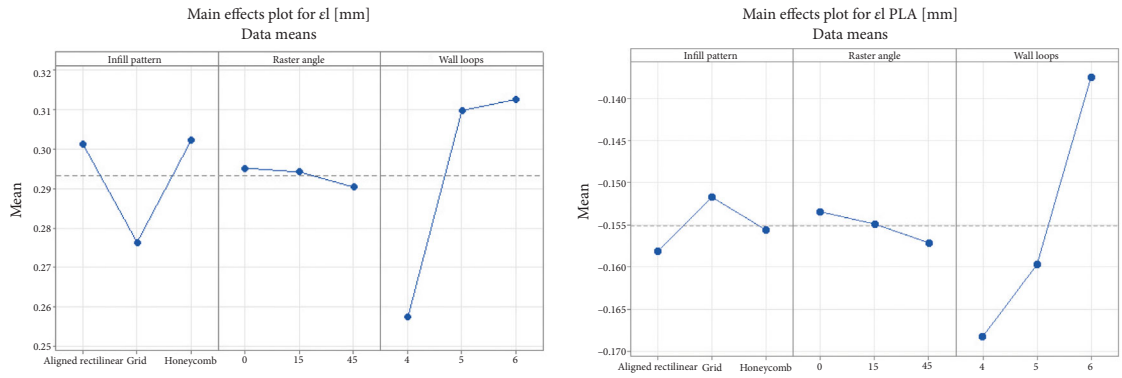

(a) (b)

FIGURE 11: Main effects plots for the width deviations of parts printed with: (a) pine wood—PLA composite filament; (b)PLA filament.

The results highlight the importance of experimental validation of print settings, as the actual behavior may differ significantly from that estimated based on generalized models.

For the WPC printed parts, lower dimensional deviations are obtained for the 45° raster angles, whereas for the PLA parts, printings carried out with 0° assured more favorable effect on the dimensional accuracy. A smaller number of wall loops can have a favorable effect on dimensional accuracy per height when printing with PLA, under certain conditions. When the number of perimeters is reduced, there is less overlap between the nozzle paths, which can lessen the build-up of errors at each layer and reduce the overextrusions of the edges of the part, resulting in a height closer to the designed one.

Differences in shrinkage and material distribution depending on the type of infill (grid, honeycomb, and rectilinear) can slightly change the final dimensions of the parts. For example, grid-type infill distributes cooling stresses more evenly, helping to reduce dimensional deviations across length and width. Increasing the number of wall loops strengthens the outer walls, limits lateral shrinkage, and maintains the shape of the part, which leads to a decrease in the experimentally observed width deviation.

Analysis of variance for the linear model of the length error of the WPC printed parts, Table 4 shows that the overall model is significant ($F = 2.93$, $p = 0.032$). Among the analyzed parameters, the number of wall layers (wall loops) is the most influential factor, having a significant effect on the error in length ($F = 7.17$, $p = 0.004$), whereas the type of filling (infill pattern) and the raster angle (raster angle) have no significant influence ($p > 0.05$). These results indicate that adjusting the number of wall layers is essential to improve the longitudinal accuracy of FDM parts.

TABLE 4: Analysis of variance for the linear model of the length error, e_l.

Source	DF	Adj SS	Adj MS	*F* value	*p* value
Model	6	0.021276	0.003546	2.93	0.032
Linear	6	0.021276	0.003546	2.93	0.032
Infill pattern	2	0.003833	0.001917	1.59	0.229
Raster angle	2	0.000119	0.000059	0.05	0.952
Wall loops	2	0.017324	0.008662	7.17	0.004
Error	20	0.024166	0.001208		
Total	26	0.045442			

Analysis of variance for length error of FDM PLA parts, presented in Table 5 indicates that the linear model is significant ($F = 4.64$, $p = 0.004$). Among the analyzed parameters, the number of wall loops has a major impact on the

TABLE 5: Analysis of variance for the linear model of the length error, e_l of PLA parts.

Source	DF	Adj SS	Adj MS	F-Value	P-Value
Model	6	0.004778	0.000796	4.64	0.004
Linear	6	0.004778	0.000796	4.64	0.004
Infill pattern	2	0.000187	0.000093	0.54	0.589
Raster angle	2	0.000061	0.000031	0.18	0.837
Wall loops	2	0.004530	0.002265	13.21	≤ 0.001
Error	20	0.003430	0.000172		
Total	26	0.008208			

longitudinal accuracy ($F = 13.21$, $p \leq 0.001$), whereas the type of filling (infill pattern) and the raster angle (raster angle) have no significant effect ($p > 0.05$). This suggests that, for PLA, adjusting the number of wall layers is the critical factor for controlling length error.

Compared with WPC printed parts, where the number of wall layers was also the dominant factor, a similarity in the behavior of the printing parameters is observed: the type of filling and the raster angle have little influence on the length error in both materials. However, the magnitude of the effect for wall loops is more pronounced in PLA, indicating that the pure polymer material responds more predictably to the change of this parameter, whereas WPC, due to the presence of wood fibers, shows a more complex and dispersed sensitivity to the same parameters. This observation emphasizes the need to adjust parameters specifically for the material used to achieve optimal dimensional accuracy.

4. Conclusions

Wood plastic composites are ideal for 3D printing of esthetic prototypes, decorative objects, or components with moderate loads due to advantages such as increased rigidity, wood appearance, biodegradability, and easy machining. The paper presents a comparative analysis of the accuracy obtained by FDM machining with a commercially available pine-PLA composite filament and a PLA filament. The results expose major differences not only in exterior appearance but also in surface roughness, dimensional, and shape accuracy. The article also investigates the influence of infill pattern, raster angle, and number of wall loops on the output parameters mentioned above.

The area surface roughness parameter Sa (arithmetical mean height) for the lateral surface of the printed parts was approximately 124.39% higher for the parts made of WPC than the PLA ones. The hole shape accuracy was approximately 215.25% higher for WPC parts than PLA. Pine wood-PLA composite parts resulted in positive deviations for the linear dimensions and negative deviations for the interior cylindric surface compared with PLA parts that had negative deviations for all the measured dimensions. The average deviation of the hole diameters printed with the PLA filaments and the specific printing parameters presented in the second section of the paper was −0.126 mm whereas for WPC parts was −0.671 mm. The part heights and widths were also significantly lower for the PLA printed parts. Superior hole accuracies were obtained for the WPC parts printed with aligned rectilinear infill, 45° raster angles and the higher number of wall loops, whereas the PLA printed parts exposed better hole accuracies for honeycomb infills, 0° raster angles and lower wall loops. For both types of filaments, the best shape accuracy was obtained with grid infill, 45° raster angles and the highest number of wall loops.

The grid infill assured better linear dimensional accuracy for the FDM generated parts. This may be due to the superior consistent mechanical resistance of the grid structures and the fact that it assures good layer adhesion and optimal support for surfaces.

Data Availability Statement

The data that support the findings of this study are available from the corresponding author upon reasonable request.

Conflicts of Interest

The authors declare no conflicts of interest.

Funding

No funding was received for this manuscript.

References

[1] ISO/ASTM 52900; International Standard, *Additive Manufacturing—General Principles—Fundamentals and Vocabulary* (ISO/ASTM International, 2021).

[2] M. Bhayana, J. Singh, A. Sharma, and M. Gupta, "A Review on Optimized FDM 3D Printed Wood/PLA Bio Composite Material Characteristics," *Materials Today: Proceedings* 17 (2023): https://doi.org/10.1016/j.matpr.2023.03.029.

[3] M. S. Wagh, S. S., P. C. Nath, et al., "Valorisation of Agro-Industrial Wastes: Circular Bioeconomy and Biorefinery Process—A Sustainable Symphony," *Process Safety and Environmental Protection* 183 (2024): 708–725, https://doi.org/10.1016/j.psep.2024.01.055.

[4] D. Krapež Tomec, M. Schwarzkopf, R. Repič, J. Žigon, B. Gospodarič, and M. Kariž, "Effect of Thermal Modification of Wood Particles for Wood-PLA Composites on Properties of Filaments, 3D-Printed Parts and Injection Moulded Parts," *European Journal of Wood and Wood Products* 82, no. 2 (2024): 403–416, https://doi.org/10.1007/s00107-023-02018-2.

[5] A. Kaptan and F. Kartal, "A Critical Review of Composite Filaments for Fused Deposition Modeling: Material Properties, Applications, and Future Directions," *European Mechanical Science* 8, no. 3 (2024): 199–209, https://doi.org/10.26701/ems.1451829.

[6] T.-C. Yang and C.-H. Yeh, "Morphology and Mechanical Properties of 3D Printed Wood Fiber/Polylactic Acid Composite Parts Using Fused Deposition Modeling (FDM): The Effects of Printing Speed," *Polymers* 12, no. 6 (2020): 1334, https://doi.org/10.3390/polym12061334.

[7] M. D. Zandi, R. Jerez-Mesa, J. Lluma-Fuentes, J. Jorba-Peiro, and J. A. Travieso-Rodriguez, "Study of the Manufacturing Process Effects of Fused Filament Fabrication and Injection Molding on Tensile Properties of Composite PLA-Wood Parts," *International Journal of Advanced Manufacturing*

Technology 108, no. 5-6 (2020): 1725–1735, https://doi.org/10.1007/s00170-020-05522-4.

[8] S. N. H. Mazlan, A. Z. Abdul Kadir, M. R. Alkahari, and T. K. Land, "Accuracy Evaluation of Thin Wall Features Fabricated by Fused Deposition Modeling Using Reinforced Composite Materials," *Progress in Additive Manufacturing* 8, no. 6 (2023): 1357–1366, https://doi.org/10.1007/s40964-023-00403-0.

[9] A. Cekic, D. Begic-Hajdarevic, K. Muhamedagic, and N. Guzanovic, "Experimental Investigations of Process Parameters Influence on Dimensional Accuracy and Mechanical Properties of FDM Manufactured Parts," in *Proceedings of the 29th DAAAM International Symposium*, ed. B. Katalinic (DAAAM International, 2018), 0210–0214, https://doi.org/10.2507/29th.daaam.proceedings.030.

[10] D. Popescu, C. Gheorghe Amza, R. Marinescu, M. Cristiana Iacob, and N. Luminița Căruțașu, "Investigations on Factors Affecting 3D-Printed Holes Dimensional Accuracy and Repeatability," *Applied Sciences* 13, no. 1 (2023): 41, https://doi.org/10.3390/app13010041.

[11] R. E. Petruse, C. Simion, and I. Bondrea, "Geometrical and Dimensional Deviations of Fused Deposition Modelling (FDM) Additive-Manufactured Parts," *Metro* 4, no. 3 (2024): 411–429, https://doi.org/10.3390/metrology4030025.

[12] M. A. Boca, A. Sover, and L. Slătineanu, "The Dimensional Accuracy of Plastic Parts Made by the Fused Filament Fabrication," *IOP Conference Series: Materials Science and Engineering* 997, no. 1 (2020): 012021, https://doi.org/10.1088/1757-899X/997/1/012021.

[13] A.-A. Ene, T. G. Alexandru, and D. Popescu, "Dimensional Accuracy in 4D-Printed PLA Objects With Holes: Experimental and Numerical Investigations," *Designs* 8, no. 3 (2024): 56, https://doi.org/10.3390/designs8030056.

[14] O. Tunçel, "The Influence of the Raster Angle on the Dimensional Accuracy of FDM-Printed PLA, PETG, and ABS Tensile Specimens," *European Mechanical Science* 8, no. 1 (2024): 11–18, https://doi.org/10.26701/ems.1392387.

[15] J. Pratama, N. Mayanda, and D. Sugiyanto, "Effect of Extruder Temperature on Dimensional Accuracy and Surface Roughness of Fused Deposition Modeled (FDMed) PLA and PLA/Wood Composite," *Rotasi* 24, no. 2 (2022): 1–9, https://doi.org/10.14710/rotasi.24.2.1-9.

[16] N. Jayakumar, G. Senthilkumar, and M. Kumar, "Investigation on Geometric, Dimensional Accuracy and Surface Roughness for 3D Printed PLA via Fused Deposition Modelling (FDM) Process," *Proceedings of the Institution of Mechanical Engineers, Part E: Journal of Process Mechanical Engineering* 9544089241312637 (2025).

[17] Z. Ahmadi, M. Najafi, A. Nejadebrahim, and M. Ataeefard, "Investigation of Printing Parameters on Dimensional Accuracy of Geometrically Complex Objects in FDM 3D Printing," *Progress in Color, Colorants and Coatings* 18, no. 4 (2025).

[18] A. Neacșa, A. Diniță, and Ș. V. Iacob, "Can the Dimensional Optimisation of 3D FDM-Manufactured Parts Be a Solution for a Correct Design?," *Materials* 18, no. 2 (2025): 408, https://doi.org/10.3390/ma18020408.

[19] A. Karadag and O. Ulkir, "Prediction of Dimensional Accuracy and Surface Quality in Additively Manufactured Biomedical Implants Using ANN," *International Journal of Precision Engineering and Manufacturing* 26, no. 5 (2025): 1187–1213.

[20] Y. Li, A. Molazem, H. I. Kuo, V. Ahmadi, and V. P. Shastri, "Comparative Analysis of Dimensional Accuracy in PLA-Based 3D Printing: Effects of Key Printing Parameters and Related Variables," *Polymers* 17, no. 12 (2025): 1698, https://doi.org/10.3390/polym17121698.

[21] M. Jusufagić and M. Obućina, "Use of Wood-Plastic Composites Obtained by 3D Printing: A Review," in *New Technologies, Development and Application VIII. NT 2025*, eds. I. Karabegović, A. Kovačević, and S. Mandžuka (1482 of Lecture Notes in Networks and Systems, , Springer, 2025), https://doi.org/10.1007/978-3-031-95194-7_23.

[22] P. L. A. AzureFilm LumberLay, "Technical Data Sheet" Accessed on July 2025, Available online: https://azurefilm.com/wp-content/uploads/2023/10/EN_TDS-LumberLay.pptx.pdf.

[23] P. L. A. AzureFilm LumberLay, "Material Safety Data Sheet" Accessed on July 2025, Available online: https://azurefilm.com/wp-content/uploads/2023/10/Wood_Pine_MSDS.pdf.

[24] FormFutura Premium PLA–Frosty White Technical Data SheetAvailable online: https://www.formfutura.com/shop/premium-pla-133?category=5#attr=2695,2700,2708,4043,5873,5874,5875,5876,5877,5878,5879,5880,5881,6433,6434,6435,6436,6860,6770 with pdf download link: https://www.formfutura.com/web/content/256614?download=true (accessed on July 2025.

[25] FormFutura Premium PLA–Frosty White Material Safety Data SheetAvailable online: https://www.formfutura.com/shop/premium-pla-133?category=5#attr=2695,2700,2708,4043,5873,5874,5875,5876,5877,5878,5879,5880,5881,6433,6434,6435,6436,6860,6770 with pdf download link: https://www.formfutura.com/web/content/256613?download=true (accessed on July 2025).